

A MECHANISTIC MODEL FOR MID-LATITUDE

MEAN TEMPERATURE STRUCTURE

by

ANTONY BRETT MULLAN

B.Sc. (Hons), University of Auckland, New Zealand
(1972)

SUBMITTED IN PARTIAL FULFILLMENT OF THE
REQUIREMENTS FOR THE DEGREE OF

DOCTOR OF SCIENCE

at the

MASSACHUSETTS INSTITUTE OF TECHNOLOGY

May, 1979

© Antony Brett Mullan, 1979

Signature of Author _____
Department of Meteorology, May 1979

Certified by _____
Thesis Supervisor

Accepted by _____
Chairman, Departmental Committee on Graduate Students

Lindgren

MASSACHUSETTS INSTITUTE OF TECHNOLOGY
LIBRARIES

JUN 23 1979

LIBRARIES

A MECHANISTIC MODEL FOR MID-LATITUDE
MEAN TEMPERATURE STRUCTURE

by

ANTONY BRETT MULLAN

Submitted to the Department of Meteorology on 17 May, 1979
in partial fulfillment of the requirements
for the Degree of Doctor of Science

ABSTRACT

A simple two-dimensional mechanistic model of the atmospheric circulation is presented. It is intended to provide insight into the relative importance of many of the physical processes affecting the equilibrium climate in middle latitudes. For this purpose, we develop equations for the mean temperature and the mean horizontal and vertical temperature gradients in the troposphere. We assume the horizontal flux of latent and sensible heat is carried entirely by the large-scale baroclinic eddies, and ignore the mean meridional circulation and oceanic transports. Vertical fluxes are present, due to both the large-scale eddies and small-scale convective motions. The small-scale transport is coupled to the large-scale dynamics through the surface wind speed variance used in evaluating the latent and sensible heat fluxes of the surface energy balance. We suggest a simple parameterization for this surface wind speed that is in good agreement with seasonal data, and is self-consistent with Stone's (1972a) parameterization of the sensible heat fluxes by baroclinic eddies.

The tropospheric radiative effects of water vapor, carbon dioxide, ozone and clouds are treated in some detail. Cloud amounts are fixed at climatological values, and several different cloud-height feedbacks are studied. We also develop a method for calculating the tropopause height from the vertical structure of the atmosphere, based on the assumption of radiative equilibrium in the lower stratosphere. Reasonable values for the mean tropopause height and its latitudinal variations are obtained. This interaction between vertical structure and tropospheric depth may be important in some climate sensitivity calculations, particularly those involving ozone changes.

Calculations are made first with a simplified version of the full model. The simplified version uses a grey radiation model, with all the vertical dynamical flux carried by the baroclinic eddies. This model differs from Stone's (1972a) primarily because of the addition of large-scale latent heat fluxes. We find the lapse rate is still unstable to

moist convective motions. The addition of a latent heat flux reduces the pole to equator temperature gradient over the case with sensible heat alone. At the same time, the vertical stability is reduced further due to the relatively smaller effect of latent heating on the large-scale vertical fluxes.

In verification tests of the full model, we find reasonable simulation of the mid-latitude tropospheric structure. In spite of uncertainties in the vertical dynamical flux parameterization, the lapse rate response is consistent with the dry model experiments of Held (1978b) and the mid-to high-latitude results of the GFDL GCM of Wetherald and Manabe (1975). Moreover, our model shows the same high sensitivity in the hydrologic cycle found by Wetherald and Manabe (1975). These results give us some confidence in the predictions of our highly parameterized model, which contains more physics than most simple climate models, and has a more realistic cloud parameterization than some GCM's.

The full model is applied to a number of standard climate calculations. It is less sensitive to external parameter changes than models with fixed cloud temperature, due to the cloud-height feedback that we use. Our findings for the surface temperature changes due to variations in solar insolation and carbon dioxide amount are consistent with other results, given the slightly different parameterizations in our model. For a 50% reduction in ozone concentration, we predict a surface temperature response that is in the opposite direction to that found by previous one-dimensional radiative-convective equilibrium models. Direct comparison is difficult since our model does not parameterize the radiative effects as realistically, and we incorporate more physics than the 1-D models in the determination of the vertical structure.

Thesis Supervisor: Peter H. Stone
Title: Professor of Meteorology

To my parents,

Mr. & Mrs. Anthony J. Mullan

ACKNOWLEDGEMENTS

I wish to thank Professor Peter H. Stone for his guidance and support throughout the course of this study. His demand for precision and physical interpretation, as well as his extensive knowledge of the literature, was a valuable learning experience for me. I also benefited from a few discussions with Professor Ron G. Prinn.

I express my gratitude to other faculty members for their entertaining lectures, the notes of which will serve as a useful reference in years to come.

Many thanks are due to Patty Farrell and Virginia P. Siggia for their skillful handling of a difficult typing job, and to Isabelle Kole for her rapid and accurate drafting of the figures.

My stay at M.I.T. was made possible by a fellowship from the New Zealand National Research Advisory Council, and leave granted by the New Zealand Meteorological Service. The patience and consideration shown by the Met. Office for my extended stay and infrequent letters home is greatly appreciated.

This research was also supported in part by the National Aeronautics and Space Administration under Grant NGR 22-009-727.

Finally, my special thanks to the many friends I have gained, both within and outside the Institute, who have made my stay in the United States such a pleasant one.

TABLE OF CONTENTS

	Page #
ABSTRACT	2
ACKNOWLEDGEMENTS	5
TABLE OF CONTENTS	6
LIST OF FIGURES	9
Chapter 1 MODELING PHILOSOPHY AND OBSERVATIONAL SUPPORT	12
1.1 Introduction	12
1.2 Outline of the dynamical model	15
1.3 Stone's model	22
1.4 Leovy's parameterization of the latent heat fluxes	24
1.5 Observed temperature structure	30
-1.5.1 Surface temperature	30
-1.5.2 Vertical temperature gradient	34
-1.5.3 Meridional temperature gradient	37
Chapter 2 DYNAMICAL MODEL	45
2.1 Derivation of basic equations	45
2.2 Temperature field	54
-2.2.1 Relation between lapse rate & static stability	56
-2.2.2 Horizontal temperature gradients $\frac{\partial T}{\partial \phi}$ and $\frac{\partial \theta}{\partial \phi}$	58
2.3 Hemispheric forcing functions	59
-2.3.1 $\langle T \rangle$ equation	60
-2.3.2 B equation	61
-2.3.3 A equation	63
Chapter 3 MODEL RESULTS WITH GREY RADIATIVE HEATING	65
3.1 Simplified equations	65
-3.1.1 Choice for weighting factor α	66
3.2 Grey radiative equilibrium state	70
3.3 Results	75
-3.3.1 Method of solution	75
-3.3.2 Variation with tropopause slope	77
-3.3.3 Addition of latent heat	85
-3.3.4 Variation with relaxation time constant	91
-3.3.5 Variation with grey absorption coefficient	93

	Page
Chapter 4 NON-GREY RADIATIVE TREATMENT AND OTHER PARAMETERIZATIONS	96
4.1 Solar insolation	96
4.2 Non-grey radiation model	99
-4.2.1 Amounts of the absorbing gases: H ₂ O, CO ₂ and O ₃	99
-4.2.2 Parameterization of long-wave radiation	107
-4.2.3 Sasamori's absorptivity formulae	110
-4.2.4 Parameterization of short-wave heating	112
4.3 Results of non-grey calculations (without clouds)	114
-4.3.1 Calculation of tropopause height H	114
-4.3.2 Infra-red emission to space	127
4.4 Small-scale moist convection	130
4.5 Surface energy balance	135
-4.5.1 Parameterization of surface wind speed variance	138
Chapter 5 RADIATIVE FEEDBACKS AND THE EFFECT OF CLOUDS	144
5.1 Cloud observations and single effective cloud model	144
5.2 Cloud-height feedbacks	152
-5.2.1 Data comparison	152
-5.2.2 Model comparison	156
5.3 Long-wave cooling calculations with clouds	164
-5.3.1 Effect of clouds	164
-5.3.2 Sensitivity of heating profile to vertical distribution of clouds	166
5.4 Short-wave heating calculations with clouds	167
Chapter 6 RESULTS OF THE FULL MODEL	178
6.1 Method of solution	178
-6.1.1 Some features of the equilibrium solution	182
6.2 Parameter sensitivity studies	187
-6.2.1 Variation with convective parameter b	187
-6.2.2 Dependence on cloud-height feedback assumption	196
-6.2.3 Dependence on other internal parameters: d, α_i , h ₀	198
6.3 Climate sensitivity studies - variation with O ₃ , CO ₂ and cloud amount	200
6.4 Climate sensitivity studies - variation with solar constant	207

	Page
Chapter 7 SUMMARY AND CONCLUSIONS	214
APPENDICES	
A1 Leovy parameterization	226
A2 Varying vertical scale H in Stone's model	228
A3 Comparison of horizontal temperature gradients $\frac{\partial T}{\partial \phi}$ and $\frac{\partial \theta}{\partial \phi}$	231
A4 Integrated Leovy factor L_y	232
A5 Analytical approximation to water vapor amount integral	235
A6 Appropriate cloud-height weighting for long- wave flux calculations	239
REFERENCES	242
BIOGRAPHICAL NOTE	248

LIST OF FIGURES

Page

Figure 1.1a.	Total energy transport (SH + PE + LH) of eddies (stationary + transient) and mean meridional circulation for January. [Taken from Oort & Rasmusson, 1971. Tables C7, C8, C9].....	16
Figure 1.1b.	As Fig. 1.1a., but for July.	17
Figure 1.2.	Latitude-height fields of relative humidity in the lower troposphere for summer and winter.	20
Figure 1.3a.	Northward eddy transport of latent heat ('ACTUAL') for January compared to the transport calculated from the sensible heat flux using Leovy's method ('LEOVY').	27
Figure 1.3b.	As Fig. 1.3a., but for July.	28
Figure 1.4.	Mean annual temperature profile at 45°N. [Taken from Oort & Rasmusson, 1971. Tables A4, A5.].....	35
Figure 1.5.	Annual (A), Winter (W) and Summer (S) meridional temperature gradients at 45°N (averaged from 30-60°).	44
Figure 2.1.	Profile of annual northward entropy flux $\frac{\rho(z)}{\rho(0)} \overline{v'\theta'}$ at 45°N (solid curve); scaled shape factor $\Lambda(x)$ (dashed curve), and constant amplitude Eady result (solid rectangle).	53
Figure 3.1.	Total eddy heating in °C/day for grey radiation model as a function of height and latitude. (Model parameters: $\bar{H} = 12.0$ km, $\sigma = 0.0$, $k_0 = 2.0$ cm ² g ⁻¹ , $h_0 = 0.0$, $\tau^* = 5.5$).	80
Figure 3.2.	Total eddy heating in °C/day for $\sigma = 0.4$. (Other parameters as in Fig. 3.1).	83
Figure 3.3.	Total eddy heating in °C/day with latent heat transport included. (i.e. $h_0 = 0.77$. Other parameters as in Fig. 3.1).	88
Figure 3.4a.	Grey radiation model sensible (SH) and latent (LH) heat flux as a function of latitude in units of m °C s ⁻¹ . (Model parameters: $\bar{H} = 12.0$, $\sigma = 0.0$, $k_0 = 2.0$, $h_0 = 0.77$, $\tau^* = 5.5$).	89

Figure 3.4b.	Observed mean annual horizontal eddy fluxes of sensible (SH) and latent (LH) heat in units of $m \text{ } ^\circ\text{C s}^{-1}$	90
Figure 3.5.	Change in mean radiative equilibrium temperature $\langle T_r \rangle$ with $\langle T \rangle$ for various values of grey absorption coefficient k_0 . (Other parameters fixed: $A = -0.5 \text{ } ^\circ\text{K}/100 \text{ km}$, $\beta = 6.5 \text{ } ^\circ\text{K}/\text{km}$, $H = 12.0 \text{ km}$, $\sigma = 0.0$).	95
Figure 4.1.	Vertical distribution of radiative heating for the various component gases of the atmosphere, as found by Manabe & Möller (1961, Figure 13). SH20, SCO2 and SO3 are the heating rates due to absorption of solar radiative by water vapor, carbon dioxide and ozone, respectively. LH20, LCO2 and LO3 are the corresponding heating rates due to long-wave radiation.	100
Figure 4.2.	Vertical temperature structure assumed in the model. Inset shows the smooth 'transition region' between the constant lapse rate troposphere and isothermal stratosphere.	102
Figure 4.3.	Variation of heating at tropopause as a function of H and d . Radiative equilibrium solutions exist where the curves cross the horizontal axis.	119
Figure 4.4.	Components in the heat balance at the tropopause. $s^4 \text{ SW1}$, $s^4 \text{ SW3}$ are short-wave heating by H_2O and O_3 , respectively. LW1 , LW2 are long-wave cooling by H_2O and CO_2	120
Figure 4.5.	Variation of parameter s with tropopause height H and transition depth d	121
Figure 4.6.	As Fig. 4.3., but with CO_2 long-wave heating omitted.	122
Figure 4.7.	Fractional absorptions FT1 and FT2 of water vapor and carbon dioxide, respectively. (A measure of the 'relative greenhouse effect').	128
Figure 4.8.	Vertical distribution of convective diabatic heating in the tropics. (Modified from Marshall Islands data of Yanai et. al., 1973).	132

	Page
Figure 4.9.	Latitudinal distribution of the components of the surface heat balance: net downward short-wave R , net upward long-wave H_B , latent heat H_L , sensible heat H_S , and vertical conduction through sea-ice H_C . (Multiply ordinate by 697 to convert to units of $W m^{-2}$). 139
Figure 4.10.	Comparison of observed surface wind speed variance (from Oort & Rasmusson, 1971. Tables B1, B2) with that predicted by Stone's theory of the unstable baroclinic eddies. (Crosses indicate values for the four seasons and the annual mean, as in Table 4.3). 143
Figure 5.1a.	Variation of cloud heights (base z_{CB} and top z_{CT}) with latitude. 150
Figure 5.1b.	Variation of cloud temperatures (base and top) and surface temperature with latitude. 151
Figure 5.2a.	Long-wave flux to space as observed by satellites (Cess, 1976) and as predicted by a least-square fit for Model '1': constant cloud height $z_C = 4.5$ km, and Model '3': constant fractional cloud height $f_{z_C} = \frac{z_C}{H} = 0.40$ 154
Figure 5.2b.	As Fig. 5.2a, but comparing observation with Model '2': constant cloud temperature $T_C = 250$ K, and Model '4': linear relation between surface temperature and cloud temperature, $T_C = .442 T_0 + 125$ K. 155
Figure 5.3.	Profiles of long-wave heating (in $^{\circ}C/day$) for clear and cloudy skies. ($\beta = 6.5$, $T_g = T_0 = 280$, $h_0 = 1$, $d = 1$, $H = 12$ and there is an infinitesimally thin cloud layer at $z_C = 6$ km). 165
Figure 5.4.	Schematic of cloud model used to calculate short-wave heating. U and D are the upward and downward fluxes in each layer. 170
Figure 6.1.	Change in equilibrium lapse rate β with convective parameter b . The straight line joins points where b is independent of latitude. The fourth point, not on the line, is the latitudinal mean of $b(\phi) = \frac{z_C(\phi)}{H(\phi)}$ 189
Figure 6.2.	Variation of critical latitude (ϕ_C) for ice formation with changing solar constant S_0 210

Chapter 1: Modeling Philosophy and Observational Support

1.1 Introduction

In recent years there has been a growing interest in the problem of climate change. Many modeling approaches have been used, but we may follow Schneider and Dickinson (1974) in identifying two basic types: 'mechanistic' and 'simulation' models. The latter type, whose primary objective is to simulate observed phenomena, has reached the peak of complexity in the three-dimensional global general circulation models. They include so many interacting physical processes that it is usually very difficult to determine the relative importance of each particular mechanism. The large amount of analysis and computer time that is required to understand the results limits the number of simple experiments (varying internal parameters and boundary conditions) that can be made.

On the other hand, mechanistic models select a limited number of physical processes for study, thus allowing an easier understanding of the causes of observed changes and the relative contribution from different terms. It is such a mechanistic model that we propose here.

Our approach is also a useful intermediate step between the simple highly-parameterized models (such as those of Sellers, 1969 and North, 1975) and the complicated GCM's. In the simple models, one usually finds a large number of empirically determined parameters which are assumed to remain constant in a climate change. This is a very strong

restriction to apply to the highly non-linear equations that describe the earth-atmosphere system. By limiting the number of processes we consider, we can treat them in a more realistic manner. In particular, in our model the dynamical fluxes and the radiative effects of clouds are treated more carefully, and the possibility of a lapse rate feedback is included. On the other hand, the model is solely a mid-latitude one. The diagram below (with a few examples given) illustrates the position of our model in a hierarchy based on the number of spatial dimensions included explicitly.

0 - dimensional		Schneider & Mass (1975)
1 - dimensional		{ Sellers (1969) North (1975) Manabe & Wetherald (1967)
2 - dimensional		{ Present model Sellers (1976) Saltzman & Vernekar (1971)
3 - dimensional		G.C.M.'s (eg Wetherald & Manabe, 1975)

Zero-dimensional models average over the whole globe (vertically and horizontally), while 1-D models may concentrate on either the horizontal (e.g. Sellers, 1969) or vertical (Manabe & Wetherald, 1967) dimension. Similarly, two-dimensional models may consider the x-y plane (Sellers, 1976) or the y-z plane (Saltzman & Vernekar, 1971). In this latter model, the vertical variations of the variables are approximated analytically, and the

equilibrium, zonally-averaged equation solved explicitly for the latitude dependence (although the radiation fields are specified and there is additional parameterization of the eddy fluxes). In our model, we prescribe the mathematical form of many of the fields in both the horizontal and vertical. Radiation is then calculated explicitly.

In the remainder of this chapter, we list the specific processes included or neglected in this model, and present observational evidence to support the use of mean temperature gradients in the troposphere. In Chapter 2, the basic model equations are derived. Assuming the net radiative heating can be approximated by a Newtonian cooling law, leads to the grey radiation model of Chapter 3. Realistic parameterizations of long and short wave radiative heating are presented in Chapter 4, where we show how they can be used to determine a tropopause height. This chapter also introduces our parameterization of small-scale moist convection, and shows how the effects of the lower boundary are coupled to the atmosphere equations. Chapter 5 deals with the additional radiative effects of clouds. In Chapter 6, we put all the parameterizations together, and carry out a number of experiments with the full model, where both internal and external parameter variations are considered. Results and conclusions are summarized in Chapter 7.

1.2 Outline of the dynamical model

The main objective of this study is to examine some of the processes affecting the zonal annual mean temperature structure of the atmosphere in middle latitudes. We are particularly interested in the meridional temperature gradient and the static stability (or alternatively, the lapse rate) that result when many of the important heat-transporting mechanisms are allowed for. We assume that the fluxes of sensible heat, latent heat and potential energy by the large-scale eddy motions are in balance with the radiative fluxes and the heat fluxes due to small-scale moist convection. Oceanic circulations are ignored so the underlying ocean, which feeds sensible heat and water vapor to the cumulus convection, is more appropriately called a 'swamp'. The meridional heat transport by the large-scale mean motions is also neglected. This latter assumption is a reasonable first approximation in mid-latitudes as we see from Figures 1.1a,b taken from the 5-year data tabulation of Oort and Rasmusson (1971), [hereafter abbreviated as O&R]. (Note that Fig. 1.1b has its ordinate stretched vertically by a factor of 2 over Fig. 1.1a).

The model has no explicit formulation of atmospheric dynamics. Instead, we use the zonally averaged thermodynamic equation to solve for the mean temperature structure together with other relevant parameters. We will take as our basic set of variables the hemispheric mean temperature $\langle T \rangle$, the mean meridional temperature gradient A ($= \langle \frac{1}{r} \frac{\partial T}{\partial \phi} \rangle$, where r is the radius of the earth), the static stability B ($\langle \frac{\partial \theta}{\partial z} \rangle$) with a corresponding tropospheric lapse rate β , and the ground temperature T_g , tropopause temperature T_H , tropopause height H and surface relative humidity h_0 . Our method of solution is outlined

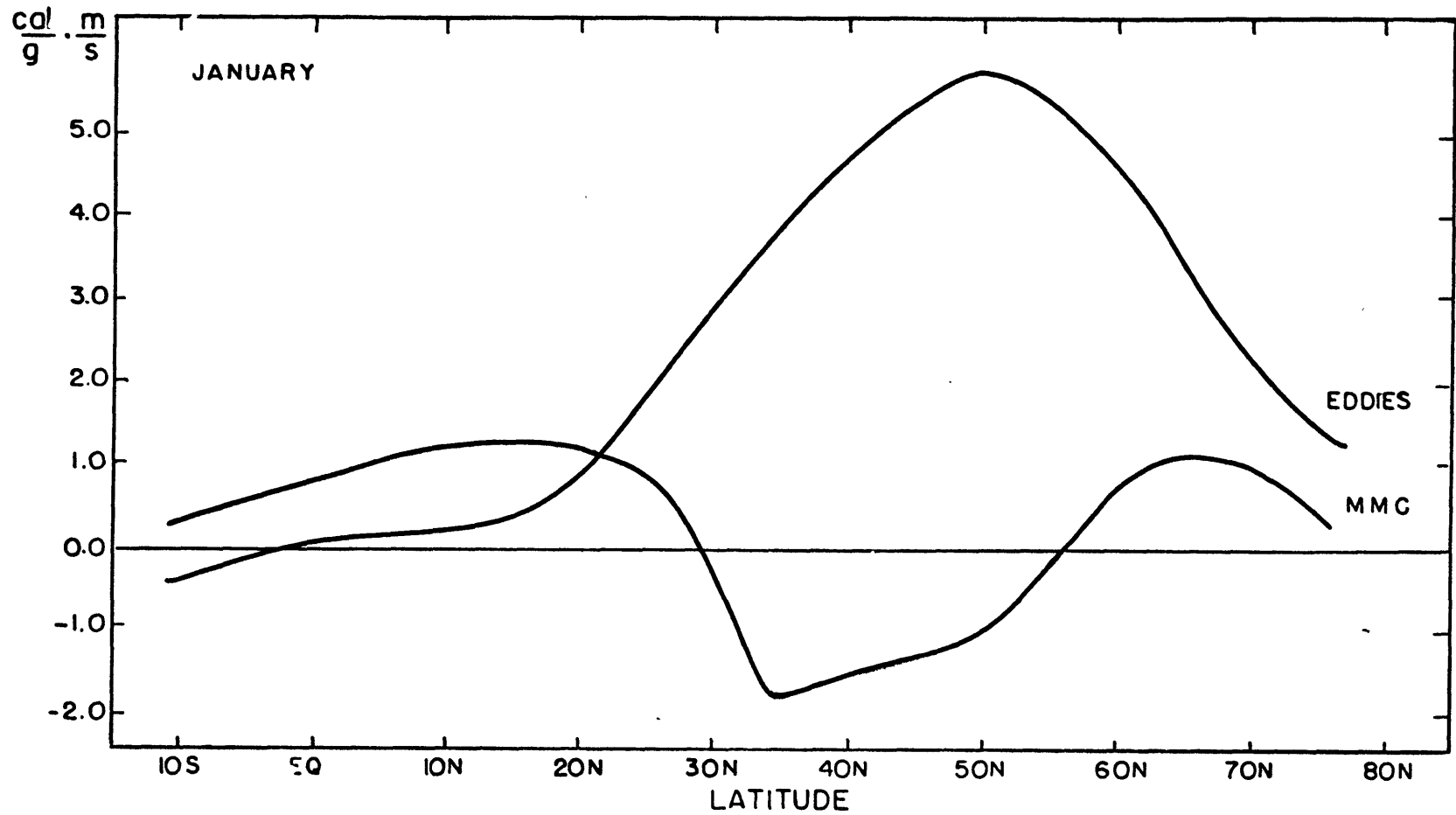


Figure 1.1a: Total energy transport (SH + PE + LH) of eddies (stationary + transient) and mean meridional circulation for January. [Taken from Oort & Rasmusson, 1971, Tables C7, C8, C9]

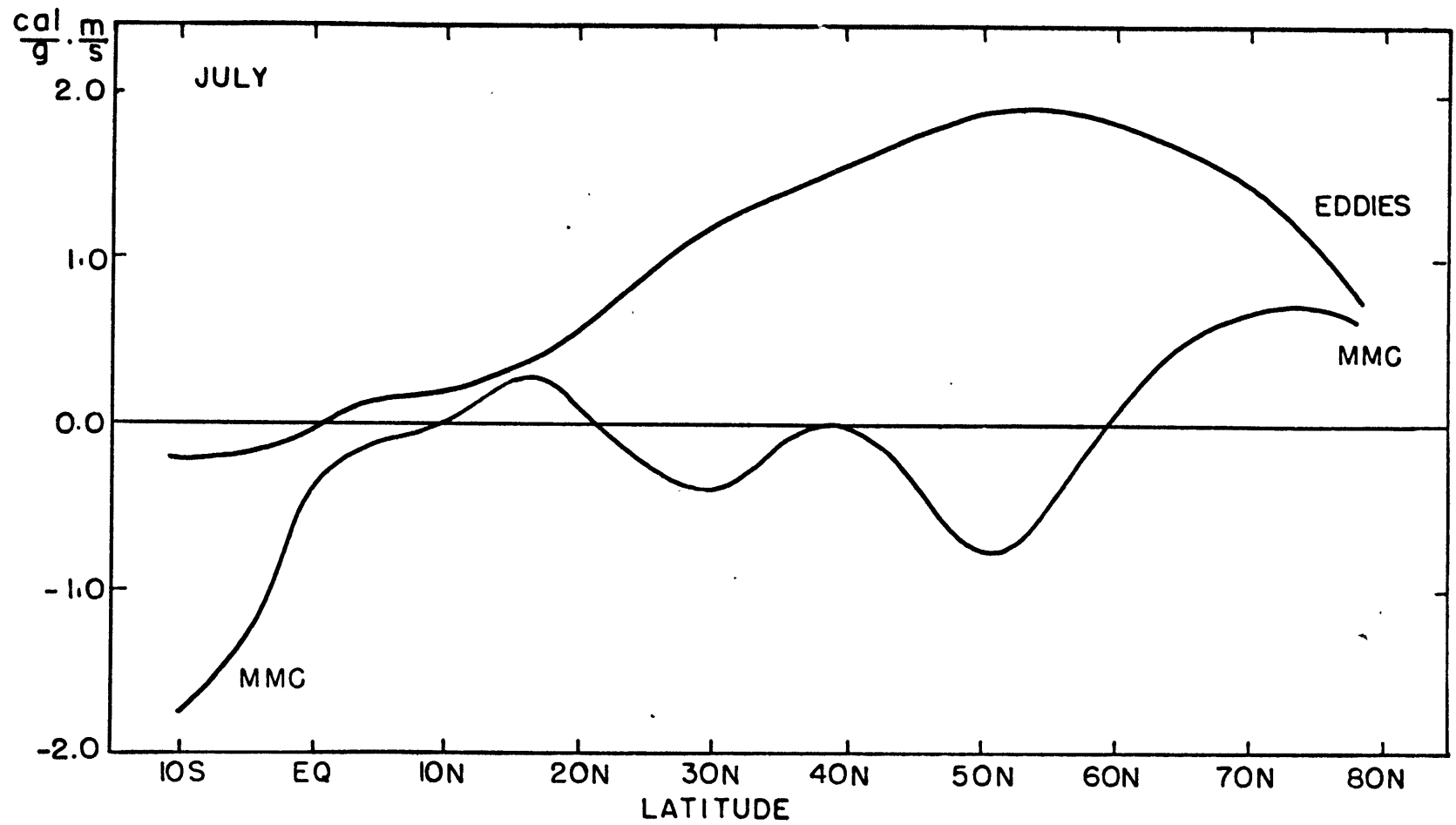


Figure 1.1b: As Fig. 1.1a, but for July.

below. (Note that the equations in this section are intended only for orientation and are not necessarily in the final form used in the model.)

We have seven variables and so would like seven equations or conditions to be satisfied. A simplified form of the steady state zonally averaged thermodynamic equation can be written

$$\frac{\partial}{\partial y} (\overline{v'\theta'} + \frac{L}{c_p} \overline{v'q'}) + \frac{\partial}{\partial z} (\overline{w'\theta'} + \frac{L}{c_p} \overline{w'q'}) = \left(\frac{p_0}{p}\right)^{\kappa} \frac{Q_{rad}}{\rho c_p} \quad (1.1)$$

where $c_p \overline{v'\theta'}$, $L \overline{v'q'}$, $c_p \overline{w'\theta'}$, $L \overline{w'q'}$ are the fluxes of sensible and latent heat by the baroclinic eddies and $Q_{rad} = - \frac{\partial}{\partial z} \overline{\mathcal{F}(z)}$ is the heating by radiation. $\overline{\mathcal{F}(z)}$ is the total radiative flux (short-wave and long-wave). Instead of solving (1.1) for the temperature at many grid points as we would in a numerical model, we apply three operators that define the mean structure. If $\langle () \rangle$ represents integration over a hemisphere, then applying $\langle () \rangle$, $\langle \frac{\partial}{\partial y} () \rangle$ and $\langle \frac{\partial}{\partial z} () \rangle$ to equation (1.1) allows us to obtain coupled non-linear equations for $\langle T \rangle$, A and B. Three additional constraints are readily found.

i) Radiative equilibrium at the tropopause:

$$\left. \frac{\partial}{\partial z} \overline{\mathcal{F}(z)} \right|_{z=H} \equiv 0 \quad (1.2)$$

ii) Idealized vertical structure relating T_H , T_0 , β :

$$T_H = T_0 - \beta H \quad (1.3)$$

where T_0 is the surface air temperature at a given latitude

iii) Sea surface flux balance:

$$S = R + Q_T - H_B - H_S - H_L \quad (1.4)$$

where S is storage, R the solar radiation term, Q_T the flux divergence due to oceanic motions (which we neglect), H_B the long-wave cooling and H_S , H_L the sensible and latent heat fluxes. There is a conduction term also when ice is present. The final constraint we require is essentially one on the relative humidity. We could readily formulate a water vapor equation but this involves knowledge of cloud formation and precipitation which is beyond the scope of this work. We avoid these problems by taking the surface relative humidity as constant. This idea was suggested by Manabe & Wetherald (1967) as being more realistic than specifying the absolute humidity. The first model justification for fixing relative humidity in climate studies can be found in Sarachik (1978). He varied the solar flux reaching the surface by 20% to simulate a climate change. The absolute humidity varies by a factor of 2, while the relative humidity changes are only about 10%. For observational support, we turn to Figure 1.2 from Telegadas & London (1954) which shows the lower troposphere relative humidity for winter and summer. We see there is remarkably little variation with season or latitude. (The substantial height variation is suitably parameterized in the model - see Section 4.2.1). To be consistent with a constant relative humidity we fix the cloud amounts at climatologically observed values. Smagorinsky (1960) analysed a considerable volume of synoptic data and found that relative humidity was indeed a very good predictor of cloud amount.

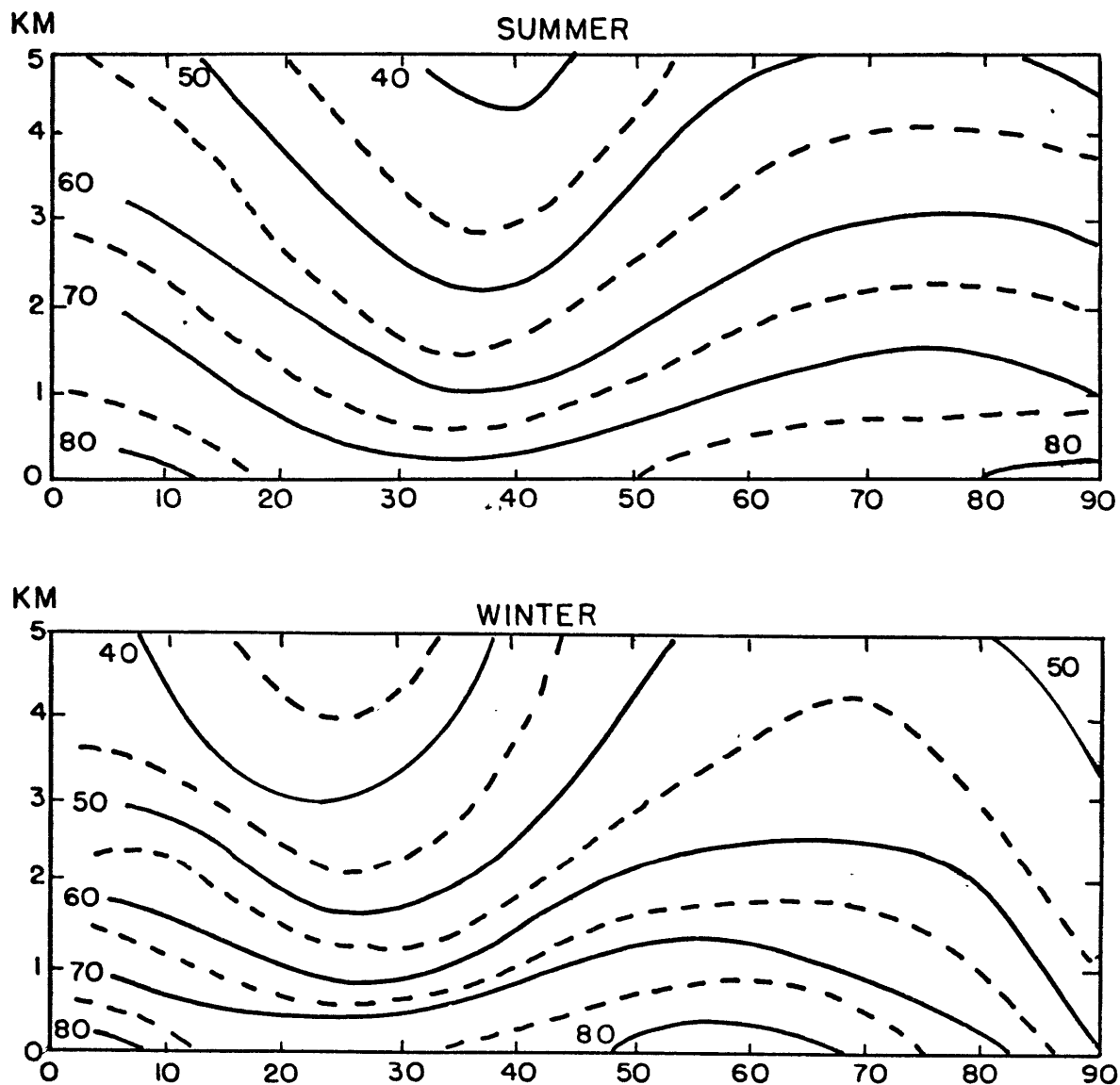


Figure 1.2: Latitude-height fields of relative humidity in the lower troposphere for summer and winter.

Another condition commonly applied in climate models is one of global radiation balance.

$$\int F(\infty)\uparrow dy = \int Q (1 - \alpha(y)) dy \quad (1.5)$$

where $F(\infty)\uparrow$ is the net outgoing long-wave flux, $Q(y)$ the incident solar radiation and $\alpha(y)$ the planetary albedo. This relation is not needed since our equation for $\langle T \rangle$ effectively says the same thing. Averaging (1.1) implies a net energy balance within the troposphere (rather than the entire atmosphere as claimed by (1.5)). Dynamical exchange of energy between the troposphere and stratosphere is negligible, and is ignored in our model. (See Section 6.1 for a discussion). Radiative processes are, of course, important in the stratosphere. In particular, ozone absorption determines how much solar radiation reaches the troposphere. The stratospheric modification of the radiation field is calculated assuming an isothermal layer above the tropopause. This is sufficiently accurate for evaluating tropospheric heating rates since such heating is sensitive to nearby temperatures and much less sensitive to temperature fields far away. However, the heating rates in the stratosphere, and in particular the thermal flux, will be in error. For this reason, the radiation balance at the top of the atmosphere as expressed by (1.5) will not be satisfied exactly.

1.3 Stone's Model

An essential part of this thesis is to allow for an interactive lapse rate unlike many previous studies where a constant value (usually 6.5 °K/km) was assumed. This problem is considered by Stone (1972a, 1972b) who derives approximate analytical expressions for the sensible heat fluxes due to baroclinically unstable motions. The basic equations Stone uses are those of Eady's (1949) model which assumes a Boussinesq, adiabatic, inviscid hydrostatic fluid on an f-plane.

$$\begin{aligned}\frac{\partial u}{\partial x} + \frac{\partial v}{\partial y} + \frac{\partial w}{\partial z} &= 0 \\ \frac{du}{dt} &= fv - \frac{1}{\rho_0} \frac{\partial P}{\partial x} \\ \frac{dv}{dt} &= -fu - \frac{1}{\rho_0} \frac{\partial P}{\partial y} \\ \frac{\partial P}{\partial z} &= \alpha \rho_0 g \theta \\ \frac{d\theta}{dt} &= 0\end{aligned}\tag{1.6}$$

where α is the thermal expansion coefficient, θ the potential temperature and P the hydrodynamic pressure, (i.e. the deviation from the pressure of a mean state with constant potential temperature). The other symbols have their usual meaning. Stone linearizes these equations about a basic state to obtain an equation for the perturbation vertical w' . This is simplified using the 'long wave' approximation and solved for a domain with rigid upper and lower boundaries. Thus, expressions for the correlations $\overline{v'\theta'}$ and $\overline{w'\theta'}$ can be derived. The amplitude, which

is undetermined by linearized stability theory, is found by assuming that the exponential growth of the unstable perturbations is eventually limited by non-linear effects at the same amplitude as the mean flow. This closure assumption is consistent with the finite-amplitude calculations of Pedlosky (1970), who found that an inviscid flow on an f -plane equilibrates when the perturbation meridional velocity is of the same order as the total shear of the zonal flow (for meridional and zonal wave numbers of the disturbance approximately equal). The fluxes that Stone derives (his equations 2.22 and 2.23 in the 1972a paper) are

$$\overline{v'\theta'} = - 0.86 \frac{g H_S^2}{f \langle T \rangle} A B \frac{\sqrt{1+Ri}}{Ri} \frac{y}{L} \left(1 - \frac{y}{L} \right) \quad (1.7)$$

$$\overline{w'\theta'} = + 0.36 f H_S^2 \frac{B}{Ri \sqrt{1+Ri}} z' (1 - z') \quad (1.8)$$

The y dependence in (1.7) has been added a posteriori to simulate the observed meridional variation. There is no latitude dependence in the correlation derived from (1.6) because of the neglect of horizontal shear in the basic zonal flow and the f -plane assumption. Equation (1.7) shows the meridional flux vanishes at equator and pole and peaks at $y = \frac{L}{2}$ (or 45°) which fits the observations (e.g. see Stephenson (1977) or O&R) reasonably well although the observed peak flux is displaced slightly poleward from 45° . Moura & Stone (1976) explain this displacement by introducing global geometry and allowing the Coriolis parameter f to vary with latitude.

Other variables introduced by (1.7) and (1.8) are the Richardson number $Ri (= \frac{f^2 \langle T \rangle}{g} \frac{B}{A^2}$ in our terminology), H_S which is identified

with the scale height of a Boussinesq atmosphere ($H_S = \frac{R\langle T \rangle}{g}$) and z' the non-dimensional vertical coordinate ($0 \leq z' \leq 1$). We will make use of Stone's model to parameterize the eddy fluxes in a more realistic troposphere where there is convergence of the meridians at the pole and the tropopause height varies with latitude. It is worth emphasizing at this point that the Coriolis parameter is kept constant in Stone's treatment, and this absence of the ' β effect' is the main potential limitation in this approach. (e.g. Held, 1978a).

We will now examine the problem of parameterizing the latent heat fluxes.

1.4 Leovy's parameterization of the latent heat fluxes

Sensible heat transport by the large-scale eddies has been investigated extensively in recent years, but there has been little work on a useful parameterization of the latent heat flux. Since we already have relations for $\overline{v'\theta'}$ and $\overline{w'\theta'}$ from Stone's model, it would be extremely convenient to be able to express the latent heat transports, $\overline{v'q'}$ and $\overline{w'q'}$, in terms of these sensible heat transports. Such a procedure is possible and was suggested by Leovy (1973) in his calculations of water vapor exchange on Mars. The method is based on the assumption that in the atmosphere the perturbations in relative humidity are much smaller than the temperature perturbations (which, of course, is consistent with constant relative humidity). This assumption is rather dubious for Mars and would seem to be much more appropriate for Earth conditions.

If e is the water vapor pressure and p the total atmospheric pressure, then the specific humidity q (g water/g air) is defined by $q = \frac{\epsilon e}{p - (1-\epsilon)e}$, where $\epsilon = \frac{R_d}{R_v} = 0.62197$, the ratio of the gas constants of dry air and water vapor. Since $e \ll p$,

$$q \approx \frac{\epsilon e}{p} \quad (1.9)$$

and for our purposes it is unnecessary to distinguish between specific humidity and mixing ratio. For a saturated atmosphere, $q = q_s(p, T)$ and the variation of saturation vapor pressure is given by the Clausius-Clapeyron equation

$$\frac{de_s}{dT} = \frac{e_s L_v}{R_v T^2} \quad (1.10)$$

L_v is the latent heat of vaporization which we assume to be independent of temperature so $\frac{L_v}{R_v} = 5419$ °K. Separating the temperature and specific humidity into a time-longitude mean and its deviation, we have

$$\begin{aligned} T &= \bar{T} + T' \\ q &= \bar{q} + q' \\ &= q_s(\bar{T} + T') \\ &= q_s(\bar{T}) + T' \frac{\partial q_s}{\partial T}(\bar{T}) + \frac{T'^2}{2!} \frac{\partial^2 q_s}{\partial T^2}(\bar{T}) + \frac{T'^3}{3!} \frac{\partial^3 q_s}{\partial T^3}(\bar{T}) + \dots \\ \text{so } \overline{v'q'} &= \overline{v'T'} \frac{\partial q_s}{\partial T}(\bar{T}) + \frac{1}{2} \overline{v'T'^2} \frac{\partial^2 q_s}{\partial T^2}(\bar{T}) + \frac{1}{6} \overline{v'T'^3} \frac{\partial^3 q_s}{\partial T^3}(\bar{T}) + \dots \end{aligned} \quad (1.11)$$

The derivatives of q_s can be found from (1.9) and (1.10) so we can calculate the magnitude of successive terms in this series (1.11). If we estimate the eddy correlations from Stone's model, then the odd correlations such as $\overline{v'T'^2}$ vanish for averages over a wavelength so the

second term of (1.11) does not contribute; furthermore,

$$\begin{aligned} \text{ratio of 3rd term: 1st term} &= \frac{1}{6} \times \frac{\overline{v'T'^3}}{\overline{v'T'}} \times \frac{\frac{\partial^3 q_s}{\partial T^3}(\bar{T})}{\frac{\partial q_s}{\partial T}(\bar{T})} \\ &= \frac{1}{6} \times \frac{3}{4} T'^2 \times 0.00377 \quad \text{for } \bar{T} = 273 \text{ K} \\ &= 0.047 \quad \text{for } T' = 10^\circ\text{C} \quad (\text{See Appendix A1}) \end{aligned}$$

Since neglecting the higher order terms of (1.11) causes an error of only 5%, we can write

$$\overline{v'q'} \approx \overline{v'T'} \frac{\partial q_s}{\partial T}(\bar{T}) \approx \overline{v'\theta'} \frac{\partial q_s}{\partial T}(\bar{T}) \quad (1.12)$$

and similarly for the vertical flux $\overline{w'q'}$. The last equality in (1.12) is appropriate for a Boussinesq gas and implies that the potential energy transport by eddies is very small. The circulation statistics of O&R indicate that the sensible heat flux is indeed more than an order of magnitude greater than the potential energy flux.

A further assumption made in practice is that the correlation between temperature and specific humidity is still valid when the relative humidity $h = \frac{e}{e_s} \approx \frac{q}{q_s}$ is not exactly unity. That is, for the relative humidity sufficiently close to 1, we can simply multiply the series (1.11) by h . We have examined the applicability of Leovy's parameterization using the data in Tables C7 and C9 in Oort and Rasmusson for northward eddy transport of sensible heat and specific humidity. The result is shown in Figures 1.3a and 1.3b for the months of January and July respectively. These figures compare the actual observed latent heat transport $\overline{v'q'}$ with that predicted by (1.12) for $h=1$.

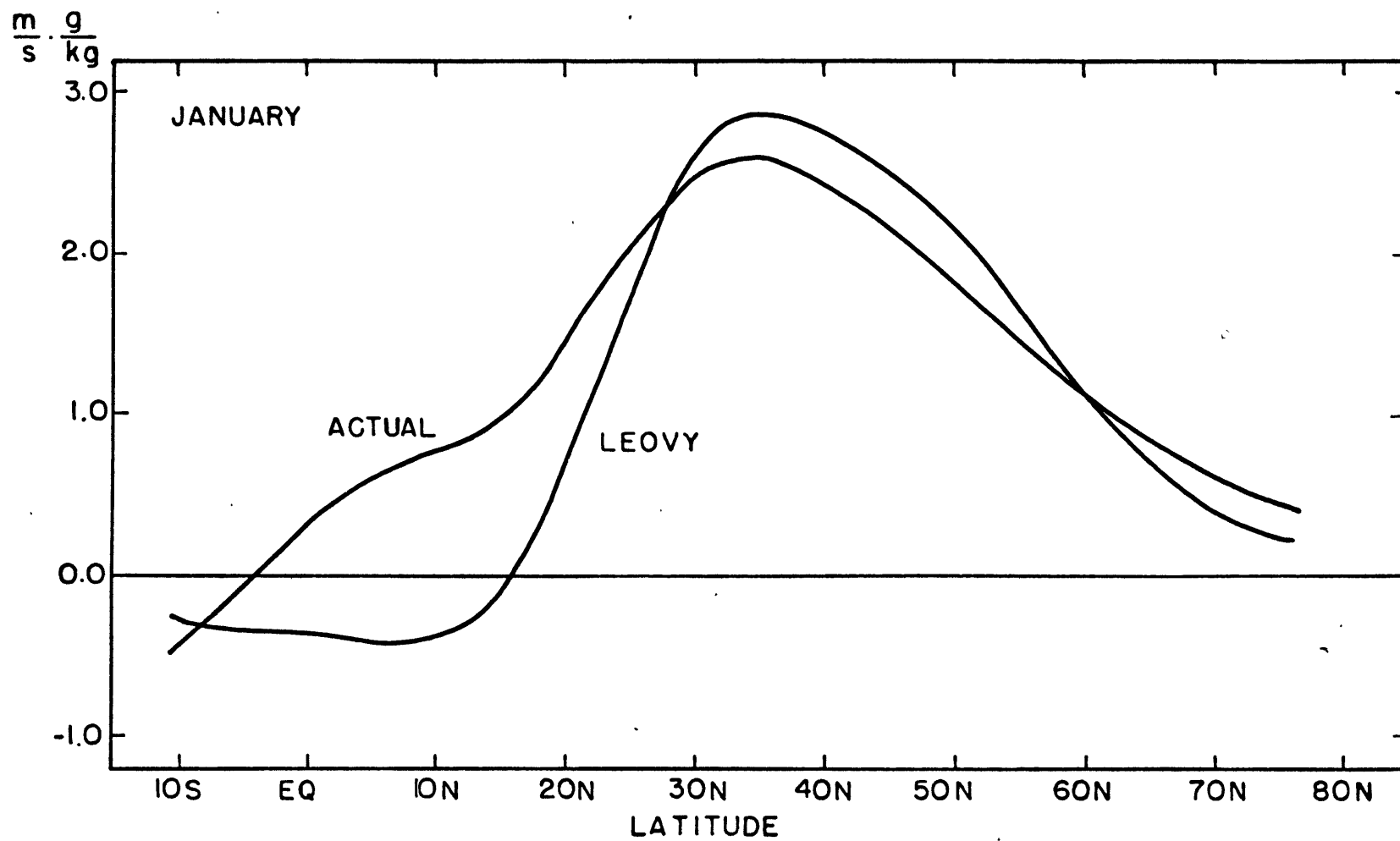


Figure 1.3a: Northward eddy transport of latent heat ('ACTUAL') for January compared to the transport calculated from the sensible heat flux using Leovy's method ('LEOVY').

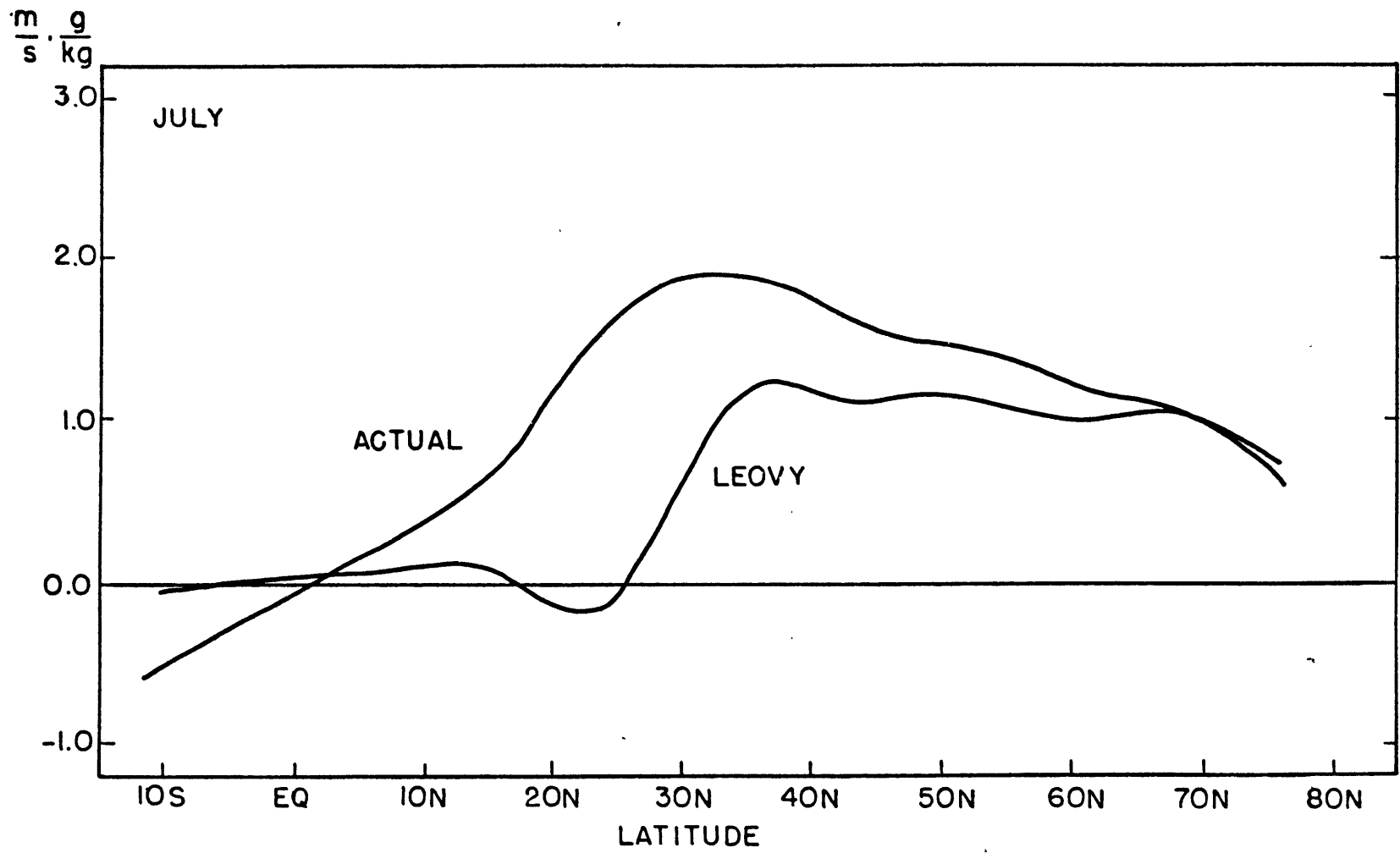


Figure 1.3b: As Fig. 1.3a, but for July.

On the whole, the agreement of the two curves is quite encouraging. As we might have expected, the parameterization is very poor at latitudes equatorward of about 25°. At these latitudes the eddy sensible heat flux is small and frequently of opposite sign to the latent heat flux, a state that can never be reflected in (1.12). For motions characteristic of the tropics, the higher order correlations of (1.11) may not be negligible, although relative humidity variations are probably the major source of error. We note that the northward sensible heat transport changes sign near the latitude of the descending branch of the Hadley cell. Since the Hadley cell is considerably stronger than baroclinic eddy motions at low latitudes, fluctuations of the Hadley cell over periods of a month will contribute significantly to the eddy flux calculated by Oort & Rasmusson. Figure 1.2 clearly shows the region of maximum subsidence corresponds closely to a minimum in the relative humidity field.

The latent heat transport is now directly related to the sensible heat transport and this allows us to include condensation in the heating equation in a very simple manner.

$$\rho c_p \frac{d\theta}{dt} = Q_{\text{rad}} - \rho L_v \frac{dq}{dt} \quad (1.13)$$

Note that a decrease in specific humidity, i.e. condensation, leads to an increase in temperature. Averaging (1.13) over time and longitude and considering just the eddy transports, we have:

$$\frac{\partial}{\partial y} [\overline{v'\theta'} (1 + \frac{L_v}{c_p} \frac{\partial q_s}{\partial T} (\overline{T}))] + \frac{\partial}{\partial z} [\overline{w'\theta'} (1 + \frac{L_v}{c_p} \frac{\partial q_s}{\partial T} (\overline{T}))] = \frac{Q_{\text{rad}}}{\rho c_p}$$

where rectilinear coordinates are again used for convenience. This corresponds to equation (1.1) except for the pressure factor $(\frac{p_0}{p})^k$ which has been omitted from this simple discussion. In practice, it is also necessary to add a term Q_{conv} representing small-scale convective heating.

1.5 Observed temperature structure

We are now almost ready to derive the actual equations used in the model. However, before we do this, it will be instructive to summarize the observed features of the mean temperature structure that are relevant to our study. In particular, how realistic is it to expand the surface temperature T_0 in the two lowest even Legendre polynomials P_0, P_2 and to represent the horizontal and vertical gradients by constant mean values (A and β)?

1.5.1 Surface Temperature

Let $T_0(\phi)$ be the observed surface temperature. Consider two different estimates \hat{T}_2 and \hat{T}_4 of T_0 .

$$\hat{T}_2 = c_0 + c_2 \sin^2\phi$$

$$\hat{T}_4 = c_0 + c_2 \sin^2\phi + c_4 \sin^4\phi$$

These relations are equivalent to expanding the temperature in the even Legendre polynomials P_0, P_2 and P_0, P_2, P_4 respectively. The moments of the temperature distribution then serve to determine the coefficients c_0, c_2, c_4 in a least squares sense.

$$\begin{aligned}
m_0 &= \int_0^{\pi/2} T_0(\phi) \cos \phi \, d\phi = c_0 + \frac{1}{3} c_2 + \frac{1}{5} c_4 \\
m_2 &= \int_0^{\pi/2} T_0(\phi) \sin^2 \phi \cos \phi \, d\phi = \frac{1}{3} c_0 + \frac{1}{5} c_2 + \frac{1}{7} c_4 \\
m_4 &= \int_0^{\pi/2} T_0(\phi) \sin^4 \phi \cos \phi \, d\phi = \frac{1}{5} c_0 + \frac{1}{7} c_2 + \frac{1}{9} c_4
\end{aligned} \tag{1.14}$$

For the \hat{T}_2 case, $c_4 \equiv 0$ and we use only the first two equations of (1.14). We will take the two sets of data shown in Table 1.1; the average surface temperature from Sellers (1965) and the 1000 mb temperature from Oort & Rasmusson (1971) (where T_0 (85) is linearly extrapolated from T_0 (65), T_0 (75)). The integrals of (1.14) are evaluated using a 9-point quadrature.

$$\int_0^{\pi/2} f_\phi \, d\phi = \frac{\pi}{1280} [81 f_5 + 51 f_{15} + 81 f_{25} + 81 f_{35} + 52 f_{45} + 81 f_{55} + 81 f_{65} + 51 f_{75} + 81 f_{85}] \tag{1.15}$$

(This expression gives, for example $\int_0^{\pi/2} \cos \phi \, d\phi - 1 = 7.1 \times 10^{-7}$
and $\int_0^{\pi/2} \cos^3 \phi \, d\phi - \frac{2}{3} = -9.87 \times 10^{-5}$)

Table 1.1 also shows the resulting least-square coefficients and the deviations between the estimated and observed temperatures. The deviations are in general too small for convenient graphical representation. It is interesting to note that although \hat{T}_4 temperatures are somewhat better than \hat{T}_2 throughout the range, it is only in very high latitudes that a really significant improvement occurs. Furthermore, due to increased oscillation in the higher order approximation the estimated mean meridional gradient \hat{A}_0 is actually worse for the \hat{T}_4 case (for both data sets), although of course the equator-to-pole temperature difference is closer to the observed value. This surface gradient is

calculated for the data as

$$A_0 = \frac{\pi}{2L} \int_0^{\pi/2} \frac{\partial T_0(\phi)}{\partial \phi} \cos \phi \, d\phi$$

$$= \frac{\pi}{2L} \left[-T_0(0) + \int_0^{\pi/2} T_0(\phi) \sin \phi \, d\phi \right]$$

where $T_0(0)$ is linearly extrapolated from 5° , 15° , and for $L=100$ the units of A_0 are $^\circ\text{C}/(100 \text{ km})$. For the least-square fit,

$$\hat{A}_0 = \frac{\pi}{L} \left(\frac{1}{3} c_2 + \frac{4}{15} c_4 \right)$$

In our model the vertically integrated meridional gradient A is an important parameter. Thus, the only real advantage of adding the extra Legendre polynomial P_4 is to improve the curvature of the temperature field near the pole. Since the area involved is small, we will assume the lower order approximation $\hat{T}_2 = c_0 + c_2 \sin^2 \phi$ to be sufficiently accurate. This reduces the complexity of the problem by having fewer unknowns. The worst temperature errors will occur poleward of the ice-line anyway, so the ice-albedo feedback is not affected (at least for the present and colder climates).

Table 1.1

Least-squares fit to observed surface temperature (see text for discussion).

a) Sellers (1965) mean surface temperature. ($^{\circ}\text{C}$)

Latitude	5°	15°	25°	35°	45°	55°	65°	75°	85°
T_0	25.5	25.1	20.4	14.0	7.5	0.5	-7.2	-15.9	-23.6
$(\hat{T}_2 - T_0)$	1.57	-0.55	-0.59	-0.57	-1.33	-1.59	-0.27	3.69	8.87
$(\hat{T}_4 - T_0)$	0.19	-1.12	0.03	0.96	0.29	-0.91	-1.26	0.96	5.04

	Data	\hat{T}_2	\hat{T}_4
Meridional gradient A_0	-0.4441	-0.4446	-0.4341

Least-squares coefficients:

	c_0	c_2	c_4
\hat{T}_2	27.396	-42.452	-
\hat{T}_4	25.904	-27.528	-17.412

b) Oort & Rasmusson (1971) 1000 mb surface temperature.

Latitude	5°	15°	25°	35°	45°	55°	65°	75°	85°
T_0	26.4	25.6	22.3	16.6	8.8	2.9	-4.2	-11.9	(-19.6)
$(\hat{T}_2 - T_0)$	1.67	0.11	-1.04	-1.34	-0.35	-1.27	-0.17	3.08	8.41
$(\hat{T}_4 - T_0)$	0.23	-0.49	-0.39	0.28	1.35	-0.56	-1.20	0.22	4.39

	Data	\hat{T}_2	\hat{T}_4
Meridional gradient A_0	-0.4172	-0.4175	-0.4066

Least-squares coefficients:

	c_0	c_2	c_4
\hat{T}_2	28.382	-39.872	-
\hat{T}_4	26.813	-24.179	-18.309

1.5.2 Vertical temperature gradient

We use the temperature and geopotential height data tabulated by Oort & Rasmusson at the standard pressure levels 1000, 950, 900, 850, 700, 500, 400, 300, 200 and 100 mb to calculate a mean lapse rate ($-\frac{\partial \bar{T}}{\partial z}$) and static stability ($\frac{\partial \bar{\theta}}{\partial z}$). Lapse rates are shown in Table 1.2 for winter, summer and annual average cases at 45° latitude. (See page 41).

The feature that immediately stands out in this table is the distinct change between gradients below 700 mb and those above. (The particular value of 700 mb may be somewhat arbitrary due to O&R's choice of pressure levels). Above 700 mb the observed temperature gradient ($\frac{\Delta \bar{T}}{\Delta z}$) is close to the commonly quoted -6.5 °K/km and fairly constant with height up to the tropopause. In the lower troposphere the gradients are significantly more stable than those above, and also show a larger seasonal variation. The annual mean temperature profile is also shown graphically in Figure 1.4.

Thus, an excellent estimate of the mass-weighted vertical gradient in the troposphere can be found by

$$\frac{\partial \bar{T}}{\partial z} \approx \frac{1}{7} \left(3 \frac{\Delta \bar{T}}{\Delta z} \Big|_{1000-700} + 4 \frac{\Delta \bar{T}}{\Delta z} \Big|_{700-300} \right) \quad (1.16)$$

Such gradients for temperature \bar{T} and potential temperature $\bar{\theta}$ are presented in Table 1.3. The upper limit for the averages is chosen to be 300 mb to avoid complications with the tropopause. Including the next higher pressure level, 200 mb, will give a misleading result for the tropospheric lapse rate poleward of about 30°.

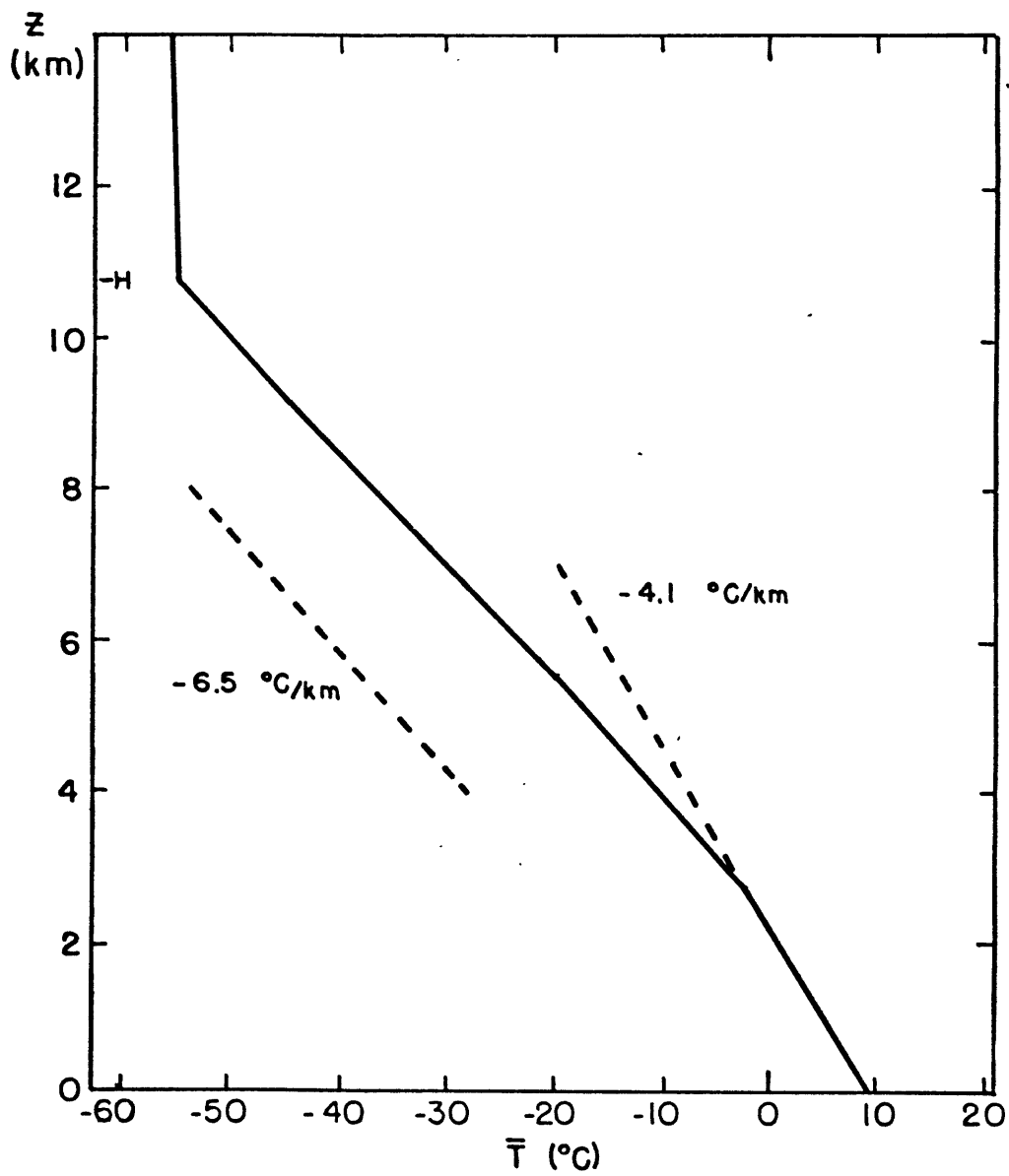


Figure 1.4: Mean annual temperature profile at 45°N.

[Taken from Oort & Rasmusson, 1971. Tables A4, A5].

Table 1.3: Mass-weighted vertical temperature gradients 1000-300 mb

(°K/km)

a) Lapse rate; $-\frac{\partial \bar{T}}{\partial z}$

	Latitude		
	30°	45°	60°
Ann	5.79	5.69	5.31
Win	5.87	5.57	4.75
Spr	5.86	5.80	5.28
Sum	5.61	5.62	5.76
Fall	5.85	5.77	5.44

b) Static stability: $\frac{\partial \bar{\theta}}{\partial z}$

	Latitude		
	30°	45°	60°
Ann	4.52	4.61	5.05
Win	4.47	4.77	5.71
Spr	4.42	4.49	5.11
Sum	4.73	4.67	4.53
Fall	4.46	4.55	4.94

There are several observations we should make on Table 1.3;

i) Mean lapse rate: The atmospheric lapse rate averaged from ground to tropopause is considerably more stable than 6.5 °K/km at all latitudes. A value of 5.7 would seem more appropriate for middle latitudes. Although (1.16) may appear a fairly crude estimate, a more careful calculation in the next section (See Section 1.5.3. where the tropopause position is determined) shows excellent agreement.

ii) Mean stability : If $B = \frac{\partial \bar{\theta}}{\partial z}$ and $\beta = -\frac{\partial \bar{T}}{\partial z}$, these gradients are commonly assumed to be related by the expression

$$B \approx \Gamma - \beta \quad (1.17)$$

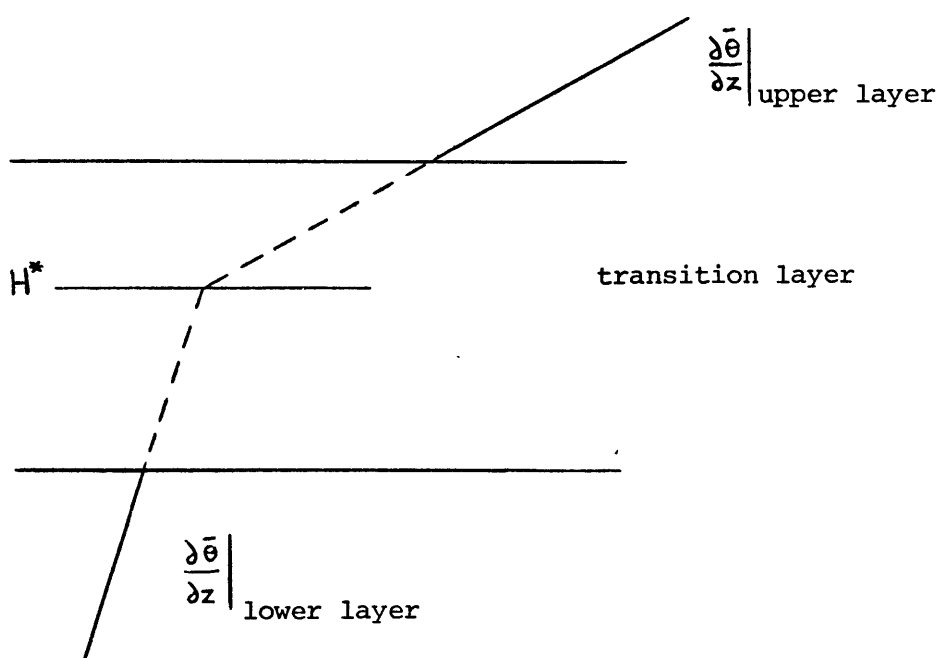
for a Boussinesq atmosphere, where $\Gamma = \frac{g}{c_p} = 9.8 \text{ }^\circ\text{K/km}$ is the dry adiabatic lapse rate. Table 1.3 shows (1.17) would considerably underestimate the stability B , (due to neglect of the pressure factor $(\frac{p_0}{p})^k$). A convenient, but more exact, relation between B and β will be derived in a later section (See Section 2.2.1).

iii) Variation with latitude and season: The seasonal variation at middle and low latitudes is surprisingly small. At 30°N the atmosphere is most stable in summer. Presumably, this is analogous (but on a much larger space and time scale) to the well-known observation that the tropical atmosphere is more stable on days of pronounced convection. By the time we reach 60°N , however, there is considerable change in the gradients throughout the year, with winter being the most stable season. Hence, the variation of $\frac{\partial \bar{T}}{\partial z}$ with latitude shows an annual cycle. For a given season, stability increases poleward except in the summer where this trend is reversed (at least in the range of latitudes we have considered).

1.5.3. Meridional temperature gradient, $\frac{\partial \bar{\theta}}{\partial y}$

Since we wish to average $\frac{\partial \bar{\theta}}{\partial y}$ over the depth of the troposphere, we will begin by determining an approximate value for the tropopause height. We use Tables A4, A5 and F7 (for \bar{T} , \bar{z} and $\bar{\theta}$) from O&R. In evaluating the vertical gradient (See Section 1.5.2.), we calculated $\frac{\partial \bar{\theta}}{\partial z}$ between each set of pressure levels: 1000-900, 900-700, 700-500, 500-400, 400-300, 300-200, 200-100, 100-50 mb. The layer in which the tropopause occurs can be identified by the sudden increase in stability, although there

are a few uncertain cases (low latitudes in summer) where it is necessary to apply the operational definition of the tropopause as the height where $-\frac{\partial \bar{T}}{\partial z}$ decreases to 2 °K/km or less. A first estimate H^* of the tropopause height is then found by extrapolating the stabilities from adjacent layers as indicated below.



For example, at 45° in annual mean we have

layer	500-400	400-300	300-200	200-100	100-50
$\frac{\partial \bar{\theta}}{\partial z}$	3.34	4.14	8.81	16.67	21.42

The tropopause lies in the 300-200 mb layer and we calculate $H^* = 10.84$ km. Table 1.4 shows the heights obtained by this method.

Table 1.4: Estimated tropopause heights (km)

Season	Latitude	H*					H
		30°	40°	45°	50°	60°	45°
Annual		14.93	11.12	10.84	10.49	9.92	10.78
Winter		14.73	10.49	10.30	10.02	9.65	10.21
Spring		13.48	10.96	10.64	10.26	9.68	10.35
Summer		15.26	11.79	11.42	11.06	10.44	11.55
Fall		15.09	11.29	11.01	10.63	9.95	10.94

The last column of Table 1.4 gives a refined estimate of H at 45°, such that $\left. \frac{\partial \bar{\theta}}{\partial y} \right|_H = 0$, (the horizontal differencing being from 40-50°). It is well-known that the horizontal temperature gradient changes sign in the lower stratosphere and we have used this fact to help pin-point H. Of course, operational definitions of tropopause height do not use this criterion, but we are working with heavily averaged data. H_{45} is within the error of the previous H^*_{45} .

We can now recalculate the vertical average $\overline{\frac{\partial \theta}{\partial z}}^z$, where $\overline{(\)}^z$ indicates a mass-weighted average from $z=0$ to $z=H_{45}$ using the 45° pressure-height distribution. These values, shown in Table 1.5, agree closely with the cruder averages of Table 1.3. The stability is again lowest in Spring, although the seasonal changes are small at this latitude. Thus, the vertical gradients are not highly sensitive to the averaging method, provided we stay below the tropopause. For example, at 45°N the mean annual tropospheric lapse rate was found to be 5.74 °K/km. If we average from 1000 to 200 mb instead (the calculated tropopause pressure being 235.6 mb) we obtain a mean

lapse rate of 5.43 °K/km.

Table 1.5: Vertically averaged static stability and lapse rate at 45°N

Season	$\overline{\frac{\partial \theta}{\partial z}}$	$-\overline{\frac{\partial T}{\partial z}}$ (°K/km)
Annual	4.59	5.74
Winter	4.75	5.61
Spring	4.48	5.83
Summer	4.70	5.70
Fall	4.51	5.82

The error would be still greater in winter or in higher latitudes where the tropopause is lower.

On the other hand, the horizontal gradients are more dependent on an accurate estimate of H , because $\frac{\partial \bar{\theta}}{\partial y}$ is changing rapidly near the tropopause. (See Figure 1.5). We can now proceed to find the meridional temperature gradients averaged over the depth of the troposphere. O&R tabulate potential temperature at standard pressure levels. Since we want to evaluate $\left. \frac{\partial \bar{\theta}}{\partial y} \right|$ at constant z rather than $\left. \frac{\partial \bar{\theta}}{\partial y} \right|$ at constant p we interpolate $\bar{\theta}$ for a range of heights assuming $\bar{\theta}$ varies linearly with z within each pressure layer. Table 1.6 shows the meridional gradients we obtain, where the horizontal differencing is taken from 30 to 60° to smooth the fields. $\frac{\partial \bar{\theta}}{\partial y}$ can be averaged vertically from ground to tropopause (H_{45}), mass-weighting with the 45° pressure profile, resulting in the mean seasonal gradients of Table 1.7.

Table 1.2: Lapse rate at 45°, $-\frac{\overline{\Delta T}}{\Delta z}$ (°K/km)

	1000-900	950-900	900-850	850-700	700-500	500-400	400-300	300-200
Ann.	4.00	4.26	4.28	4.82	6.06	7.11	6.76	3.91
Win.	5.00	4.36	4.17	4.36	6.11	7.06	6.33	2.55
Sum.	2.54	3.07	3.97	5.19	6.03	7.02	7.09	5.17

Table 1.6: Meridional gradient $\frac{\partial \bar{\theta}}{\partial y}$ at 45°N in °K/100 km (using 30-60° differencing)

Season	Height (km)							
	0.5	1.0	1.5	3.0	5.5	7.0	9.0	H ₄₅
Annual	-.573	-.549	-.545	-.539	-.549	-.558	-.482	-.127
Winter	-.730	-.669	-.626	-.601	-.630	-.595	-.487	-.279
Spring	-.589	-.570	-.580	-.576	-.569	-.560	-.430	-.116
Summer	-.372	-.374	-.394	-.408	-.410	-.458	-.466	+.030
Fall	-.605	-.584	-.575	-.568	-.586	-.602	-.522	-.098

Table 1.7: Troposphericly averaged meridional gradient $\frac{\partial \bar{\theta}}{\partial y}$ at 45°

	30-60° avg. (°K/100 km)
Annual	-0.522
Winter	-0.607
Spring	-0.542
Summer	-0.386
Fall	-0.552

H_{45} in Table 1.6 is the tropopause height at 45° latitude. It is defined in such a way that the gradients in the final column of Table 1.6 would be zero for 40-50° differencing. The non-zero values we actually obtain are due to smoothing over a larger latitude range.

The annual, winter and summer profiles of $\frac{\partial \bar{\theta}}{\partial y}$ are graphed in Figure 1.5. The lines become dashed above the tropopause. It is clear that the assumption of constant meridional gradient is a reasonable approximation throughout most of the troposphere. In our model we actually assume $\frac{\partial T}{\partial y}$ is invariant with height, but this differs from $\frac{\partial \theta}{\partial y}$ by at most a few percent. (See Section 2.2.2.). The gradients are largest in winter and smallest in summer, as we expect, until we approach close to the stratosphere. An apparent reversal then occurs due to seasonal variation in H .

Finally, we will calculate typical values for the Richardson number, an important variable in Stone's theory. The Richardson number is defined by

$$Ri = \frac{f^2 \frac{\partial \bar{\theta}}{\partial z}}{\alpha g \left(\frac{\partial \bar{\theta}}{\partial y} \right)^2} \quad (1.18)$$

where $\alpha = \frac{1}{T}$ is a thermal expansion coefficient. We take the mean

mass-weighted averages of \bar{T} , $\frac{\partial \bar{\theta}}{\partial z}$ and $\frac{\partial \bar{\theta}}{\partial y}$ at 45°. When the Coriolis parameter f is evaluated at 45° also,

$$Ri = 0.01081 \bar{T} \frac{\frac{\partial \bar{\theta}}{\partial z}}{\left(\frac{\partial \bar{\theta}}{\partial y}\right)^2}$$

Table 1.8 shows the vertically averaged mean temperature and the resulting Richardson numbers.

Table 1.8: Richardson number and vertically averaged temperature at 45°.

	$\bar{T}_{(45)}^z$ (°K)	Ri
Annual	259.1	47.2
Winter	252.7	35.2
Spring	257.7	42.6
Summer	266.0	90.6
Fall	260.3	41.7

The large Richardson number in summer is due to the much smaller meridional temperature gradient for that season.

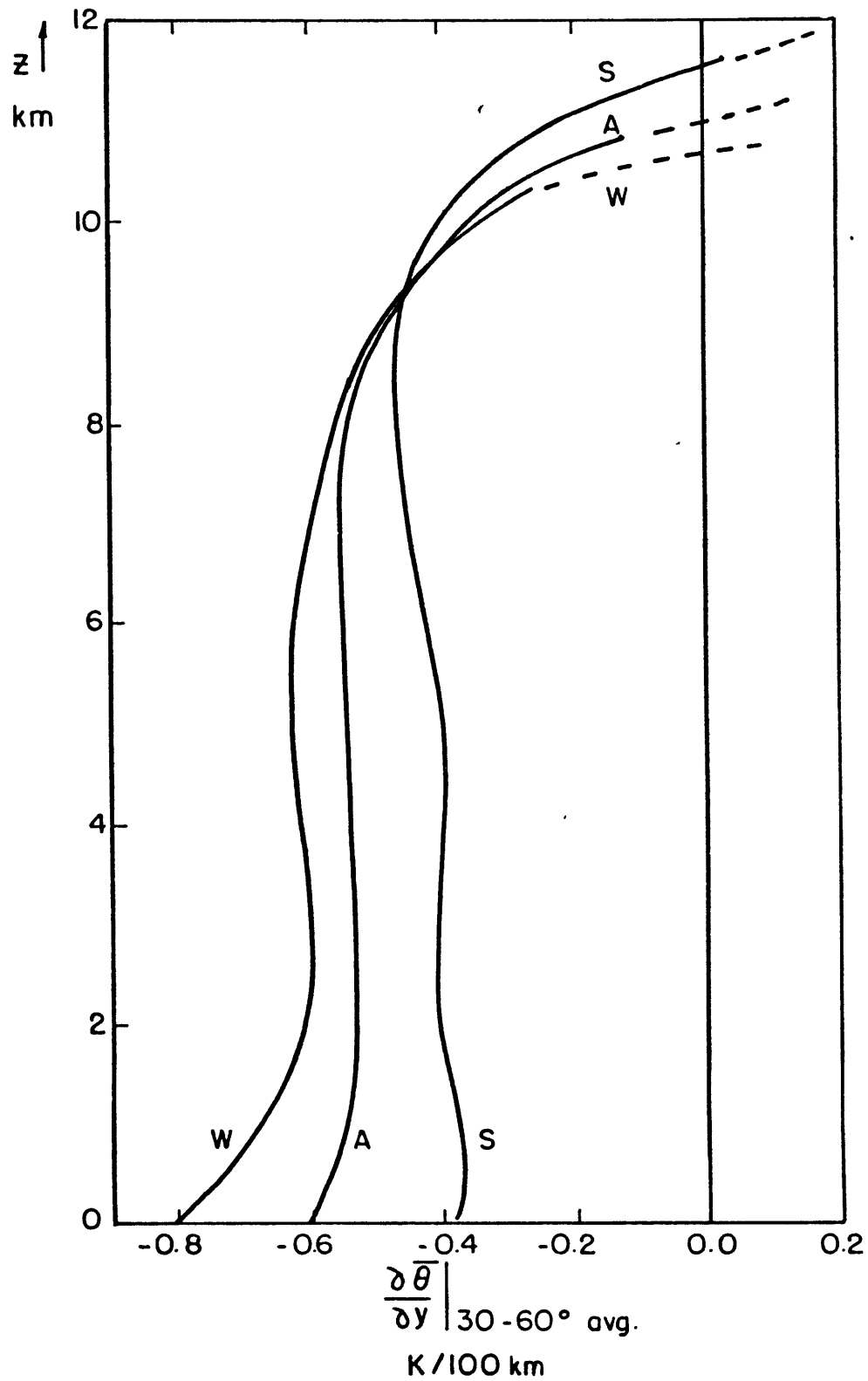


Figure 1.5: Annual (A), Winter (W) and Summer (S) meridional temperature gradients at 45°N (averaged from 30-60°).

Chapter 2: Dynamical Model

2.1 Derivation of basic equations

We begin with the atmospheric temperature equation in its most general form;

$$\frac{\partial \bar{\theta}}{\partial t} + \frac{1}{r \cos \phi} \frac{\partial}{\partial \phi} [\overline{v' \theta'} \cos \phi] + \frac{\partial}{\partial z} [\overline{w' \theta'}] = \left(\frac{p_0}{p} \right)^\kappa \times \left[\frac{Q_{\text{rad}}}{\rho c_p} + \frac{Q_{\text{conv}}}{\rho c_p} + \frac{Q_{\text{LH}}}{\rho c_p} \right] \quad (2.1)$$

where ($\overline{\quad}$) indicates an average over longitude and the only approximation so far is in neglecting the transport by the mean motions.

Equation (2.1) is averaged zonally and written in spherical coordinates so we can calculate the effect on the heat transports of convergence of the meridians. If L is the equator to pole distance (10^7 m), then the radius of the earth $r = \frac{2L}{\pi}$. At this stage in the derivation we will combine the net radiative heating Q_{rad} and small-scale convective heating Q_{conv} into a single term, H .

$$H(\phi, z) = \left(\frac{p_0}{p} \right)^\kappa \left[\frac{Q_{\text{rad}}}{\rho c_p} + \frac{Q_{\text{conv}}}{\rho c_p} \right] \quad (2.2)$$

The large-scale latent heating from condensation, Q_{LH} , may be written as in (1.13).

$$\begin{aligned} \frac{Q_{\text{LH}}}{\rho c_p} &= - \frac{L_v}{c_p} \frac{d\bar{q}}{dt} \\ &= - \frac{L_v}{c_p} \left[\frac{\partial \bar{q}}{\partial t} + \frac{1}{r \cos \phi} \frac{\partial}{\partial \phi} (\overline{v' q'} \cos \phi) + \frac{\partial}{\partial z} \overline{w' q'} \right] \end{aligned} \quad (2.3)$$

where the mean transport is again neglected. Considering just the steady state equation and combining (2.1) and (2.3) through Leovy's parameterization (See Section 1.4) we arrive at

$$\frac{1}{r \cos \phi} \frac{\partial}{\partial \phi} [\overline{v'\theta'} (1 + \mathcal{L}(\phi, z)) \cos \phi] + \frac{\partial}{\partial z} [\overline{w'\theta'} (1 + \mathcal{L}(\phi, z))] \doteq \mathcal{H}(\phi, z) \quad (2.4)$$

We consider only the steady-state solution since to evaluate the time-dependent part $(\frac{\partial \bar{\theta}}{\partial t} + (\frac{p_0}{p})^\kappa \frac{L_v}{c_p} \frac{\partial \bar{q}}{\partial t})$ requires explicit calculation of component terms in a continuity equation for water substance. The parameterization of precipitation is beyond the intended scope of the model. (In the present case, precipitation can be obtained as a residual). Actually, since the 'turnover time' for water vapor in the atmosphere is only about 2 days, the $\frac{\partial \bar{q}}{\partial t}$ term is not important in seasonal calculations. A much more serious difficulty in a time-dependent model would be determining the cross-equatorial transports.

The Leovy term $\mathcal{L}(\phi, z)$ accounts for the eddy latent heat flux.

$$\mathcal{L}(\phi, z) = h \frac{L_v}{c_p} \frac{\partial \bar{q}_s}{\partial T} \quad (2.5)$$

where h is the relative humidity and the other variables are defined as in Section 1.4. (Strictly, of course, there should be a $(\frac{p_0}{p})^\kappa$ factor included from (2.1) which cannot be taken inside the ϕ and z derivatives in the flux divergence. This unduly complicates equation (2.4).

Since $\mathcal{L}(\phi, z)$ decreases rapidly away from the ground and Leovy's parameterization is only approximate anyway, we will neglect this factor here.) The relative humidity is assumed to vary linearly with pressure in the vertical (See Section 4.2.1 for further discussion) so $h = h_0 \frac{p}{p_0}$,

where all zero subscripts indicate an atmospheric variable evaluated at $z = 0$. The Clausius-Clapeyron equation (1.10) can be integrated under the assumption that $\frac{L_V}{R_V}$ is independent of temperature. Thus

$$\begin{aligned} \mathcal{L}(\phi, z) &= \frac{h_0 L_V^2}{c_p R_V} \frac{p}{p_0} \frac{\bar{q}_s}{T^2} \\ &= \frac{\epsilon e_3 h_0 L_V^2}{c_p R_V p_0} \times \frac{e^{-a\left(\frac{1}{T} - \frac{1}{T_3}\right)}}{\frac{1}{T^2}} \\ &= 0.6780 h_0 \left(\frac{T_3}{T}\right)^2 e^{-a\left(\frac{1}{T} - \frac{1}{T_3}\right)} \end{aligned} \quad (2.6)$$

where the constants have the following values:

$$\begin{aligned} \text{surface pressure } p_0 &= 1013 \text{ mb} \\ \text{triple point water vapor pressure } e_3 &= 6.1123 \text{ mb} \\ \text{triple point temperature } T_3 &= 273.16 \text{ K} \\ \epsilon &= 0.62197 \\ a = \frac{L_V}{R_V} &= 5419 \text{ K} \\ \frac{L_V^2}{c_p R_V} &= 1.348 \times 10^7 \text{ K} \end{aligned}$$

The eddy flux correlations $\overline{v'\theta'}$ and $\overline{w'\theta'}$ are essentially those given by (1.7), (1.8) and derived by Stone (1972a). The simple Eady model on which these equations are based assumed a flat rigid lid and neglected horizontal shear of the zonal flow and the β effect. The resulting correlations are therefore independent of latitude, and this is unrealistic. Thus Stone included an ad hoc latitude dependence $6 \frac{Y}{L} (1 - \frac{Y}{L})$ in $\overline{v'\theta'}$. We will use a similar expression in terms of ϕ .

$$\begin{aligned}\overline{v'\theta'} &= 3 V \sin \phi \cos \phi \Lambda(\phi, z) \\ \overline{w'\theta'} &= 3 W \sin \phi \cos \phi \frac{z}{H(\phi)} \left(1 - \frac{z}{H(\phi)}\right)\end{aligned}\quad (2.7)$$

where V and W are amplitudes independent of latitude and height.

$$\begin{aligned}V &= -0.144 \frac{g H_S^2}{f \langle T \rangle} A B \frac{\sqrt{1+Ri}}{Ri} \\ W &= 0.360 f H_S^2 \frac{B}{Ri \sqrt{1+Ri}}\end{aligned}\quad (2.8)$$

$A = \left\langle \frac{1}{r} \frac{\partial \theta}{\partial \phi} \right\rangle$ and $B = \left\langle \frac{\partial \theta}{\partial z} \right\rangle$ are the meridional and vertical potential temperature gradients averaged hemispherically.

$$\text{Hemispheric average } \langle () \rangle = \frac{1}{H} \int_0^{\pi/2} \int_0^H () dz \cos \phi d\phi \quad (2.9)$$

where $\bar{H} = \int_0^{\pi/2} H(\phi) \cos \phi d\phi$ is the mean tropopause height. The Richardson number Ri is taken to be

$$Ri = \frac{f^2 \langle T \rangle}{g} \frac{B}{A^2} \quad (2.10)$$

and the atmospheric scale height

$$H_S = \frac{R \langle T \rangle}{g} \quad (2.11)$$

There are several points in equations (2.7) that need further discussion;

i) Both horizontal and vertical fluxes contain the primary latitude dependence $3 \sin \phi \cos \phi$ (The '3' is simply a normalizing factor). In a recent paper, Stone (1978) proved that the total flux will vary in this way provided that each hemisphere is in equilibrium separately and the latitudinal variation of all relevant fields can be described by just the first two even terms of an orthogonal expansion. (ie. the structure of the

atmosphere-ocean system is dominated by the planetary scale). Then the total flux is constrained to peak near 35° latitude, or the flux per unit area (represented in 2.7) to peak near 45° . We include the same dependence in the vertical flux so the ratio $\frac{\overline{w'\theta'}}{\overline{v'\theta'}}$ is almost independent of latitude. This ratio is intimately related to the slope of the potential temperature isotherms according to baroclinic stability theory.

ii) There are now two distinct vertical scales in the problem, the scale height H_S and the tropopause height $H(\phi)$. The tropopause is an important feature of the real atmosphere and we calculate $H(\phi)$ explicitly in our model. It is then necessary to rescale Stone's non-dimensional z' as $z/H(\phi)$. In the original paper (Stone, 1972b), the vertical variable z was scaled by an unspecified parameter H . In subsequent calculations Stone (1972a, 1973) identified this scale with the scale height which we have denoted by H_S . This is still the correct quantity to use in the mean amplitudes (2.8) to obtain the total mass-weighted transport appropriate to the atmosphere. In appendix A2 we show that the results of Stone's (1973) paper are altered only minimally by using $H(\phi)$ in the z -dependent part of (2.7), provided that all parameters with an implied vertical integration ($\langle T \rangle$, $\langle \frac{\partial \theta_r}{\partial z} \rangle$ etc) are averaged over this same height.

iii) Shape factor $\Lambda(\phi, z)$: In Stone's model the horizontal heat transport $c_p \overline{v'\theta'}$ has no vertical structure. However, it can be shown both physically and mathematically that the introduction of a variable tropopause height $H(\phi)$ makes it necessary to modify the fluxes $\overline{v'\theta'}$ or $\overline{w'\theta'}$ in some way. The use of a shape factor Λ defined so that $\Lambda = 0$ at $z = H(\phi)$ proves to be a convenient solution to this problem.

The divergence theorem below is a well-known result in vector analysis (see for example Hildebrand p. 290).

$$\iiint_{\mathcal{R}} \nabla \cdot \underline{v} \, d\tau = \iint_{\mathcal{S}} \underline{v} \cdot \underline{n} \, d\sigma \quad (2.12)$$

This theorem is a consequence of conservation of mass, and states that the divergence of a vector field \underline{v} integrated over a volume \mathcal{R} is zero if there is no net outflow across the boundaries \mathcal{S} of that region. The result is applicable to our equation (2.4). We want to approximate in a consistent way that the baroclinic eddies are contained entirely within the troposphere. From (2.7) we see there is no eddy flux across equator or pole or through the lower surface (assumed flat). However, unless Λ modifies the vertical profile of $\overline{v'\theta'}$, there will be a horizontal flux of energy through the sloping tropopause and this is physically undesirable.

We can arrive at a similar conclusion mathematically. Apply the hemispheric averaging operator $\langle \rangle$ to the left hand side of (2.4).

Making use of (2.7) we find

$$\langle \text{LHS (2.4)} \rangle = \frac{1}{rH} \int_0^{\pi/2} \left\{ \int_0^{H(\phi)} \frac{\partial}{\partial \phi} [\overline{v'\theta'} (1+\lambda) \cos \phi] \, dz \right\} d\phi$$

The double integral can be simplified by a useful formula (2.13) from differential calculus. (See Hildebrand p. 360).

$$\frac{d}{dx} \int_{A(x)}^{B(x)} f(x,t) \, dt = \int_A^B \frac{\partial f}{\partial x} \, dt + f(x,B) \frac{dB}{dx} - f(x,A) \frac{dA}{dx} \quad (2.13)$$

thus,

$$\begin{aligned}
\langle \text{LHS 2.4} \rangle &= \frac{1}{rH} \int_0^{\pi/2} \left\{ \frac{\partial}{\partial \phi} \int_0^{H(\phi)} \overline{v'\theta'} (1+\lambda) \cos \phi \, dz - \left[\overline{v'\theta'} (1+\lambda) \right] \Big|_H \frac{dH}{d\phi} \right\} d\phi \\
&= \frac{1}{rH} \left\{ \left[\cos \phi \int_0^H \overline{v'\theta'} (1+\lambda) \, dz \right] \Big|_0^{\pi/2} - \int_0^{\pi/2} \left[\overline{v'\theta'} (1+\lambda) \right] \Big|_H \frac{dH}{d\phi} \, d\phi \right\}
\end{aligned} \tag{2.14}$$

The first term of (2.14) vanishes identically at equator and pole but the second term will remain unless either $\overline{v'\theta'} = 0$ at $z = H$, or $\frac{dH}{d\phi} = 0$.

The particular form of Λ is somewhat arbitrary of course, but we will be guided by observations.

Define

$$\Lambda(x) = \begin{cases} K_S & , 0 \leq x \leq x_* \\ K_S \left(\frac{e^{-\lambda x} - e^{-\lambda}}{e^{-\lambda x_*} - e^{-\lambda}} \right) & , x_* \leq x \leq 1 \end{cases} \tag{2.15}$$

where $x = \frac{z}{H(\phi)}$ is a non-dimensional vertical coordinate. This expression introduces three constants K_S , λ and x_* , two of which must be determined from a fit to data while the third is found from the normalization condition,

$$\int_0^1 \Lambda(x) \, dx = \frac{K_S}{\lambda} \frac{[(1+\lambda x_*)e^{-\lambda x_*} - (1+\lambda)e^{-\lambda}]}{(e^{-\lambda x_*} - e^{-\lambda})} \equiv 1 \tag{2.16}$$

We use eddy flux data from Oort & Rasmusson. The northward entropy transport is observed to have considerable vertical structure, the most noticeable feature being a general decrease with altitude. Stone's model predicts a constant amplitude. One of the reasons for this discrepancy is the neglect of the variation of Coriolis parameter with latitude. Inclusion of the β effect produces a $\overline{v'\theta'}$ profile that decreases smoothly with height (Green, 1970). The latitude of the peak

flux is also shifted poleward slightly (Moura & Stone, 1976) but we will neglect this effect here. The shape factor given by (2.15) has the desired exponential decrease with height, reaching zero at the tropopause $x = 1$.

In Figure 2.1 the observed entropy flux at mid-latitudes is shown as a function of z (solid curve). $\overline{v'\theta'}$ is averaged over $40-50^\circ$ for a slightly smoother profile). The variable actually presented is $\frac{\rho(z)}{\rho(0)} \overline{v'\theta'}$. Green (1970) argues that one can ignore the effect of the variation of density with height (as in Eady's model) provided we consider $\rho \overline{v'\theta'}$ say (rather than $\overline{v'\theta'}$) when making a comparison with observation. The dimensionless scale x is calculated using the 45° tropopause height from Section 1.5.3. of $H = 10.78$ km. $\Lambda(x)$ is plotted on the same figure (dashed curve), scaled to give an equal area. The rectangle, also of equal area, is the constant amplitude Eady result. The constants appearing in (2.15) were chosen to give a reasonable fit to the observed profile, and at the same time match $\Lambda(\frac{1}{2})$ with observation. We use

$$\lambda = 2.50, \quad x_* = 0.20$$

$$\text{resulting in } K_S = 2.11, \quad \Lambda(\frac{1}{2}) = 0.82$$

Substituting the constant values

$$g = 9.81 \quad \text{m s}^{-2}$$

$$f = 1.03 \times 10^{-4} \quad \text{s}^{-1} \quad (\text{at } 45^\circ \text{ latitude})$$

$$g/R = 34.18 \quad ^\circ\text{K/km}$$

equations (2.8) and (2.10) can now be written

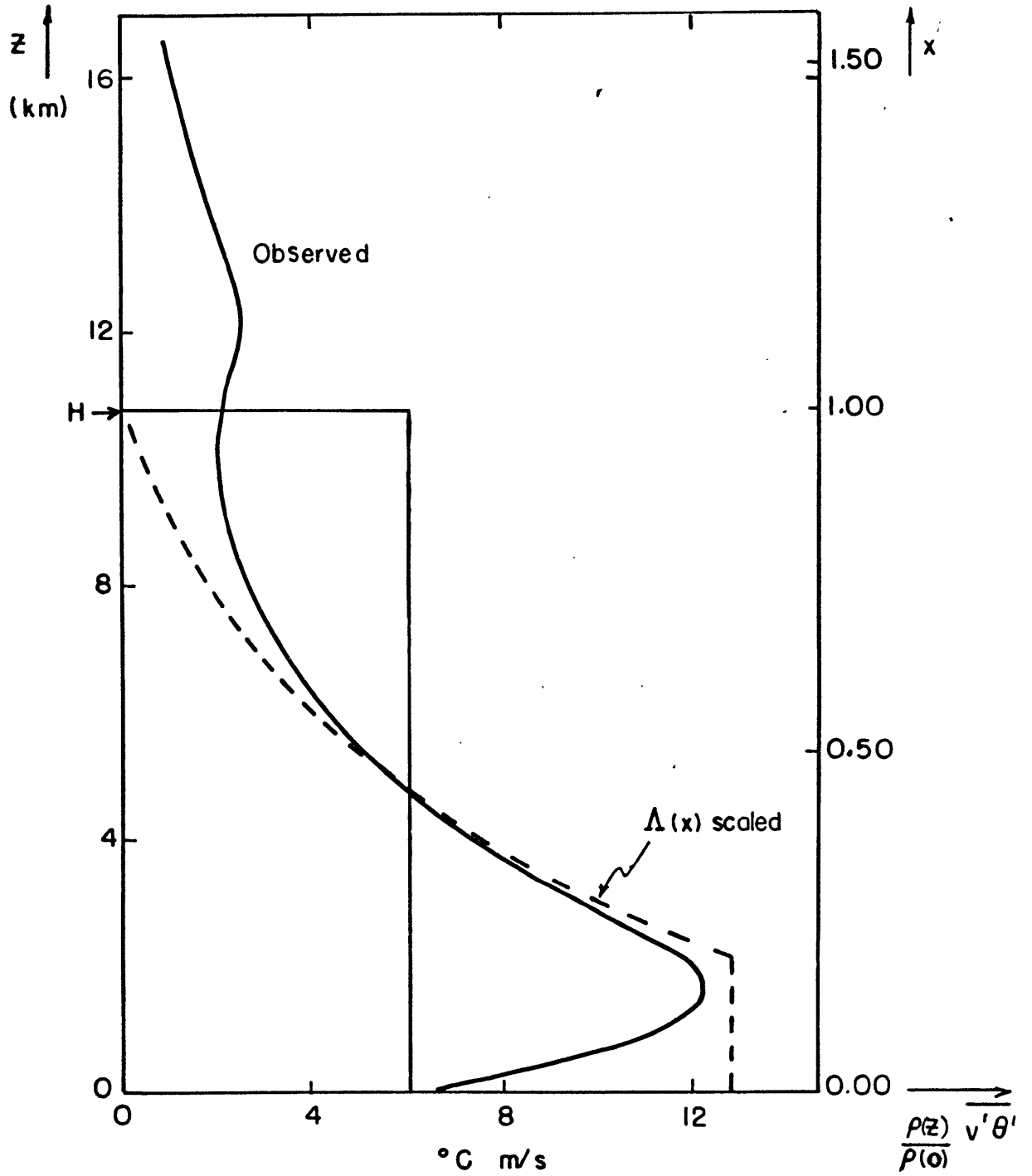


Figure 2.1: Profile of annual northward entropy flux $\frac{\rho(z)}{\rho(0)} \overline{v'\theta'}$ at 45°N (solid curve); scaled shape factor $\Lambda(x)$ (dashed curve), and constant amplitude Eady result (solid rectangle).

$$\begin{aligned}
 V &= - 0.1174 \langle T \rangle A B \frac{\sqrt{1+Ri}}{Ri} \quad \text{m } ^\circ\text{K s}^{-1} \\
 W &= 3.174 \times 10^{-5} \langle T \rangle^2 \frac{B}{Ri\sqrt{1+Ri}} \quad \text{m } ^\circ\text{K s}^{-1} \\
 Ri &= .01081 \langle T \rangle \frac{B}{A^2}
 \end{aligned} \tag{2.17}$$

where A is in units of $^\circ\text{K}/100 \text{ km}$ and B in $^\circ\text{K}/\text{km}$.

2.2 Temperature Field

A simple yet adequate representation of the surface temperature is given by the two lowest even Legendre polynomials (See Section 1.5.1.). For the vertical structure we assume a constant lapse rate β . However, unlike many simple models, the value of this lapse rate is not specified a priori but is calculated internally. Thus,

$$T(\phi, z) = c_0 + c_2 \sin^2 \phi - \beta z \tag{2.18}$$

The coefficients c_0 , c_2 and lapse rate β can be expressed in terms of the mean parameters of the model; $\langle T \rangle$, A and B

$$\begin{aligned}
 \langle T \rangle &= c_0 + \frac{c_2}{3} \left[\frac{3}{H} \int_0^{\pi/2} H \sin^2 \phi \cos \phi d\phi \right] - \frac{\beta H}{2} \left[\frac{1}{H^2} \int_0^{\pi/2} H^2 \cos \phi d\phi \right] \\
 A &\doteq \left\langle \frac{1}{r} \frac{\partial T}{\partial \phi} \right\rangle = \frac{\pi c_2}{3L} \left[\frac{3}{H} \int_0^{\pi/2} H \sin \phi \cos^2 \phi d\phi \right] \\
 B &= \left\langle \frac{\partial \theta}{\partial z} \right\rangle = \frac{1}{H} \int_0^{\pi/2} \int_0^H \frac{\partial}{\partial z} \theta(\phi, z) dz \cos \phi d\phi
 \end{aligned} \tag{2.19}$$

where now $L = 100$ (in units of 100 km). The three square-bracketed expressions in (2.19) are written so that they are unity for constant H.

In the complete model, the tropopause height is determined from a radiative equilibrium condition (Eq. 1.2) and $H(\phi)$ depends on the surface temperature $T_0(\phi)$, lapse rate and ozone structure. Since the surface temperature has the most significant effect (See Section 4.3.1.) we will evaluate the bracketed integrals assuming H has the same latitude dependence as T_0 (although in a later example, Section 3.1, we assume an even simpler form).

$$H(\phi) = b_0 + b_2 \sin^2\phi \quad (2.20)$$

In the full model the coefficients b_0, b_2 are found by fitting (2.20) to values of H determined by radiative equilibrium calculations at two latitudes. In the simple grey model of Chapter 3 we just specify the latitude distribution of H . If we now define

$$\begin{aligned} n_1 &= \frac{3}{H} \int_0^{\pi/2} H \sin \phi \cos^2 \phi \, d\phi \\ n_2 &= \frac{3}{H} \int_0^{\pi/2} H \sin^2 \phi \cos \phi \, d\phi \\ n_3 &= \frac{1}{H^2} \int_0^{\pi/2} H^2 \cos \phi \, d\phi \end{aligned} \quad (2.21)$$

then for $H(\phi)$ expressed as in equation (2.20),

$$\begin{aligned} n_1 &= 1 + \frac{1}{15} \frac{b_2}{H} \\ n_2 &= 1 + \frac{4}{45} \frac{b_2}{H} \\ n_3 &= 1 + \frac{4}{45} \left(\frac{b_2}{H}\right)^2 \end{aligned}$$

where

$$\bar{H} = \int_0^{\pi/2} H \cos \phi \, d\phi = b_0 + \frac{1}{3} b_2 \quad (2.22)$$

The Legendre coefficient b_2 is negative, and typically $\frac{b_2}{\bar{H}} \approx -0.4$

We can also calculate the pressure field. Rewriting the temperature from (2.18) as $T(z) = T_0 - \beta z$ we can integrate the hydrostatic relation $\frac{\partial p}{\partial z} = -\rho g = \frac{-p g}{RT}$ to obtain

$$p = p_0 \left(\frac{T}{T_0} \right)^\gamma \quad (2.23)$$

where $\gamma = \frac{g}{R\beta}$. Then, the potential temperature is

$$\theta = T \left(\frac{p_0}{p} \right)^\kappa = T \left(\frac{T_0}{T} \right)^{\kappa\gamma} \quad (2.24)$$

where $\kappa = \frac{R}{c_p} = \frac{2}{7}$. We are now in a position to comment on the gradients of T and θ .

2.2.1. Relation between lapse rate and static stability

In our model we predict a value for the stability B ($\langle \frac{\partial \theta}{\partial z} \rangle$) and from this must determine the appropriate lapse rate β ($-\frac{\partial T}{\partial z}$). To a first approximation (assumed by Stone, 1973), B and β are related by

$$B \approx \Gamma - \beta \quad (2.25)$$

where $\Gamma = \frac{g}{c_p} = 9.8$ °K/km is the dry adiabatic lapse rate. Thus, for example, $\beta = 6.5$ °K/km implies $B = 3.3$ °K/km. However, this Boussinesq relation is not accurate enough for our purposes. Referring to Table 1.3 we see the mean annual 45° lapse rate of 5.7 °K/km corresponds to the local stability $\frac{\partial \theta}{\partial z}$ of 4.6 °K/km not 4.1 °K/km as the simple formula

above would indicate. Therefore, let us apply the model definition of B (2.19) and substitute for the potential temperature θ from (2.24).

$$B = \frac{1}{\bar{H}} \int_0^{\pi/2} T_0(\phi) \cos \phi \left[\left(1 - \frac{\beta H(\phi)}{T_0(\phi)}\right)^{\left(1 - \frac{\Gamma}{\beta}\right)} - 1 \right] d\phi \quad (2.26)$$

This expression for B is the exact one in terms of our model but is now too complicated. It is too awkward and time consuming to invert the above integral at each iteration in order to find β . We will seek a simpler relation.

Define $X = \frac{\bar{H}}{\bar{T}_0}$, which is independent of ϕ . (The overbar ($\bar{\quad}$) implies integration over latitude as in 2.22). Then

$$B = \frac{1}{\bar{H}} \left\{ (1 - \beta X)^{\left(1 - \frac{\Gamma}{\beta}\right)} \int_0^{\pi/2} T_0 \cos \phi (1 + \varepsilon)^{\left(1 - \frac{\Gamma}{\beta}\right)} d\phi - \bar{T}_0 \right\}$$

where $\varepsilon(\phi) = \beta \frac{X - \frac{H(\phi)}{T_0(\phi)}}{(1 - \beta X)}$ is small.

Consider a numerical example: $\beta = 6.5 \text{ } ^\circ\text{K/km}$
 $H = 15 - 6 \sin^2 \phi \text{ km}$
 $T_0 = 300 - 51 \sin^2 \phi \text{ } ^\circ\text{K}$

We find $\bar{H} = 13.0$, $\bar{T}_0 = 283.0$, $X = 0.046$ and $\varepsilon(\phi)$ has extrema of -0.038 at the equator and $+0.091$ at the pole. Approximating $(1 + \varepsilon)^{\left(1 - \frac{\Gamma}{\beta}\right)} \approx 1 + \left(1 - \frac{\Gamma}{\beta}\right) \varepsilon$, the integration is trivial. The further simplification $\overline{(T_0 \varepsilon)} = 0$ occurs because of the definition of X and ε , so that

$$B \doteq \frac{1}{X} \left[(1 - \beta X)^{\left(1 - \frac{\Gamma}{\beta}\right)} - 1 \right] \quad (2.27)$$

Since X is itself small, we make a further expansion of (2.27).

$$B = (\Gamma - \beta) \left\{ 1 + \frac{1}{2} \Gamma X \left[1 + \frac{1}{3} (\Gamma + \beta) X + \frac{1}{12} (\Gamma + \beta) (\Gamma + 2\beta) X^2 + \dots \right] \right\}$$

The zeroth order approximation (neglecting terms of $O(X)$ and higher) is just the familiar expression (2.25). We will use an approximation that is better than second order in that it evaluates the $O(X^2)$ term exactly and approximates the higher ones.

$$B \approx (\Gamma - \beta) \left\{ 1 + \frac{\frac{1}{2} \Gamma X}{1 - \frac{1}{3}(\Gamma + \beta)X} \right\} \quad (2.28)$$

This form has the advantage that β can readily be found by solving a quadratic.

$$\beta = \frac{3}{2X} \left\{ \left[1 + X \left(\frac{1}{2} \Gamma - \frac{1}{3} B \right) \right] - \sqrt{\left[1 + X \left(\frac{1}{2} \Gamma - \frac{1}{3} B \right) \right]^2 - \frac{4}{3} X \left[(\Gamma - B) + \frac{1}{3} \Gamma X \left(\frac{1}{2} \Gamma + B \right) \right]} \right\} \quad (2.29)$$

As a numerical check, we use the example given above. The exact integral (2.26) results in

$$B = 4.307 \quad ^\circ\text{K/km.}$$

Compare this with $B = 4.295$ from (2.27)

and $B = 4.290$ from (2.28)

Our final representation (2.28) is considerably more accurate than the crude estimate of $B = 3.3$ from (2.25).

2.2.2. Horizontal temperature gradients $\frac{\partial T}{\partial \phi}$ and $\frac{\partial \theta}{\partial \phi}$

In (2.19) we assumed $A \approx \left\langle \frac{1}{r} \frac{\partial T}{\partial \theta} \right\rangle$, but this gradient should really be defined in terms of the potential temperature θ .

$$A = \frac{1}{rH} \int_0^{\pi/2} \int_0^{H(\phi)} \frac{\partial \theta}{\partial \phi} (\phi, z) dz \cos \phi d\phi \quad (2.30)$$

From (2.24),

$$\frac{\partial \theta}{\partial \phi} = \frac{\partial T}{\partial \phi} \times \left[K\gamma \left(\frac{T_0}{T}\right)^{K\gamma-1} - (K\gamma-1) \left(\frac{T_0}{T}\right)^{K\gamma} \right] \quad (2.31)$$

$$\text{and } \frac{\partial T}{\partial \phi} = \frac{\partial T_0}{\partial \phi} = 2 c_2 \sin \phi \cos \phi, \text{ independent of } z.$$

The term in (2.31) in square brackets is very nearly unity. For example, if $\beta = 6.5$, $T_0 = 283$ and $H = 13$

$$\frac{\frac{\partial \theta}{\partial \phi}}{\frac{\partial T}{\partial \phi}} = \begin{cases} 1.0 & \text{at } z = 0 \\ 0.989 & \text{at } z = \frac{1}{2}H \\ 0.939 & \text{at } z = H \end{cases}$$

Thus, the mean potential temperature gradient ($\langle \frac{1}{r} \frac{\partial \theta}{\partial \phi} \rangle$) will be only 2-3% smaller than $\langle \frac{1}{r} \frac{\partial T}{\partial \phi} \rangle$. (See appendix A3 for a more complete evaluation of 2.30). This difference has negligible effect on our model results.

2.3 Hemispheric Forcing Functions

We wish to solve the thermodynamic equation (2.4) for the temperature structure. In the more common numerical approach, a mathematical grid would be set up and the diabatic heating $\overline{H}(\phi, z)$ evaluated at each grid point (ϕ_i, z_j) . Equation (2.4) could then be solved iteratively for the temperature at each (ϕ_i, z_j) provided the boundary conditions and appropriate constitutive relations were known. In particular, the eddy flux correlations $\overline{v'\theta'}$ and $\overline{w'\theta'}$ would need to be provided and their calculation would involve the complete equations of motion. In the present work we adopt a considerably simpler approach.

The eddy fluxes are parameterized in terms of three variables $\langle T \rangle$, A and B that describe the mean temperature field. These same three variables specify the temperature $T(\phi, z)$ at any point in the troposphere, if suitable approximations for the latitude and height variation are made. The form we choose for $T(\phi, z)$ is (2.18). The observational data to justify such a structure was presented in Section 1.5. The coefficients c_0, c_2 are related to the solution variables by (2.19) which we can now write in a more condensed form as

$$\begin{aligned} \langle T \rangle &= c_0 + \frac{1}{3} c_2 n_2 - \frac{1}{2} \beta \bar{H} n_3 \\ A &= \frac{\pi c_2 n_1}{3L} \end{aligned} \quad \} \quad (2.32)$$

where n_1, n_2, n_3 are defined in (2.21) and the relation between β and B is given by (2.28).

Thus, in our case the thermodynamic equation need only be solved at three 'points' instead of at a large number of grid points. Of course, it is more fitting to apply different averaging operators to (2.4) than to evaluate it at three arbitrary points. The choice of averaging operators is suggested by the nature of the variables we are calculating (See Section 2.3.1. - 2.3.3.). The advantage of this analytical approach is that it is conceptually simpler and the mechanisms affecting the mean gradients more understandable. At the same time there is a corresponding sacrifice of structural detail.

2.3.1. $\langle T \rangle$ Equation

The operator we use in this case is just the hemispheric average (2.9). In Section 2.1 it was shown that the left hand side of (2.4)

averages to zero if we confine the baroclinic eddy fluxes to the troposphere. Therefore, the $\langle T \rangle$ equation is

$$0 = \langle \mathcal{H}(\phi, z) \rangle \quad (2.33)$$

In general we calculate \mathcal{H} from (2.2), but in this section we will find it instructive to consider also the special case where \mathcal{H} is given by a Newtonian cooling law, i.e.,

$$\mathcal{H}(\phi, z) = \frac{T_r - T}{\tau} \quad (2.34)$$

This expression states that the radiative heating is proportional to the deviation of temperature $T(\phi, z)$ from the radiative equilibrium temperature $T_r(\phi, z)$. Spiegel (1957) originally developed the same linearized formula for studying deviations from a steady state. τ is the radiative relaxation time constant for the system. It is assumed to be a simple constant, dependent on the scale of the disturbance but independent of position. In Chapter 3 we discuss in more detail some of the problems involved in this formulation (2.34). Substituting (2.34) into (2.33),

$$\langle T \rangle = \langle T_r \rangle \quad (2.35)$$

or, the mean temperature is just equal to the mean radiative equilibrium temperature.

2.3.2. B Equation

We average (2.4) separately over the upper and lower halves of the troposphere and subtract to obtain a forcing function for the mean

vertical gradient. We find:

$$\begin{aligned}
 \text{Upper integral} &= \frac{2}{H} \int_0^{\pi/2} \int_{H/2}^H (\text{L.H.S. 2.4}) dz \cos\phi d\phi \\
 &= \frac{2}{H} \int_0^{\pi/2} \left\{ \int_{H/2}^H \frac{1}{r} \frac{\partial}{\partial\phi} (\overline{v'\theta'}) (1+\alpha) \cos\phi dz + [\overline{w'\theta'}]_{H/2}^H \cos\phi \right\} d\phi \\
 &= \frac{2}{H} \int_0^{\pi/2} \left\{ \frac{1}{r} \frac{d}{d\phi} \int_{H/2}^H \overline{v'\theta'} (1+\alpha) \cos\phi d\phi - \frac{dH}{d\phi} \frac{1}{r} [\overline{v'\theta'} (1+\alpha) \cos\phi] \Big|_H \right. \\
 &\quad \left. + \frac{1}{2} \frac{dH}{d\phi} \frac{1}{r} [\overline{v'\theta'} (1+\alpha) \cos\phi] \Big|_{H/2} - \frac{3}{4} W \sin\phi \cos^2\phi (1+\alpha(\phi, \frac{H}{2})) \right\} d\phi
 \end{aligned}$$

again making use of the differential calculus formula (2.13). Of the four terms in the above expression, the first and second vanish when the boundary conditions on $\overline{v'\theta'}$ are applied. Thus

Upper integral =

$$\frac{1}{rH} \int_0^{\pi/2} \frac{dH}{d\phi} \overline{v'\theta'} \Big|_{H/2} (1+\alpha(\phi, \frac{H}{2})) \cos\phi d\phi - \frac{3W}{2H} \int_0^{\pi/2} \sin\phi \cos^2\phi (1+\alpha(\phi, \frac{H}{2})) d\phi$$

The lower integral, $\frac{2}{H} \int_0^{\pi/2} \int_0^{H/2} (\text{L.H.S. 2.4}) dz \cos\phi d\phi$, is found to be the same as the upper integral but with reversed sign, (as is also obvious from 2.33). Thus, we may write the B equation as

$$- \frac{3}{H} \int_0^{\pi/2} \left[W - \frac{2V}{r} \frac{dH}{d\phi} \Lambda(\phi, \frac{H}{2}) \right] (1+\alpha(\phi, \frac{H}{2})) \sin\phi \cos^2\phi d\phi = \quad (2.36)$$

$$\frac{2}{H} \int_0^{\pi/2} \left[\int_{H/2}^H H dz - \int_0^{H/2} H dz \right] \cos\phi d\phi$$

An interpretation for this averaging operator is clearer if we substitute the linearized heating law (2.34) into the right hand side of (2.36).

$$\begin{aligned}
\text{R.H.S. (2.36)} &= \frac{2}{\tau H} \int_0^{\pi/2} \left[\int_{H/2}^H (T_r - T) dz - \int_0^{H/2} (T_r - T) dz \right] \cos \phi d\phi \\
&= \frac{1}{\tau} \left\{ \frac{2}{H} \int_0^{\pi/2} \left(\int_{H/2}^H T_r dz - \int_0^{H/2} T_r dz \right) \cos \phi d\phi + \frac{1}{2} \beta \bar{H} n_3 \right\} \\
&= \frac{\bar{H} n_3}{2 \tau} (\beta - \beta_r) \tag{2.37}
\end{aligned}$$

$$\text{where } \beta_r = \frac{4}{n_3 \bar{H}^2} \int_0^{\pi/2} \left(\int_{H/2}^H T_r dz - \int_0^{H/2} T_r dz \right) \cos \phi d\phi$$

is defined as the radiative equilibrium lapse rate. We can think of the deviation of the lapse rate from its radiative equilibrium value as being controlled by the stabilizing effect of the dynamic fluxes, which of course are themselves responsive to the temperature gradients. The assumption of a constant lapse rate β makes our dynamical model analogous to two-layer model, where temperatures specified at two points in the vertical, only allow a mean gradient to be resolved. It is therefore appropriate to determine a vertical forcing as the difference of the upper and lower integrals as we have done, rather than using $\langle \frac{\partial}{\partial z} (2.4) \rangle$ say. This alternative average would only produce the same result for a linear function.

2.3.3. A Equation

This time we average the thermodynamic equation separately for high and low latitudes, and difference them with a 'suitable weighting' α . After a little manipulation we have the A equation.

$$\begin{aligned}
\frac{3V}{r} (1+\alpha) \left[\sin \phi \cos^2 \phi \int_0^{H(\phi)} \Lambda(\phi, z) (1+\alpha(\phi, z)) dz \right] \Big|_{\phi=\phi_\alpha} &= \\
\alpha \int_0^{\phi_\alpha} \int_0^H \mathcal{H} dz \cos \phi d\phi - \int_{\phi_\alpha}^{\pi/2} \int_0^H \mathcal{H} dz \cos \phi d\phi &\tag{2.38}
\end{aligned}$$

For convenience in evaluating the integrals of (2.38) we select $\phi_\alpha = \frac{\pi}{4}$. Presumably many choices for α are possible since we apply the same operator to both sides of equation (2.4). We will allow equal weighting by mass for the high and low latitude parts. Mathematically, this requires the following condition on α :

$$\alpha \int_0^{\pi/4} \int_0^{\dot{H}(\phi)} 1 \, dz \cos\phi \, d\phi - \int_{\pi/4}^{\pi/2} \int_0^{H(\phi)} 1 \, dz \cos\phi \, d\phi = 0$$

or,

$$\alpha = \frac{\overline{H}}{\int_0^{\pi/4} H(\phi) \cos\phi \, d\phi} - 1 \quad (2.39)$$

For a constant tropopause height, $\alpha = \sqrt{2} - 1$. If Spiegel's formula is used for the heating, then this choice of α makes the right hand side of (2.38) proportional to the deviation of A from a radiative equilibrium 'pseudo-gradient' A_r . We show this in the following section where a particularly simple form of $H(\phi)$ is assumed.

Chapter 3: Model Results with Grey Radiative Heating

3.1 Simplified Equations

In this chapter we solve the system of equations (2.33), (2.36), and (2.38) with the heating $H(\phi, z)$ of the simple Newtonian form (2.34). This H should not be thought of as approximating the observed long wave heating which we know is everywhere negative (and therefore cannot satisfy 2.33). One of the assumptions involved in deriving (2.34) is that the deviation from radiative equilibrium ($T_r - T$) is small. In practice, the difference may be as large as 20%, the deviation reaching a maximum at the ground and at the tropopause. The advantage of our analytical approach is that various physical or geometrical effects can be added one at a time, and the results studied unambiguously. For the purpose of examining how the addition of a latent heat flux changes the temperature gradients, for example, a Newtonian heating law is quite adequate. If the absolute values are still not realistic, a more exact form for the heating will be necessary (Chapter 4). This will not invalidate the comparative results of this section.

The radiative equilibrium temperature T_r is calculated from grey radiation theory. Since sensible tropopause height variations are not produced by this method (see Section 3.3.5), we will simply prescribe $H(\phi)$. We can then simulate a realistic tropospheric geometry by allowing $H(\phi)$ to decrease at high latitudes. We will find that this effect is at least as important as the convergence of the meridians (i.e. spherical geometry). As long as we are specifying H anyway, we might as well choose a form that offers maximum simplification of the equations. Thus,

$$H(\phi) = \bar{H} [1 - \sigma(\phi + 1 - \frac{\pi}{2})] \quad (3.1)$$

so that $\frac{dH}{d\phi} = -\sigma\bar{H}$ is independent of latitude, and the integral in equation (2.36) can be evaluated more readily. σ is the constant fractional slope of the tropopause, and has a value of approximately 0.4 for the earth. The temperature structure $T(\phi, z)$ is still given by (2.18) and (2.32), where the weighting factors n_1, n_2, n_3 can now be expressed solely in terms of σ .

$$\begin{aligned} n_1 &= 1 + \sigma(\frac{\pi}{2} - \frac{5}{3}) \\ n_2 &= 1 - \frac{1}{3}\sigma \\ n_3 &= 1 + \sigma^2(\pi - 3) \end{aligned} \quad (3.2)$$

3.1.1 Choice for weighting factor α

As indicated in Section 2.3.3, the right hand side of equation (2.38) can be made proportional to the deviation of the meridional temperature gradient A from an approximate radiative equilibrium gradient A_r' . Concentrating on just that part involving T on the RHS of equation (2.38),

$$\begin{aligned} \{ \} &\equiv \{ \alpha \int_0^\phi \int_0^H T dz \cos \phi d\phi - \int_{\phi_\alpha}^{\pi/2} \int_0^H T dz \cos \phi d\phi_\alpha \} \\ &= \alpha \int_0^\phi \alpha [(C_0 + C_2 \sin^2 \phi)H - \frac{1}{2} \beta H^2] \cos \phi d\phi \\ &\quad - \int_{\phi_\alpha}^{\pi/2} [(C_0 + C_2 \sin^2 \phi)H - \frac{1}{2} \beta H^2] \cos \phi d\phi \end{aligned}$$

Substituting $H(\phi) = H_0 - S\phi$ where $S = \sigma\bar{H}$,

$$H_0 = H(0) = \bar{H} [1 + \sigma(\frac{\pi}{2} - 1)]$$

$$\begin{aligned}
\{ \} = & (C_0 H_0 - \frac{1}{2} \beta H_0^2) \left[(1+\alpha) \sin \phi_\alpha - 1 \right] \\
& - (C_0 - \beta H_0) S \left[(1+\alpha) \phi_\alpha \sin \phi_\alpha + \cos \phi_\alpha - (\frac{\pi}{2} + \alpha) \right] \\
& + \frac{1}{3} C_2 H_0 \left[(1+\alpha) \sin^3 \phi_\alpha - 1 \right] \\
& - \frac{1}{9} C_2 S \left[(1+\alpha) (3 \phi_\alpha \sin^3 \phi_\alpha + \sin^2 \phi_\alpha \cos \phi_\alpha + 2 \cos \phi_\alpha) \right. \\
& \quad \left. - (\frac{3}{2} \pi + 2\alpha) \right] \\
& - \frac{1}{2} \beta S^2 \left[(1+\alpha) (\phi_\alpha^2 \sin \phi_\alpha + 2 \phi_\alpha \cos \phi_\alpha - 2 \sin \phi_\alpha) - (\frac{\pi^2}{4} - 2) \right]
\end{aligned}
\tag{3.3}$$

The weighting factor α is chosen so that regions poleward and equatorward of the dividing latitude ϕ_α have equal masses. This eliminates several large terms (involving C_0 and the mean part of $\frac{1}{2} \beta H^2$) from (3.3). Expressing this condition on α mathematically, we have

$$H_0 \left[(1+\alpha) \sin \phi_\alpha - 1 \right] - S \left[(1+\alpha) (\phi_\alpha \sin \phi_\alpha + \cos \phi_\alpha) - (\frac{\pi}{2} + \alpha) \right] = 0$$

or, expanding H_0 and putting $\sigma = \frac{S}{H}$,

$$\sin \phi_\alpha - \sigma \left[(\phi_\alpha - \frac{\pi}{2} + 1) \sin \phi_\alpha + \cos \phi_\alpha - 1 \right] = \frac{1}{1+\alpha} \tag{3.4}$$

After considerable algebra, we simplify the remaining terms in (3.3).

$$\{ \} = \frac{1}{3} C_2 \bar{H} f_\sigma - \frac{1}{2} \beta \bar{H}^2 g_\sigma$$

where

$$\begin{aligned}
 f_{\sigma} &= (1+\alpha) \sin^3 \phi_{\alpha} - 1 \\
 &\quad - \sigma(1+\alpha) \left[\left(\phi_{\alpha} - \frac{\pi}{2} + 1 \right) \sin^3 \phi_{\alpha} + \frac{1}{3} \sin^2 \phi_{\alpha} \cos \phi_{\alpha} + \frac{2}{3} \cos \phi_{\alpha} - 1 \right] - \frac{1}{3} \sigma \alpha \\
 g_{\sigma} &= - \left[(1+\alpha) \sin \phi_{\alpha} - 1 \right] \\
 &\quad + \sigma^2 (1+\alpha) \left[\left\{ \left(\phi_{\alpha} - \frac{\pi}{2} + 1 \right)^2 - 2 \right\} \sin \phi_{\alpha} + 2 \left(\phi_{\alpha} - \frac{\pi}{2} + 1 \right) \cos \phi_{\alpha} + 1 \right] + (\pi-3) \sigma^2 \alpha
 \end{aligned} \tag{3.5}$$

For the case $\phi_{\alpha} = \frac{\pi}{4}$, $\alpha = \frac{\sqrt{2}}{1 + \sigma \left(\frac{\pi}{4} - 2 + \sqrt{2} \right)} - 1$

$$f_{\sigma} = -\frac{1}{2} + \frac{\sigma}{6} \left[2 - (\sqrt{2} - 1)(1+\alpha) \right]$$

$$g_{\sigma} = \left(1 - \frac{1+\alpha}{\sqrt{2}} \right) + \sigma^2 \left[1 + \alpha(\pi-2) + \frac{1+\alpha}{\sqrt{2}} \left(\frac{\pi^2}{16} - \pi + 1 \right) \right]$$

When $\sigma = 0$, $f_{\sigma} = -\frac{1}{2}$ and $g_{\sigma} = 0$, so that { } above is directly proportional to the meridional gradient A . A different choice for the weight would give a more complicated expression involving the other mean parameters $\langle T \rangle$ and β as well. Equations (2.33), (2.36), and (2.38) now can be written as

$$\left. \begin{aligned}
 0 &= \frac{(\langle T_r \rangle - \langle T \rangle)}{\tau} \\
 -\frac{1}{H} \left(W + \frac{2V}{r} \bar{H}_{\sigma} \Lambda_{\frac{1}{2}} \right) I_z &= \frac{\bar{H} n_3}{2} \left\{ \frac{\beta - \beta_r}{\tau} \right\} \\
 \frac{3V}{2\sqrt{2}r} (1+\alpha); H \left(\frac{\pi}{4} \right) L_y &= \frac{\bar{L} H f_{\sigma}}{\pi n_1} \frac{(A_r' - A)}{\tau}
 \end{aligned} \right\} \tag{3.6}$$

where $\Lambda_{\frac{1}{2}} = \Lambda(\phi, \frac{H}{2}) = 0.82$,

$$A_r' = \frac{\pi n_1}{LH f_\sigma} \left\{ \left[\alpha \int_0^{\pi/4} \int_0^H T_r dz \cos \phi d\phi - \int_{\pi/4}^{\pi/2} \int_0^H T_r dz \cos \phi d\phi \right] + \frac{1}{2} \beta \bar{H}^2 g_\sigma \right\} \quad (3.7)$$

For a flat-topped troposphere ($\sigma = 0$), $A_r' = A_r$, the radiative equilibrium meridional gradient. For $\sigma \neq 0$, A_r' is modified by the g_σ factor. The integrated Leovy factors (L_y, L_z) are given by

$$\begin{aligned} L_z &= 3 \int_0^{\pi/2} \left[1 + \mathcal{L}(\phi, \frac{H}{2}) \right] \sin \phi \cos^2 \phi d\phi \\ &= 1 + 3 \int_0^{\pi/2} \mathcal{L}(\phi, \frac{H}{2}) \sin \phi \cos^2 \phi d\phi \end{aligned}$$

and

$$\begin{aligned} L_y &= \frac{1}{H(\phi_\alpha)} \int_0^{H(\phi_\alpha)} \Lambda(\phi_\alpha, z) (1 + \mathcal{L}(\phi_\alpha, z)) dz \\ &= 1 + \int_0^1 \Lambda(\phi_\alpha, x) \mathcal{L}(\phi_\alpha, x) dx; \quad x = \frac{z}{H(\phi_\alpha)} \\ &= 1 + 0.6780 h_0 \frac{T_3 e^{a/T_3 K_s}}{a\beta H} \left[e^{-a/T_0} - e^{-a/T_H} - \frac{e^{-\lambda x_*}}{e^{-\lambda x_*} - e^{-\lambda}} \frac{\lambda}{(\lambda + \frac{a\beta H}{T_*^2})} e^{-a/T_*} \right] \end{aligned} \quad (3.38)$$

(See Appendix A4)

where T_0 , H , and $T_* = T_0 - \beta H x_*$ are all evaluated at latitude $\phi_\alpha = \frac{\pi}{4}$ ($x_* = 0.20$, $K_s = 2.11$, $\lambda = 2.50$). These integrated Leovy factors are defined in such a way that when latent heat fluxes are omitted, $L_y = L_z = 1$.

When latent heat transport is included in the model, one should be careful not to interpret L_y, L_z as the ratio of latent to sensible heat.

We will also modify the right hand side of the B equation in (3.6), replacing $(\beta - \beta_r)$ by $(B_r' - B)$ where

$$B_r' = \Gamma - \beta_r + \frac{\frac{1}{2}\Gamma X(\Gamma - \beta)}{1 - \frac{1}{3}X(\Gamma + \beta)}, \quad \text{after (2.28).}$$

Once the radiative terms $\langle T_r \rangle$, A_r' , and B_r' are defined in terms of $\langle T \rangle$, A , and B , the system of equations (3.6) is complete.

3.2 Grey radiative equilibrium state

The radiative equilibrium temperature $T_r(\phi, z)$ is calculated from the grey radiation approximation (e.g. see Goody, 1964).

$$T_r(\phi, z) = \frac{T_e(\phi)}{2^{1/4}} \left[1 + \frac{3}{2} \tau_w(\phi, z) \right]^{1/4}; \quad z > 0 \quad (3.9)$$

where τ_w is the optical depth of the absorbing gas (in our case, water vapor). $T_e(\phi)$ is the 'effective temperature' defined by the incoming solar radiation $Q(\phi)$ and planetary albedo $\alpha(\phi)$.

$$T_e(\phi) = \left[\frac{Q(\phi)}{\sigma} (1 - \alpha(\phi)) \right]^{1/4} \quad (3.10)$$

σ = Boltzmann constant = 8.13×10^{-11} cal cm⁻² min⁻¹ K⁻⁴ (not to be confused with the tropopause slope). Table 3.1 shows values of the effective

temperature determined from equation (3.10). The mean annual radiation \bar{Q} is calculated for a solar constant of $2 \text{ cal cm}^{-2} \text{ min}^{-1}$ (see Section 4.1) and the albedo $\bar{\alpha}$ is estimated from Figure 1 in Vonder Haar and Suomi (1971). Averaging over latitude, $\bar{Q} = 0.5$ and $\bar{\alpha} = 0.30$.

Table 3.1: Effective Temperature T_e (K)

latitude ϕ	$Q(\phi), \text{ cal cm}^{-2} \text{ min}^{-1}$	$\alpha(\phi)$	$T_e(\phi), \text{ K}$
5	0.61670	0.24	275.55
15	0.59814	0.245	273.00
25	0.56262	0.265	267.06
35	0.51148	0.30	257.61
45	0.44687	0.345	244.95
55	0.37206	0.385	230.33
65	0.29318	0.415	214.31
75	0.22993	0.455	198.14
85	0.19777	0.50	186.75

Rather than simply specifying the absorber path length τ_w , as is commonly done in radiative equilibrium calculations (e.g. Manabe and Möller, 1961), we allow an extra degree of freedom by having τ_w depend on the internally computed temperatures, i.e. we fix the relative humidity rather than the absolute humidity.

$$\tau_w(\phi, z) = k_0 \int_z^{\infty} \rho_w(z) dz \quad (3.11)$$

where k_0 is the grey absorption coefficient (in $\text{cm}^2 \text{ g}^{-1}$) and ρ_w is the water vapor density

$$\rho_w = \frac{e_w}{R_w T} = \frac{h_0 e_3 p}{R_w T p_0} e^{-a\left(\frac{1}{T} - \frac{1}{T_3}\right)}$$

where e_w is the partial pressure of the water vapor (defined in terms of the saturation vapor pressure using the Clausius-Clapeyron relation) and the other variables are defined in Sections 1.4 and 2.1. Note that τ_w is determined from the actual temperature field rather than the radiative equilibrium temperature field. Thus,

$$\tau_w(\phi, z) = \frac{k_0 h_0 e_3 e^{a/T_3}}{p_0 R_w} \int_z^H \frac{p}{T} e^{-a/T} dz' + \tau_w(\phi, H)$$

with $\tau_w(\phi, H) = \frac{k_0 r_H p_H}{g}$ representing the stratospheric optical depth

(assuming constant temperature $T = T_H$ and constant water vapor mixing ratio r_H). To evaluate the tropospheric integral, we substitute for pressure p from (2.23) and change variables

$$s = \frac{a}{T}; \quad \text{where } T = T_0 - \beta z' \tag{3.12}$$

$$\tau_w(\phi, z) = \frac{k_0 h_0 e_3 e^{a/T_3}}{R_w \beta} \left(\frac{a}{T_0}\right)^\gamma \int_{\frac{a}{T(z)}}^{\frac{a}{T_H}} \frac{e^{-s}}{s^{\gamma+1}} ds + \tau_w(\phi, H)$$

We meet almost the same integral in Section 4.2.1, when computing the reduced water vapor path length. Since the path length must be calculated many times in the radiative routines, we need an extremely efficient procedure for evaluating this integral. A highly accurate analytical method was found and is outlined in Appendix A5. We shall simply state the result here.

$$\tau_w(\phi, z) \doteq 0.02444 \frac{k_0 h_0}{\beta} T_0 \left(\frac{T}{T_0} \right)^{\gamma+1} e^{-a \left(\frac{1}{T} - \frac{1}{T_3} \right)} \frac{G_1}{\left(1 + \frac{\mu T}{a} \right)^\eta} + \tau_w(\phi, H) \quad (3.13)$$

$$\text{where } \tau_w(\phi, H) = 3.8753 k_0 h_0 \left(\frac{T_H}{T_0} \right)^\gamma e^{-a \left(\frac{1}{T_H} - \frac{1}{T_3} \right)}$$

$$\text{and } \mu\eta = (\gamma+1) \frac{G_2}{G_1}, \quad \mu(\eta+1) = 2(\gamma+2) \frac{G_3}{G_1}$$

$$\text{and } G_1, G_2, G_3, \text{ are all functions of } D = a \left(\frac{1}{T_H} - \frac{1}{T(z)} \right)$$

$$G_1 = 1 - e^{-D}$$

$$G_2 = 1 - e^{-D(1+D)}$$

$$G_3 = 1 - e^{-D(1+D+\frac{1}{2}D^2)}$$

Table 3.2 shows sample calculations for the surface optical depth $\tau_w(\phi, 0)$ for several combinations of β and H with the surface relative humidity $h_0 = 0.77$. Surface temperatures were taken from Sellers (1965), and are the same as those values used in Table 1.1. We see that $\tau_w(\phi, 0) = \tau_0$ varies with latitude by more than an order of magnitude. However, for a hemispheric mean surface optical depth of 4, recommended by Goody (Chapter 8), we want $k_0 \approx 2 \text{ cm}^2 \text{ g}^{-1}$. We will adopt this value in subsequent calculations.

Defining a function

$$F_\zeta(\phi) = \int_0^\zeta \left[1 + \frac{3}{2} \tau_w(\phi, x) \right]^{\frac{1}{4}} dx \quad (3.14)$$

where $x = \frac{z}{H(\phi)}$, the radiative terms of system (3.6) are calculated self-

Table 3.2: $\tau_w(\phi, 0)/k_0$ for $h_0 = 0.77$

ϕ	$T_0(\phi), K$	$\beta = 6.5 \text{ K/km}$	$\beta = 6.0$	$\beta = 6.5$
		$H = 12.0 \text{ km}$	$H = 12.0$	$H = 14.0$
5	298.7	3.5475	3.7766	3.5477
15	298.3	3.4587	3.6821	3.4589
25	293.6	2.5548	2.7202	2.5551
35	287.2	1.6649	1.7732	1.6652
45	280.7	1.0568	1.1259	1.0570
55	273.7	0.6326	0.6741	0.6327
65	266.0	0.3488	0.3719	0.3488
75	257.3	0.1707	0.1820	0.1707
85	249.6	0.0870	0.0928	0.0870
hemispheric average 2.0561			2.1893	2.0563

consistently from the temperature structure we are solving for.

$$\begin{aligned}
 \langle T_r \rangle &= \frac{1}{2^{1/4} \bar{H}} \int_0^{\pi/2} T_e(\phi) H(\phi) F_1(\phi) \cos \phi \, d\phi \\
 \beta_r &= \frac{4}{2^{1/4} n_3 \bar{H}^2} \int_0^{\pi/2} T_e(\phi) H(\phi) \left[2 F_{1/2}(\phi) - F_1(\phi) \right] \cos \phi \, d\phi \\
 A_r &= \frac{\pi n_1}{L \bar{H} f_\sigma} \left\{ \frac{1}{2^{1/4}} \left[\alpha \int_0^{\pi/4} T_e(\phi) H(\phi) F_1(\phi) \cos \phi \, d\phi \right. \right. \\
 &\quad \left. \left. - \int_{\pi/4}^{\pi/2} T_e(\phi) H(\phi) F_1(\phi) \cos \phi \, d\phi \right] + \frac{1}{2} \beta \bar{H}^2 g_\sigma \right\}
 \end{aligned} \tag{3.15}$$

3.3 Results

3.3.1 Method of Solution

We have to solve the system of equations (3.6) together with the constitutive equations for the Richardson number (Equation 2.10) and the radiative terms (Equation 3.15). Scaling the radiative relaxation time constant $\tau = 10^6 \tau^*$ sec, and substituting for all the other constants so that the vertical gradients B, B_r', β are in units of $^\circ\text{K}/\text{km}$, the horizontal gradients A, A_r' in $^\circ\text{K}/100 \text{ km}$ and the tropopause height in km, we have the following set.

$$\begin{aligned}
 \langle T \rangle &= \langle T_r \rangle \\
 A_r' - A &= k_A A B \frac{\sqrt{1+Ri}}{Ri} \\
 B_r' - B &= -k_B \frac{B}{Ri\sqrt{1+Ri}} + k_S A B \frac{\sqrt{1+Ri}}{Ri} \\
 Ri &= k_R \frac{B}{A^2}
 \end{aligned}
 \tag{3.16}$$

where

$$\begin{aligned}
 k_A &= .001738 \left[\frac{H(\phi)}{\bar{H}} \frac{(1+\alpha)}{-f\sigma} \sin \phi \cos^2 \phi \right]_{\phi=\frac{\pi}{4}} \tau^* n_1 L_Y \langle T \rangle \\
 k_B &= .06348 \frac{\tau^* L_Z \langle T \rangle^2}{n_3 \bar{H}^2} \\
 k_S &= .06049 \frac{\tau^* L_Z \langle T \rangle}{n_3 \bar{H}} \sigma \\
 k_R &= .01081 \langle T \rangle
 \end{aligned}$$

The coefficients k_A , k_B , k_S , and k_R are all positive. We solve (3.16) iteratively using the following steps:

- (1) Initialize: a) input \bar{H} , σ , τ^* ; calculate n_1 , n_2 , n_3 , α , f_σ , g_σ
 b) input first guess at β , A , $\langle T \rangle$
- (2) Iterate for $\langle T \rangle$: a) from 1a, 1b calculate C_0 , C_2
 b) evaluate $F_1(\phi)$, $F_{1/2}(\phi)$, and thus $\langle T_r \rangle$, A_r' , B_r'
 c) loop until solution for $\langle T \rangle = \langle T_r \rangle$ converges
- (3) Calculate L_y , L_z , and thus, k_A , k_B , k_R , k_S
- (4) Solve (3.16) for A , B : calculate corresponding β
- (5) Go back to 1b and repeat process until values for A , B converge.

It turns out that the $\langle T \rangle = \langle T_r \rangle$ iteration has two possible solutions and the root we want is the unstable one. It is found by the standard 'secant method' (see, for example, Acton, Ch. 2). There is further discussion of the nature of the roots at the end of this chapter (section 3.3.5). This leaves only step 4 in the list above to be explained. Considering the system (3.16) again, substitute for R_i in the A equation.

$$(A_r' - A)^2 = \frac{k_A^2 A^6}{k_R^2} \left(1 + k_R \frac{B}{A^2}\right) \quad (3.17)$$

Now multiply the A and B equations together, substituting for R_i in the result.

$$(B_r' - B)(A_r' - A) = -\frac{k_A k_B}{k_R^2} A^5 + \frac{k_S}{k_A} (A_r' - A)^2 \quad (3.18)$$

Eliminating B between (3.17) and (3.18) leads to a ninth order polynomial for the meridional gradient A.

$$\begin{aligned} F(A) &= A^4 \left[a_1 A^5 - (A^2 - a_2)(A - A_r') - a_3(A - A_r')^2 \right] + a_4(A - A_r')^3 \\ &= 0 \end{aligned} \quad (3.19)$$

where

$$a_1 = \frac{k_A k_B}{k_R}, \quad a_2 = -k_R B_r', \quad a_3 = \frac{k_S k_R}{k_A}, \quad a_4 = \left(\frac{k_R}{k_A} \right)^2$$

Equation (3.19) has only one real root and is readily solved by the Newton-Raphson technique. For an initial guess of $A = -0.5$, this method generally converges to 5 decimal place accuracy within five or six iterations.

In the remainder of this chapter, we will examine the predictions of this simple model for the mid-latitude eddy fluxes and temperature gradients. Since the exact values of the time constant τ and grey absorption coefficient k_0 are uncertain, we should test how sensitive our results are to the numbers we have chosen. This will highlight some difficulties with the linearized heating formulation and with grey radiation calculations in general.

3.3.2 Variation with tropopause slope

There are five input parameters we must specify for any solution. These are: the tropopause mean height \bar{H} and slope σ ; the grey absorption coefficient k_0 ; surface relative humidity h_0 ; and radiative time constant τ . The basic solution, with which other results are compared, has the following parameter values.

$$\begin{aligned} \bar{H} &= 12.0 \text{ km} \\ \sigma &= 0.0 \\ k_0 &= 2.0 \text{ cm}^2 \text{ g}^{-1} \\ h_0 &= 0.0 \\ \tau^* &= 5.5 \text{ sec (i.e. } \tau \text{ scaled down by a factor of } 10^6) \end{aligned}$$

Thus, the basic state is a flat-topped dry troposphere. $h_0 = 0.0$ implies only that the latent heat fluxes are absent. h_0 is fixed at the climatological value of 0.77 for all radiative calculations. $\tau^* = 11$ was used by Stone in his 1972a paper, but this is probably too large, due to a small error in Goody's derivation. The results obtained for this input set are as follows:

Radiative terms:	A_r'	=	-1.4668	°K/100 km
	B_r'	=	-1.042	°K/km
	$\langle T_r \rangle$	=	250.84	°K
Temperature gradients:	A	=	-0.5877	°K/100 km
	B	=	2.927	°K/km
	β	=	7.476	°K/km
	Ri	=	22.977	

It is interesting to compare these results with the third line of Table A1 (Appendix A2). Our model differs significantly from Stone's at this point only in allowing convergence of the meridians. The resulting gradients show a small difference compared to the great improvement over radiative-convective equilibrium. Moreover, about half the deviation is attributable to the different time constant. (For $\tau^* = 11$, our model predicts A =

-0.4575 and $B = 2.259$). The baroclinic fluxes have stabilized the troposphere to an extent that dry convection can be eliminated as a major vertical transport process. However, the static stability is still less than that required to stabilize moist processes. Other discrepancies with observation are also apparent. The meridional gradient A is too intense. A typical mid-latitude gradient is -0.5 °K/100 km (Table 1.7), so we expect a hemispheric average to be somewhat weaker (about -0.4 °K/100 km). The resulting surface temperatures are too high. The ground temperature at the equator, $T_0(0)$, is 314°K with the pole 56 degrees colder. The ground is not in radiative equilibrium, of course, even though the large scale vertical flux $\overline{w'\theta'}$ vanishes at $z = 0$. It is implicitly assumed that small scale fluxes are present in the boundary layer, although they act only in a passive sense.

Figure 3.1 shows contours of the total eddy flux heating in °C/day for this simplest of cases. The figure combines the effects of horizontal eddies, which cool the equatorial region and warm high latitudes, and vertical eddies which stabilize the atmosphere by cooling low levels and heating the upper troposphere. The net effect on the vertical structure is to stabilize the temperature profile throughout low and middle latitudes. Near the pole at the surface, heating due to strong convergence of the horizontal transport overwhelms the weakly stabilizing effect of the vertical fluxes. Thus, in high latitudes, the effect of the dynamics is to destabilize the temperature structure. This agrees with results obtained by Held and Suarez (1978), using a more complex model (see their Figure 23 or 25). The net integrated heating, with appropriate weighting by surface area is, of course, zero.

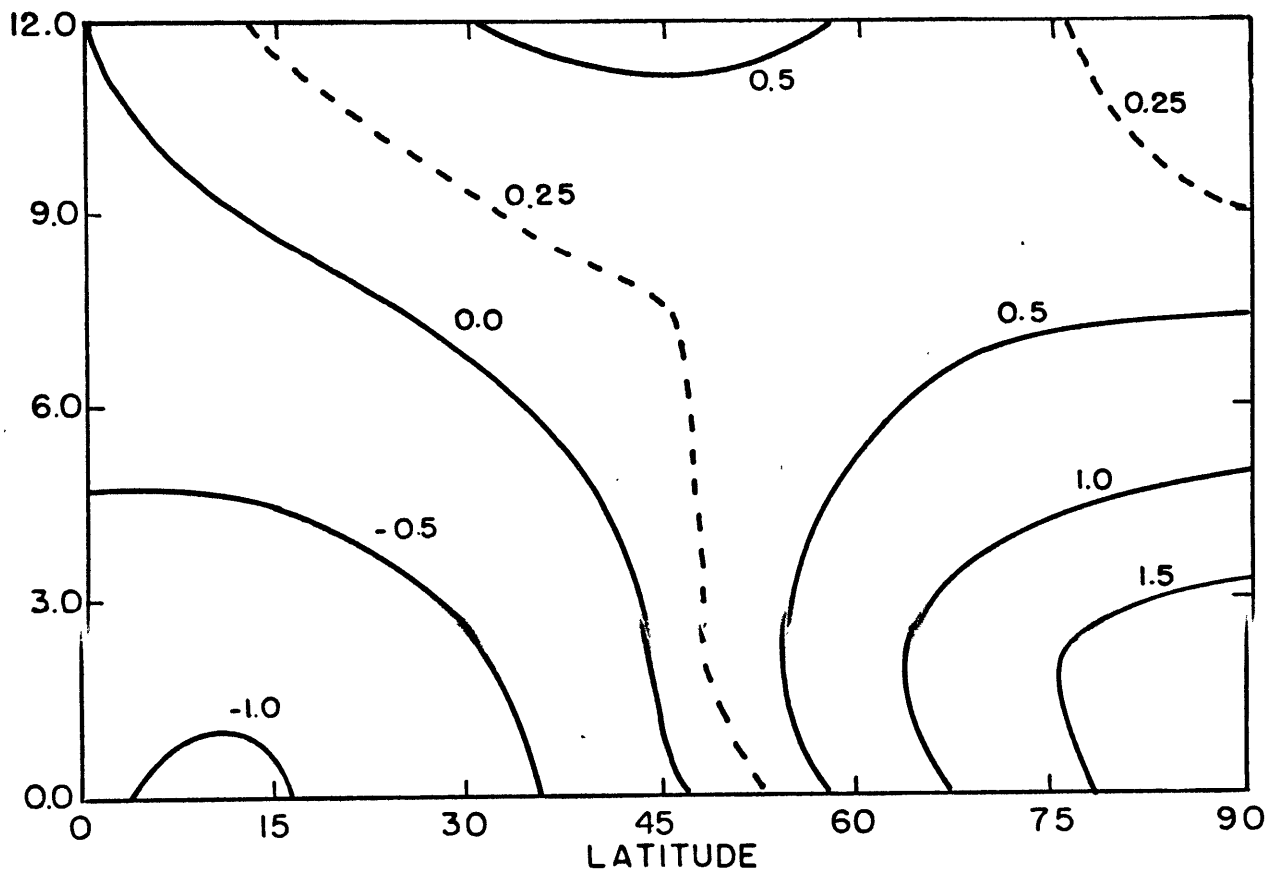


Figure 3.1: Total eddy heating in °C/day for grey radiation model as a function of height and latitude. (Model parameters: $\bar{H} = 12.0$ km, $\sigma = 0.0$, $k_0 = 2.0$ cm² g⁻¹, $h_0 = 0.0$, $\tau^* = 5.5$).

Let us now look at how a sloping tropopause affects the solution. Results are summarized in Table 3.3. The last two columns of this table represent the total integrated horizontal and vertical fluxes, respectively, in units of $m \text{ } ^\circ\text{C sec}^{-1}$. The vertically integrated horizontal sensible heat flux (normalized by \bar{H}) is

$$\frac{1}{\bar{H}} \int_0^{H(\phi)} \overline{v'\theta'} dz = 3V \frac{H(\phi)}{\bar{H}} \sin \phi \cos \phi$$

Integrating over latitude gives Vn_1 .

Table 3.3: Variation with tropopause slope σ
($\bar{H} = 12.0$, $k_0 = 2.0$, $h_0 = 0.0$, $\tau^* = 5.5$)

σ	$\langle T \rangle$	A	B	β	Ri	Vn_1	$\frac{1}{6} Wn_1 \times 10^{-3}$
0.0	250.8	-.588	2.93	7.48	23.0	10.80	8.66
0.1	251.5	-.588	3.05	7.38	24.1	10.92	8.41
0.2	252.1	-.585	3.21	7.25	25.6	10.98	8.02
0.3	252.5	-.579	3.40	7.10	27.7	10.97	7.51
0.4	252.8	-.570	3.63	6.92	30.4	10.87	6.90
0.5	253.0	-.559	3.88	6.72	33.9	10.68	6.23
0.6	253.1	-.545	4.16	6.50	38.4	10.38	5.52

Comments on Table 3.3 are listed below.

(i) Increasing σ from zero to the observed slope 0.4 weakens the horizontal gradient A by 2.9%, but increases the stability B by 23.8%. Thus, allowing for a sloping tropopause has considerably more effect on the vertical gradient than on the horizontal one. [NOTE: It may seem deceptive to calculate a percentage change using B rather than β , which varies by only 7.4% over the same range. However, B is the important output variable in this model and lapse rate β is merely a derived quantity, in spite of

the radiative feedback. As evidence of this, we present Table 3.4, where the B- β interrelation is determined by the zeroth order formula $B = \Gamma - \beta$ rather than the more exact form (2.28). What we find, curiously enough, is that B (and A) remains almost unchanged and it is the lapse rate β that adjusts. The stability differs from that of Table 3.3 by at most 0.1 °K/km ($\approx 3\%$), whereas β differs by about 0.7 °K/km ($\approx 10\%$) at all slopes.]

Table 3.4: Variation with σ using $B = \Gamma - \beta$
(Compare with Table 3.3)

σ	A	B	β	Ri
0.0	-.598	3.03	6.77	23.2
0.1	-.597	3.12	6.68	24.1
0.2	-.593	3.25	6.55	25.4
0.3	-.587	3.42	6.39	27.3
0.4	-.578	3.61	6.19	29.8

(ii) The total horizontal sensible heat flux is almost independent of the slope of the upper boundary. On the other hand, the vertical flux is affected substantially. $\frac{1}{6} W_{n_1}$ decreases by 20% as the fractional slope σ steepens to 0.4. This number, however, is somewhat misleading. Figure 3.2 shows heating contours for $\sigma = 0.4$ and should be compared with Figure 3.1 ($\sigma = 0.0$). The magnitude and location of the heating are fairly similar. Certainly the heating is no weaker, and there is a region in the middle and upper troposphere centered about 65° north where the eddies are depositing up to 0.2 °C/day more heat. The entire upper troposphere from about 30° to 80° latitude is stabilized with respect to Figure 3.1.

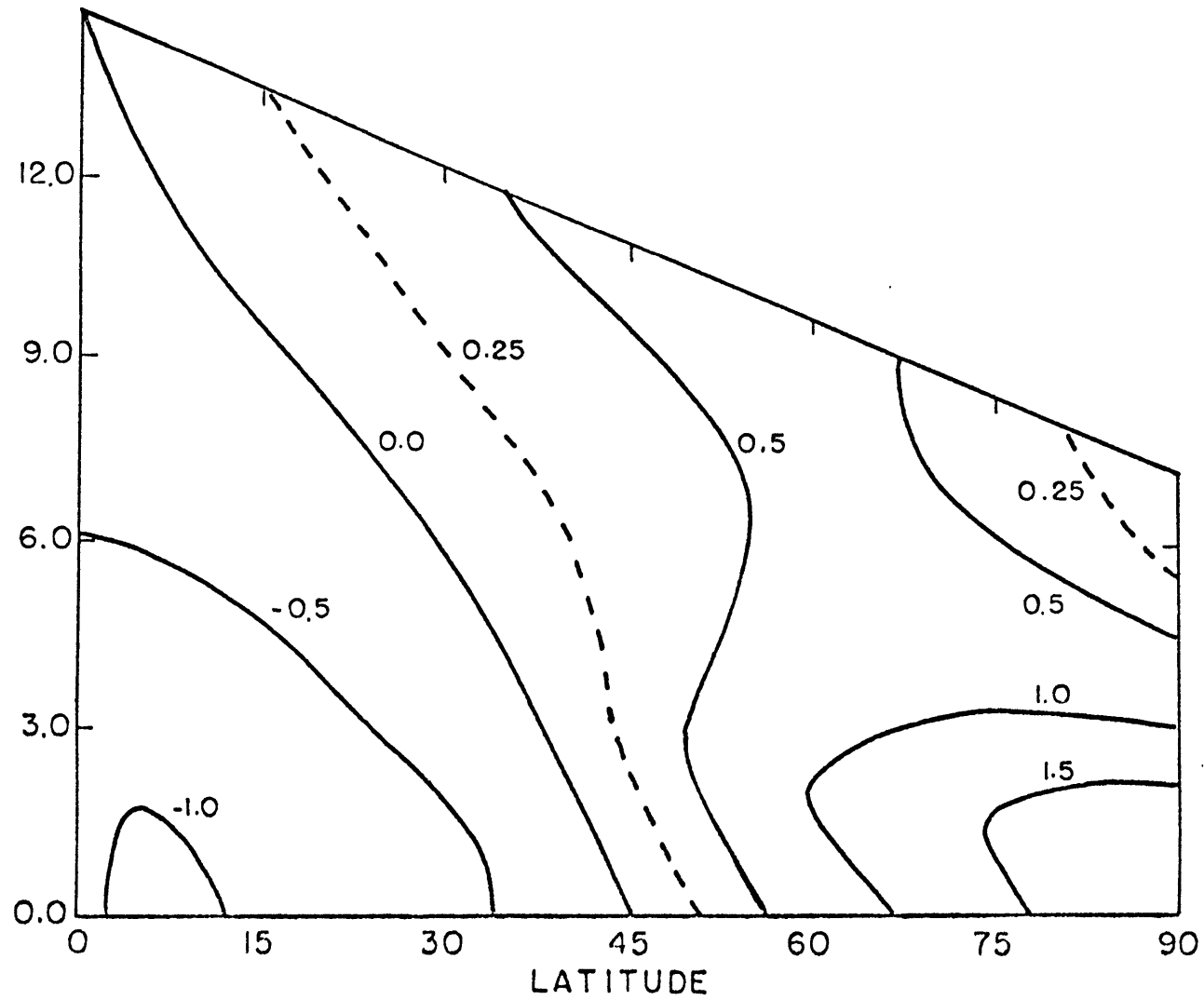


Figure 3.2: Total eddy heating in °C/day for $\sigma = 0.4$. (Other parameters as in Fig. 3.1).

(iii) At first sight, it is confusing how the stability can increase at the same time as the vertical stabilizing flux $\overline{w'\theta'}$ is decreasing. A closer examination of Equations (3.16) serves to clarify the situation. A sloping tropopause affects only the vertical forcing equation, through the term involving k_S . This term is due to the horizontal flux $\overline{v'\theta'}$ rather than $\overline{w'\theta'}$. The equation for $(B_r' - B)$ says that the vertical flux acts to stabilize the temperature structure (k_B term) directly. In addition, when (and only when) the tropopause height decreases with latitude, the horizontal flux has a direct stabilizing effect too. Both terms are of the same sign. The relative magnitude of these two parts is given by

$$-\frac{k_S}{k_B} A (1+Ri) = -\frac{k_S}{k_B} A Ri = -.0103 \bar{H} \frac{B}{A} \sigma = 0.75 \sigma$$

(for $\bar{H} = 12.0$, $A = -0.5$, $B = 3.0$). For $\sigma = 0.4$, about 25% of the total B forcing is attributable to the horizontal flux. Thus, the 'effective' vertical flux is larger, even though $\overline{w'\theta'}$ by itself is 20% less.

Therefore, it would seem to be just as important for the net heating to allow a sloping upper boundary as to allow convergence of the meridians. The two geometrical effects act together and reinforce one another.

(iv) It may be tempting to ascribe the modification of A and B with σ entirely to the hemispheric average. After all, for σ non-zero the integrand ($\int_0^H \frac{\partial\theta}{\partial\phi} dz$ and $\int_0^H \frac{\partial\theta}{\partial z} dz$, respectively), which is already larger in low latitudes, is weighted more strongly than the simple $\cos \phi$ factor for constant H. However, this is not too satisfying, as it doesn't explain why V_{n_1} (where the same integral as for A is involved) first increases,

reaching a maximum at about $\sigma = 0.25$. It is preferable to consider that A changes in response to the altered stability. We have seen from (iii) that a sloping tropopause has the same effect as adding a second stabilizing flux and this will increase the stability B. In turn, this enhances the efficiency of the poleward heat transport (from the A equation) and reduces the pole to equator temperature gradient. Now negative feedbacks come into play and limit the change in A without, of course, altering the direction of the change.

3.3.3 Addition of latent heat

In the previous section, we assumed the baroclinic eddies transported only sensible heat. (Actually, potential energy as well, but this is very small). The integrated Leovy terms L_y , L_z were set to 1.0. Now we allow a second major flux: latent heat. Table 3.5 shows the model results with and without the latent heat transport (for $\bar{H} = 12.0$, $\sigma = 0$, $k_0 = 2.0$, and $\tau^* = 5.5$).

Table 3.5: Addition of latent heat

h_0	$\langle T \rangle$	A	B	β	Ri	L_y	L_z
0.0	250.8	-.588	2.93	7.48	23.0	1.0	1.0
0.77	250.5	-.522	2.21	8.04	22.0	1.471	1.118

The addition of a second physical flux has reduced the meridional temperature gradient, as expected, but at the same time, this has fed back on the vertical fluxes and reduced the stability too. The Leovy factors L_y , L_z give a measure of how important the latent heat flux is, although the ratio

of latent to sensible cannot be obtained directly from these numbers.

Horizontal transports are apparently more sensitive to inclusion of latent heat than are vertical ones. The normalized vertically integrated horizontal flux is given by

$$3 v \frac{H(\phi)}{H} \sin \phi \cos \phi \left(1 + \int_0^1 \Lambda(\phi, x) \mathcal{L}(\phi, x) dx \right)$$

Let $Q_H(\phi) = \int_0^1 \Lambda(\phi, x) \mathcal{L}(\phi, x) dx$ denote the latent heat ratio at each latitude. Similarly, the total vertical flux is

$$\frac{1}{2} w \frac{H(\phi)}{H} \sin \phi \cos \phi \left(1 + Q_V(\phi) \right), \text{ where } Q_V(\phi) = 6 \int_0^1 x(1-x) \mathcal{L}(\phi, x) dx$$

Table 3.6 shows these latent heat ratios as a function of latitude, together with the sensible heat variation ($3 \sin \phi \cos \phi$). Integrating over a hemisphere, we find the ratio of latent to sensible heat is 0.812 : 1.0 for the horizontal flux and 0.288 : 1.0 for the vertical flux.

Table 3.6: Latent heat ratios

	5	15	25	35	45	55	65	75	85
<u>SH</u>									
$3 \sin \phi \cos \phi$	0.261	0.750	1.149	1.410	1.500	1.410	1.149	0.750	0.261
<u>LH</u>									
$Q_H(\phi)$	1.946	1.661	1.222	0.793	0.471	0.271	0.162	0.108	0.087
$Q_V(\phi)$	0.732	0.616	0.440	0.275	0.156	0.086	0.049	0.032	0.025

However, the total horizontal flux has not been increased by 81% over the case with sensible heat alone. The amplitude of the sensible heat transport has been reduced and the total flux is only 24% larger (Table 3.7).

The total vertical flux is almost unchanged.

Table 3.7: Integrated flux changes when latent heating is added

h_0	Horizontal flux ($m \text{ } ^\circ\text{C}/\text{sec}$)		Vertical flux ($\times 10^{-3} m \text{ } ^\circ\text{C}/\text{sec}$)	
	S.H. alone (Vn_1)	Total	S.H. alone ($\frac{1}{6} Wn_1$)	Total
0.0	10.80	10.80	8.66	8.66
0.77	7.40	13.40	6.95	8.96

This behavior is not unexpected. Theoretical work by Stone (1978), mentioned in Section 2.1, indicates that there are strong constraints on the total flux. Other models, such as that of Manabe et al. (1965, Figure 12B5), exhibit a similar response.

Figure 3.3 shows the net eddy heating for this case. The equatorial cooling is greatly intensified and the region of heating consequently expands to lower latitudes. The magnitude of the cooling is probably unrealistic, as the surface temperatures are still much too high, being virtually unchanged from the example without latent heat. For the same reason, the profile of the horizontal latent heat transport peaks at too low a latitude ($\sim 25^\circ$) compared to observation ($30\text{-}35^\circ$). Figure 3.4a illustrates this latitudinal variation (essentially, a graph of part of Table 3.6). Figure 3.4b is included to facilitate comparison with the observed mean annual transports. (Data taken from Oort and Rasmusson, 1971). The model peak SH flux agrees very closely with observation, but presumably this is fortuitous. The mean hemispheric fluxes are considerably overestimated (the observed average for latent and sensible fluxes being 3.22 and $4.16 m \text{ } ^\circ\text{C sec}^{-1}$, respectively), although the ratio of latent to sensible in the hemispheric

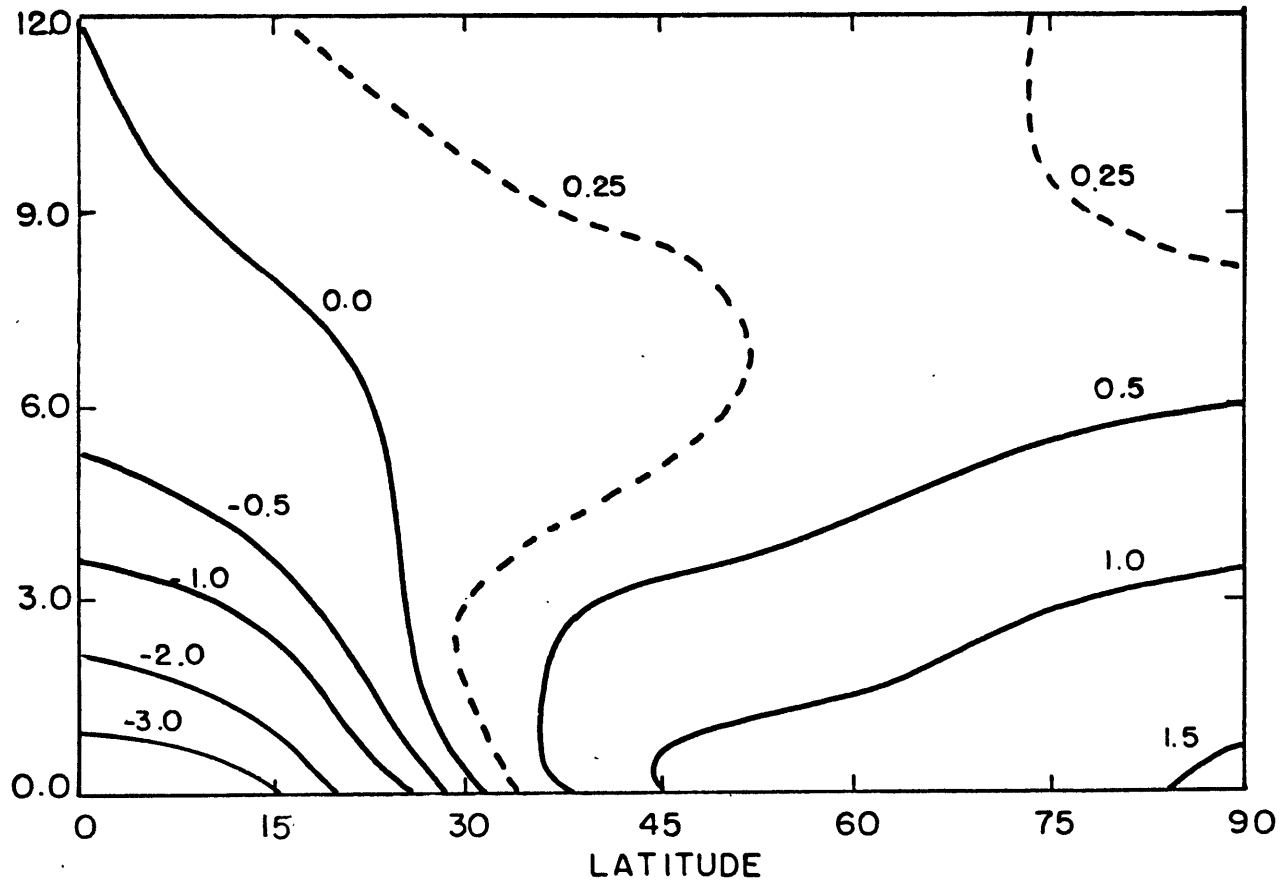


Figure 3.3: Total eddy heating in °C/day with latent heat transport included. (i.e. $h_0 = 0.77$. Other parameters as in Fig. 3.1).

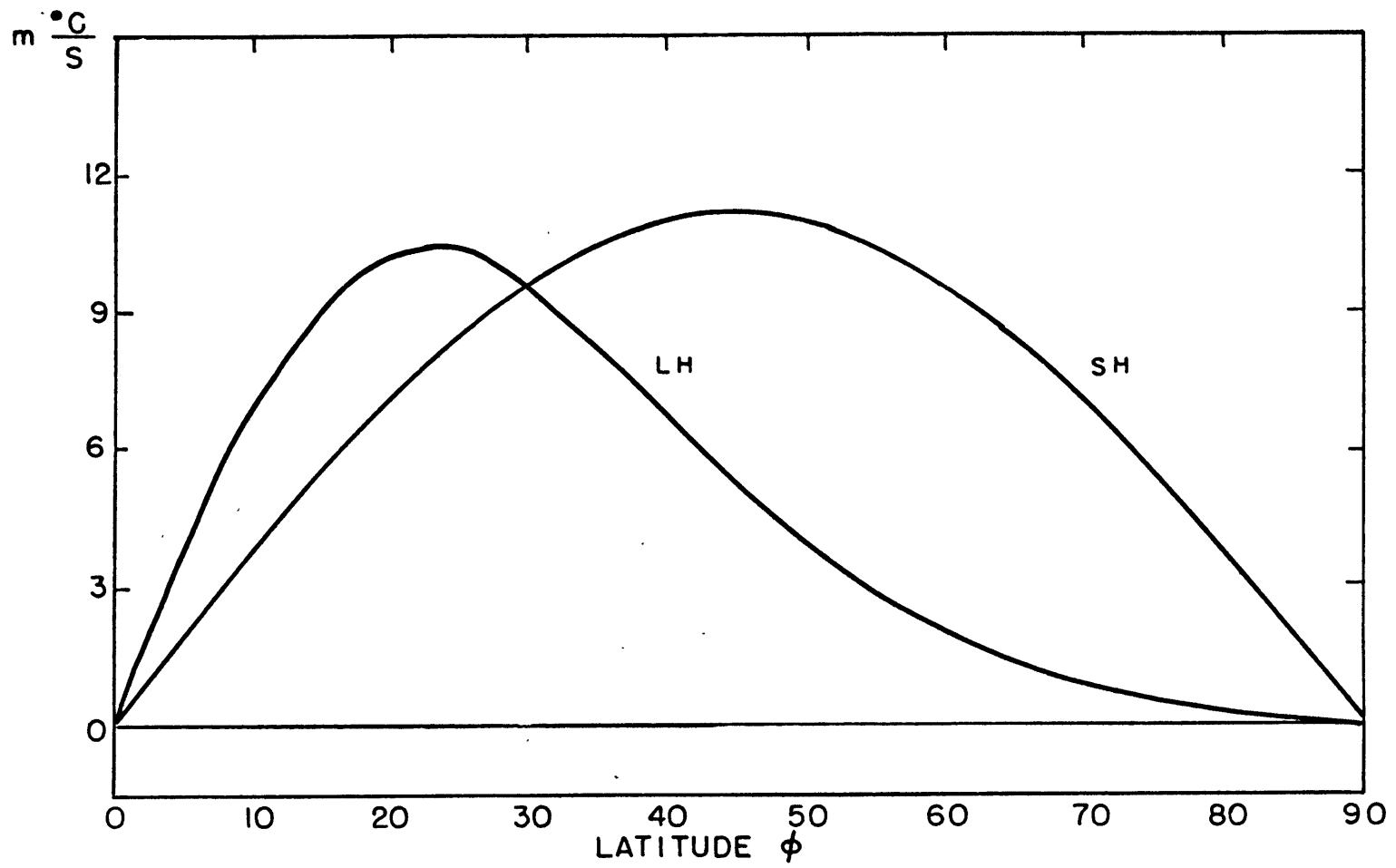


Figure 3.4a: Grey radiation model sensible (SH) and latent (LH) heat flux as a function of latitude in units of $m \cdot ^\circ C \cdot s^{-1}$. (Model parameters: $\bar{H} = 12.0$, $\sigma = 0.0$, $k_0 = 2.0$, $h_0 = 0.77$, $\tau^* = 5.5$).

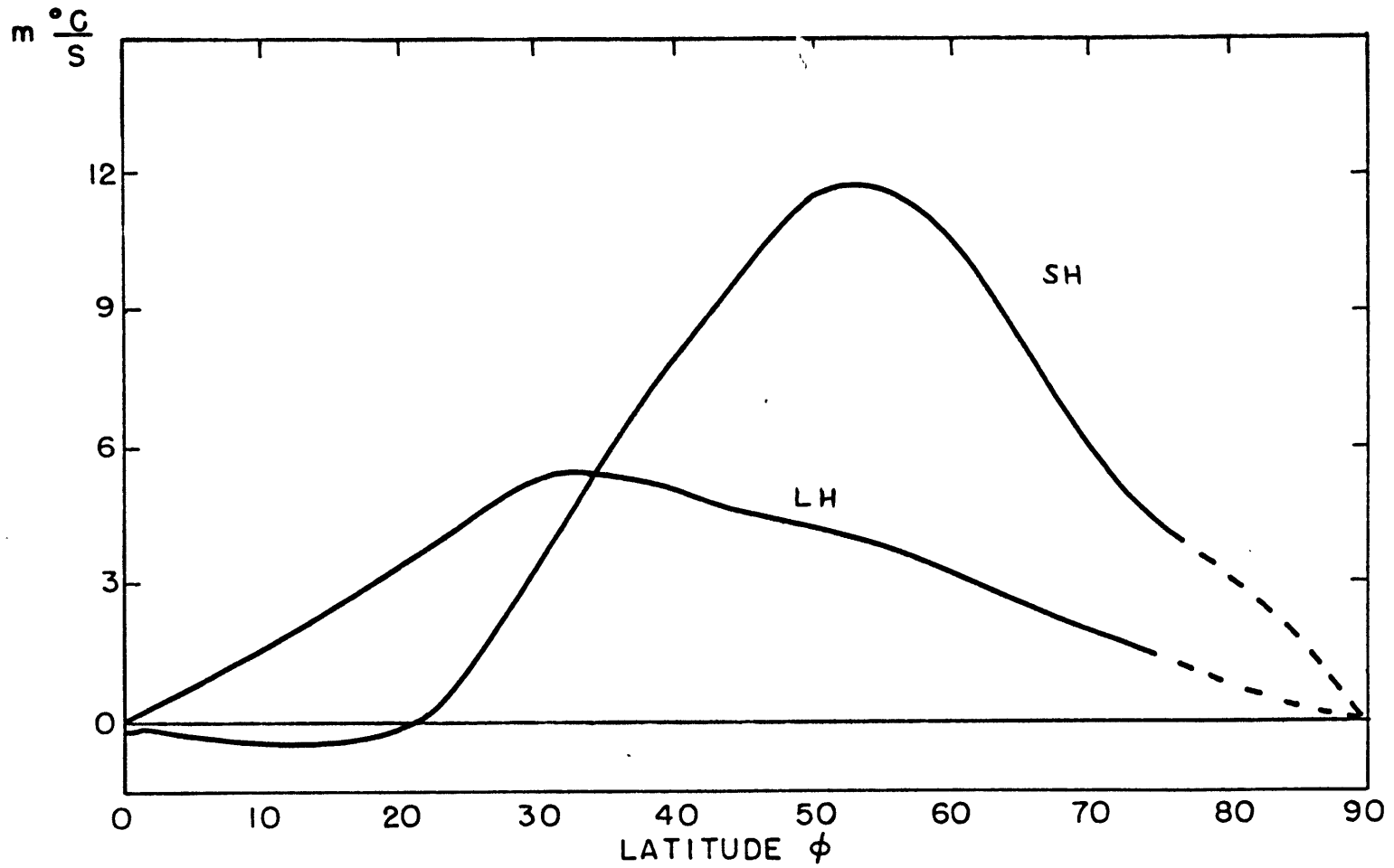


Figure 3.4b: Observed mean annual horizontal eddy fluxes of sensible (SH) and latent (LH) heat in units of $m \text{ } ^\circ\text{C} \text{ s}^{-1}$.

mean (0.77 : 1.00 for the data) is reasonable. The parameter whose value is most uncertain in this grey radiation model is the relaxation time constant τ . Increasing τ by a factor of 2 reduces the fluxes by nearly the same amount and would 'improve' agreement of model and data for the horizontal transports. However, attempting to fit results in this way is hardly justified in such a simple model, particularly since absence of observations means we have no check on the vertical fluxes. Implications of varying τ are considered in the following section.

3.3.4 Variation with relaxation time constant

Table 3.8 shows how the model results vary for a considerable range of relaxation time τ .

Table 3.8: Variation with τ^* (for $\bar{H} = 12.0$, $\sigma = 0.0$, $k_0 = 2.0$, $h_0 = 0.0$)

τ^*	$\langle T \rangle$	A	B	β	Ri	Vn_1	$\frac{1}{6} Wn_1 \times 10^{-3}$
22.0	253.7	-.348	1.73	8.42	39.3	2.89	2.36
16.5	253.4	-.390	1.93	8.26	34.8	3.86	3.16
11.0	252.8	-.458	2.26	8.00	29.5	5.74	4.69
8.5	252.2	-.510	2.52	7.80	26.4	7.53	6.12
5.5	250.8	-.588	2.93	7.48	23.0	10.80	8.66
4.0	249.4	-.651	3.28	7.20	20.8	14.01	11.07
3.0	247.9	-.708	3.61	6.95	19.3	17.37	13.51
2.0	245.4	-.785	4.10	6.57	17.6	22.67	17.14

Our model results, at least for stability B, are more sensitive than those of Stone (1972a, Table 1) because we allow for radiative feedback. As τ^* becomes small, the solution parameters change more rapidly, and eventually our procedure for calculating the radiative equilibrium temperature breaks down. The meridional gradient and the total integrated fluxes clearly become unrealistic for short τ^* .

Our choice of $\tau^* = 5.5$ is rather arbitrary, but the number of theoretical objections to the use of Newtonian cooling (equation 2.34) makes an exact selection impractical. As pointed out earlier, equation 2.34 is normally used for studying small deviations from a steady-state temperature. We use the radiative equilibrium state T_r instead, which varies widely from the observed atmospheric structure. This raises serious doubts about the validity of the linearization. A formal derivation of τ shows it to be a strong function of wavenumber, and an explicit evaluation assumes there is a single dominant scale for the heating. Calculations by Prinn (1977) also show that τ can have considerable spatial variation, decreasing near the boundaries, and being extremely sensitive to how the surface temperature responds. For the largest justifiable vertical wavelength in the troposphere, ($\lambda \approx 31$ km, about twice the tropopause height) Spiegel's (1957) formula gives $\tau^* \approx 7.7$. Prinn determines that for these very long waves horizontal stratification becomes important and increases the radiative damping rate, making τ^* closer to about 2. Any errors in the modeling of the amplitude of the dynamical fluxes or the radiative heating can be incorporated into τ since it is a simple multiplicative factor. Since $\tau^* = 2$ is clearly unrealistic for our model, we have compromised with a slightly larger value.

For the finite and often large perturbations from radiative equilibrium, the damping calculated from linear theory appears unsuitable, and perhaps τ^* should simply be found empirically. As noted above, $\tau^* = 11$ gives better values for the horizontal gradient and fluxes. The stability is still much too low because surface fluxes have been neglected at this point. However, it is not our intention in this chapter to seek a best

fit to observation (B cannot be adjusted simultaneously anyway), but merely to make some qualitative remarks, and these do not depend on any particular choice for the damping. The conclusions we drew about relative changes will still be applicable to the more complete model using non-grey radiative computations and including surface feedback.

3.3.5 Variation with grey absorption coefficient

Table 3.9 shows how our results change for different values of the absorption coefficient k_0 .

Table 3.9: Variation with k_0 (for $\bar{H} = 12.0$, $\sigma = 0.0$, $h_0 = 0.0$, $\tau^* = 5,5$)

$k_0, \text{cm}^2\text{g}^{-1}$	$\langle T \rangle$	A	B	β	Ri
1.0	268.6	-.699	2.17	8.05	12.9
1.5	257.9	-.638	2.48	7.82	17.0
2.0	250.8	-.588	2.93	7.48	23.0
2.5	246.0	-.548	3.46	7.07	30.7
3.0	242.4	-.517	4.04	6.62	39.6

Changes in the model gradients are agreeably moderate for deviations up to 50% from the nominal value of k_0 . However, a particularly unsettling feature of Table 3.9 is the variation of $\langle T \rangle$ (or $\langle T_r \rangle$). As the absorption coefficient increases, the mean temperature is seen to decrease, which is contrary to all physical intuition. The problem lies in the peculiar way the boundary conditions and the constraint of fixed tropopause height force the solution.

To gain an understanding of what is happening here, it is useful to refer to Figure 3.5. This shows how the mean radiative equilibrium temperature $\langle T_r \rangle$ varies with $\langle T \rangle$ for fixed $A = -0.5$, $\beta = 6.5$. For a given ab-

sorption there are, in general, two possible solutions where $\langle T \rangle = \langle T_r \rangle$. For $k_0 = 2.0$, these are at $\langle T \rangle = 218.0$ and 256.8 for this parameter set. The upper solution is the one we must take. For the lower value, $\langle T \rangle = 218.0$ °K, we calculate the tropopause temperature $T_H(\phi) = T_0(\phi) - \beta H(\phi)$ to be everywhere less than the 'skin temperature' $T_r(\infty) = \frac{1}{2^{1/4}} T_e(\phi)$ (i.e. value at the top of the atmosphere where the optical depth is zero). Since in a grey model with H_2O the only radiatively active absorber, it is impossible for the temperature to increase with height, this implies the lower solution must be rejected.

A problem arises when we vary k_0 and find a larger mean temperature for a smaller absorption coefficient. This behavior is seen in the dashed curves of Figure 3.5. The situation is obviously artificial because we cannot vary k_0 independently of the temperature in any physical system. One way to avoid this difficulty is to prescribe the water vapor concentration as a function of height rather than have it depend on local temperature. In the following non-grey radiative treatment (Chapter 4), the problem does not occur since the absorption coefficient is found in an internally consistent manner. The lower solution for $\langle T \rangle = \langle T_r \rangle$ is also absent.

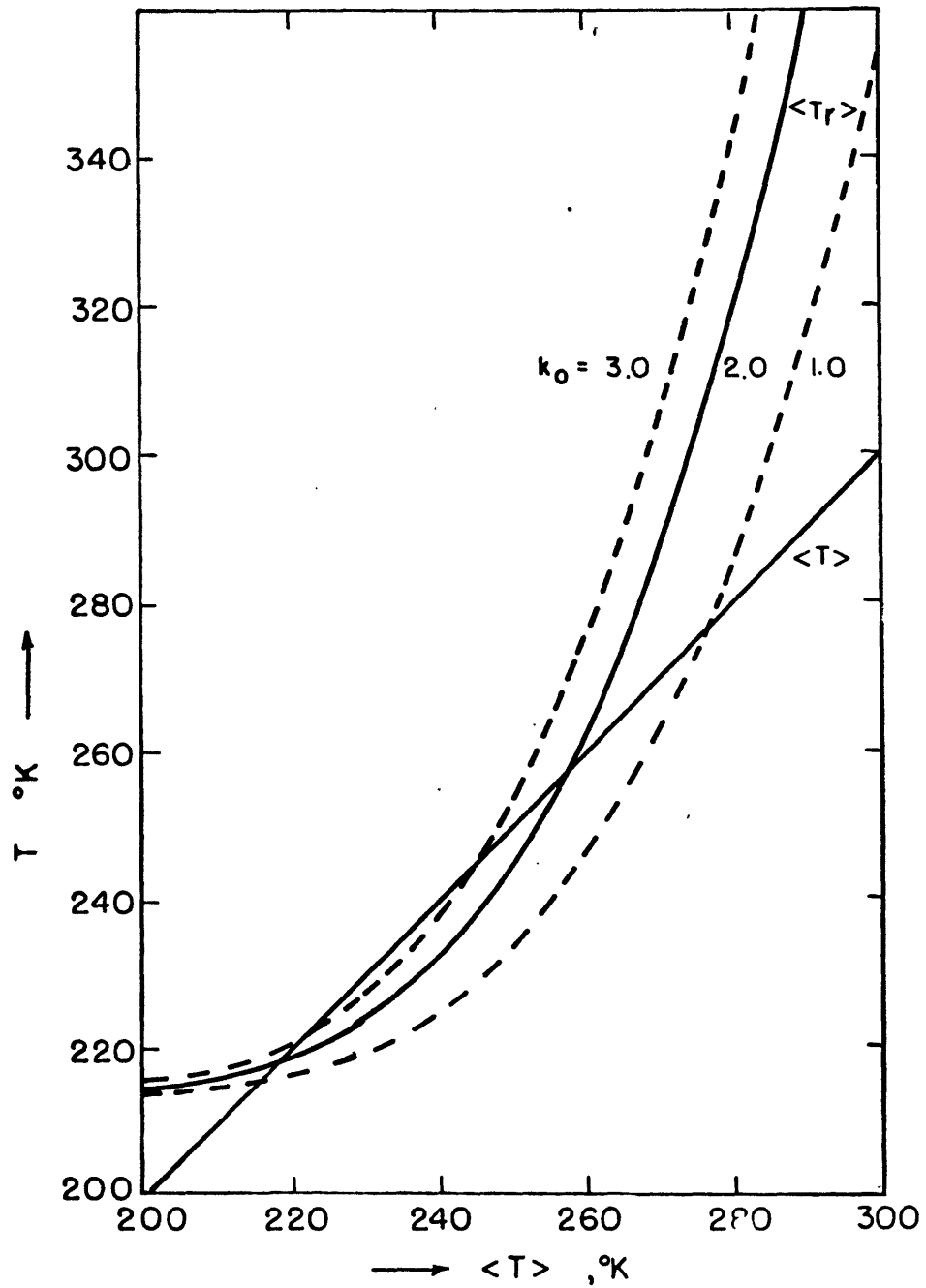


Figure 3.5: Change in mean radiative equilibrium temperature $\langle T_r \rangle$ with $\langle T \rangle$ for various values of grey absorption coefficient k_0 . (Other parameters fixed: $A = -0.5$ $^{\circ}\text{K}/100$ km, $\beta = 6.5$ $^{\circ}\text{K}/\text{km}$, $\bar{H} = 12.0$ km, $\sigma = 0.0$).

Chapter 4: Non-grey Radiative Treatment and Other Parameterizations

4.1 Solar Insolation

Gal-Chen and Schneider (1976) considered the relative importance of radiative and dynamical parameterizations on the sensitivity of their model's climate to perturbations in solar input. They concluded that the radiation balance was the dominant factor in determining the equilibrium climate, with the dynamical fluxes acting to modulate the solutions. For this reason, it is essential to parameterize the relevant radiative processes as accurately as we can. In Chapter 3, we discovered a number of shortcomings in the grey radiation approach. In this chapter (Section 4.2), we describe the non-grey treatment of the long-wave radiation field used in the full model. Clouds present in the terrestrial atmosphere are of great importance in evaluating the net radiation balance, and an entire chapter is set aside to consider this problem (Chapter 5).

We will now calculate how the solar insolation Q and zenith angle ζ vary with season and latitude. Simple formulae for the time variation of the earth-sun distance and declination angle are assumed. This allows us to calculate Q and ζ as functions of time in a very straightforward manner, although as far as this thesis is concerned, we use only the annual average values.

The solar radiation falling on a horizontal surface of the earth is given by

$$Q = S_0 \left(\frac{\bar{d}}{d}\right)^2 \cos \zeta \quad (4.1)$$

where S_0 = solar constant, taken as $2 \text{ cal cm}^{-2} \text{ min}^{-1}$,

d = earth-sun distance, with \bar{d} the mean annual distance,

and the cosine of the zenith angle is related to latitude ϕ , declination angle δ and hour angle h (measured in radians) by

$$\cos \zeta = \sin \phi \sin \delta + \cos \phi \cos \delta \cos h \quad (4.2)$$

[Note: The symbols d , h , H , and τ in this section are used in other chapters to represent different variables. Since the variables we identify these symbols with here never occur outside this one section, there should be no confusion.]

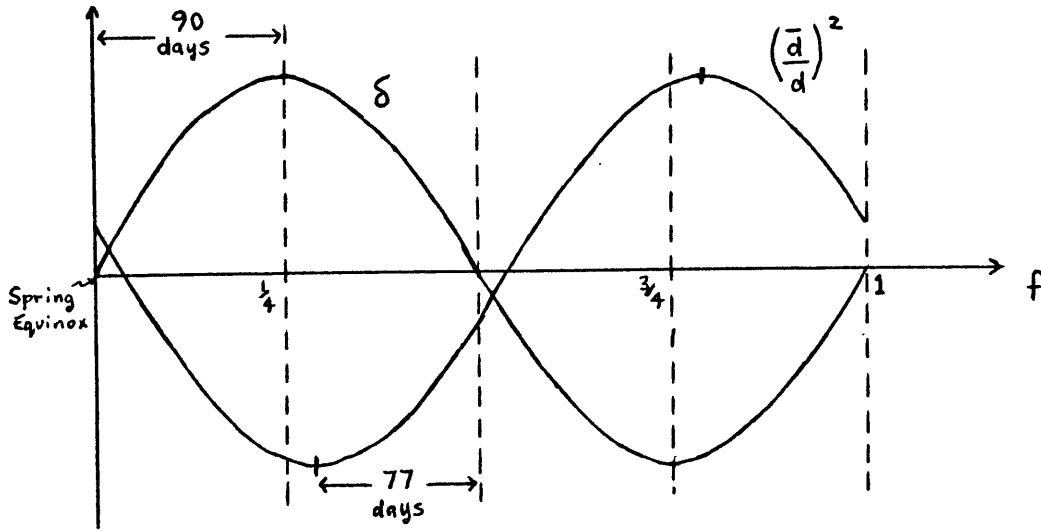
We average Q over a day. Set $h = \frac{2\pi}{\tau} t$, where t is time and $\tau = 1$ day. Integrate (4.1) with respect to h between the limits $\pm H$, where the $\frac{1}{2}$ day length H itself varies with latitude and time.

$$\cos H = -\tan \phi \tan \delta \quad (4.3)$$

Equation (4.3) is valid for $\cos H$ between ± 1 . In very high latitudes where this condition is violated, H is set equal to π or 0 according to whether the sun is above or below the horizon. Then

$$\begin{aligned} Q(\phi, t) &= \frac{S_0}{\pi} \left(\frac{\bar{d}}{d}\right)^2 [H \sin \phi \sin \delta + \sin H \cos \phi \cos \delta] \\ &= \frac{S_0}{\pi} \left(\frac{\bar{d}}{d}\right)^2 \cos \phi \cos \delta [\sin H - H \cos H] \end{aligned} \quad (4.4)$$

using (4.3). We represent the annual variation of δ and d analytically, taking the time origin at the spring equinox.



In this schematic illustration of how δ and $(\frac{\bar{d}}{d})^2$ vary about their mean value, f is the fraction of the year elapsed since the spring equinox. Assuming the year has 360 equal divisions ('days'), then for our purposes it is sufficiently accurate to take

$$\left(\frac{\bar{d}}{d}\right)^2 = 1 + 0.0335 \sin[2\pi(f+0.462)] \quad (4.5)$$

so the earth is closest to the sun in early January, about 77 days before the spring equinox. The mean zenith angle $\bar{\zeta}$ is defined by

$$\cos \bar{\zeta} = \frac{\int \cos \zeta dt}{\int dt} \quad (4.6)$$

The integration limits depend on the use of $\cos \bar{\zeta}$. If we are employing it to find mean solar insolation ($Q = S_0 \cos \bar{\zeta}$), then we average over a whole day. However, if $\mu_0 = \cos \bar{\zeta}$ is used for radiative heating calculations (as in path length magnification factor $M(\mu_0)$ or Rayleigh scattering

$\bar{R}_r(\mu_0)$ introduced later), we average $\cos \zeta$ only over daylight hours (since the total insolation is already weighted appropriately).

$$\begin{aligned} \cos \bar{\zeta} &= \frac{\int_{-H}^H [\sin \phi \sin \delta + \cos \phi \cos \delta \cos h] dh}{\int_{-H}^H dh} \\ &= \frac{[H \sin \phi \sin \delta + \sin H \cos \phi \cos \delta]}{H} \end{aligned} \quad (4.7)$$

Equation (4.7) gives the correct mean $\cos \bar{\zeta}$ for one day. In averaging over many days, each day must be weighted by its amount of daylight

i.e.
$$\cos \bar{\zeta} = \frac{\Sigma [H \sin \phi \sin \delta + \sin H \cos \phi \cos \delta]}{\Sigma H}$$

but not
$$\Sigma \left(\frac{H \sin \phi \sin \delta + \sin H \cos \phi \cos \delta}{H} \right)$$

This distinction is important in high latitudes where (4.3) is invalid.

4.2 Non-grey Radiation Model

4.2.1 Amounts of the absorbing gases: H_2O , CO_2 and O_3

The major radiatively active gases in the earth's atmosphere are water vapor, carbon dioxide, and ozone. Heating in the troposphere is determined mainly by long-wave emission and short-wave absorption due to water vapor, while in the stratosphere long-wave heating by both H_2O and CO_2 and short-wave heating by O_3 are all important. This behavior is shown very clearly in Figure 4.1, taken from Manabe and Möller (1961). Their radiative calculations also indicate that long-wave heating by ozone is of some significance near the tropopause. In our model we neglect this term,

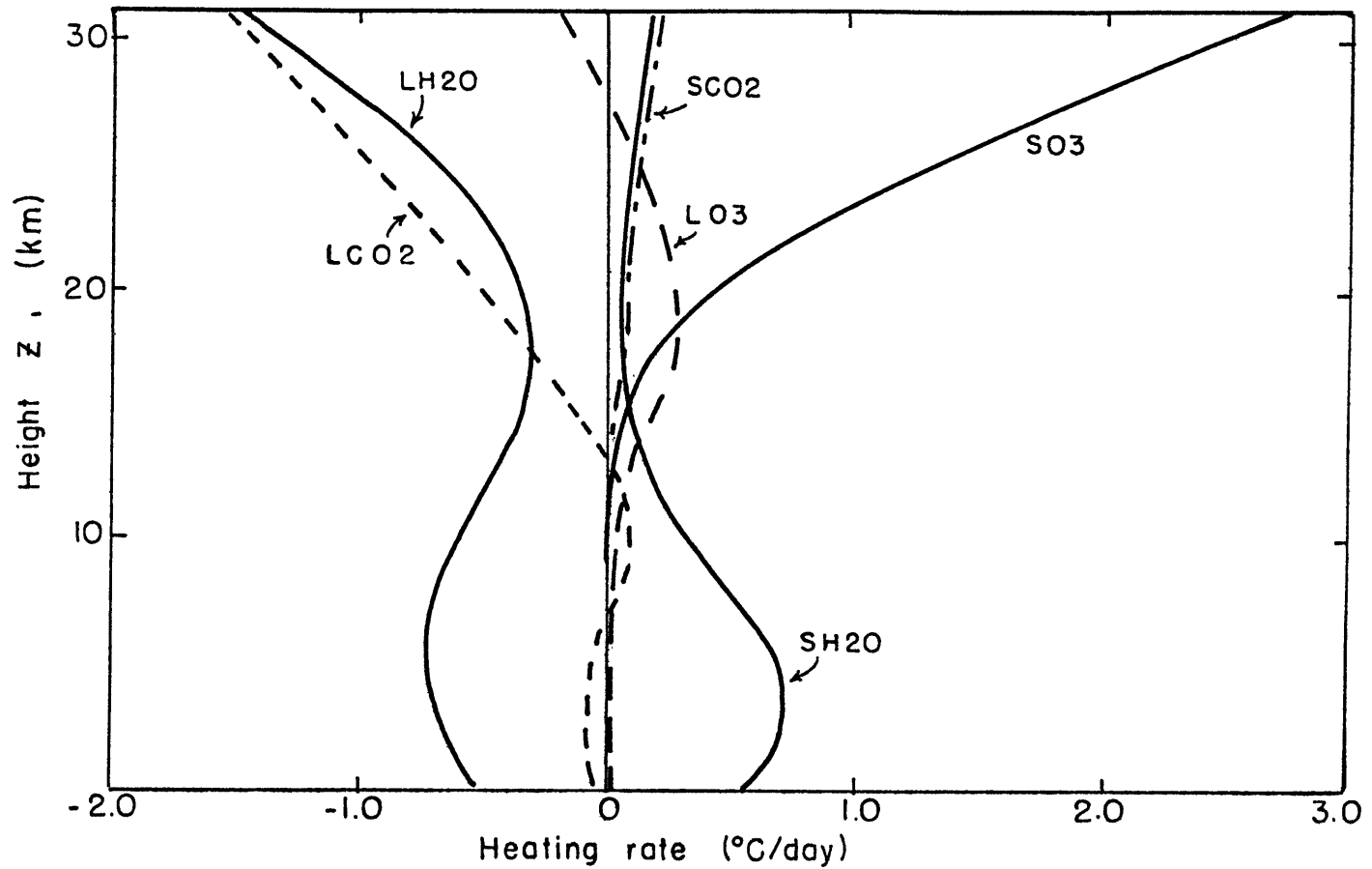


Figure 4.1: Vertical distribution of radiative heating for the various component gases of the atmosphere, as found by Manabe & Möller (1961, Figure 13). SH20, SC02 and S03 are the heating rates due to absorption of solar radiation by water vapor, carbon dioxide and ozone, respectively. LH20, LC02 and L03 are the corresponding heating rates due to long-wave radiation.

because to evaluate it with any accuracy requires a detailed knowledge of the stratospheric temperature profile. Since our main concern is with the tropospheric heat balance, we take the simplest possible temperature structure (i.e. isothermal) for the stratosphere. The heating by H_2O and CO_2 is less sensitive to this approximation as the column amount of these gases decreases rapidly with height.

We specify the mathematical form of the temperature structure in the atmosphere, leaving the actual values of the parameters to be determined by the model. When calculating the column amount of the absorbing gases, we assume a constant lapse-rate troposphere capped by an isothermal stratosphere. We will discover, when computing the long-wave heating rates, that it is also necessary to add a "transition region" at the tropopause. The complete temperature structure is shown in Figure 4.2. The surface air temperature T_0 at $z = 0$ can be identified with the value at standard anemometer level. z_* is at a sufficiently great height that the effective amounts of water vapor and carbon dioxide above z_* are negligible. The temperature profile can be expressed algebraically as follows.

$$\left. \begin{aligned} \text{For } 0 \leq z \leq H; \quad T &= T_0 - \beta z \\ H \leq z \leq H+d; \quad T &= T_H - \beta(z-H) + \frac{\beta}{2d} (z-H)^2 \\ H+d \leq z \leq z_*; \quad T &= T_d \end{aligned} \right\} \quad (4.8)$$

where the transition region is of thickness d and the quadratic dependence is chosen to match both temperature and temperature gradients at $z = H$ and $H+d$.

$$T_d = T_H - \frac{1}{2} \beta d$$

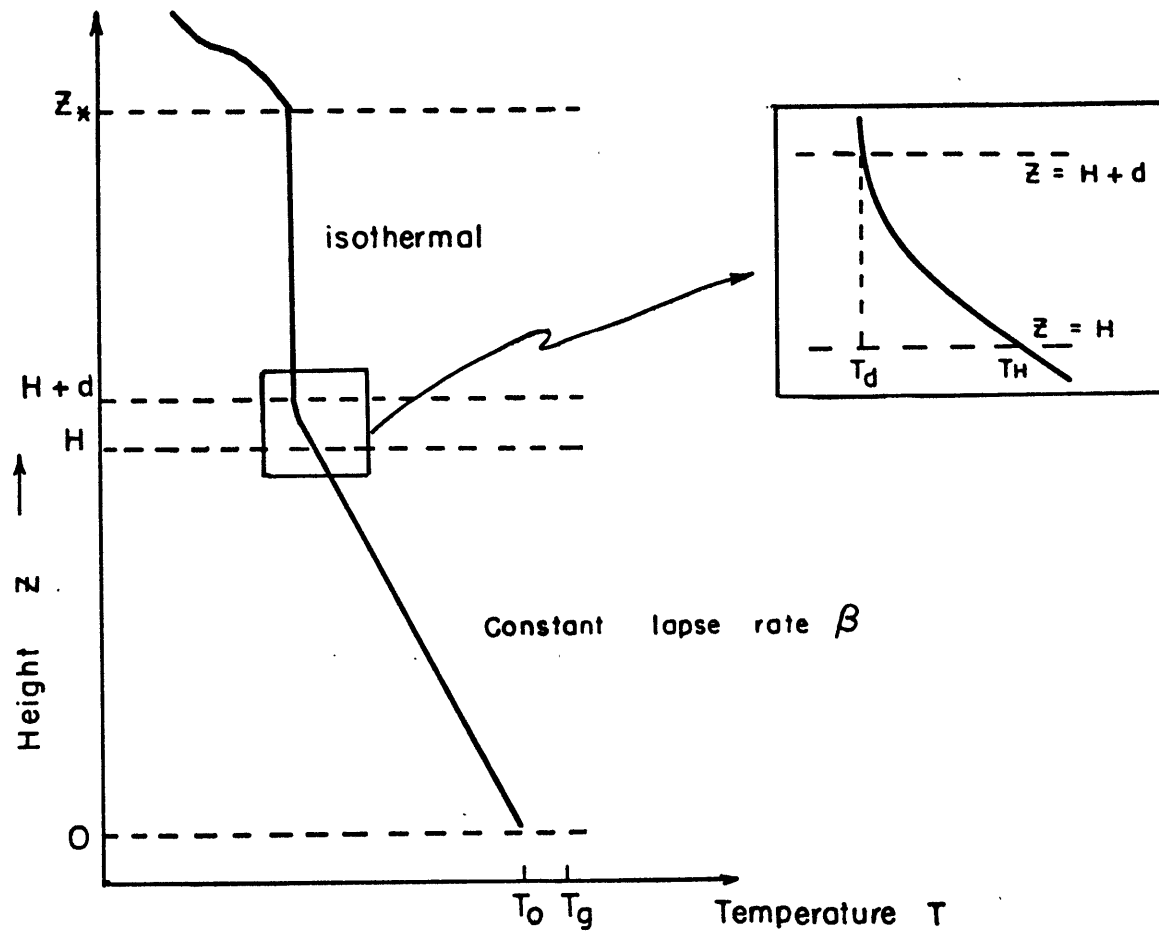


Figure 4.2: Vertical temperature structure assumed in the model. Inset shows the smooth 'transition region' between the constant lapse rate troposphere and isothermal stratosphere.

The pressure variation in the troposphere was given previously in equation (2.23). For the stratosphere we have an even simpler relation.

$$p = p_H \exp \left[-\frac{g}{RT_H} (z-H) \right]$$

where $p_H = p_0 \left(\frac{T_H}{T_0} \right)^{\frac{g}{R\beta}}$

a) Water vapor amount

We define the reduced water vapor amount in $g \text{ cm}^{-2}$ to be

$$u_1(z) = \frac{1}{g} \int_0^{p(z)} m \frac{p}{p_0} \left(\frac{T_3}{T} \right)^{\frac{1}{2}} dp \quad (4.9)$$

where the factor $\left(\frac{p}{p_0} \right) \left(\frac{T_3}{T} \right)^{\frac{1}{2}}$ is a commonly used approximation to correct for the variation of pressure and temperature along the path (Curtis-Godson approximation).

$$m = \text{mixing ratio} = \frac{\epsilon e}{p-e} \quad (4.10)$$

$e = h e_s$, where h is relative humidity and e_s the saturation water vapor pressure defined by the Clausius-Clapeyron relation

$$e_s = e_3 \exp \left[-a \left(\frac{1}{T} - \frac{1}{T_3} \right) \right] \quad (4.11)$$

The other symbols were defined in Section 2.1. We specify the vertical distribution of relative humidity

$$h = h_0 \frac{p}{p_0} \quad (4.12)$$

This form was used by Cess (1974) and is similar to the form used by Manabe and Wetherald (1967). We take the surface pressure $p_0 = 1013 \text{ mb}$.

Manabe and Wetherald (1967) also found it desirable in their calculations to specify a lower limit on the mixing ratio ($m_{\min} = 3 \times 10^{-6}$). We do not use this condition in our model. Since the tropopause height H is calculated from a differential constraint (1.2), we find it necessary to avoid discontinuities in the slopes of our variables in the troposphere (hence, the use of the transition region to smooth the temperature field). In the stratosphere, it is sufficient to hold the mixing ratio constant at its tropopause value.

$$\begin{aligned} \text{For } z \geq H; \quad m &= m_H = \frac{\epsilon h_0 e_3}{p_0} \exp \left[-a \left(\frac{1}{T_H} - \frac{1}{T_3} \right) \right] \\ &= 3.753 \times 10^{-3} h_0 \exp \left[-a \left(\frac{1}{T_H} - \frac{1}{T_3} \right) \right] \end{aligned}$$

Thus, in the stratosphere

$$u_1(z) = \frac{m_H}{g} \left(\frac{T_3}{T_H} \right)^{\frac{1}{2}} \frac{p^2}{2p_0} = u_1(H) \exp \left[-\frac{2g}{RT_H} (z-H) \right] \quad (4.13)$$

$$\text{where } u_1(H) = \frac{m_H p_0}{2g} \left(\frac{T_3}{T_H} \right)^{\frac{1}{2}} \left(\frac{T_H}{T_0} \right)^{2\gamma} \quad \text{and } \gamma = \frac{g}{R\beta} = \frac{34.18}{\beta} \quad \text{for } \beta$$

in units of $^{\circ}\text{K}/\text{km}$. In the troposphere, we want to evaluate the integral (4.9) analytically.

$$u_1(z) = u_1(H) + \frac{\epsilon T_3^{\frac{1}{2}}}{g p_0} \int_{P_H}^P \frac{f(T) p T^{-\frac{1}{2}}}{(1-f(T))} dp \quad (4.14)$$

where the temporarily defined function $f(T) = \frac{h_0 e_3}{p_0} \exp \left[-a \left(\frac{1}{T} - \frac{1}{T_3} \right) \right]$.

This integral is very similar to the one for optical depth encountered in Section 3.2, although slightly more complicated still. It is sufficient

here to state that a highly accurate analytical approximation to (4.14) can be found. (Refer to Appendix A5 for the details).

b) Carbon dioxide amount

By allowing for both CO₂ and O₃ in the full model, we can change the concentrations of these gases in later climate sensitivity studies. In any case, short-wave heating by ozone is necessary to determine the equilibrium tropopause height.

We assume CO₂ to be well-mixed, with a mixing ratio of

$$r_c = 4.56 \times 10^{-4} \text{ g/g} \quad (4.15)$$

which corresponds to a volume concentration of 300 ppm. The carbon dioxide amount is readily evaluated.

$$\begin{aligned} u_2(z) \quad (\text{in g cm}^{-2}) &= \frac{1}{g} \int r_c \frac{p}{p_0} dp \\ &= \frac{r_c}{g p_0} \frac{p^2}{2} \end{aligned}$$

This column amount is converted to units of cm STP by multiplying by $\frac{R_{\text{CO}_2} T_3}{p_0}$, where R_{CO_2} is the gas constant appropriate to carbon dioxide.

This gives us an amount at the ground of $u_2(0) = 120 \text{ cm}$.

$$\text{Thus, for } z \leq H; \quad u_2(z) = 120 \left(\frac{T}{T_0} \right)^{2\gamma} \quad (4.16)$$

$$\text{and for } z \geq H; \quad u_2(z) = u_2(H) \exp \left[- \frac{2g}{RT_H} (z-H) \right]$$

c) Ozone amount

We seek simple functional forms for the ozone concentration as a function of height, latitude, and season. We use the function suggested by Green (1964).

$$\text{Total ozone amount above height } z = u_3(z) = a \frac{\left(1 + e^{-\frac{z-b}{c}}\right)}{\left(1 + e^{-\frac{b}{c}}\right)} \quad (4.17)$$

so that a = total ozone column amount in cm STP

b = height of ozone peak concentration in km

and

$$\frac{a}{4c} \left(1 - e^{-\frac{b}{c}}\right) \approx \frac{a}{4c} = \text{ozone peak concentration in (cm STP)/km.}$$

We use Figure 10 of Manabe and Möller (1961) to estimate 'a' (which also agrees with the more recent measurements of Prabhakara et al., 1971) and Figures 2 and 3 from Hering and Borden (1964) to determine b and c .

Low latitude (10°) : $a = 0.25$, $b = 25$, $c = 4.0$ km

Mid-latitude (45°) : $a = 0.32 + 0.06 \cos 2\pi f$, $b = 21$, $c = 4.4$ km

High latitude (75°): $a = 0.36 + 0.07 \cos 2\pi f$, $b = 18$, $c = 3.8$ km

f is the fraction of year from the spring equinox as in Section 4.1. The maximum ozone column amounts occur in spring. Our fitted values compare well with those of Lacis and Hansen (1974) used in general circulation model calculations.

Low latitude : $a = 0.25$, $b = 25$, $c = 4$

Mid-latitude winter : $a = 0.4$, $b = 20$, $c = 5$

Polar winter : $a = 0.5$, $b = 18$, $c = 4$

For intermediate latitudes, we interpolate the constants a , b , c linearly with ϕ . The ozone amount at any height is the derivative of (4.17);

$$\text{i.e.} \quad -\frac{du_3}{dz} = \frac{u_3(z)}{c} \frac{e^{\frac{z-b}{c}}}{\left(1+e^{\frac{z-b}{c}}\right)}$$

4.2.2 Parameterization of long-wave radiation

It is now time to evaluate the upward and downward long-wave fluxes $F(z)\uparrow$, $F(z)\downarrow$, and their derivatives. Consider a point z lying in the interval $(0, H)$. Then

$$\begin{aligned} F_\nu(z)\uparrow &= -\int_0^{u_g - u(z)} B_\nu(T') \frac{d\mathcal{T}}{du} du + \epsilon B_\nu(T_g) \mathcal{T}(u_g - u(z)) \\ F_\nu(z)\downarrow &= -\int_0^{u(z)} B_\nu(T') \frac{d\mathcal{T}}{du} du \end{aligned} \quad (4.18)$$

where $u(z)$ is the amount of absorber above height z , $\mathcal{T}(u)$ is the transmissivity over path length u , and the long-wave fluxes are still a function of frequency ν at this point. du is the difference in water vapor amount between an observer (at z) and the layer of air at z' . We assume the long-wave emissivity ϵ of the ground to be unity. Concentrating initially on the upward long-wave flux, we integrate (4.18) by parts, rearrange, and arrive at

$$F_\nu(z)\uparrow = B_\nu(T_g) - \int_{T(z)}^{T_g} [1 - \mathcal{T}(u')] \frac{dB_\nu}{dT'} dT'$$

where $u' = u(z') - u(z)$; z' (or T') being the integration variable. In

order to evaluate this integral, we use the method developed by Sasamori (1968) and define a mean absorptivity

$$A(u, T) = \frac{\int_0^\infty (1 - \Pi(u)) \frac{dB_\nu(T)}{dT} d\nu}{4\sigma T^3} \quad (4.19)$$

where transmissivity $\Pi(u) = \frac{2}{\Delta\nu} \int_{\Delta\nu} Ei_3(K_\nu u) d\nu$

and $Ei_3(K_\nu u) = \int_1^\infty \frac{e^{-K_\nu u t}}{t^3} dt$ (to correct for diffuse beam)

Since $A(u, T)$ varies slowly with T over the normal range of atmospheric temperatures, we replace it by $\bar{A}(u)$, an average over T from -50°C to $+30^\circ\text{C}$. This allows us to integrate $F_\nu(z)^\uparrow$ over frequency.

$$F(z)^\uparrow = \int_0^\infty F_\nu(z)^\uparrow d\nu. \quad \text{Then for } 0 \leq z \leq H,$$

$$F(z)^\uparrow \doteq \sigma T_g^4 - 4\sigma \int_T^T \bar{A}(u(z') - u(z)) T'^3 dT' \quad (4.20)$$

Equation (4.20) can also be used to evaluate the long-wave flux to space, $F(\infty)^\uparrow$, by setting $u(z) = 0$ and the lower integration limit to $T = T_d$.

Similarly, we can integrate the downward long-wave flux in (4.18) over frequency. We assume the isothermal layer extends to a great height z_* by which point the amount of all absorbers is negligible so that further temperature variations are unimportant. Since this assumption is not appropriate for ozone (and leads to a large error in evaluating $\frac{\partial}{\partial z} F(z)^\uparrow$ due to O_3), we are forced to neglect ozone long-wave heating. Fortunately, Figure 4.1 indicates that the long-wave contribution to the heating by O_3 is small compared to the H_2O and CO_2 heating in the troposphere. Then,

$$F(z) \downarrow \doteq 4\sigma \int_{T_d}^T \bar{A}(u') T'^3 dT' + 4\sigma \int_0^{T_d} \bar{A}(u') T'^3 dT' \quad (4.21)$$

where $u' = u(z) - u(z')$.

The second term of (4.21) is the contribution from absorbers above $z = z_*$, and from the definition of z_* ; $u' = u(z) - u(z')$

$$\doteq u(z) \quad \text{for } z \geq z_*$$

Thus, \bar{A} can be removed from the second integral and we have:

$$\text{For } 0 < z \leq H+d; \quad F(z) \downarrow = \sigma T_d^4 \bar{A}(u(z)) + 4\sigma \int_{T_d}^T \bar{A}(u(z) - u(z')) T'^3 dT' \quad (4.22)$$

The net upward flux, $(F(z) \uparrow - F(z) \downarrow)$ can be differentiated to give the heating rate.

$$\begin{aligned} \frac{\partial}{\partial z} (F(z) \uparrow - F(z) \downarrow) &= -\sigma \frac{du'}{dz} \left\{ 4 \int_T^{T_d} g \frac{d\bar{A}(u')}{du'} T'^3 dT' \right. \\ &\quad \left. - T_d^4 \frac{d\bar{A}}{du}(u(z)) - 4 \int_{T_d}^T \frac{d\bar{A}(u')}{du'} T'^3 dT' \right\} \end{aligned} \quad (4.23)$$

where $\frac{du'}{dz}$ is independent of z' and so can be removed from the integrals.

Equation (4.23) is valid for $z \leq H$, and the signs are correct as indicated if we define $\frac{du'}{dz}$ to have the sign appropriate to the upward flux part.

$$\text{i.e. } \frac{du_1'}{dz} = \frac{2g}{RT_H} u_1(H) \frac{m}{m_H} \left(\frac{T}{T_H} \right)^{2\gamma - \frac{3}{2}} \quad \text{for water vapor,}$$

$$\text{and } \frac{du_2'}{dz} = \frac{2g}{RT_H} u_2(H) \left(\frac{T}{T_H} \right)^{2\gamma - 1} \quad \text{for carbon dioxide.}$$

Expressions for \bar{A} and $\frac{d\bar{A}}{du}$ are developed in the next section.

4.2.3 Sasamori's absorptivity formulae

We adopt the approach of Sasamori (1968) and neglect the explicit temperature dependence of the absorptivity A . i.e. $A(u, T)$ becomes $\bar{A}(u)$, where the absorber amount u is an implicit function of temperature and pressure. For water vapor,

$$\bar{A}_1(u) = \begin{cases} 0.81705(u+7.7736 \times 10^{-5})^{0.11818} - 0.26706; & u \leq 0.01 \\ 0.1042 \ln(u+8.724 \times 10^{-3}) + 0.6220 & ; u \geq 0.01 \end{cases} \quad (4.24)$$

and therefore

$$\frac{d\bar{A}_1}{du}(u) = \begin{cases} \frac{406}{(1+12864u)^{0.88182}}; & u \leq 0.01 \\ \frac{11.94}{(1+114.6u)} & ; u \geq 0.01 \end{cases}$$

For carbon dioxide,

$$A_2(u) = \begin{cases} 0.092818(u+0.024369)^{0.26004} - 0.035330; & u \leq 1 \text{ cm} \\ 0.02371 \ln u + 0.05807 & ; u \geq 1 \text{ cm} \end{cases} \quad (4.25)$$

and

$$\frac{dA_2}{du}(u) = \begin{cases} \frac{0.377}{(1+41.036u)^{0.73996}}; & u \leq 1 \text{ cm} \\ \frac{0.02371}{u} & ; u \geq 1 \text{ cm} \end{cases}$$

Equations (4.24) and (4.25) are similar to Sasamori's formulae (14), (15), (17), and (18), although the constants have been altered where necessary to improve the match of \bar{A} and $\frac{d\bar{A}}{du}$ at the 'crossover' amount (e.g. $u = 0.01$ g cm⁻² for water), and to satisfy exactly the known boundary conditions; namely

$$\bar{A}(0) = 0$$

$$\text{and } \frac{d\bar{A}}{du}(0) = 2 \bar{K}_p$$

According to Goody (1964), the Planck mean absorption coefficients \bar{K}_p for water vapor and carbon dioxide are $203 \text{ cm}^2 \text{ g}^{-1}$ and $96 \text{ cm}^2 \text{ g}^{-1}$ (or 0.1885 cm^{-1}), respectively. Since the function $\frac{d\bar{A}}{du}$ peaks very sharply at $u = 0$, it is important to specify this value correctly.

Near the $15 \mu\text{m}$ band of CO_2 , we have weak overlapping absorption by the water vapor continuum. This effect must be corrected for.

$$\text{Absorption due to } \text{H}_2\text{O plus } \text{CO}_2 = \bar{A}_1(u_1) + \tau_{12}(u_1) \bar{A}_2(u_2) \quad (4.26)$$

where τ_{12} , the transmissivity of water vapor in the presence of CO_2 , is given adequately by Sasamori's equation (21).

$$\tau_{12}(u) = 1.3302 - 0.832(u + 0.0286)^{0.260} \quad (4.27)$$

The transmissivity given by (4.27) actually decreases too rapidly at long water vapor path lengths. After examining the graph of τ_{12} in Sasamori's paper and the likely range of u_1 in the model, we set a lower cutoff at $\tau_{12} = 0.2$.

In the heating equations, we need to calculate $\frac{d\bar{A}}{du}$ and thus $\frac{d\tau_{12}}{du}$. We don't have a great deal of confidence in the derivative of this empirical expression for τ_{12} (there is no good theoretical value for $\left. \frac{d\tau_{12}(0)}{du} \right|_{15 \mu\text{m band}}$). Fortunately, it is found that the term $\bar{A}_2 \frac{d\tau_{12}}{du}$ is much smaller than $\tau_{12} \frac{d\bar{A}_2}{du}$ at the tropopause, so our calculation of H is not affected. On the other hand, $\frac{d\tau_{12}}{du}$ becomes very important near the

ground, and omission of this term changes the sign of the CO_2 long-wave heating. For this reason, we will evaluate the internal tropospheric heating by differencing the fluxes at two levels rather than using the differential form (4.23). In debugging tests of the computer program, these two procedures yielded the same vertically integrated heating rates in the absence of clouds.

4.2.4 Parameterization of short-wave heating

We parameterize the short-wave absorption by water vapor and ozone after Lacis and Hansen (1974). The water vapor-absorption B_1 is divided into a part due to the direct beam and part due to the reflected beam. For clear skies

$$B_1(u_1) = B_1(y) + R_g B_1(y^*) ; \quad R_g = \text{ground albedo.}$$

The water vapor amount $y = M u_1(z)$, where the magnification factor $M = \frac{35}{(1224 \cos^2 \bar{\zeta} + 1)^{1/2}} \approx \sec \bar{\zeta}$ except for large zenith angle. The amount of water vapor traversed by the diffuse beam is

$$y^* = M u_1(0) + \frac{5}{3} [u_1(0) - u_1(z)]$$

where the average magnification for the diffuse radiation is $\frac{5}{3}$. For y measured in cm, Lacis and Hansen (1974) obtained an empirical fit to the absorption curve of Yamamoto (1962).

$$B_1(y) = \frac{2.9 y}{(1 + 141.5 y)^{0.635} + 5.925 y} \quad (4.28)$$

Similarly, for ozone, the net absorption $B_3(u_3)$ is given by

$$B_3(u_3) = B_3(x) + R B_3(x^*)$$

where

$$x = M u_3(z)$$

$$x^* = M u_3(0) + 1.9(u_3(0) - u_3(z))$$

and

$$B_3(x) = \frac{1.082 x}{(1 + 138.6 x)^{0.805}} + \frac{0.0658 x}{1 + (103.6 x)^3} + \frac{0.02118 x}{1 + .042 x + .000323 x^2} \quad (4.29)$$

The first two terms in (4.29) represent the ultraviolet absorption by ozone and the third term is the fraction of incident solar flux absorbed by the Chappuis band from the visual part of the spectrum. The albedo R includes the effective albedo of the lower atmosphere. Allowing for multiple reflections,

$$R = R_a(\bar{\zeta}) + [1 - R_a(\bar{\zeta})] \frac{(1 - \bar{R}_a) R_g}{(1 - \bar{R}_a R_g)}$$

where $R_a(\bar{\zeta})$ = albedo of atmosphere due to Rayleigh scattering (neglecting clouds)

$$= \frac{0.219}{1 + 0.816 \cos \bar{\zeta}}$$

\bar{R}_a is the average $R_a(\bar{\zeta})$ over all zenith angles, equal to $2 \int_0^{\pi/2} R_a(\bar{\zeta}) \cos \bar{\zeta} d(\cos \bar{\zeta}) = 0.144$.

The parameterizations above apply to clear skies and equations (4.28), (4.29) are used in differential form in our determination of the tropopause height (see Section 4.3.1). Figure 15 of Lacis and Hansen (1974) indicates that the heating at height z is almost unaffected by clouds below that level (because heating due to reflected radiation is small). Therefore, we expect that neglecting the effect of clouds when calculating H will not

cause a serious error. At the cloud layer itself, the heating is increased considerably (e.g. from about 1.0 to 2.5 °C/day for middle clouds) in the upper part of the layer, and there is reduced heating below the clouds. Thus, when we evaluate the net radiative heating $\frac{Q_{\text{rad}}}{\rho c_p}$ in its various forms in the forcing equations (2.33, 2.36, and 2.38), we must consider clouds. The parameterization of short-wave heating with clouds is discussed in Chapter 5.

4.3 Results of non-grey calculations (without clouds)

4.3.1 Tropopause height calculation

Temperature profiles for the atmosphere, calculated on the assumption of radiative equilibrium, typically show a pronounced minimum in the temperature at about 10 km and a superadiabatic 'troposphere' (e.g. Manabe and Möller, 1961). In general, the tropopause temperature is too low (about 180°K). If the surface is also in pure radiative balance, the lower atmosphere has an average lapse rate of 17 °K/km (Möller and Manabe, 1961), while fixing the surface temperature at its observed value (and thus, implicitly assuming dynamical fluxes are present) leads to temperature gradients close to the dry adiabatic, 10 °K/km (Manabe and Möller, 1961). The presence of this unstable region means moist convection will set in and adjust the profile. Manabe and Strickler (1964) allowed such a convective adjustment (to 6.5 °K/km) in their calculations. They found the temperature of the upper troposphere to be warmer and more realistic than for pure radiative equilibrium.

In the present model, we allow a constant lapse rate in the tropo-

sphere, whose value is determined by the overall heating balance between large-scale dynamics, small-scale moist convection, and radiation. At the tropopause itself, we take the conventional approach and assume radiative equilibrium. As noted by Goody (1964, Ch. 8), there is still no agreement in the literature as to the validity of this hypothesis. Nevertheless, we know it will at least give us a temperature minimum at about the right height, and seems a reasonable first approximation. We will therefore start by outlining the procedure used in this thesis to calculate H , and at the end of the section, when we have some numbers to look at, we will return briefly to this validity question.

The tropopause position is found by solving for the height H at which the condition for radiative equilibrium is satisfied.

$$\text{Net radiative heating} = - \frac{\partial}{\partial z} \mathcal{F}(z) \Big|_{z=H} = 0 \quad (4.30)$$

where $\mathcal{F}(z)$ is the sum of the short-wave and long-wave fluxes, and can be written in terms of previously defined functions.

$$\begin{aligned} \mathcal{F}(z) = S_0 \cos \bar{\zeta} \left[B_1(u_1(z)) + B_3(u_3(z)) \right] + (F_1(z)\uparrow - F_1(z)\downarrow) \\ + (F_2(z)\uparrow - F_2(z)\downarrow) \end{aligned} \quad (4.31)$$

The subscripts 1, 2, and 3 refer to water vapor, carbon dioxide, and ozone, respectively. Equation (4.30) can then be written

$$S_0 \cos \bar{\zeta} (SW1+SW3) - \sigma (LW1+LW2) = 0 \quad \text{at } z = H \quad (4.32)$$

The short-wave (SW1, SW3) and long-wave (LW1, LW2) parts are defined below.

$$\begin{aligned} \text{SW1} &= -\frac{du_1}{dz} \left\{ M \frac{dB_1}{dy} \Big|_{y=Mu_1(z)} + \frac{5}{3} R_g \frac{dB_1}{dy^*} \Big|_{y^*=Mu_1(0) + \frac{5}{3}(u_1(0)-u_1(z))} \right\} \\ \text{SW3} &= -\frac{du_3}{dz} \left\{ M \frac{dB_3}{dx} \Big|_{x=Mu_3(z)} + 1.9R \frac{dB_3}{dx^*} \Big|_{x^*=Mu_3(0) + 1.9(u_3(0)-u_3(z))} \right\} \quad (4.33) \end{aligned}$$

where $\frac{dB_1}{dy}$ and $\frac{dB_3}{dx}$ are the derivatives of (4.28) and (4.29), and $\frac{du_1}{dz}$, $\frac{du_3}{dz}$ can be found analytically from (4.14) and (4.17), respectively.

$$\text{LW1} = \frac{1}{\sigma} \frac{\partial}{\partial z} (F_1(z) \uparrow - F_1(z) \downarrow) \quad \text{and} \quad \text{LW2} = \frac{1}{\sigma} \frac{\partial}{\partial z} (F_2(z) \uparrow - F_2(z) \downarrow)$$

are defined so they are positive for long-wave cooling. Then

$$\begin{aligned} \text{LW1} &= \frac{du_1}{dz} \left\{ 4 \int_{T(z)}^{T_g} \frac{d\bar{A}_1(u_1(z') - u_1(z))}{du_1'} T'^3 dT' - T_d^4 \frac{d\bar{A}_1(u_1(z))}{du_1} \right. \\ &\quad \left. - 4 \int_{T_d}^{T(z)} \frac{d\bar{A}_1(u_1(z) - u_1(z'))}{du_1'} T'^3 dT' \right\} \quad (4.34) \end{aligned}$$

The expression for carbon dioxide, LW2, is similar to (4.34) but is even longer, consisting of a $\tau_{12} \frac{d\bar{A}_2}{du_2}$ part and a $A_2 \frac{d\tau_{12}}{du_1}$ part. We will avoid the details here. Using the short-hand notation of (4.32), we define a new heating function \mathcal{H}_R .

$$\mathcal{H}_R(z, H, d) = s^4 (\text{SW1} + \text{SW3}) - (\text{LW1} + \text{LW2}) \quad (4.35)$$

Note that s depends only on external conditions. \mathcal{H}_R is a function of the tropopause height H and the transition depth d as well as height z .

Equation (4.30) may be expressed as

$$\mathcal{H}_R(H, H, d) = 0 \quad (4.36)$$

Transition depth d: The temperature structure in the transition region is chosen to give continuity of temperature and temperature gradient at $z = H$ and $H+d$. We have yet to make a particular choice for d . We can appeal to an operational definition of the tropopause to place an upper limit on this parameter:

"The tropopause is the lowest level at which the lapse rate decreases to 2 °K/km or less, provided also that the average lapse rate between this level and all higher levels within 2 km does not exceed 2 °K/km." (Fairbridge, 1967). This statement implies $d \leq \frac{8}{\beta}$ km. Of course, the definition is somewhat arbitrary and is applied to instantaneous profiles rather than mean profiles, but it seems to give a reasonable value. A lower limit must be placed on d for mathematical reasons. As the transition depth tends to zero, the temperature gradient at $z = H$ approaches a discontinuity, and this causes problems in evaluating the flux derivatives. In order to evaluate the heating due to the downward long-wave flux ($\frac{\partial}{\partial z} F(z)\downarrow$), there must be a limited region above $z = H$ where the temperature can vary. This is less critical for the water vapor heating because the concentration of H_2O decreases more rapidly with height. Table 4.1 shows an example of this behavior for a particular set of parameter values. Only the downward flux depends on the transition depth d . In this table, the heating rate was calculated from the flux derivatives using

$$\begin{aligned} \frac{\partial T}{\partial t} &= -\sigma \frac{R T_H}{c_p p_0} \left(\frac{T_0}{T_H} \right)^{\gamma} \left[\frac{1}{\sigma} \frac{\partial}{\partial z} (F(z)\uparrow - F(z)\downarrow) \right]_{z=H} \\ &= -1.551 \times 10^{-3} \left[\frac{1}{\sigma} \frac{\partial}{\partial z} F(z)\uparrow - \frac{1}{\sigma} \frac{\partial}{\partial z} F(z)\downarrow \right]_{z=H} \quad ^\circ\text{C/day} \end{aligned}$$

Table 4.1: Change in long-wave heating components of LW₁, LW₂ with d for 45°N mean annual conditions (of solar insolation and ozone amount) and $\beta = 6.5$, $h_0 = 1$, $T_g = T_0 = 280.7$, $H = 12$.

	d, km	H ₂ O	CO ₂
Heating by upward flux, $\frac{1}{\sigma} \frac{\partial}{\partial z} F(z) \uparrow \Big _H$	--	-44.695	-230.41 (in °K ⁴ /cm)
Heating by downward flux, $\frac{1}{\sigma} \frac{\partial}{\partial z} F(z) \downarrow \Big _H$, as a function of d	8/β	-99.645	-232.32
	1.00	-98.936	-224.90
	0.75	-98.093	-214.95
	0.50	-97.161	-201.91
	0.25	-96.124	-182.55
	0.00	-94.966	-134.85
Heating rate (in °C/day)	8/β	-.085	-.003
	1.00	-.084	.009
	0.75	-.083	.024
	0.50	-.081	.044
	0.25	-.080	.074
	0.00	-.078	.148

From Table 4.1, we see that the value we calculate for CO₂ heating becomes unrealistic for small d and eventually prevents a radiative balance from occurring (as the short-wave heating is always positive).

Figure 4.3 shows the behavior of the function H_R in (4.36) as H and d vary (the other parameter values are the same as for Table 4.1).

Figures 4.4, 4.5, and 4.6 are all part of the same sequence. Figure 4.4

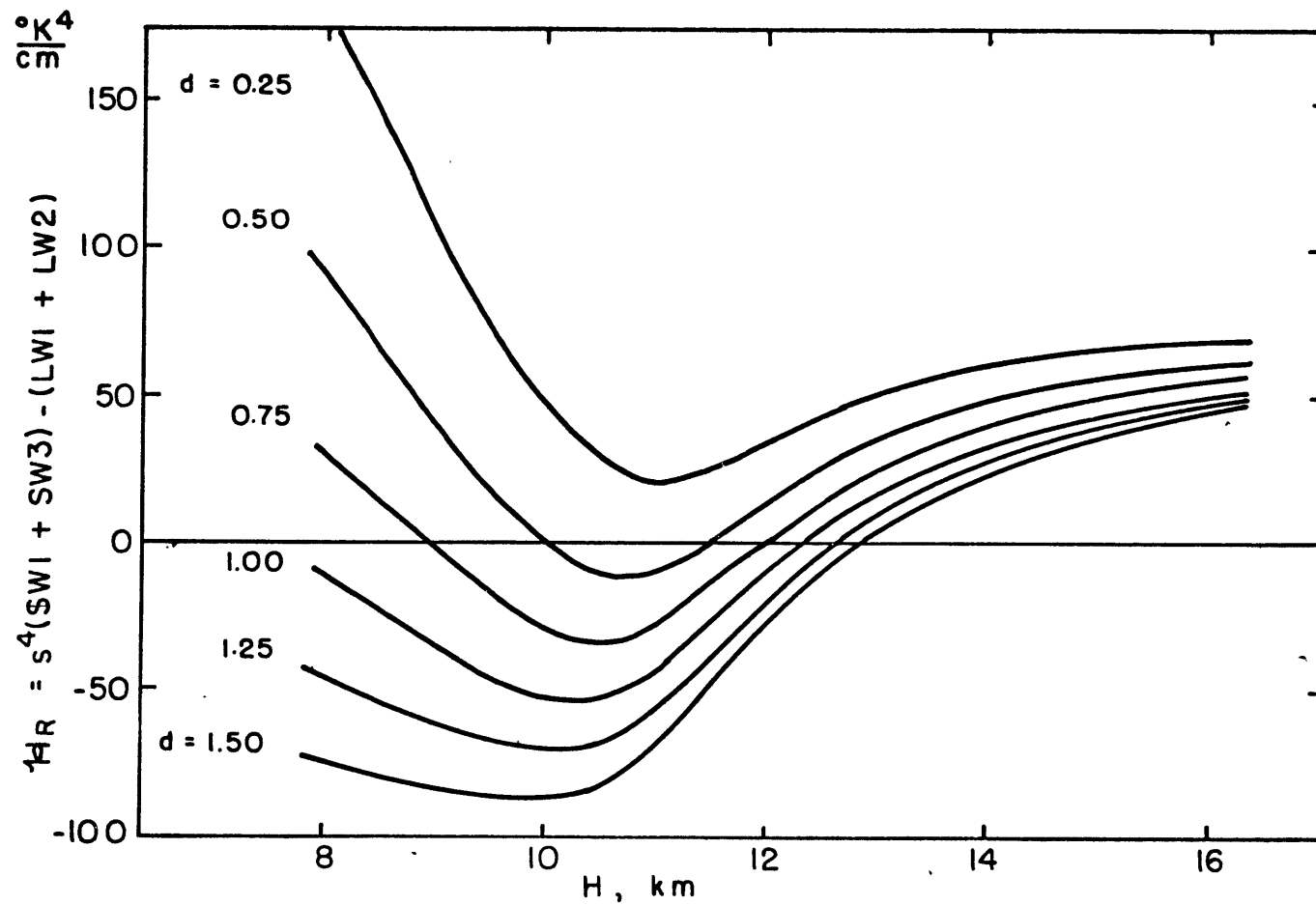


Figure 4.3: Variation of heating at tropopause as a function of H and d . Radiative equilibrium solutions exist where the curves cross the horizontal axis.

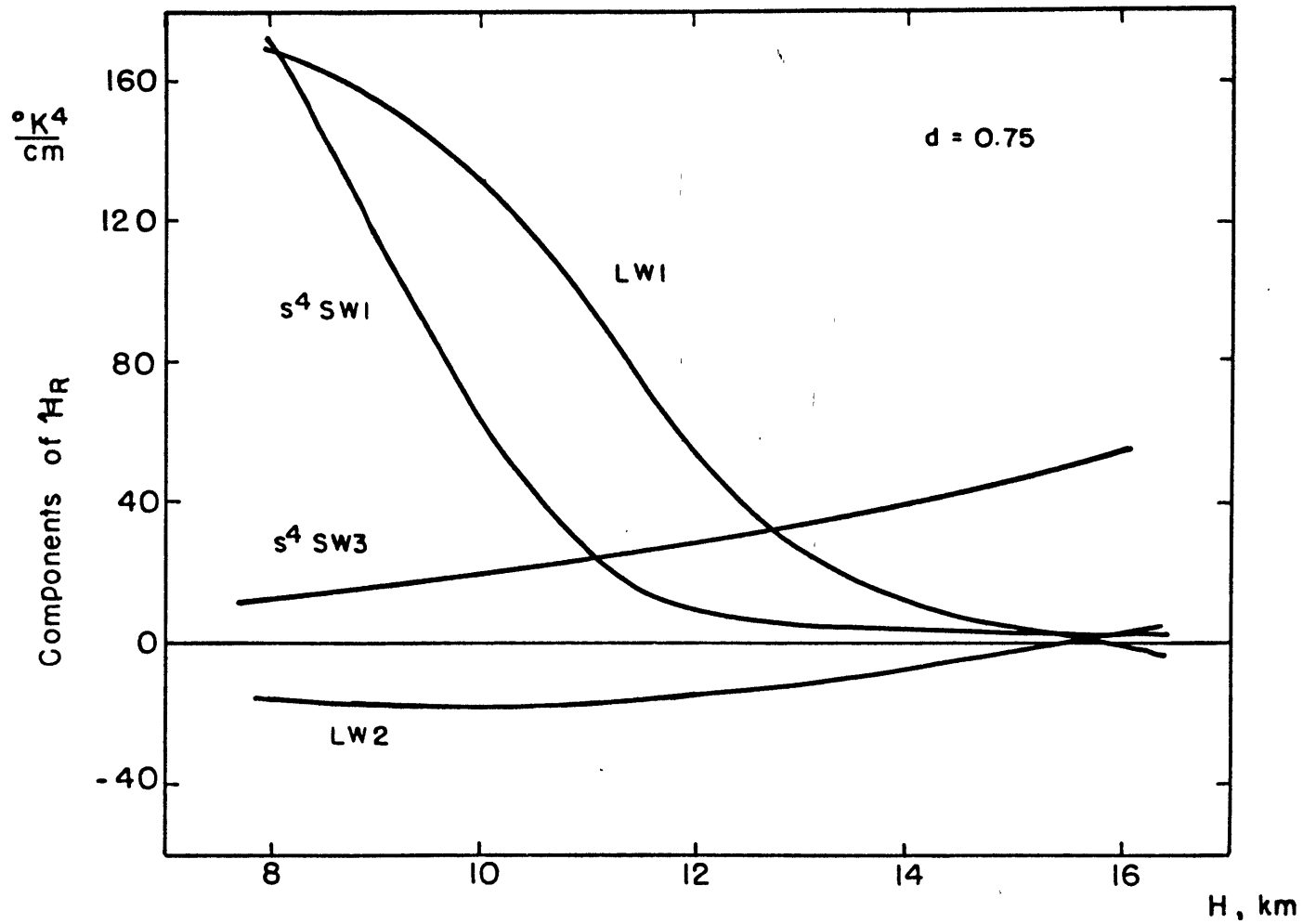


Figure 4.4: Components in the heat balance at the tropopause. $s^4 SW1$, $s^4 SW3$ are short-wave heating by H_2O and O_3 , respectively. $LW1$, $LW2$ are long-wave cooling by H_2O and CO_2 .

$$s = \left(\frac{LW1 + LW2}{SW1 + SW3} \right)^{1/4}$$

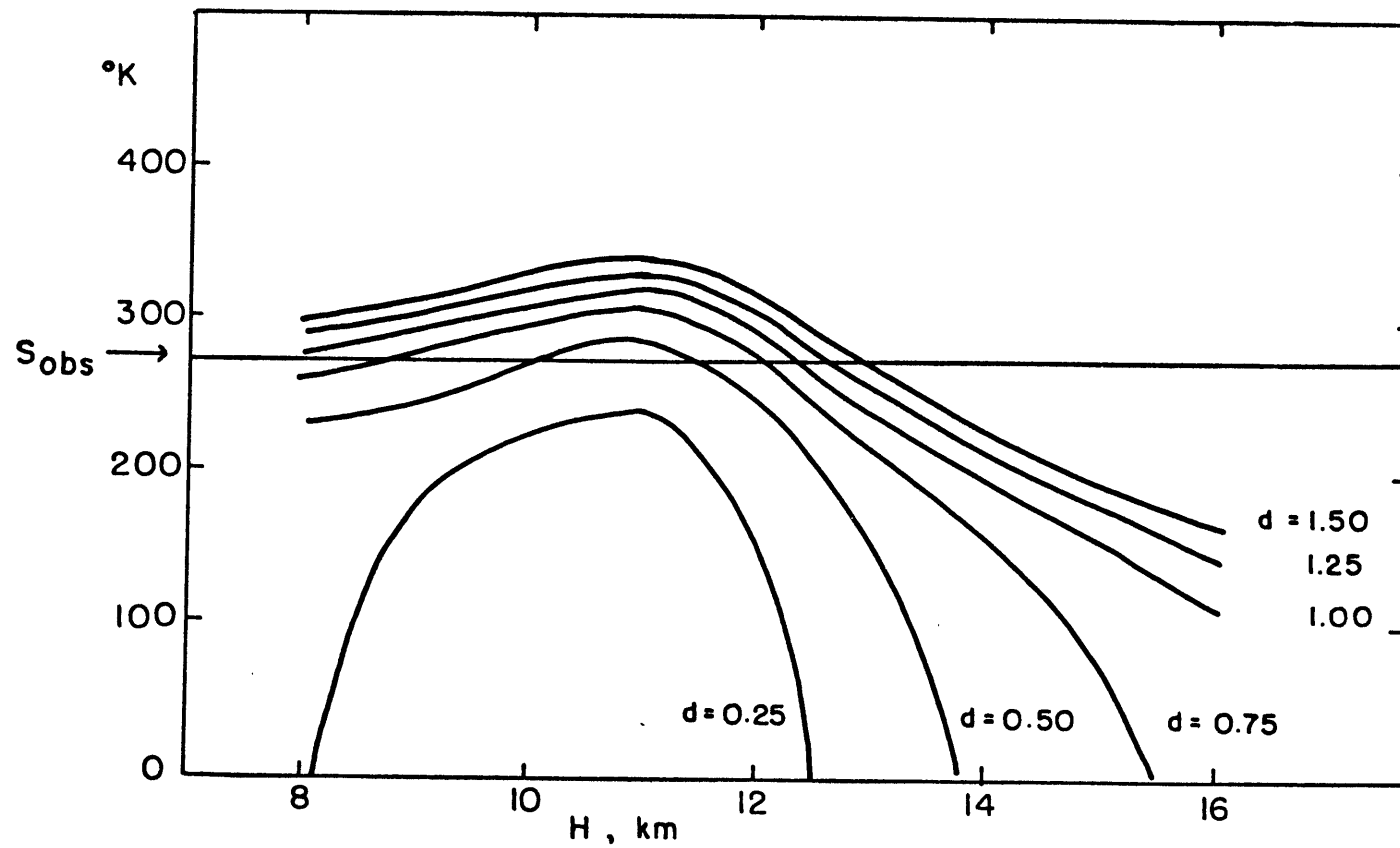


Figure 4.5: Variation of parameter s with tropopause height H and transition depth d .

$$H_R = s^4 (SW1 + SW3) - LWI$$

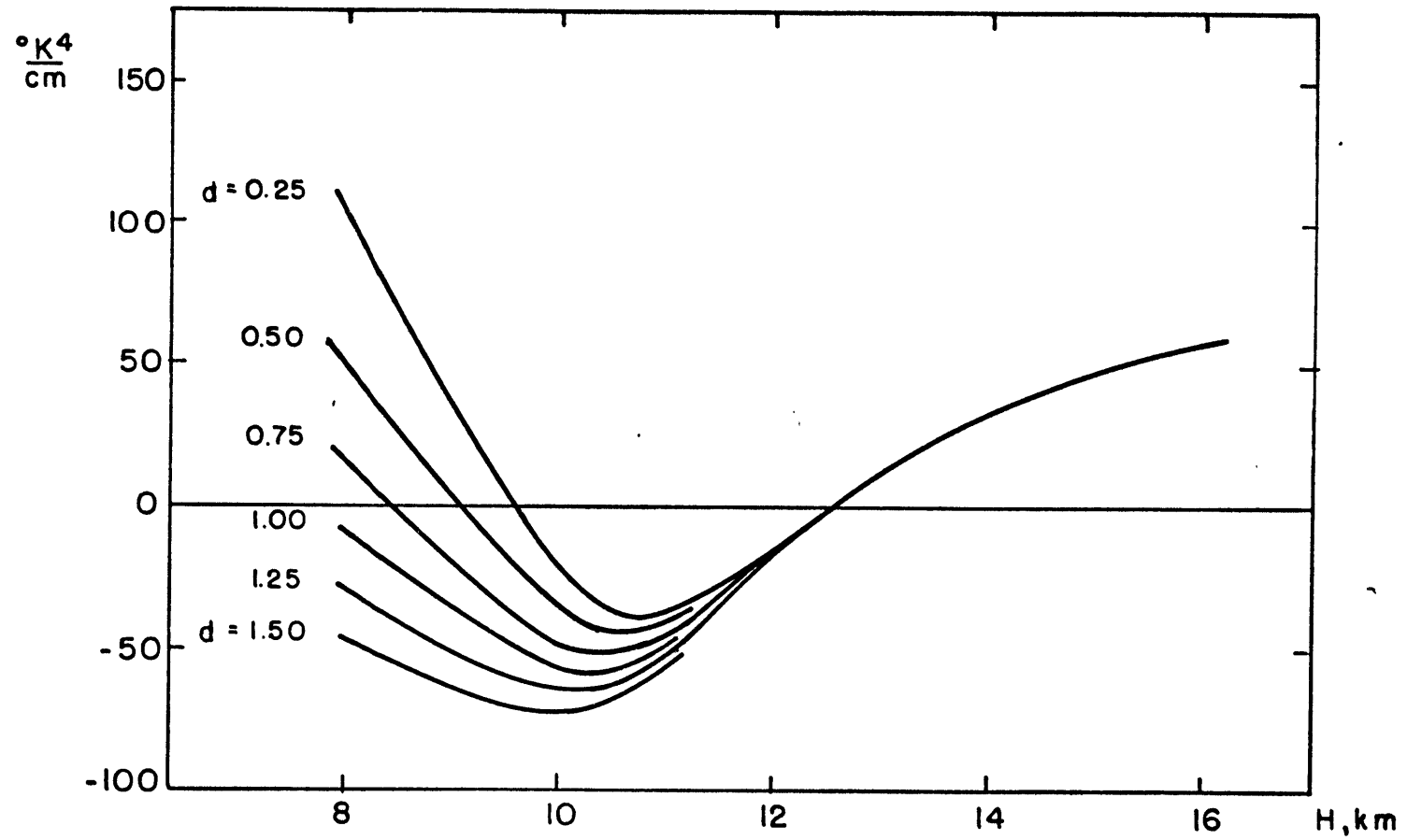


Figure 4.6: As Fig. 4.3, but with CO_2 long-wave heating omitted.

displays the four components of H_R and explains the general shape of the curves in 4.3. The short-wave terms, which are independent of d , show the expected variation. Absorption of solar radiation by water vapor dominates at small H (for a given T_0, β) but gives way to ozone heating at greater heights. The minimum at intermediate H produces a corresponding minimum in the heating curves of 4.3. Concentrating on that first figure again, we see that there are two roots (or none at all) for each value of d . These occur where $H_R = 0$. The physically meaningful solution is the larger root. This can be recognized by applying a small perturbation to the solution. For example, consider the lower root at $H \approx 10$ for a transition depth of 0.50 km. If H is perturbed negatively so that T_H increases slightly, Figure 4.3 indicates that the net heating becomes positive and this will tend to increase T_H further. i.e. the lower root where $\frac{\partial H_R}{\partial H} < 0$ is unstable, and the upper root is the appropriate root.

In practice, we rearrange equation (4.35) and calculate

$$s = \left(\frac{LW1+LW2}{SW1+SW3} \right)^{1/4} \quad (4.37)$$

where all the terms on the right hand side are evaluated at $z = H$. A plot of this function is shown in Figure 4.5, and we solve numerically for the height H at which $s = s_{obs} = \left(\frac{S_0 \cos \bar{\zeta}}{\sigma} \right)^{1/4}$. The reason that curves 4.5 are used in place of 4.3 is that a numerical solution is much simpler. Calculating s at any two points above the root allows us to extrapolate the curve with more confidence.

As a further modification, we neglect the heating contribution due to carbon dioxide. We found in Table 4.1 that this component was very sensitive to the choice of transition depth, although it remained small

for moderate d . Figure 4.6 shows H_R when CO_2 heating is neglected. We can see immediately the advantage of this simplification. The tropopause height for radiative equilibrium is now essentially independent of transition depth. The solution for H is the same as given by Figure 4.3 with d between 1.0 and 1.25.

So far we have considered the behavior of the H_R curves for a particular surface temperature and lapse rate. It is interesting to see how the tropopause height varies with these quantities and other parameters of the model. The behavior is represented accurately by

$$H = 12.21 + 0.105(T_0 - 270) - 2.69(\beta - 6.5) \quad (4.38)$$

$$- 2.29 \times 10^{-2}(s - 250) + 1.01(h_0 - 1) - 3.0 \times 10^{-3}(u_2(0) - 120)$$

Equation (4.38) relates the tropopause height (in km) to the surface temperature T_0 (in $^{\circ}\text{K}$), the lapse rate β , the solar parameter s , and the relative humidity and CO_2 column amount (s has units of $^{\circ}\text{K}$ and is simply related to the equivalent temperature T_e ; $s = \frac{T_e}{(1-\alpha)^{1/4}}$ where α is the planetary albedo). Equation (4.38) was obtained as a least-squares fit to solutions of H calculated for a range of parameter values. It applies to the special case of transition depth $d = \frac{8}{\beta}$ and 45° mean annual conditions for solar insolation and ozone amounts (the variation with s being determined from Figure 4.5). The formula is therefore of only limited practical use. Its main interest lies in the signs and relative magnitudes of the term. As far as latitudinal variation is concerned, the major parameter affecting tropopause height is the surface temperature, $T_0(\phi)$ (lapse rate, relative humidity, and CO_2 amount are all assumed to be in-

dependent of latitude). This justifies the use of equation (2.20) for approximating the meridional structure of $H(\phi)$ in the full model.

Table 4.2 shows the variation of H with latitude for annual mean insolation and observed surface temperatures. The calculations were done using a more realistic lapse rate of $6.0 \text{ }^\circ\text{K/km}$ and surface relative humidity $h_0 = 0.8$. On the whole, the results are encouraging. The equatorial tropopause is a little low, partly due to our neglect of the effects of penetrating cumulus convection (e.g. see Sarachik, 1978). Since our imposed surface temperature and solar insolation fields vary smoothly with latitude, the tropopause break at the latitude of the jet is not simulated. This is clearly a dynamically induced effect, and we cannot expect radiative equilibrium to hold here. The resulting tropopause heights we calculate in this region are too high. More realistic values would be obtained if we included subsidence heating by the mean meridional motions (associated with the rising and descending branches of the Hadley and Ferrel circulation). According to Figure 7.19 of Newell et al. (1974), these motions produce adiabatic heating at the latitude of the jet and cooling at the equator. This would adjust our calculated $H(\phi)$ towards the observed heights in both cases.

This brings us back to the question of the validity of the radiative equilibrium assumption. Some specific latitudinal departures from radiative equilibrium were discussed in the previous paragraph. As far as tropospheric averages are concerned, we can argue on simple energetics grounds that radiative equilibrium at the tropopause is a reasonable assumption. Dopplick (1971) found the total boundary flux into the stratosphere (going into both mean and eddy kinetic energy) to be about $160 \frac{\text{mW}}{\text{m}^2}$ ($= 160 \frac{\text{erg}}{\text{cm}^2\text{-sec}}$).

Table 4.2: Variation of tropopause height with latitude (for $\beta = 6.0$,
 $h_0 = 0.8$)

Latitude	s ($^{\circ}\text{K}$)	$\cos \bar{\zeta}$	T_0 ($^{\circ}\text{K}$)	H (km)
5	295.118	0.6172	299.55	16.035
15	292.872	0.5995	298.75	15.821
25	288.424	0.5649	295.45	15.209
35	281.634	0.5145	289.75	14.345
45	272.285	0.4506	281.95	13.265
55	260.094	0.3764	276.05	12.482
65	245.053	0.2980	268.95	11.497
75	230.609	0.2350	261.95	10.638
85	222.083	0.2030	252.95	9.698

Miller (1970) calculated the upward potential energy flux ($[\omega'z']$) for different wavenumbers. He found a total over the first four wavenumbers of about $100 \frac{\text{erg}}{\text{cm}^2\text{-sec}}$. Taking this estimate and assuming the energy is distributed through the entire mass of the stratosphere, we can calculate a heating rate of about 0.005 $^{\circ}\text{C}/\text{day}$. From Table 4.1, this value is small compared to the long-wave heating rate of water vapor. A data study by Chiu and Greenfield (1959) brought out the importance of horizontal advection of heat when studying daily changes

in the temperature of the lower stratosphere. However, it is not clear how the neglect of horizontal advection will affect long-term mean values of the tropopause height.

4.3.2 Infrared emission to space

The infrared emission to space can be calculated from (4.20)

$$F(\infty)\uparrow = \sigma T_g^4 - 4\sigma \int_{T_d}^T g \bar{A}(u(z')) T'^3 dT' \quad (4.39)$$

where the total absorptivity \bar{A} has contributions from both water vapor and carbon dioxide (Eq. 4.26).

Let us consider a simple example where $T_g = T_0$. We may write

$$F(\infty)\uparrow = \sigma T_0^4 [1 - (FT1+FT2)] \quad (4.40)$$

where $F(\infty)\uparrow$ is a function of T_0 , β , h_0 , H , and $u_2(0)$ and

$$FT1 = 4 \int_{T_d/T_0}^1 \bar{A}_1(u_1(z')) \left(\frac{T'}{T_0} \right)^3 d \left(\frac{T'}{T_0} \right)$$

$$FT2 = 4 \int_{T_d/T_0}^1 \tau_{12}(u_1(z')) \bar{A}_2(u_2(z')) \left(\frac{T'}{T_0} \right)^3 d \left(\frac{T'}{T_0} \right)$$

We can think of FT1 and FT2 as a measure of the 'relative greenhouse effect' of the two absorbers, H_2O and CO_2 . However, because of the somewhat artificial separation of the two gases in determining \bar{A} , it is really only the sum that is physically meaningful. Figure 4.7 shows the two fractional absorptions FT1 and FT2 as functions of tropopause height for $T_0 = 280$ °K, $\beta = 6.5$, $h_0 = 1.0$, $u_2(0) = 120$ and $d = 1.0$. The water vapor component is clearly insensitive to an exact knowledge of H . While this

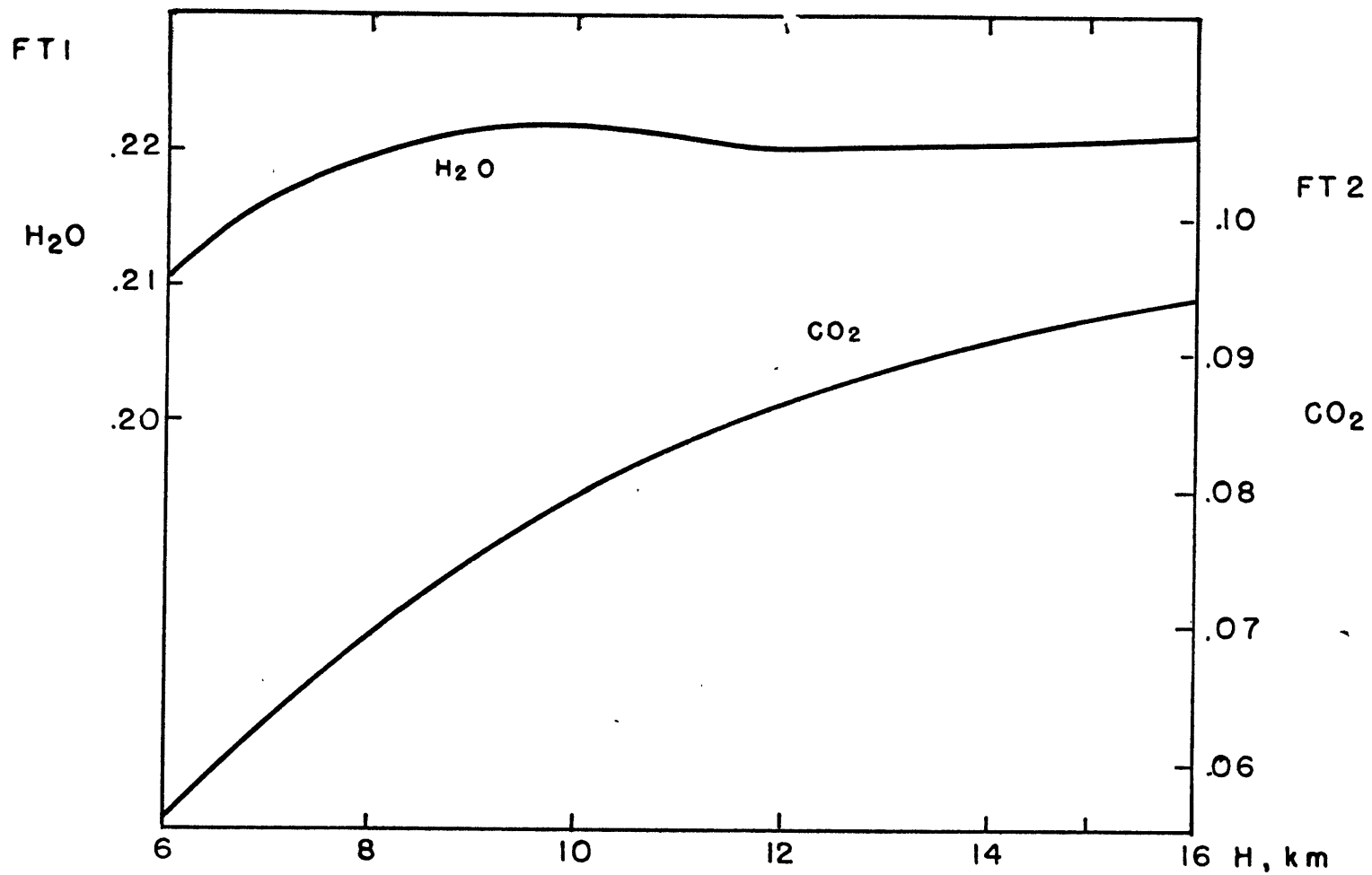


Figure 4.7: Fractional absorptions FT1 and FT2 of water vapor and carbon dioxide, respectively. (A measure of the 'relative greenhouse effect').

is not true for carbon dioxide, FT2 is only 40% of FT1.

We can calculate $F(\infty)\uparrow$ for a range of parameter values as we did for H (equation 4.38), and determine a linear regression equation (a linear fit is better for this parameter than for tropopause height H). For $F(\infty)\uparrow$ in units of $\text{cal cm}^{-2} \text{min}^{-1}$,

$$\begin{aligned} F(\infty)\uparrow = & 0.3341 + 0.3517 \times 10^{-2} (T_0 - 273.2) - 0.25 \times 10^{-2} (H - 12) \\ & - 0.248 \times 10^{-1} (h_0 - 1.0) - 0.687 \times 10^{-2} (\beta - 6.5) \\ & - 0.55 \times 10^{-4} (u_2(0) - 120) \end{aligned} \quad (4.41)$$

In M.K.S. units, W m^{-2} ,

$$\begin{aligned} F(\infty)\uparrow = & 232.8 + 2.45 (T_0 - 273.2) - 1.73 (H - 12) - 17.3 (h_0 - 1.0) \\ & - 4.78 (\beta - 6.5) - 0.038 (u_2(0) - 120) \end{aligned} \quad (4.42)$$

In the absence of clouds, which is the situation considered in (4.41), Budyko (1969) gives

$$F(\infty)\uparrow = 223 + 2.2 T_s \text{ W m}^{-2}$$

for the surface temperature, T_s , in $^{\circ}\text{C}$. We set $h_0 = 1$, $\beta = 6.5$, and $u_2(0) = 120$ in (4.42). We also note that H varies with latitude and can therefore be represented as a function of T_0 . As a rough approximation, consider $(H - 12) \approx \frac{2}{15} (T_0 - 273.2)$, so that H varies from 8 to 16 km as the surface temperature increases from -30°C to $+30^{\circ}\text{C}$. Then we have

$$F(\infty)\uparrow \approx 232.8 + 2.22 (T_0 - 273.2)$$

from (4.42), which shows good agreement with Budyko's formula.

4.4 Small-scale moist convection

It is well known that small-scale moist convection is an important stabilizing process in the earth's atmosphere, particularly in low latitudes. We have already mentioned its simulation in one-dimensional radiative-convective models, such as that of Manabe and Strickler (1964). In Chapter 3, where moist convective heating was omitted, the large-scale vertical eddies stabilized the atmosphere with respect to dry convection, but the predicted lapse rate was still conditionally unstable as far as moist convection was concerned. Obviously, a more realistic treatment must include moist processes. In line with the analytical nature of this model, we want to include the effects of cumulus convection in a 'continuous manner'. By contrast, numerical models (and perhaps the atmosphere, too) carry out a 'convective adjustment' where fields are changed in a nearly discontinuous manner.

There is no simple theory for describing the vertical distribution of cumulus heating. Parameterization in terms of the large-scale variables, such as that of Arakawa and Schubert (1974), cannot be applied in this model. Instead, we will take the common approach (e.g. Schneider and Lindzen, 1977) in simple models of prescribing the vertical structure. Although the shape of the heating profile is specified, its amplitude is free to be determined by the model from the surface flux balances.

We have made the assumption that the net radiative heating, $\frac{Q_{\text{rad}}}{\rho c_p} = -\frac{\partial}{\partial z} \mathcal{F}(z)$, is zero at the tropopause. Referring back to Equation (2.1), this implies that in equilibrium the large-scale dynamical heating must balance the convective heating at this level. The expression we will use for the convective heating takes the form (4.42)

$$\frac{Q_{\text{conv}}}{\rho c_p} = K(\phi) \left\{ \frac{\frac{x-b}{c}}{\left(1+e^{\frac{x-b}{c}}\right)^2} - \frac{\frac{1-b}{c}}{\left(1+e^{\frac{1-b}{c}}\right)^2} \right\} + (1-\mu)^{\frac{\Gamma}{\beta}} H_E \quad (4.42)$$

where $x = \frac{z}{H}$ is a normalized height. [Note: The use of normalized height x allows a convenient separation of variables when performing the horizontal and vertical integrations required in the forcing equations 2.36 and 2.38]. The term in curly brackets determines the vertical variation of the heating, and vanishes at the tropopause, $x = 1$. The convective parameter b denotes the level of maximum heating, and c measures how rapidly the heating decreases away from the peak. Small c implies the heating is concentrated close to $x = b$. The form of the heating function is similar to that used to describe the ozone distribution, and matches observed heating profiles (such as Figure 4.8 below) quite well by appropriate choice of the parameters b and c . The last term in (4.42) represents the correction at the tropopause needed to satisfy radiative equilibrium.

$$H_E = \frac{\sin \phi \cos \phi}{H} (1 + \mathcal{L}(\phi, H)) \left[\frac{V}{r} \frac{dH}{d\phi} \left(\frac{K_S \lambda e^{-\lambda}}{e^{-\lambda x_*} - e^{-\lambda}} \right) - 3W \right] \quad (4.43)$$

is the left-hand side of (2.1) evaluated at $z = H$ and the pressure factor $(p/p_0)^{\kappa} = (1 - \mu x)^{\Gamma/\beta} = (1 - \mu)^{\Gamma/\beta}$ at $z = H$ for $\mu = \frac{\beta H}{T_0}$. Figure 4.8 shows a convective diabatic heating profile for low latitudes. It is taken from Yanai et al.[†] (1973) for Marshall Islands (5-12°N) data, and modified slightly for our purposes. Assuming $T_0 = 300^\circ\text{K}$, $\beta = 6.5^\circ\text{K/km}$, and $H = 16.5 \text{ km}$, we can plot the heating in terms of our normalized variable x . To satisfy (4.42), we have also forced the heating to go to zero

[†] [Note: $(Q_1 - Q_2)$ from Yanai et al. is actually more appropriate than the sum of subsidence heating and evaporative cooling from Fig 19 that we use.]

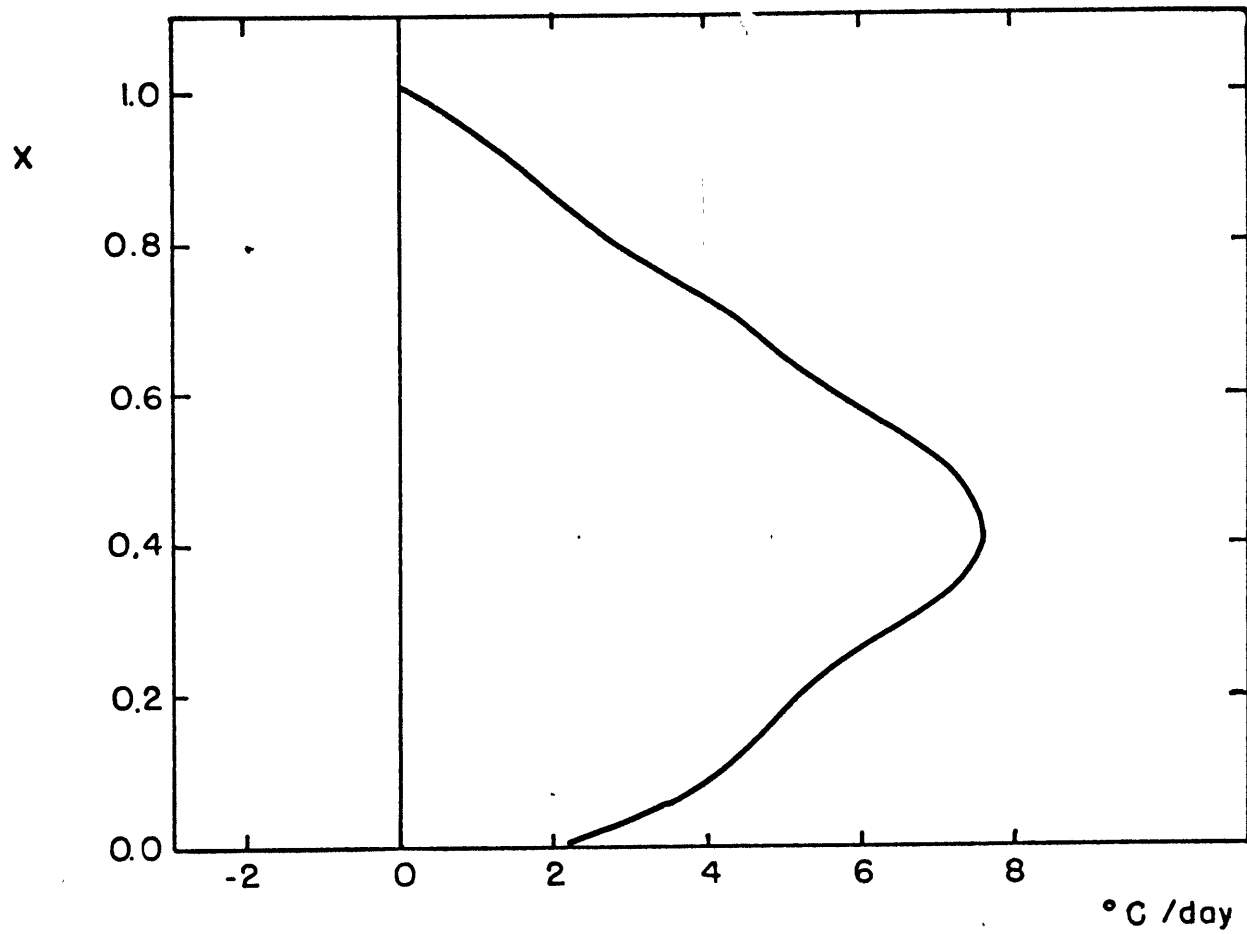


Figure 4.8: Vertical distribution of convective diabatic heating in the tropics.
(Modified from Marshall Islands data of Yanai et. al., 1973).

at $x = 1$. (H_E is very small in the tropics where the baroclinic eddies are weak). A least squares fit of the functional form (4.42) to the profile of Figure 4.8 gives us $b = 0.42$ and $c = 0.23$. In the model calculations, we take $c = 0.23$ and use a somewhat smaller value of b , given by

$$b = \frac{z_c(\phi)}{H(\phi)} \quad (4.44)$$

where z_c is an average cloud height calculated from observation (see Section 5.1). These parameters ($z_c(\phi)$ and c) are held fixed in future climate sensitivity studies of the model.

Yanai's heating profile determines values of b and c that are appropriate for the tropics. We expect the small-scale heating distribution in mid-latitudes to be different, since the large-scale eddies take over much of the vertical flux in this region. Indeed, assuming $b = 0.42$ (in place of (4.44), where b is approximately 0.34) deposits too much heat at high levels and gives an unrealistically stable lapse rate. Moreover, the very fact of specifying the vertical heating profile eliminates one of the major feedback mechanisms in the atmosphere. We expect the partitioning of the total vertical transport between small and large scale parts to vary with latitude and season. Any specific choice of b and c prevents this free adjustment. This deficiency in the model must bias our results. We will examine this effect in more detail in Section 6.2.1.

It only remains to determine the amplitude $K(\phi)$ of the convective heating. Setting

$$\frac{Q_{\text{conv}}}{\rho c_p} = - \frac{1}{\rho c_p H} \frac{\partial}{\partial x} \mathcal{J}_c(\phi, x) \quad (4.45)$$

we integrate (4.42) and apply boundary conditions to the convective flux γ_c .

$$\begin{aligned}\gamma_c(\phi, 1) &= 0 \\ \gamma_c(\phi, 0) &= (H_S + H_L)\end{aligned}\tag{4.46}$$

so the cumulus convection is confined within the troposphere and is forced at the ground by the amount of sensible heat (H_S) and latent heat (H_L) that is available. As a special case, if the sum ($H_S + H_L$) is negative (as may occur in high latitudes), we set $b = 0$ and $c = 0.05$ to confine the cooling close to the ground. This approximates the findings of Deardorff (1972) that the boundary layer flux varies parabolically with height, being a maximum at the ground and zero at $z = 1.5$ km in neutral conditions.

4.5 Surface Energy Balance

The surface heat balance can be written

$$S = R + Q_T - H_B - H_S - H_L - H_C \quad (4.47)$$

where S = heat storage (in the ocean)

R = net short-wave radiation absorbed at the surface

Q_T = meridional heat transport by oceanic motions

H_B = net upward long-wave flux from the surface

H_S = sensible heat flux

H_L = latent heat flux

H_C = heat conducted away vertically when sea ice is present.

In this model, we concentrate on the equilibrium solution ($S = 0$), and ignore oceanic transports (Q_T). If the subscripts 'w' and 'i' represent water and ice, respectively, then the net surface flux balance is composed of two parts, S_w and S_i . Along latitude circles with a fractional ice cover f_i , (4.47) requires

$$(1 - f_i)S_w + f_i S_i = 0$$

S_w and S_i vanish separately at other latitudes where there is no ice or 100% ice, respectively. Equation (4.48) shows the flux balance over water in more detail.

$$S_w = A_w Q - (\sigma T_w^4 - F(0)\downarrow) - \rho_0 c_p C_{Dw} U_s (T_w - T_0) - \rho_0 L_w C_{Dw} U_s [q_s(T_w) - h_0 q_s(T_0)] \quad (4.48)$$

The ordering of the terms is the same as in (4.47). The net SW radiation absorbed at the surface, R , is denoted by $A_w Q$, where Q is the solar insolation at the top of the atmosphere (Table 3.1), and the factor A_w allows for short-wave absorption in the atmosphere and for the total albedo of atmosphere and surface. Since this factor includes the effect of clouds, the particular formulation used in the model is described in Section 5.4.

The second term, H_B , in (4.48) is the difference between the black-body emission by the surface (σT_w^4) and the downward long-wave radiation from the atmosphere, $F(0)\downarrow$, given by (4.22). For completeness, we present a linear regression formula below for the net upward long-wave flux at the surface. This is analogous to (4.41) for the emission to space, and applies in the absence of clouds and with the ground temperature T_g equal to the surface air temperature T_0 .

$$\begin{aligned} H_B &= (\sigma T_0^4 - F(0)\downarrow) = 0.1541 - 0.4773(h_0^{-1.0}) \\ &\quad - 0.172 \times 10^{-3} (T_0 - 273.2) + 0.430 \times 10^{-2} (\beta - 6.5) \\ &\quad - 0.37 \times 10^{-4} (u_2(0) - 120) + 0.9 \times 10^{-4} (H - 12) \end{aligned}$$

in units of $\text{cal cm}^{-2} \text{min}^{-1}$. In W m^{-2} ,

$$\begin{aligned} H_B &= 107.4 - 332.5(h_0^{-1.0}) - 0.120(T_0 - 273.2) \\ &\quad + 3.00(\beta - 6.5) - 0.026(u_2(0) - 120) + 0.06(H - 12) \end{aligned}$$

The major change from (4.41) is the much greater importance assumed by the surface relative humidity h_0 .

H_S and H_L are determined from the bulk aerodynamic formulae. $\rho_0 = \frac{0.353}{T_0} \text{ g cm}^{-3}$ is the surface air density; the drag coefficient C_D is

1.3×10^{-3} for water and 2.6×10^{-3} for ice (Kraus, 1972); the latent heat of vaporization L is 584 cal g^{-1} over water and 625 cal g^{-1} over ice. The parameterization of surface wind speed U_s is discussed in the following section.

There is a similar equation to (4.48) for an ice-covered surface, where the subscripted quantities A_i , T_i , C_{Di} , and L_i are used, and there is an additional term allowing for heat conduction through the ice.

$$H_C = \frac{k(T_f - T_i)}{h_i} \quad (4.49)$$

We take $k = 5 \times 10^{-3} \text{ cal cm}^{-1} \text{ sec}^{-1} \text{ K}^{-1}$ for the conductivity of sea ice, and $h_i = 3 \text{ m}$ for a typical thickness (Groen, 1967). $T_f = 271.2 \text{ }^\circ\text{K}$ is the freezing point of sea water.

Knowing the downward solar and infrared fluxes at the surface, equation (4.47) can be solved iteratively by the Newton-Raphson method for the ground temperature. This calculation is carried out every 10° of latitude starting at 5° . Eventually a latitude is reached where the solution of (4.48) gives a water temperature below the freezing point T_f . The latitude ϕ_c where T_w first equals T_f is found by linear extrapolation. Poleward of that position, the surface consists of water at temperature T_f and a fraction f_i of sea ice at temperature T_i . Determining f_i and T_i independently requires a time-dependent calculation, so we assume the fraction of sea ice increases linearly with latitude poleward of ϕ_c , i.e.

$$f_i = \frac{\phi - \phi_c}{\Delta}, \quad \phi \geq \phi_c,$$

with a limiting value of $f_i = 1$ at $\phi = \phi_c + \Delta$. We choose $\Delta = 15^\circ$ to exceed

the 10° latitude resolution of the surface flux calculation. The mean ground temperature is then $T_g = (1-f_i)T_w + f_i T_i$.

We anticipate our later results at this point and consider Figure 4.9. This figure shows the components of the surface energy balance equation (4.47) in the full model calculations for current conditions. H_B peaks at the latitude (25°) of minimum cloudiness where $F(0)\downarrow$ is smallest, and R , which is weighted by the solar insolation, peaks at a slightly lower latitude. H_L is strongly controlled by the surface temperature through the Clausius-Clapeyron relation. This leaves H_S as a residual, and the sensible heat flux peaks at middle latitudes. This agrees with observational studies (see, for example, Figure 3 in Hantel, 1976). The sea ice conduction term, H_C , becomes comparable to the latent and sensible fluxes near the pole. The model surface temperatures are a little too cold, with $\phi_c = 55^\circ$ and complete ice cover occurring at 70° latitude.

4.5.1 Parameterization of surface wind speed variance

Calculation of the surface fluxes H_S , H_L by the drag formulation requires that a surface mean wind speed U_S be specified. e.g. sensible heat flux $H_S = \rho_0 c_p C_D U_S (T_w - T_0)$. This wind speed U_S is not the zonal mean value as parameterized by Green (1970) (i.e. the barotropic component \bar{U}_S), which is very small (typically $\sim 2 \text{ m sec}^{-1}$), but is the root mean square of the total wind.

$$U_S = \sqrt{\bar{U}_S^2 + U'_S{}^2} \quad (4.50)$$

The eddy component is much the larger and we seek a method of parameter-

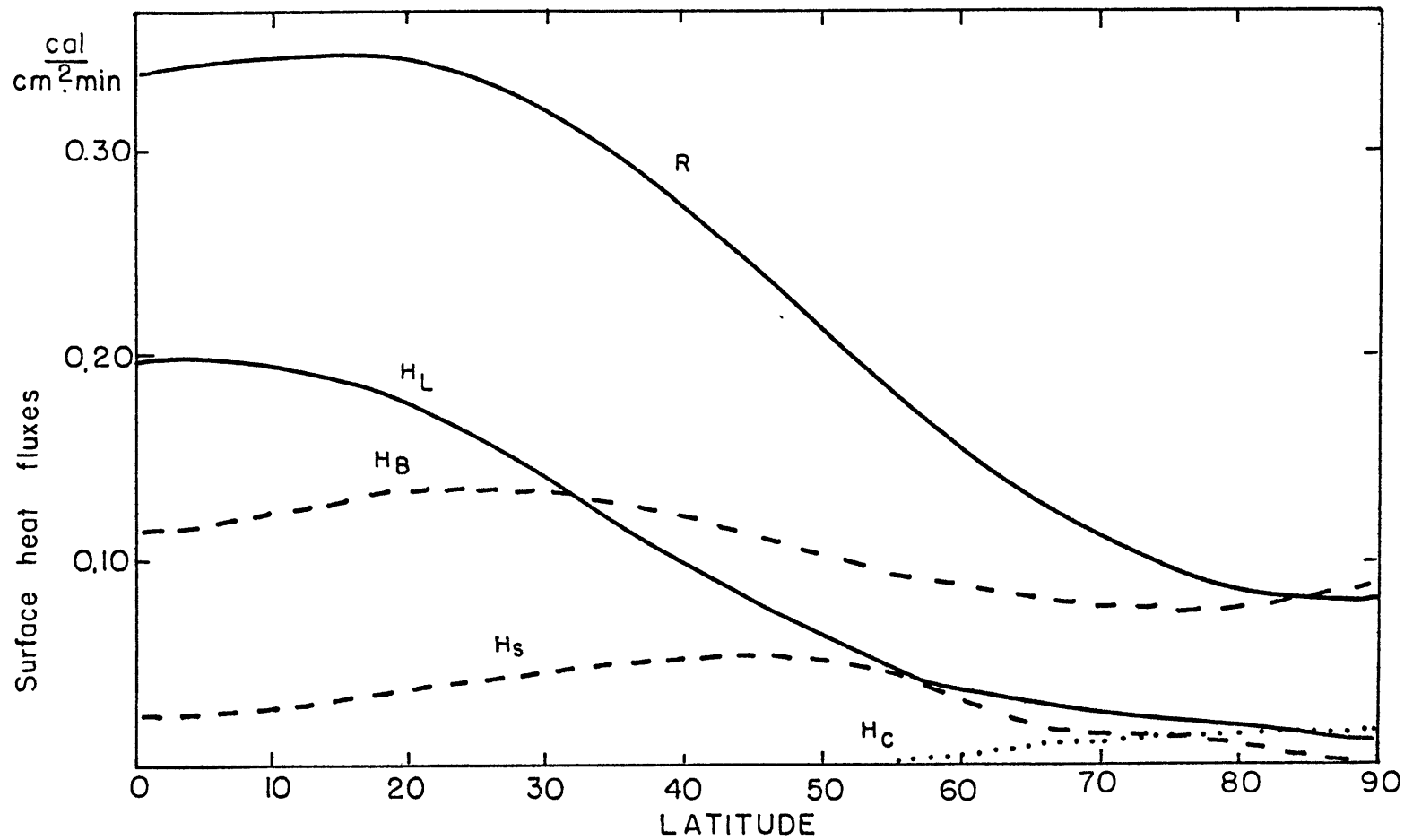


Figure 4.9: Latitudinal distribution of the components of the surface heat balance: net downward short-wave R , net upward long-wave H_B , latent heat H_L , sensible heat H_S , and vertical conduction through sea-ice H_C . (Multiply ordinate by 697. to convert to units of W m^{-2})

izing it consistent with the rest of the model (rather than specifying an arbitrary constant value). Since Stone's model has been used for the eddy heat fluxes, we will see how well it predicts the wind speed variance. Stone (1973) doesn't actually calculate this quantity himself, but it can readily be obtained from his expressions for the eddy velocities u' and v' .

$$\overline{u'^2+v'^2} = 1.094 \left(\frac{9}{5(1+Ri)} \right) \left[x^2 + \frac{1}{12} \right] \left[x^2 + \frac{29+24 Ri}{60} \right] \quad (4.51)$$

where $(\overline{\quad})$ indicates an average over horizontal wavelength, and x is a non-dimensional height which varies from $x = -\frac{1}{2}$ at the ground to $x = +\frac{1}{2}$ at the 'tropopause lid'. By writing the height dependence in terms of x (rather than Stone's non-dimensional $z = x + \frac{1}{2}$), it is seen clearly from (4.51) that the variance is symmetrical about the mid-point $x = 0$. At the ground,

$$\overline{u'^2+v'^2} \Big|_{\text{gnd}} = 0.2626 \left(\frac{Ri + \frac{11}{6}}{Ri + 1} \right) \quad (4.52)$$

Equation (4.52) is written in the dimensionless variables used by Stone (1972b). The scaling factor for $(\overline{u'^2+v'^2})$ is

$$\begin{aligned} \left(\frac{\alpha g}{f_0} H_S \frac{\partial \theta_0}{\partial y} \right)^2 &= \left(\frac{R}{f_0} \right)^2 A^2 \quad \text{using his notation} \\ &= 776.46 A^2 \left(\frac{\text{m}}{\text{s}} \right)^2 \end{aligned}$$

where A is the meridional gradient in $^\circ\text{K}/100 \text{ km}$. Thus, Stone's model predicts that

$$\overline{u'^2+v'^2} \Big|_{\text{gnd}} = 203.9 \left(\frac{Ri + \frac{11}{6}}{Ri + 1} \right) A^2 \left(\frac{\text{m}}{\text{s}} \right)^2 \quad (4.53)$$

The dependence on the Richardson number Ri is very small and can be neg-

lected in practice.

Consulting Oort and Rasmusson's tables (B1a, B1b, B2a, B2b), we find that the total wind speed variance is actually a minimum at the ground and increases monotonically with height up to the tropopause. Equation (4.51) does not agree with this observed vertical variation. However, the variance at the ground agrees remarkably well with that predicted by (4.53). Part of the problem no doubt lies in the neglect of density variations with height in the baroclinic flux parameterization (see Green's (1970) comment in Section 2.1 about this). Diagnostic studies of tropospheric energy spectra give us a further clue that (4.53) may be appropriate near the ground. Burrows (1976) calculates the energy in different wavenumbers and comments on the vertical structure in mid-latitudes. He finds that above 700 mb (700-100 mb), most of the eddy kinetic energy is contained in scales $n = 2$ and $n = 4$. In the lower troposphere, the shorter baroclinic waves dominate. For example, at 850 mb, $n = 6$ (the baroclinically most unstable mode) contains more kinetic energy than all other scales. Thus, we consider there is some justification for accepting equation (4.53). The fact that U_S can be determined consistently from Stone's parameterization is aesthetically pleasing, too.

Let us now examine the agreement with data. Table 4.3 shows the observed surface wind speed variance averaged from 30-60° latitude, and that predicted by (4.53) using the mean meridional gradient A and Richardson number Ri from Tables 1.7 and 1.8, respectively.

Figure 4.10 shows these results graphically. The seasonal variation is represented fairly well. Moreover, an examination of Oort and Rasmusson's tables shows that U_S varies latitudinally in a manner consis-

Table 4.3: Surface wind speed variance, ($\frac{m}{s}$)²

	observed (30-60° avg)	Predicted
Annual	59.1	56.6
Winter	76.5	76.8
Spring	61.0	60.9
Summer	40.8	30.7
Fall	57.9	63.4

tent with (4.53), except near the equator, if we take A to be the local gradient. That is, U_S peaks in mid-latitudes where the temperature gradient is largest. However, we don't wish to stretch the use of this parameterization too far. We know it cannot be justified theoretically at low latitudes. Thus, for input into the surface flux calculation, we will take U_S to be independent of latitude and use the hemispherically averaged meridional gradient

$$U_S = 14.28 |A| \quad \text{m/s} \quad (4.54)$$

where the Richardson number factor has been neglected.

Experimental calculations with the flux balance equation (4.48) show that the water to air temperature deviation ($T_w - T_0$) becomes unrealistically large for small wind speeds U_S . We therefore place a lower limit of 5 m/s on the value of U_S calculated from (4.54). Table 4.3 indicates that for the smaller temperature gradient in summer, equation (4.54) is already underestimating the surface wind variance.

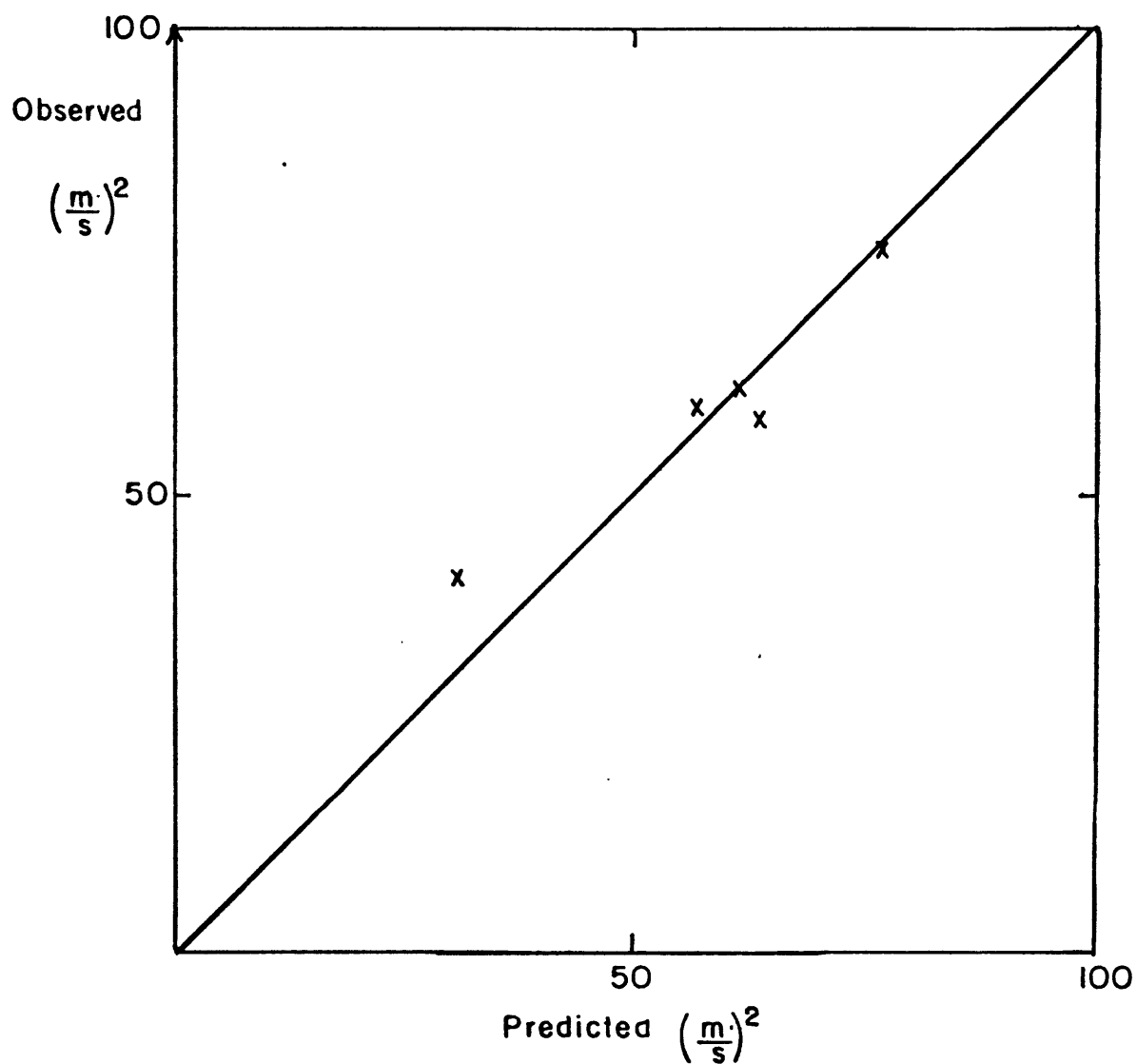


Figure 4.10: Comparison of observed surface wind speed variance (from Oort & Rasmusson, 1971. Tables B1, B2) with that predicted by Stone's theory of the unstable baroclinic eddies. (Crosses indicate values for the four seasons and the annual mean, as in Table 4.3).

Chapter 5: Radiative Feedbacks and the Effect of Clouds

5.1 Cloud observations and the single effective cloud model.

Our model does not predict cloud formation and so cloud heights and amounts must be specified in some fashion. The basic data we use is shown in Table 5.1 below. This was published by Manabe (1969) and is frequently used in GFDL general circulation model studies. The original source for this data, however, is London (1957).

We will take the three layers of cloud in Table 5.1 and 'reduce' them to a single effective cloud layer. The reason we do this is to allow for various cloud-height feedbacks (see Section 5.2), rather than just fixing the height. Since there is not complete agreement in the literature as to how cloud heights will vary with climate, it is clearly unwarranted sophistication to attempt to vary multiple layers of cloud, particularly in our model where only the mean features are resolved.

At each latitude the amount and height for the single effective cloud is determined so that the boundary fluxes (to the ground and to space) of both long and short wave radiation are approximately the same as for the three cloud case. We start by correcting for cloud overlap as seen from both boundaries; i.e. looking down from space and up from the surface. In calculating cloud amounts we assume random overlap between layers.

Table 5.1: Cloud data from Manabe (1969)

Latitude	High Cloud		Middle Cloud		Low Cloud		
	Amount (%)	Height (km)	Amount	Height	Amount	Cloud Top	Cloud Base
5	22.5	9.82	7.5	4.40	31.7	3.04	1.47
15	18.1	10.35	6.4	4.50	26.4	3.08	1.70
25	16.0	10.50	6.3	4.41	24.8	2.91	1.71
35	18.1	10.03	7.9	4.10	30.2	2.70	1.65
45	21.0	8.65	11.0	3.79	38.8	2.47	1.50
55	24.2	7.55	13.1	3.56	43.8	2.24	1.31
65	25.4	7.13	11.9	3.50	44.4	2.10	1.20
75	25.2	7.01	11.1	3.44	42.4	1.98	1.05
85	20.5	6.98	9.2	3.43	37.5	1.88	1.00

Table 5.2a: 'Reduced down' cloud data.

Latitude	5	15	25	35	45	55	65	75	85	Hemispheric Mean
Cloud amounts										
High	22.5	18.1	16.0	18.1	21.0	24.2	25.4	25.2	20.5	
Middle	5.8	5.3	5.3	6.4	8.7	9.9	8.9	8.3	7.3	
Low	22.7	20.2	19.5	22.8	27.3	28.9	29.2	28.2	27.1	
Total	51.0	43.6	40.8	47.3	57.0	63.0	63.5	61.7	54.9	51.0
Cloud Tops										
Height (km)	6.19	6.27	6.08	5.69	4.95	4.49	4.31	4.23	3.99	5.53
Temperature (°C)	-8.0	-8.8	-10.0	-13.4	-16.0	-19.2	-22.5	-25.6	(-28.5)	-13.5

Table 5.2b: 'Reduced up' cloud data

Latitude	5	15	25	35	45	55	65	75	85	Hemispheric Mean
Cloud amounts										
High	14.2	12.5	11.3	11.6	11.5	11.8	12.5	12.9	11.6	
Middle	5.1	4.7	4.7	5.5	6.7	7.4	6.6	6.4	5.8	
Low	31.7	26.4	24.8	30.2	38.8	43.8	44.4	42.4	37.5	
Total	51.0	43.6	40.8	47.3	57.0	63.0	63.5	61.7	54.9	51.0
Cloud bases										
Height (km)	4.09	4.48	4.46	3.99	3.21	2.74	2.61	2.54	2.52	3.75
Temperature (°C)	4.1	1.9	-0.3	-3.1	-5.5	-9.0	-12.9	-16.4	(-19.5)	-3.0

e.g. For cloud amounts n , reduced from the top down:

$$\begin{aligned} n'_{\text{high}} &= n_{\text{high}} \\ n'_{\text{middle}} &= n_{\text{middle}} \times (1 - n_{\text{high}}) \\ n'_{\text{low}} &= n_{\text{low}} \times (1 - n_{\text{high}}) (1 - n_{\text{middle}}) \\ &= n_{\text{low}} \times (1 - n_{\text{high}} - n'_{\text{middle}}) \end{aligned}$$

where the primed amounts are those corrected for overlap. There are similar expressions for effective cloud amounts as seen from the surface. Tables 5.2a and 5.2b show the resulting percentage cloud cover. The corresponding cloud heights and temperatures are also given. A mean cloud height (top or base) is determined by taking a linear combination of the individual heights (Table 5.1), weighting each value by the appropriate cloud amount at that level (reduced down or reduced up, respectively). The cloud temperatures are found by interpolation from the temperature-height tables of Oort & Rasmusson.

Weighting of the cloud heights in this manner will give the correct boundary fluxes of long-wave radiation provided these fluxes vary linearly with cloud height (see Appendix A6). The accuracy of this assumption can be tested very easily. We calculate the long-wave flux to space for clear skies, $F_{\text{clear}}^{(\infty)\uparrow}$, as given by equation (4.39) and the corresponding flux for cloudy skies, $F_{\text{cloudy}}^{(\infty)\uparrow}$, over a range of cloud-top heights z_c .

$$F_{\text{cloudy}}^{(\infty)\uparrow} = \sigma T_c^4 - 4\sigma \int_{T_d}^{T_c} (\bar{A}_1 + \tau_{12} \bar{A}_2) T'^3 dT' \quad (5.1)$$

where we have simply replaced the ground temperature $T_g = T_0$ in (4.39) by the cloud-top temperature $T_c = T_0 - \beta z_c$. Table 5.3 shows the results of these calculations at three latitudes. The surface temperature $T_0(\phi)$ was taken from Table 1.16 and the tropopause height determined for $\beta = 6.5$ and $h_0 = 0.77$. (Note: We have stated previously that the observed lapse rate is somewhat less than 6.5 °K/km. However, since most models in the literature assume this value, we will use it too in the following sections for the sake of easy comparison).

Table 5.3: Long-wave flux to space (in $\text{cal cm}^{-2} \text{min}^{-1}$) as a function of cloud-top height z_c .

Latitude	T_0 (°C)	H(km)	$F_{\text{clear}}^{(\infty)\uparrow}$	Regression equation for $F_{\text{cloud}}^{(\infty)\uparrow}$	Correlation coefficient
15	25.6	14.44	0.41498	$0.42691 - 0.01900 z_c$	-0.9988
45	8.8	11.84	0.35919	$0.36841 - 0.01932 z_c$	-0.9996
75	-11.9	9.42	0.29184	$0.29495 - 0.01817 z_c$	-1.0000

The flux to space from cloudy skies was evaluated at $z_c = 2, 3, 4, 5, 6, 7$ km and a linear regression equation calculated. The correlation coefficient between $F_{\text{cloudy}}^{(\infty)\uparrow}$ and z_c is very large, and the clear-sky flux provides a more useful test. For a perfect linear fit, $F_{\text{cloudy}}^{(\infty)\uparrow}$ evaluated from the regression equation for $z_c = 0$ should be exactly equal to $F_{\text{clear}}^{(\infty)\uparrow}$. Clearly, the assumption that the long-wave flux varies linearly with cloud height is a good one. The linearity is poorest at high temperatures (i.e. at low

latitudes or near the ground). For example, at 45° the maximum error in F_{cloudy} within the range $z_c = 2-7$ km is $0.0014 \text{ cal cm}^{-2} \text{ min}^{-1}$ at $z_c = 2$ km. However, extrapolating to $z_c = 0$, we find a much larger error of 0.0092 (or 2.6%). We could show similarly that the downward long-wave flux at the ground also varies linearly with cloud height.

For climate calculations it is important to know how cloud heights vary with the surface temperature. It seems sensible to take advantage of the only climate variations for which we have adequate data, namely the normal latitudinal and seasonal changes. Figures 5.1a and 5.1b illustrate the reduced cloud heights and temperatures we found in Tables 5.2a, b. Various cloud-height feedback models have been proposed; constant cloud height (e.g. Schneider, 1972) and constant cloud temperature (Cess, 1974) being the usual ones. It would seem from Figs. 5.1a, b that neither of these assumptions fits the observed latitudinal data particularly well. Of course, physically it is the infrared flux variation that we want to simulate, rather than the temperature per se (see Section 5.2). The seasonal cloud heights tabulated by Rodgers (1967) show a similar behavior, with greater heights (and higher temperatures) occurring in summer. The surface temperatures, which are shown in Fig. 5.1b for comparison, are highly correlated to the cloud temperatures. The calculated linear regression equations and the associated correlation coefficients are shown below.

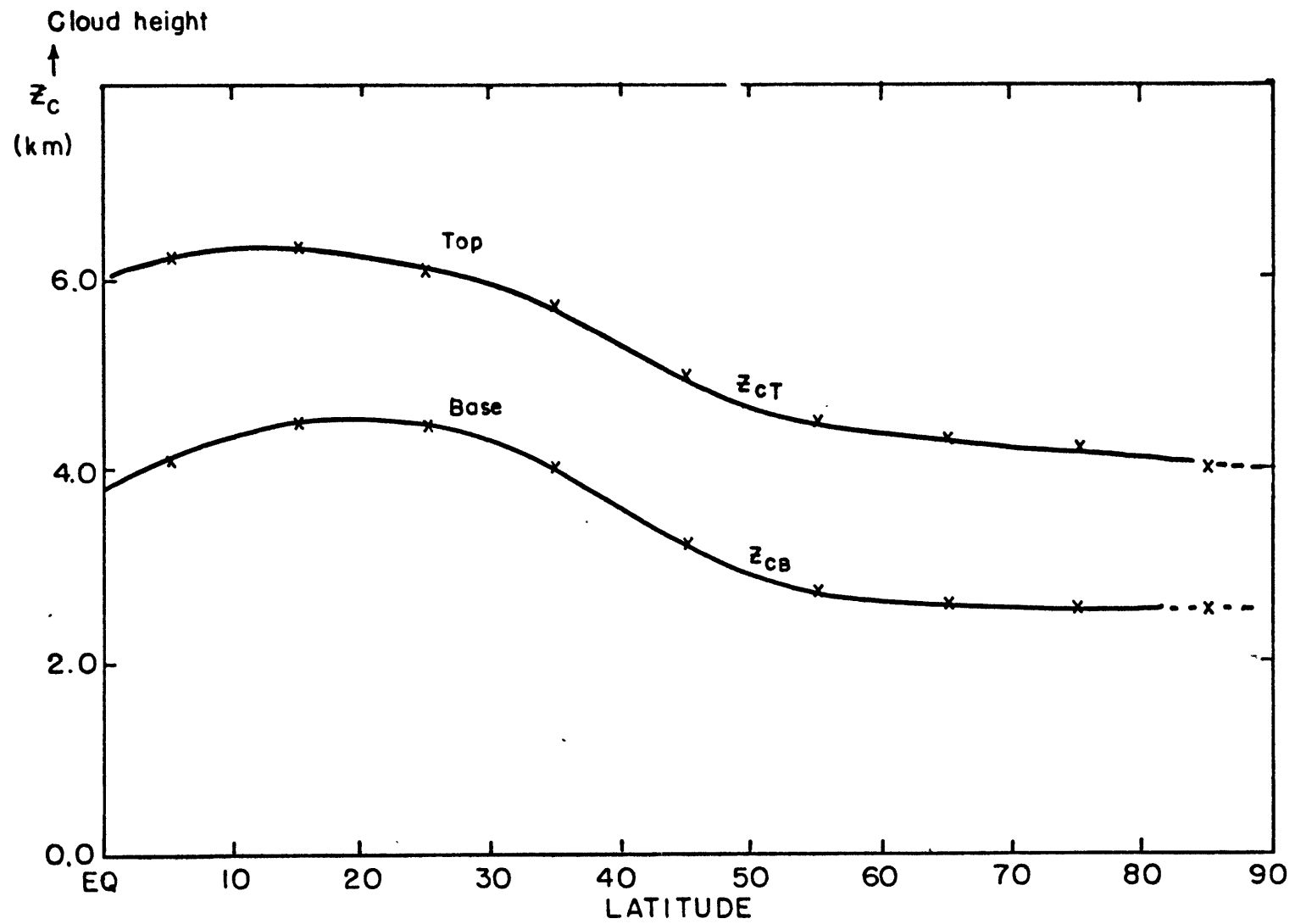


Figure 5.1a: Variation of cloud heights (base z_{cB} and top z_{cT}) with latitude.

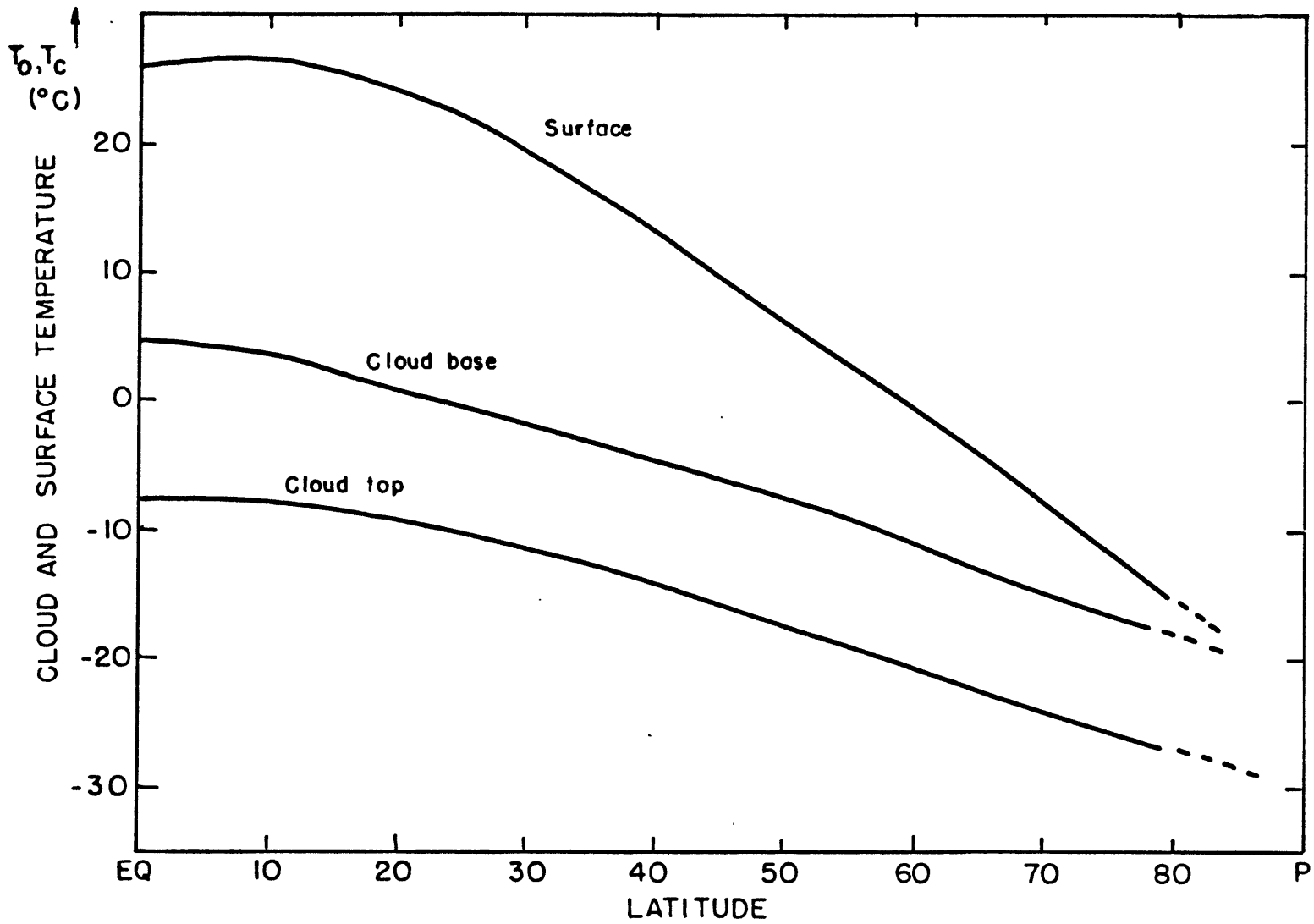


Figure 5.lb: Variation of cloud temperatures (base and top) and surface temperature with latitude.

Cloud-top temperature ($^{\circ}\text{C}$); $\hat{T}_{\text{CT}} = 0.444 T_0 - 20.2$; $R = 0.9984$

Cloud-base temperature ($^{\circ}\text{C}$); $\hat{T}_{\text{CB}} = 0.487 T_0 - 10.3$; $R = 0.9954$

(5.2)

Equations (5.2) describe the variation of cloud temperature with surface temperature assumed in our model. In the following section we will examine the radiative feedbacks associated with this and with three other possible cloud-height feedback models. The specific parameterization used for long-wave and short-wave heating in the presence of clouds is considered in Sections 5.3 and 5.4 respectively.

5.2 Cloud-height feedbacks

5.2.1. Data comparison

In this section we will consider four different cloud-height feedback models:

Model 1 : Fixed cloud height z_c

Model 2 : Fixed cloud temperature $T_c = T_0 - \beta z_c$

Model 3 : Fixed cloud fractional height $fz_c = \frac{z_c(\phi)}{H(\phi)}$

Model 4 : Fixed linear relation between cloud and surface

temperatures. $T_c = a_c T_0 + b_c$ (5.2a)

Initially, we consider these different models to have their parameters fixed with respect to latitude. We calculate the best fit for each model in turn to the satellite-observed Northern Hemisphere infrared emission to space as reported by Cess (1976).

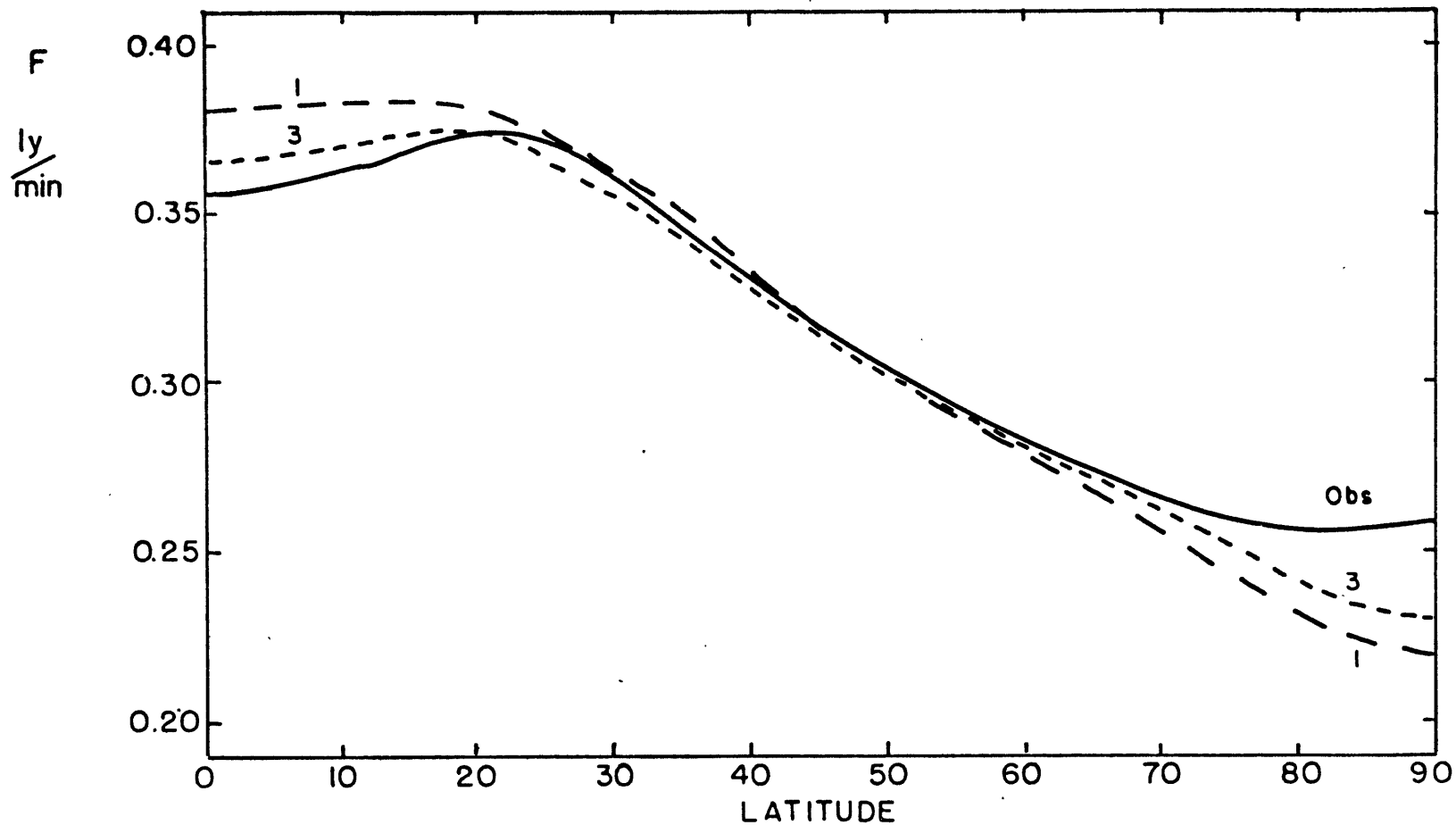


Figure 5.2a: Long-wave flux to space as observed by satellites (Cess, 1976) and as predicted by a least-square fit for Model '1': constant cloud height $z_c = 4.5$ km, and Model '3': constant fractional cloud height $f_{z_c} = \frac{z_c}{H} = 0.40$.

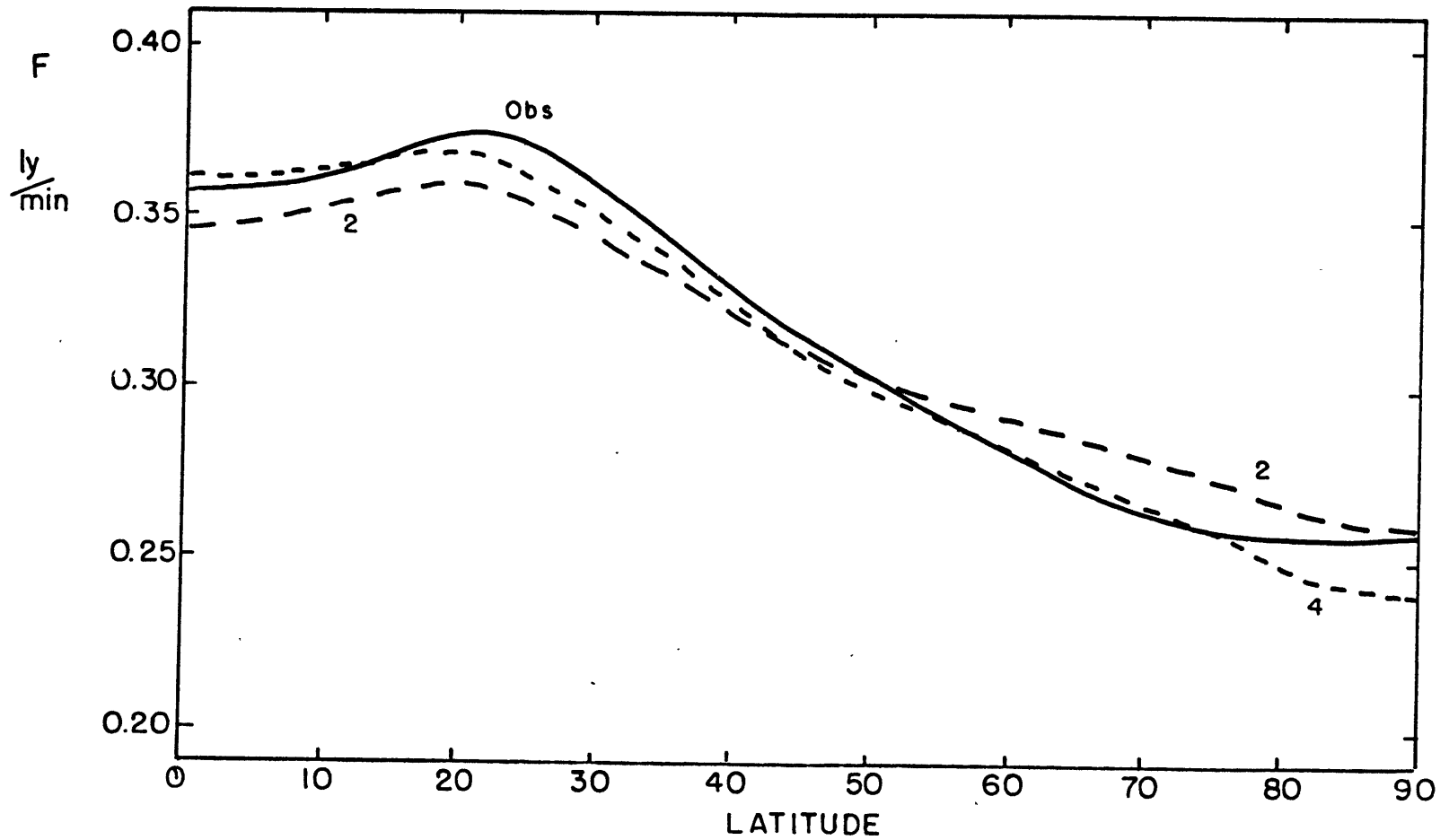


Figure 5.2b: As Fig. 5.2a, but comparing observation with Model '2' : constant cloud temperature $T_c = 250$ K, and Model '4' : linear relation between surface temperature and cloud temperature, $T_c = .442 T_0 + 125$ K.

Table 5.4 lists the best-fit parameter values for each model, along with the root mean square error calculated from the nine data points used. The results are illustrated graphically in Figures 5.2a,b. In computing the model results of Table 5.4 we have used $\beta = 6.5$, $h_0 = 0.77$ and the surface temperatures T_0 (from Table 1.1b) and cloud amounts n (from Table 5.2a) as indicated. In case 3, the model tropopause heights are also needed.

All the models fit the observed variation with latitude pretty well, although the constant cloud height model ('1') does poorest, predicting too strong a latitudinal gradient for $F(\infty)\uparrow$ (compare slopes in Fig. 5.2a). Conversely, the meridional gradient with fixed cloud temperature ('2') is too weak. The R.M.S. error in Table 5.4 is a simple arithmetic average over the nine latitude points shown. Weighting the error by $\cos\phi$ would improve slightly the fit of models 3 and 4 relative to 1 and 2. (As a cautionary note on the interpretation of Table 5.4, it should be recognized that model 4 has two constants, a_c fitted to the cloud temperature and b_c fitted independently to the thermal flux).

5.2.2. Model comparison

In this section we will compare the long-wave radiative feedbacks of the four different cloud-height models with the results published by Coakley (1977) for a vertical-column energy balance model. There are two reasons for doing this study. Calculating the sensitivity of

the thermal flux to the various parameters such as T_0 , β , h_0 serves as a useful check on the long-wave radiative parameterization we have developed. In addition, when we come to look at the results of the full model in Chapter 6, it will be helpful to know how the Model 4 cloud-height assumption ($T_c = a_c T_0 + b_c$) affects our solutions. Most of the results in the literature are for fixed cloud altitude (Model 1) or fixed cloud temperature (Model 2).

We compute $F_{\text{clear}}^{(\infty)\uparrow}$ and $F_{\text{cloudy}}^{(\infty)\uparrow}$ for each model with varying values of β , h_0 and the relevant cloud parameter z_c , T_c , fz_c , or b_c . (We keep a_c fixed at 0.442). The total thermal flux to space is then

$$\begin{aligned} F_T &= F_{\text{clear}}^{(\infty)\uparrow} - n (F_{\text{clear}}^{(\infty)\uparrow} - F_{\text{cloudy}}^{(\infty)\uparrow}) \\ &= (a_1 + b_1 T_0) - n (a_2 + b_2 T_0) \end{aligned} \quad (5.3)$$

We evaluate F_T at each latitude for the given parameter set, and determine the coefficients a_1 , b_1 , a_2 , b_2 by a least squares fit. The symbols used in (5.3) are taken from Budyko (1969), where T_0 is in $^{\circ}\text{C}$ and F_T in $\text{cal cm}^{-2} \text{min}^{-1}$. For later reference, Budyko's regression formula corresponding to (5.3) is

$$F_T (\text{Budyko}) = (0.319 + 0.0032 T_0) - n (0.068 + 0.0023 T_0) \quad (5.4)$$

It is apparent from satellite data that a_1 in (5.4) is too small (which is consistent with Budyko's assumption of a larger global albedo of 0.33). There seems to be considerable uncertainty in the other coefficients too (Cess 1976).

Following Coakley, we carry out a zero-dimensional energy balance

calculation. For $\beta = 6.5$, $h_0 = 0.77$, $n = 0.5$ and $T_0 = 15^\circ\text{C}$ we determine the value of the appropriate cloud parameter that gives net radiation balance.

$$\begin{aligned} \text{i.e. } F_T &= F_S, \text{ the net incoming short-wave flux} \\ &= [1 - (1-n)\alpha_s - n\alpha_c] \frac{S_0}{4} = 0.3395 \text{ ly min}^{-1} \quad (5.5) \end{aligned}$$

where we use Coakley's figures of surface albedo $\alpha_s = 0.1$, cloud albedo $\alpha_c = 0.5$ and solar constant $S_0 = 1.94 \text{ ly min}^{-1}$. We then find the partial derivatives of F_T evaluated for this basic state. The results are collected in Table 5.5. Coakley's values are shown for comparison. He uses a constant cloud temperature model developed by Cess (1974) in which water vapor is the only radiatively active gas, the lapse rate is constant throughout the atmosphere and there is a single cloud layer.

Comments on Table 5.5

(i) Model 2 shows the best agreement with data (final column) for $\frac{\partial F_T}{\partial T_0}$. This derivative is the most clearly defined observationally of those presented in the Table. Cess (1976) gives recent estimates for the Northern and Southern hemispheres determined from satellite data, and they agree quite well with Budyko's. These empirical formulae correlate the outgoing flux with surface temperature and cloud amount only, and explicitly omit other factors such as lapse rate and cloud temperature.

(ii) The partial derivatives $\frac{\partial F_T}{\partial h_0}$ and $\frac{\partial F_T}{\partial T_c}$ agree well with Coakley's. Our estimate of $\frac{\partial F_T}{\partial n}$ is intermediate between that of Coakley and that of Budyko. Note that $\frac{\partial F_T}{\partial n}$ is independent of the cloud-height

Table 5.5: Partial deviations of F_T for $T_0 = 15$ °C, $\beta = 6.5$ r/km, $h_0 = 0.77$, $n = 0.5$ and the equilibrium cloud parameter as indicated.

	Model 1	Model 2	Model 3	Model 4	Coakley	Budyko
Description	Const. z_C	Const. T_C	Const. fz_C	$T_C = .442 T_0 + b_C$	Const. T_C	
Equilibrium cloud parameter	$z_C = 4.834$ km	$T_C = -15.61$ °C	$fz_C = 0.3684$	$b_C = -22.67$ °C		
<u>Derivatives</u>						
$\frac{\partial F_T}{\partial T_0}$	0.00335	0.00205	0.00289	0.00255	0.0016 (0.0035)*	0.0021
$\frac{\partial F_T}{\partial n}$	-0.0809	-0.0809	-0.0809	-0.0809	-0.073	-0.103
$\frac{\partial F_T}{\partial \beta}$	-0.01217	-0.00478	-0.00726	-0.00486	-0.0035	
$\frac{\partial F_T}{\partial h_0}$	-0.0341	-0.0339	-0.0365	-0.0338	-0.031	
$\frac{\partial F_T}{\partial T_C}$	0.00151	0.00153	0.00150	0.00154	0.0015	
$\Delta T_0 _{\Delta n = .01}$	-0.338	-0.552	-0.392	-0.443	-0.76 (-0.42)*	

* Coakley's values for a constant cloud height model.

model, as is $\frac{\partial F_T}{\partial T_C}$. (The slight differences in the tabulated values of $\frac{\partial F_T}{\partial T_C}$ arise from errors in approximating F_T by the linear fit (5.3)). The derivative of the thermal flux with respect to lapse rate, $\frac{\partial F_T}{\partial \beta}$, appears to be somewhat stronger than Coakley's for our radiative flux parameterization. Other estimates of $\frac{\partial F_T}{\partial \beta}$ are not available for comparison.

(iii) The various cloud-height assumptions produce large differences in the sensitivity to surface temperature and lapse rate ($\frac{\partial F_T}{\partial T_0}$ and $\frac{\partial F_T}{\partial \beta}$). However, these two effects oppose each other and partially cancel. For example,

$$\frac{\partial F_T}{\partial T_0} + \frac{\partial F_T}{\partial \beta} \frac{\Delta \beta}{\Delta T_0} = \begin{cases} .00213 & \text{for Model 1} \\ .00157 & \text{" 2} \\ .00216 & \text{" 3} \\ .00207 & \text{" 4} \end{cases}$$

if we assume $\frac{\Delta \beta}{\Delta T_0} = 0.1$. ($\frac{\partial F_T}{\partial T_0}$ alone shows a larger variation between models).

(iv) For net radiative balance, we have

$$F_T(T_0, \beta, h_0, T_C, n) = F_S(n, S_0)$$

Thus, the change in surface temperature, ΔT_0 , to be expected for a given change in solar constant, ΔS_0 , can be found (see Coakley's equation 8) from

$$\left\{ \frac{\partial F_T}{\partial T_0} + \frac{\partial F_T}{\partial \beta} \frac{\Delta \beta}{\Delta T_0} + \frac{\partial F_T}{\partial h_0} \frac{\Delta h_0}{\Delta T_0} + \frac{\partial F_T}{\partial T_C} \frac{\Delta T_C}{\Delta T_0} + \left(\frac{\partial F_T}{\partial n} - \frac{\partial F_S}{\partial n} \right) \frac{\Delta n}{\Delta T_0} \right\} \Delta T_0 = \frac{\partial F_S}{\partial S_0} \Delta S_0 \quad (5.6)$$

The surface temperature change associated with a change in cloud

amount only (with all other parameters constant) is then

$$\frac{\Delta T_0}{\Delta n} = \frac{(-\frac{\partial F_T}{\partial n} + \frac{\partial F_S}{\partial n})}{\frac{\partial F_T}{\partial T_0}}$$

This change ΔT_0 for $\Delta n = 0.01$ is also given in Table 5.5.

In equation (5.6), there are four feedback factors ($\frac{\Delta \beta}{\Delta T_0}$, $\frac{\Delta h_0}{\Delta T_0}$, $\frac{\Delta T_c}{\Delta T_0}$, and $\frac{\Delta n}{\Delta T_0}$) that must be known before a complete calculation of the surface temperature change can be made. The cloud-top temperature feedback is known for each model.

$$\frac{\Delta T_c}{\Delta T_0} = \begin{cases} 1.0 & \text{in Model 1} \\ 0.0 & \text{" 2} \\ 0.691 & \text{" 3} \\ 0.442 & \text{" 4 (chosen to agree with data} \\ & \text{of Section 5.2.1.)} \end{cases}$$

(For Model 3, $\frac{\Delta T_c}{\Delta T_0} = 1 - \beta f z_c \frac{\Delta H}{\Delta T_0}$ and the linear regression equation between tropopause height H and surface temperature T_0 in °C is $H = 10.95 + 0.129 T_0$). The other feedback factors are very poorly known, but we follow Coakley and assume

$$\frac{\Delta \beta}{\Delta T_0} = 0.1 \quad (\text{appropriate if } \beta \text{ is determined by moist adiabatic processes}).$$

$$\frac{\Delta h_0}{\Delta T_0} = 0.01 \quad (\text{assumes absolute humidity varies as if the atmosphere was saturated}).$$

$$\frac{\Delta n}{\Delta T_0} = -0.01 \quad (\text{Schneider \& Washington, 1973})$$

It is interesting to compare the factor $\frac{\Delta \beta}{\Delta T_0}$ above with the values calculated in our full model. These are shown in Table 5.6a below, where the lapse rate β and hemispheric mean temperature \bar{T}_0 are taken from Tables 6.8 and 6.12.

Table 5.6a: Lapse rate feedback predicted by the full model (But see cautionary note in summary, Chapter 7).

	$\frac{\Delta\beta}{\Delta T_0}$
Increase solar constant S_0 : $0 \rightarrow + 2\frac{1}{2}\%$.059
Decrease solar constant S_0 : $0 \rightarrow - 2\frac{1}{2}\%$.059 (.067)*
Double CO_2 amount	.080
Halve O_3 amount	.101

(* : the value obtained for constant cloud temperature model, $T_{CT} = 260$ K).

Using the feedback factors above, we calculate the surface temperature response (Table 5.6b) for a 2% change in solar constant.

Table 5.6b: Surface temperature response (with and without cloud amount feedback) to a 2% change in solar constant.

Model	ΔT_0 for $\frac{\Delta n}{\Delta T_0} = -0.01$	ΔT_0 for $\frac{\Delta n}{\Delta T_0} = 0.$
1	3.13 K	2.06
2	67.	5.51
3	3.99	2.40
4	5.32	2.80
Coakley	-25.	7.22

Clearly, the constant cloud temperature models ('2' and Coakley) give unrealistic answers if we include the postulated cloud amount feedback. However, we cannot draw firm conclusions from Table 5.6b since even the sign of the feedback factors is uncertain, particularly in the case of $\frac{\Delta n}{\Delta T_0}$. All we can say is that the absence of cloud

temperature feedback ($\frac{\Delta T_C}{\Delta T_0} = 0$) in the fixed cloud-temperature models makes them much more sensitive to climate changes.

The right-hand column of Table 5.6 applies when cloud amount feedback is neglected. We can compare the deviation temperature here with those found by Wetherald & Manabe (1975) in the GFDL general circulation model (with fixed cloud heights and amounts).

For an S_0 increase of 2%; $\Delta T_0 = +3.04$ °C

For an S_0 decrease of 2%; $\Delta T_0 = -4.37$ °C

The response is larger than for Model 1 (Table 5.6) because ice-albedo feedback is included in Wetherald & Manabe's calculations.

In summary, there has been considerable confusion in the literature on the most appropriate cloud-height feedback assumption to use in climate calculations. For example, Cess (1974, 1975) advocated the use of constant cloud temperature models. Further comparisons with satellite data (Cess, 1976) indicated a fixed cloud height model more closely simulated the observed thermal flux changes. These comparisons, however, are highly model dependent. In view of these uncertainties, we have decided to use the compromise model 4 for our nominal calculations. Some results for model 2, which fits the observed $\frac{\partial F_T}{\partial T_0}$ better, will also be calculated.

5.3 Long-wave cooling calculations with clouds

5.3.1. Effect of clouds

When clouds are present in the model, the total long-wave flux is a weighted combination of the clear-sky fluxes (equations 4.20 or 4.22 as appropriate) and the analogous cloudy-sky fluxes. The cloudy upward flux $F(z)\uparrow$ above the clouds has T_g in (4.20) replaced by T_{cT} (the cloud-top temperature). For the cloudy downward flux $F(z)\downarrow$, equation (4.22) needs to be modified below the clouds.

$$F(z)\downarrow = \sigma T_{cB}^4 + 4\sigma \int_{T_{cB}}^{T(z)} \frac{1}{A} (u(z) - u(z')) T'^3 dT' \quad (5.8)$$

where T_{cB} is the cloud-base temperature.

The effect of clouds on the long-wave radiative heating profile is shown in Figure 5.3. For this example we have taken $\beta = 6.5$, $T_g = T_0 = 280$, $h_0 = 1.0$, $u_2(0) = 120$, $d = 1$. Furthermore, we have assumed the tropopause height $H = 12$ km (although this will not be completely consistent with the net heating profile). There is an infinitely thin layer of 'black' cloud at $z_c = 6$ km. Figure 5.3 gives the heating in °C/day for clear skies and for 100% cloud cover. We should note that the heating just below and just above the cloud layer at $z_c = 6$ sums to the same value we obtain for clear-sky heating. In general, the presence of the cloud has increased the heating below the cloud (i.e. weakened the long-wave cooling), and reduced the heating above. However, within about 2-3 km above the cloud layer, the two heating profiles (clear and cloudy) are very close to each other. This justifies our neglect of clouds in the

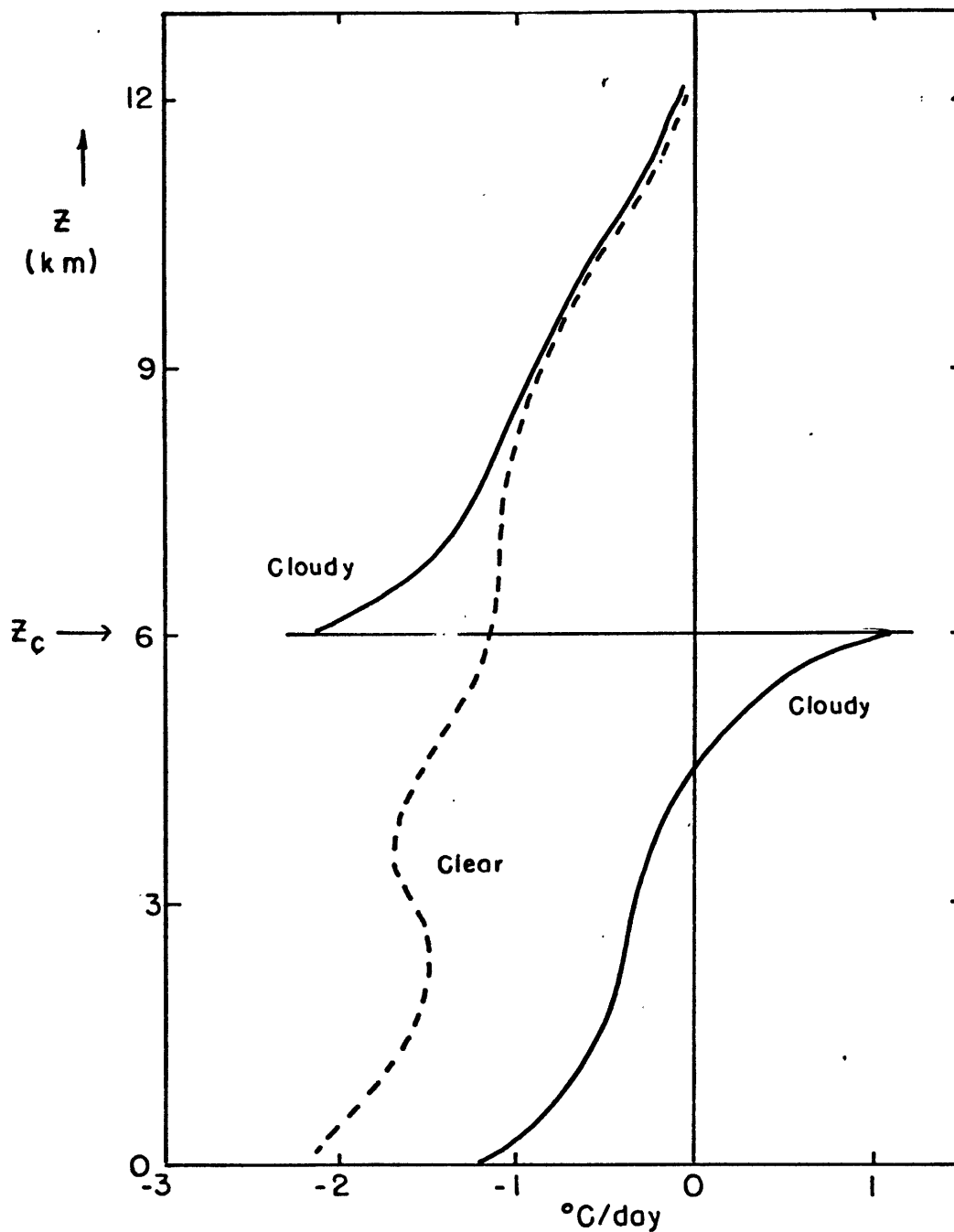


Figure 5.3: Profiles of long-wave heating (in °C/day) for clear and cloudy skies. ($\beta = 6.5$, $T_g = T_0 = 280$, $h_0 = 1$, $d = 1$, $H = 12$ and there is an infinitesimally thin cloud layer at $z_c = 6$ km).

calculation of tropopause height. Note also the two extrema in the clear-sky heating profile. This is a very common feature in thermal flux calculations (e.g. Dopplick, 1970) and arises simply because we are determining a temperature change in °C/day (i.e. dividing by the air density ρ). The derivative of the net upward flux, $\frac{\partial}{\partial z} (F(z)\uparrow - F(z)\downarrow)$, decreases monotonically with height.

5.3.2. Sensitivity of heating profile to vertical distribution of clouds

We saw in Figure 5.3 that clouds significantly altered the net tropospheric long-wave heating, particularly below the cloud layer. Considering that we have simplified the multi-level cloud structure of the real atmosphere to a single effective cloud layer, it is worthwhile investigating the sensitivity of the heating profile to this vertical distribution. Ohring & Adler (1978), in a climate sensitivity study, concluded that the response of the surface temperature to a change in total cloud amount may well depend on the relative changes of high, middle and low clouds. The radiation calculations of Cox (1969) showed the heating distribution was very sensitive to cloud position, and that maximum tropospheric mean cooling was obtained by having a cloud layer very close to the ground.

In our model we have calculated the effective cloud height so as to give the same boundary fluxes as the 3-layer case. The average mass-weighted heating will therefore be the same, although a

simple vertical average, $\frac{1}{H} \int_0^H \frac{Q_{\text{rad}}}{\rho c_p} dz$ (such as used in our forcing equations 2.33 and 2.38), will not be the same. More importantly, the vertical difference, $\frac{2}{H} \left[\int_{H/2}^H \frac{Q_{\text{rad}}}{\rho c_p} dz - \int_0^{H/2} \frac{Q_{\text{rad}}}{\rho c_p} dz \right]$, used in the B forcing equation (2.36) is substantially different. This will produce a systematic bias in the model. The heating in upper and lower layers is shown in Table 5.7 for the observed surface temperatures of Table 1.1b and the cloud amounts and heights of Tables 5.1, 5.2a and 5.2b. The model calculates the tropopause height H appropriate for $\beta = 6.0$, $h_0 = 0.8$. For comparison, the heating without clouds is also tabulated. The main thing to notice in this table is that the heating difference between upper and lower layers is larger for the single cloud model. This behavior is due primarily to increased long-wave cooling in the lower layer for the 1-cloud case. In low latitudes the cooling in the upper half of the troposphere is almost independent of the cloud distribution. This is not true in higher latitudes where the high cloud amount increases and its altitude decreases towards the mid-level $H/2$.

5.4 Short-wave heating calculations with clouds.

Tropospheric short-wave heating for partly-cloudy skies is calculated using the multiple-scattering model of Lacis & Hansen (1974). The following summary adopts the notation of that paper. The atmosphere is divided into 6 layers in the vertical to adequately resolve the cloud layer in the lower troposphere (See Figure 5.4). We will evaluate the upward and downward fluxes (U_ℓ and D_ℓ respectively)

Table 5.7: Heating in °C/day height-averaged over lower ($0 - \frac{H}{2}$) and upper ($\frac{H}{2} - H$) halves of the troposphere for single and multiple layer clouds. Other parameters as in text.

Latitude:	5	15	25	35	45	55	65	75	85
<u>No clouds</u>									
($0 - \frac{H}{2}$) avg.	-1.87	-1.85	-1.78	-1.65	-1.47	-1.34	-1.18	-1.03	-0.85
($\frac{H}{2} - H$) avg.	-1.03	-1.02	-0.97	-0.87	-0.74	-0.65	-0.56	-0.47	-0.36
<u>1 cloud layer</u>									
($0 - \frac{H}{2}$) avg.	-2.07	-2.01	-1.94	-1.87	-1.83	-1.80	-1.68	-1.54	-1.32
($\frac{H}{2} - H$) avg.	-1.05	-1.04	-0.99	-0.90	-0.77	-0.68	-0.58	-0.49	-0.38
<u>3 cloud layer</u>									
($0 - \frac{H}{2}$) avg.	-1.81	-1.84	-1.81	-1.73	-1.61	-1.50	-1.38	-1.27	-1.14
($\frac{H}{2} - H$) avg.	-1.17	-1.06	-0.96	-0.88	-0.88	-0.91	-0.82	-0.69	-0.48
Tropopause H (km)	16.04	15.82	15.21	14.35	13.27	12.48	11.50	10.64	9.70

entering each layer $\ell = 1$ to 6 and obtain the total absorption A_ℓ by summing over that region of the solar spectrum where water vapor absorption is significant. Lacis & Hansen develop a discrete probability distribution $p(k_n)$ for the absorptivity A_{wv} (previously defined as $B_1(y)$ in equation 4.28) as a function of y , the effective water vapor amount traversed by the solar beam.

$$A_{wv}(y) \approx 1 - \sum_{n=1}^N p(k_n) e^{-k_n y} \quad (5.9)$$

where the summation in (5.9) approximates the integral of fractional absorption $p(k) e^{-ky}$ over frequency k (in cm^{-1}). Table 5.8 gives the values for the probabilities $p(k_n)$ and coefficients k_n found by Lacis & Hansen from a least square fit to absorptivity measurements.

Table 5.8: Discrete probability distribution of water vapor absorption coefficients for $N = 8$. (Lacis & Hansen, Table 1).

n	k_n, cm^{-1}	$p(k_n)$
1	4×10^{-5}	0.6470
2	0.002	0.0698
3	0.035	0.1443
4	0.377	0.0584
5	1.95	0.0335
6	9.40	0.0225
7	44.6	0.0158
8	190.	<u>0.0087</u>
		1.0000

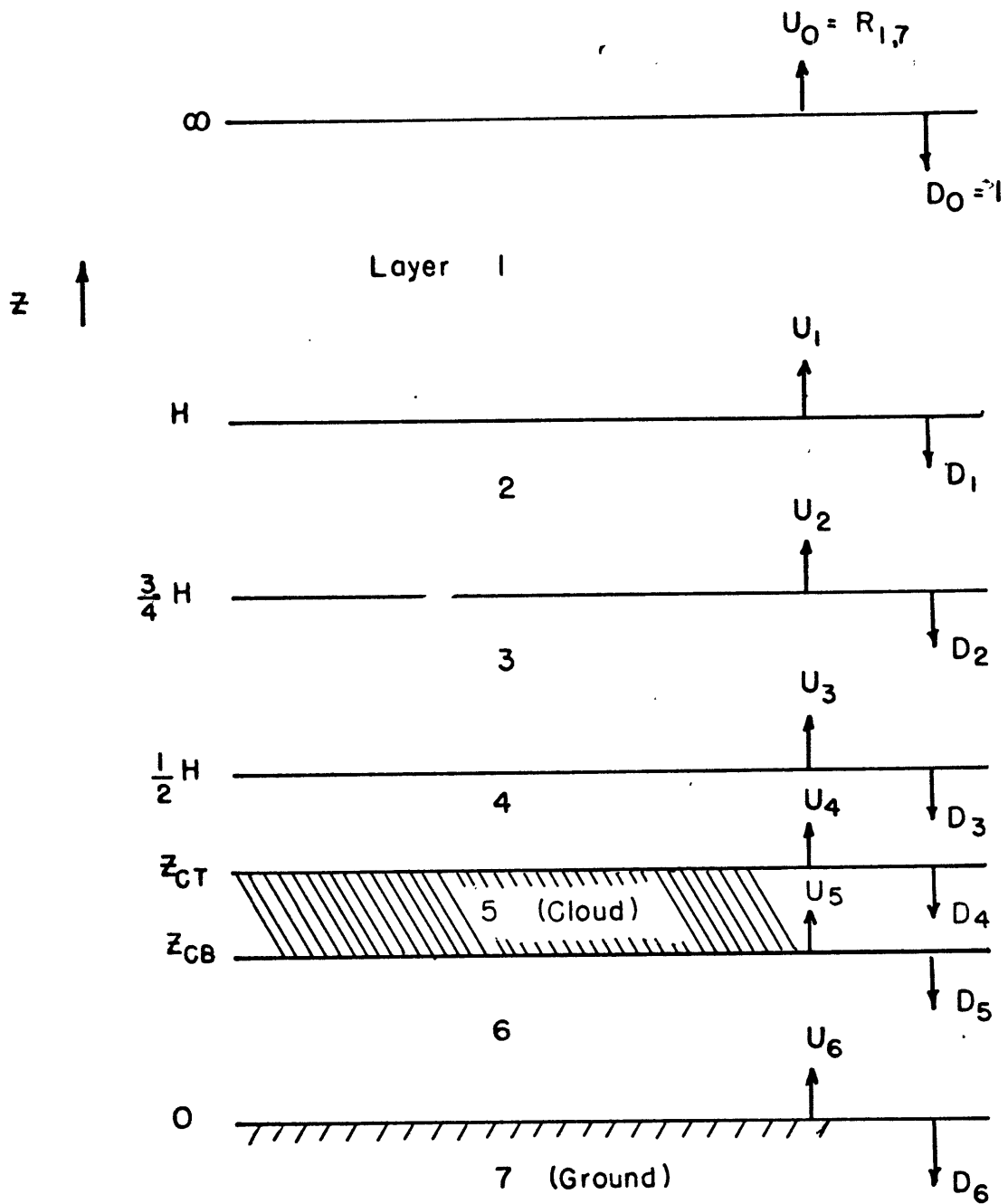


Figure 5.4: Schematic of cloud model used to calculate short-wave heating. U and D are the upward and downward fluxes in each layer.

The individual reflection and transmission functions (R_ℓ and T_ℓ) for the layers are calculated for each value of n in Table 5.8. Above the cloud: For layers $\ell = 1, 4$ $R_\ell = 0$ and $T_\ell = e^{-Mk_n w_\ell}$ where M is the magnification factor given in section 4.2.4. and w_ℓ is the effective water vapor amount in a vertical path through the layer as defined by equation (4.9).

Below the cloud: $R_6 = 0$ $R_7 = R_g$, the ground albedo

$$T_6 = e^{-\frac{5}{3} k_n w_6}, \quad \text{assuming a magnification of } \frac{5}{3}$$

$$T_7 = 0 \quad \text{for scattered radiation.}$$

For the cloud layer itself we use the two-stream equations of Sagan & Pollack (1967).

$$R_5 = \frac{\sqrt{3} \tau^c (1-g) \left(\frac{1-e^{-2t}}{2t}\right)}{\left[(1+e^{-2t}) + \sqrt{3} \tau^c (1-g+2x) \left(\frac{1-e^{-2t}}{2t}\right) \right]}$$

$$T_5 = \frac{2e^{-t}}{\left[(1+e^{-2t}) + \sqrt{3} \tau^c (1-g+2x) \left(\frac{1-e^{-2t}}{2t}\right) \right]} \quad (5.10)$$

$$t = \sqrt{3} \tau^c [x(1-g+x)]^{1/2}$$

$$x = k_n \frac{w_5}{\tau^c}$$

where $g = 0.85$ is an asymmetry factor for clouds, τ^c is the optical thickness due to cloud particles in the 5th layer, and

$$w_5 = \frac{1}{g} \frac{P_{cB}}{P_{cT}} \int m_s \frac{p}{p_0} \left(\frac{T_3}{T} \right)^{1/2} dp \quad (5.11)$$

after (4.9) where we use the saturation mixing ratio m_s . (The total optical depth of the cloud layer is $\tau = \tau^C + k_n w_5$).

The reflection and transmission functions for illumination from below, R_ℓ^* and T_ℓ^* , are the same as for illumination from above. The reflection and transmission for a composite layer formed by adding two layers are

$$R_{ab} = R_a + \frac{R_b T_a T_a^*}{(1 - R_a^* R_b)} \quad ; \quad R_{ab}^* = R_b^* + \frac{R_a^* T_b^* T_b}{(1 - R_a^* R_b)} \quad (5.12)$$

$$T_{ab} = \frac{T_a T_b}{(1 - R_a^* R_b)} \quad ; \quad T_{ab}^* = \frac{T_b^* T_a^*}{(1 - R_a^* R_b)}$$

where the subscripts 'a' and 'b' refer to the top and bottom layers respectively, and the denominator accounts for multiple reflections between the two layers.

To obtain the short-wave absorption in each layer we now carry out the following steps for each n.

Step 1: The layers are added, going down, to obtain $R_{1,\ell}$ and $T_{1,\ell}$ for $\ell = 2, 7$ and $R_{1,\ell}^*$ and $T_{1,\ell}^*$ for $\ell = 2, 6$. [The notation $R_{1,\ell}$ means the composite reflection function for layers 1 through ℓ and is found by adding layers 1 plus 2, then the composite 1, 2 plus 3, etc.].

Step 2: The layers are added one at a time, going up, to obtain $R_{7-\ell,7}$, $\ell = 1, 5$ starting with the ground layer $R_7 = R_g$ and $T_7 = 0$.

Step 3: The upward and downward fluxes at the boundary between two layers are then found by the procedure of Lacis & Hansen to be

$$\begin{aligned}
 D_6 &= T_6 D_5 & U_6 &= R_G T_6 D_5 \\
 D_5 & & U_5 &= R_G T_6^2 D_5 \\
 D_4 &= T_1 T_2 T_3 T_4 & U_4 &= T_1 T_2 T_3 T_4 R_{5,7} \\
 D_3 &= T_1 T_2 T_3 & U_3 &= T_4 U_4 \\
 D_2 &= T_1 T_2 & U_2 &= T_3 T_4 U_4 \\
 D_1 &= T_1 & U_1 &= T_2 T_3 T_4 U_4
 \end{aligned}$$

where $D_5 = \frac{T_1 T_2 T_3 T_4 T_5}{(1 - R_G R_5 T_6^2)}$ and $R_{5,7} = R_5 + \frac{R_G (T_5 T_6)^2}{(1 - R_G R_5 T_6^2)}$

Step 4: Finally, the absorption in each layer is found from the net flux entering that layer

$$\begin{aligned}
 A_6 &= p [U_6 - D_6 - U_5 + D_5] = p (1 - T_6) (D_5 + U_6) \\
 A_5 &= p [U_5 - D_5 - U_4 + D_4] \\
 A_4 &= p [U_4 - D_4 - U_3 + D_3] = p (1 - T_4) (D_3 + U_4) \\
 A_3 &= p [U_3 - D_3 - U_2 + D_2] = p (1 - T_3) (D_2 + U_3) \\
 A_2 &= p [U_2 - D_2 - U_1 + D_1] = p (1 - T_2) (D_1 + U_2) \\
 A_1 &= p [U_1 - D_1 - R_{1,7} + 1] = p (1 - T_1) (1 + U_1)
 \end{aligned}$$

where there is an implied summation over $n = 2,8$ (the absorption for $n = 1$ being negligible).

Some useful quantities that come out of this model are listed below.

- i) Downward SW flux as the surface = $\sum_n p (D_6 - U_6)$
- ii) Total SW albedo (atmos. + cloud + ground) = $\sum_n p R_{1,7}$ (5.13)

$$\text{iii) SW albedo of cloud alone} = \sum_n p R_g$$

Table 5.9 shows an example of the model results. We assume $T_0 = 22.3^\circ\text{C}$, $\beta = 6.5$, $h_0 = 0.77$, $H = 14.06$ and a cloud layer extending from $z = 4.5 - 6.1$ km. The table shows the heating in each layer (corresponding to Figure 5.4) along with the three quantities defined in (5.13) which we denote by A_g , α and α_c respectively. The calculation is done for several values of the cloud optical depth τ^c (together with $\tau^c = 0$ to simulate clear-sky short-wave heating). The ground albedo $R_g = 0.07$, and we use a zenith angle appropriate to 25° latitude.

The change in the heating profile when clouds are added has the same overall character as shown by the more detailed calculations of Lacis & Hansen (see their Figure 15 for 45 layers). That is, the heating is increased above the clouds and reduced below them. We find in Table 5.9 that the heating averaged over the 'cloud' itself (layer 5) does not change greatly with optical depth.

This two-stream approximation for the cloud heating also allows us to calculate the cloud albedo α_c as a function of optical depth. For subsequent computations with the full model, we choose

$$\tau^c = 9.0 \quad (5.14)$$

which corresponds closely to $\alpha_c = 0.5$. (For a fixed optical depth the cloud albedo does change slowly with latitude as the zenith angle varies, although it remains close to 0.5. Ohring & Adler (1978) calculated the optical depth of a single effective cloud

Table 5.9: Short-wave heating ($^{\circ}\text{C}/\text{day}$) for each layer of Figure 5.4 for a range of cloud optical depths τ^{C} . Also tabulated is the net downward flux at the surface A_{g} , the cloud albedo α_{c} and the total albedo α at the top of the atmosphere.

Optical Depth τ^{C}	Heating by layer						A_{g}	α	α_{c}
	1	2	3	4	5	6			
0	0.009	0.133	0.604	0.715	0.758	0.804	0.768	0.056	0.
8	0.009	0.135	0.633	0.837	0.795	0.273	0.402	0.485	0.480
10	0.009	0.135	0.637	0.853	0.783	0.240	0.358	0.533	0.533
12	0.009	0.135	0.640	0.867	0.772	0.213	0.323	0.572	0.575

layer by weighting the amounts of low, middle and high clouds. They concluded that τ^C 'showed no significant variation ... with latitude'. Of course, this may not be true in a climate change with very different cloud temperatures).

The quantities of interest in the full model are the average heating in the upper and lower halves of the troposphere, and the boundary fluxes which we obtain from A_g and α . For the internal heating under cloudy skies we use exactly the model above and add in afterwards the heating due to ozone (derived from equation 4.29). Ozone absorption is included in the boundary summations (5.13) (i) and (ii) for $n = 1$ where the water vapor absorption is negligible. i.e. $p(k_1) = 0.647$ is replaced by

$0.647 - B_3 (M u_3(0))$ in (5.13) (i) for the flux at the ground, and $0.647 - B_3 ((M + 1.9) u_3(0))$ in (5.13)(ii) for the planetary albedo, where the ozone absorption B_3 is given by (4.29).

For calculations with clear skies we use the same procedure with $\tau^C = 0$ (and the regular water vapor mixing ratio in layer 5), but make allowance for Rayleigh scattering in the spectral region of negligible water vapor absorption ($n = 1$). This is done by replacing R_5 (the reflection function for the 5th layer which will be zero for no cloud present) by $\bar{R}_r (\mu_0)$, the atmospheric albedo due to Rayleigh scattering as given by Lacis & Hansen (1974).

$$\bar{R}_r (\mu_0) = \frac{0.28}{(1 + 6.43 \mu_0)} \quad (5.15)$$

where $\mu_0 = \cos \bar{\zeta}$, and $\bar{R}_r^* = 0.0685$ is the spherical albedo of

the Rayleigh atmosphere for illumination from below (used for determining composite layer reflection and transmission functions in 5.12). Similarly, the transmission for the same layer is $T_5 = 1 - \bar{R}_R(\mu_0)$. Of course, the Rayleigh scattering does not really occur wholly in layer 5 but it is concentrated mainly in the lower part of the troposphere where the air molecule density is greatest.

Finally, the short-wave cloud model requires the ground albedos to be specified. The values we take are

$$R_g = \begin{cases} 0.07 & \text{for water} \\ 0.35 & \text{for sea ice} \end{cases} \quad (5.16)$$

The amount of sea ice present is decided by the surface temperature as described in section 4.5. These albedos determine the fraction of solar radiation reaching the ground that is used in the surface energy balance equation (4.47). The value of 0.35 is an appropriate value for seasonal sea ice according to Budyko (1956). Actually, it is rather small for high latitudes in the annual mean. The data of Schultz & Gates (1972) indicate a value closer to 0.55.

Chapter 6: Results of the Full Model

6.1 Method of Solution

In the full model we again solve the coupled hemispheric forcing equations (2.33), (2.38), and (2.36) for the mean temperature $\langle T \rangle$ and the mean gradients A and B. We arrive at a system of equations similar to (3.16), although the radiative equilibrium terms $\langle T \rangle_r$, A_r , and B_r are no longer calculated explicitly since the full form for the heating function $H(\phi, z)$ is used (Equation 2.2, instead of the Newtonian cooling 2.34).

If we define $F_{\langle T \rangle}$, F_A , and F_B as the right-hand sides of the forcing functions (2.33), (2.38), and (2.36), respectively, then we have

$$\begin{aligned}
 F_{\langle T \rangle} &= \langle H(\phi, z) \rangle = 0 \\
 F_A &= k_A A B \frac{\sqrt{1+Ri}}{Ri} \\
 F_B &= -k_B \frac{B}{Ri\sqrt{1+Ri}} + k_S A B \frac{\sqrt{1+Ri}}{Ri} \\
 Ri &= k_R \frac{B}{A^2}
 \end{aligned} \tag{6.1}$$

where the coefficients k_A , k_B and k_S are modified slightly from Section 3.3.1 to allow for the more complicated tropopause structure. The radiative relaxation time constant τ does not appear explicitly. For $F_{\langle T \rangle}$, F_A and F_B in units of °C/day,

$$k_A = .010618(1+\alpha) \frac{H(\pi/4)}{H} \langle T \rangle L_y$$

$$k_B = 5.4845 \times 10^{-3} \frac{\langle T \rangle^2}{H} L_z$$

$$k_S = -5.0984 \times 10^{-3} b_2 \frac{\langle T \rangle}{H} L_s$$

where α is the weighting factor in the A equation (2.38), b_2 comes from $\frac{dH}{d\phi} = 2 b_2 \sin \phi \cos \phi$, and the integrated Leovy factors are unity when latent heat flux is neglected.

$$\mathcal{L}_y = 1 + \frac{1}{H(\pi/4)} \int_0^{H(\pi/4)} \Lambda(\frac{\pi}{4}, z) \mathcal{L}(\frac{\pi}{4}, z) dz$$

$$\mathcal{L}_z = 1 + 3 \int_0^{\pi/2} \mathcal{L}(\phi, \frac{H}{2}) \sin \phi \cos^2 \phi d\phi$$

$$\mathcal{L}_s = 1 + \frac{15}{2} \int_0^{\pi/2} \mathcal{L}(\phi, \frac{H}{2}) \sin^2 \phi \cos^3 \phi d\phi$$

An initial guess for the temperature structure ($\langle T \rangle$, A, B) allows us to calculate the convective and radiative forcing terms $F_{\langle T \rangle}$, F_A and F_B . Then Equations (6.1) can be inverted directly to obtain the mean gradients and the Richardson number.

$$\left. \begin{aligned} A &= - \left| \frac{k_R}{k_A k_B} F_A (F_B - \frac{k_S}{k_A} F_A) \right|^{\frac{1}{5}} \\ Ri &= \left(\frac{k_R F_A}{k_A A^3} \right)^2 - 1 \\ B &= \frac{A^2 Ri}{k_R} \end{aligned} \right\} (6.2)$$

These new gradients permit a second estimate of the forcing F_A , F_B , and so on. However, this iteration procedure using (6.2) is very unstable, and convergence to a solution is difficult and unreliable. The method we finally settled on is outlined below:

- Step 1:
- a) Assume a value for the mean hemispheric temperature $\langle T \rangle$.
 - b) Take an initial guess for meridional gradient A and lapse rate β .
 - c) Calculate the temperature coefficients C_0, C_2 using 1a, b and an initial guess for the tropopause height coefficients b_0, b_2 .
- Step 2: Calculate the total radiative and convective heating.
- a) Call subroutine IRFLUX - computes the downward long-wave flux at the surface and the upward LW flux to space (although this last quantity is not used directly in the model. See discussion of Equation (1.5) in Section 1.2).
 - b) Call subroutine HRAD - computes the net radiative heating (LW and SW) in the upper and lower halves of the troposphere at latitudes $5^\circ, 25^\circ, 45^\circ, 65^\circ,$ and 85° . In this step we also obtain the planetary albedo and the fractional absorption of short-wave radiation at the ground as described in Section 5.4.
 - c) Call subroutine SFCFLX - computes the surface flux balance using the output of steps 2a, b. The new ground temperature T_g that we obtain is used to correct the heating estimates the next time through the loop. The sensible and latent heat fluxes from the surface are used to calculate the small-scale convective heating below.
 - d) Call subroutine HEATING - computes the convective heating part of the forcing equations (2.33), (2.36) and (2.38).
- Step 3: Knowing the surface air temperature $T_0(\phi)$ from 1c and the ground temperature and albedo from 2c, we recalculate the tropopause height $H(\phi)$ at two latitudes, 25° and 75° . We can then determine the coefficients b_0, b_2 in Equation (2.20) to get the latitude structure of H . These coefficients are used in Step 1b to evaluate the surface temperature on the next iteration.

Step 4: The radiative and convection terms of (6.1) are now known and we can evaluate how well they balance the dynamical terms. The system (6.2) is not used for reasons explained previously. Instead, let us define

$$x = A^2, \quad y = k_R B$$

$$\text{and } r = \frac{k_R}{k_B} \left(F_B - \frac{k_S}{k_A} F_A \right), \quad s = \frac{k_R F_A}{k_A}$$

Then Equation (6.2) can be written as

$$\left. \begin{aligned} f(x, y) &= x - (rs)^{\frac{2}{5}} = 0 \\ g(x, y) &= y - \left(\frac{s}{x}\right)^2 + x = 0 \end{aligned} \right\} \quad (6.3)$$

where r and s are very complicated functions of x and y , that we cannot write down explicitly. When the system reaches the equilibrium gradients A and B (appropriate to the assumed $\langle T \rangle$), then $f = g = 0$ in (6.3). However, for some other choice of A and B in Step 1b, the functions f and g are different from zero.

Step 5: We iterate the system from Step 1c through Step 4 with our initial guess for A and β until the functions f and g in (6.3) converge. (In practice, it requires about 6 loops before the fields of $T_g(\phi)$, $H(\phi)$ and radiative and convective heating reach constant values). New values of A and β are taken (still for the same $\langle T \rangle$) and the iteration is repeated from Step 1b. When we have three sets of results (f, g corresponding to A, β guesses), we apply the two-dimensional false-position method (see, for example, Acton (1970), Chapter 14) to solve for those gradients that satisfy $f = g = 0$.

Step 6: We now have equilibrium gradients for the assumed mean hemispheric temperature $\langle T \rangle$. If we evaluate $F_{\langle T \rangle}$ at this point it will not, in general, be zero. Referring back to Equation (2.1), we can identify $F_{\langle T \rangle}$ as $\frac{d\langle \theta \rangle}{dt}$. Therefore, the mean temperature of the model will change until equilibrium is reached.

There is no need to carry out a time-stepping procedure explicitly. Evaluation of $F_{\langle T \rangle}$ for a different mean temperature permits us to extrapolate to the desired solution.

When the tropopause heating imbalance ($\frac{\partial \langle \theta \rangle}{\partial t}$) is typically 0.0002 °C/day or less, we consider the model to have reached equilibrium. This would imply a negligible mean temperature change over a time-step of 20 days, for example, if we were ever to extend the model to do seasonal calculations. The error is also somewhat smaller than the mean tropospheric cooling due to dynamical exchange of energy with the stratosphere, which we have ignored. In Section 4.3.1 we mentioned the energy fluxes into the stratosphere that were obtained by Dopplick (1971) and Miller (1970). They correspond to a cooling rate (averaged over the entire mass of the troposphere) of about 0.001 °C/day.

6.1.1 Some features of the equilibrium solution

We discuss below some of the features of the equilibrium solution. They are expanded upon later when we examine the sensitivity of our results to the assumed parameter values and to changing climatic variables. At this stage, it will be helpful to the reader to summarize the prescribed parameters of the model.

- i) absorber amounts - surface relative humidity $h_0 = 0.8$
 - carbon dioxide column amount $u_2(0) = 120 \text{ cm}$
 - ozone distribution as in Section 4.2.1c.
- ii) transition depth $d = 1.0 \text{ km}$ in the calculation of tropopause height $H(\phi)$.

- iii) solar insolation, zenith angle, and cloud amount as specified previously in Tables 3.1, 4.2, and 5.2, respectively.
- iv) cloud temperatures related to the surface temperature by Equation (5.2), with the added limitation that the cloud base cannot approach closer to the ground than 1 km. In practice, this condition has to be applied in high latitudes. Equation (5.2) breaks down here when used in the model where the lapse rate is independent of latitude. The limit on z_{CB} has just come into effect at 65° in the nominal model, and moves equatorward to 35° for a 15% decrease in the solar constant. Thus, the model eventually breaks down and reverts to the constant cloud-height case. For this reason, it may be unwise to extend the model results too far from present conditions, although the variation of the ice latitude ϕ_C in Figure 6.2 is reasonably constant as S_0 decreases. (This difficulty at high latitudes is just as bad for the constant cloud temperature assumption). It is not clear what should be done when the cloud approaches the ground. Another possible solution is simply to let it disappear.
- v) cloud optical depth for short-wave radiation is constant with latitude at a value of $\tau^c = 9.0$.
- vi) convective parameters b and c , which describe how the sensible and latent heat fluxes from the surface are distributed vertically by small-scale convection. $b = \frac{z_c(\phi)}{H(\phi)}$, where z_c is the average height of cloud top and cloud base at each latitude as given in Table 5.2, and $c = 0.23$.
- vii) surface short-wave albedos: $\alpha_w = 0.07$
 $\alpha_i = 0.35$
- viii) In addition, there are the parameterizations we have used for the dynamic transports, and the simplified meridional and vertical structure of the temperature field.

Unless otherwise noted, all model experiments have the parameter values listed above. In the following sections we study in detail how these

particular choices bias our results.

The mean temperature structure is described primarily by $\langle T \rangle$, A and β . In the nominal model, we find

$$\begin{aligned}\langle T \rangle &= 242.08 \text{ }^\circ\text{K} \\ A &= -0.4383 \text{ }^\circ\text{K}/100 \text{ km} \\ \beta &= 5.881 \text{ }^\circ\text{K}/\text{km} \\ B &= 5.176 \text{ }^\circ\text{K}/\text{km}\end{aligned}$$

The stability is considerably greater than in the grey radiation model of Chapter 3. The horizontal temperature gradient is also more realistic, although now it is slightly low. (For comparison with the data of Table 1.7, the gradient at 45° latitude in the model is about 50% greater than the hemisphere mean A). We obtain a mean Richardson number $Ri = 70.5$, which lies in the observed mid-latitude seasonal range of Table 1.8. Additional results are shown in Table 6.1. The final column lists the hemispheric means of the quantities given. Figure 4.9 in an earlier chapter illustrated the latitude variation of the surface flux components.

The global albedo $\overline{\alpha_p}$ predicted by the model (0.31) is close to observed values (Vonder Haar and Suomi, 1971) in spite of the small value we used for ice albedo. This is because $\overline{\alpha_p}$ is more strongly controlled by the cloud amount (0.51) and cloud albedo (0.50) than by high latitude surface albedos.

A general criticism we can make of the model is that the ground temperature and surface air temperature are too low. This is due mainly to the cloud-top temperatures (Equation 5.2) that we used. Changing the constant b_c (in Equation 5.2a) so the cloud temperatures are colder, will

Table 6.1. Latitude variation of some of the model fields. The LW and SW heating (in °C/day) is the actual heating multiplied by $(p_0/p)^K$ and averaged vertically.

	5	15	25	35	45	55	65	75	85	hemi- spheric mean
T_0 (°C)	23.7	21.1	16.3	9.8	2.4	-4.9	-11.4	-16.2	-18.8	9.6
T_g (°C)	25.4	23.3	19.1	13.1	5.9	-2.1	-9.3	-15.8	-18.8	12.1
H (km)	15.74	15.38	14.72	13.82	12.80	11.78	10.89	10.22	9.87	13.79
$b(\phi) = z_c/H$.327	.350	.358	.350	.319	.307	.318	.332	.331	.336
Planetary albedo α_p	.288	.259	.249	.276	.316	.379	.421	.436	.440	.307
Cloud albedo α_c	.499		.501		.506		.512		.517	.504
mean tropo- spheric heating										
LW	-1.975		-1.723		-1.438		-1.246		-1.106	-1.628
SW	0.612		0.518		0.347		0.207		0.140	0.443

increase the surface temperatures of the model. We recall that in Chapter 5 we calculated the mean observed cloud-top temperature to be about 260 °K (Table 5.2a) using the cloud-amount data of London (1957). A least-squares fit to satellite-observed fluxes, however, led to a mean cloud-top temperature of 250°K (Table 5.4, where $T_c = 250^\circ\text{K}$ is the best fit for the 5° resolution). Presumably, this difference occurs because the independently measured cloud amounts and thermal emission are not consistent with each other (there are almost as many estimates of cloud amount as there are sources of reference).

The surface temperatures could therefore be 'improved' by suitable tuning of the model. We choose not to take this approach. Many of the highly parameterized climate models of the Sellers' (1969) type are finely tuned to the present climatic conditions, and their application to very different conditions is often doubtful. In this model we specify a limited number of internal parameters, and hope the results are not too unrealistic for 'reasonable' choices. (In the following section, we look at the variation with alternate selections). In fact, it is not wise to think of our model as a global climate model at all, in view of the important low-latitude processes we have neglected. Its results should be applied to middle and high latitudes only. Even then, it should be considered as a 'process model' rather than a climate model.

To conclude this section, we present Table 6.2 below for comparison with Table 3.7 for the grey radiation model. The most significant change from Table 3.7 is the great reduction in the vertical large-scale transports that occurs for the more stable conditions of the full model. The horizontal sensible heat flux (when water vapor transport is included) is

Table 6.2: Integrated horizontal and vertical baroclinic fluxes (sensible plus latent)

h_0	Ri	<u>Horizontal flux</u> ($m \frac{^{\circ}C}{s}$)		<u>Vertical flux</u> ($\times 10^{-3} m \frac{^{\circ}C}{s}$)	
		S.H. alone	Total	S.H. alone	Total
0.0	61.5	8.71	8.71	3.22	3.22
0.8	70.5	7.51	10.19	2.61	2.96

almost unchanged from the grey model. The latent heat transport is reduced by about half because of the lower surface temperatures, although the total horizontal flux is still larger than the observed atmospheric flux. This is to be expected since we have neglected oceanic transports, which make an important contribution to the global energy balance.

6.2 Parameter Sensitivity Studies

6.2.1 Variation with convective parameter b

In Chapter 4 we described the parameterization used for small-scale heating. The surface fluxes of latent and sensible heat are distributed vertically according to a specified profile which depends on the two parameters b and c. An undesirable consequence of prescribing the heating profile is that feedback between the small-scale and large-scale vertical fluxes is essentially eliminated. In a regime where the large-scale eddies dominate, we would expect the small-scale flux to be confined close to the ground. On the other hand, at high temperatures convective adjustment becomes a dominant heating mechanism in the atmosphere, and almost the entire

vertical transport must be carried by the small-scale motions. (When we talk here about 'small-scale' fluxes, we are not thinking just of boundary layer turbulence and moist convection, but also include mesoscale eddies which are known to be of major importance in the vertical transport of heat and water vapor (Priestley, 1967)). This problem of dividing the vertical fluxes of heat and moisture between the large and small scales is a very difficult one to parameterize realistically. Many two-layer models simply ignore it and deposit all the heat in the lower layer, for example. Alternatively, if the tropical circulation is of prime interest, the heating may be divided more equally between upper and lower layers. In addition, a convective adjustment will produce some redistribution of heating at latitudes where the baroclinic eddies become too weak to stabilize the vertical temperature structure. This latter feedback is absent from our model which concentrates on the baroclinic regime in middle and high latitudes. It is important to know what effect this omission has on our results.

Table 6.3 shows the mean temperature structure predicted by the model with $b(\phi) = \frac{z_c(\phi)}{H(\phi)}$ and for various other values of b independent of latitude. The net convective heating, $\langle (\frac{p_0}{p})^\kappa \frac{Q_{\text{conv}}}{\rho c_p} \rangle$ (which, of course, equals the net radiative heating, $\langle (\frac{p_0}{p})^\kappa \frac{Q_{\text{rad}}}{\rho c_p} \rangle$ from (2.33)), is a convenient measure of the intensity of the small-scale motions. It is clear that the mean stability B (or lapse-rate β) is the most sensitive to varying values of the convective parameter b . This variation of lapse rate with b is also demonstrated in Figure 6.1. The graph shows the point $\bar{b} = 0.3355$, which is the mean latitudinal value of $b(\phi) = \frac{z_c(\phi)}{H(\phi)}$ for the full model (given in Table 6.1).

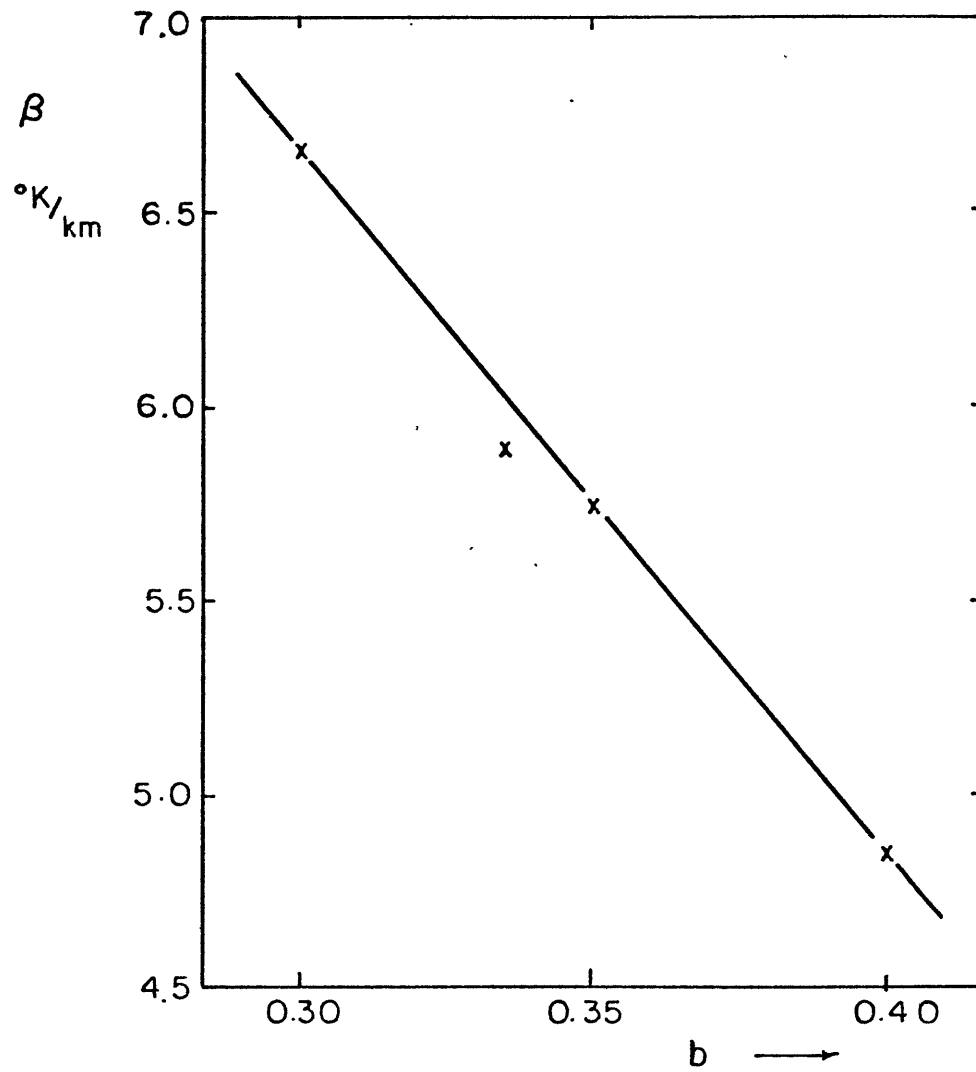


Figure 6.1: Change in equilibrium lapse rate β with convective parameter b . The straight line joins points where b is independent of latitude. The fourth point, not on the line, is the latitudinal mean of b $(\phi) = \frac{z_c(\phi)}{H(\phi)}$.

Table 6.3: Variation of model mean parameters with convective parameter b .

\bar{b}	T (°K)	A	β	B	$\left\langle \left(\frac{p_0}{p} \right)^{\kappa} \frac{Q_{\text{conv}}}{\rho c_p} \right\rangle$ (°C/day)
Constant b : 0.30	241.45	-0.4595	6.651	4.077	1.166
0.35	242.29	-0.4278	5.731	5.398	1.207
0.40	243.20	-0.4048	4.849	6.757	1.280
$b(\phi) = \frac{z}{H} \frac{c}{H}$ with mean value $\bar{b} = 0.3355$	242.08	-0.4383	5.881	5.176	1.199
$b(\phi) = \begin{cases} \left(\frac{45-\phi}{90} \right), & \phi \leq 45^\circ \\ 0, & \phi \geq 45^\circ \end{cases}$	240.95	-0.4926	6.446	4.359	1.168

The fact that this point does not lie exactly on the curve indicates greater sensitivity to low latitude values of $b(\phi)$. Clearly, we could vary b to tune the model to present conditions, if desired.

A distinctly different latitudinal form for $b(\phi)$ is suggested in the last line of Table 6.3.

$$b = \begin{cases} \left(\frac{45-\phi}{90} \right) & 0 \leq \phi \leq 45 \\ 0 & 45 \leq \phi \leq 90 \end{cases} \quad (6.4)$$

Equation (6.4) recognizes implicitly that convective adjustment dominates in equatorial regions and rapidly becomes negligible in middle and high latitudes. In climate sensitivity experiments with a two-layer model, Held and Suarez (1978) show this qualitative behavior in their Figure 24. (Of course, the particular linear form of (6.4) is still quite arbitrary).

Table 6.4 shows the convective flux $\overline{J}_{\text{conv}}$ as defined in Section 4.4 and the large-scale vertical flux $\overline{J}_{\text{dyn}} = \rho c_p \overline{w'\theta'} (1 + \mathcal{L})$ at 45° latitude for these two choices of b : Equation (6.4) and $b = \frac{z_c}{H}$.

Table 6.4: Vertical flux (in W m^{-2}) at 45° due to small-scale convection ($\overline{J}_{\text{conv}}$) and large-scale eddies ($\overline{J}_{\text{dyn}}$) for two choices of the convective parameter b .

$x = \frac{z}{H}$	$b = \frac{z_c}{H}$		b given by Eq. (6.4)	
	$\overline{J}_{\text{conv}}$	$\overline{J}_{\text{dyn}}$	$\overline{J}_{\text{conv}}$	$\overline{J}_{\text{dyn}}$
1.0	0.	0.	0.	0.
0.9	-0.2	0.7	-0.8	1.2
0.8	0.5	1.5	-1.3	2.6
0.7	2.9	2.4	-1.2	4.0
0.6	7.6	3.2	-0.0	5.3
0.5	15.7	4.0	3.1	6.5
0.4	27.6	4.6	9.5	7.3
0.3	42.8	4.9	20.7	7.7
0.2	59.9	4.7	38.0	7.3
0.1	76.8	3.4	62.4	5.2
0.0	91.3	0.	93.0	0.

It is surprising how weak the vertical eddy transport is compared to the small-scale flux. This is especially true for the case $b = \frac{z_c}{H}$. The right-hand columns of the table where $b = 0$ at 45° show the dynamical flux exceeding the small-scale term just below mid-troposphere.

Observational data on the vertical eddy fluxes are very scarce. It is also impractical to separate the vertical transport into large and small scales, since a wide spectrum of eddies contributes to the total vertical

flux (while the meridional transport is produced almost entirely by large-scale eddies). However, Hantel (1976) obtains as a residual the total vertical eddy transport of moist static energy. His results are summarized in Figure 6.3. Hantel divided the atmosphere into 16 equal-mass boxes, and the numbers shown are the eddy fluxes (over all scales) at the boundaries of these boxes. We have averaged Hantel's values for summer and winter solstice seasons.

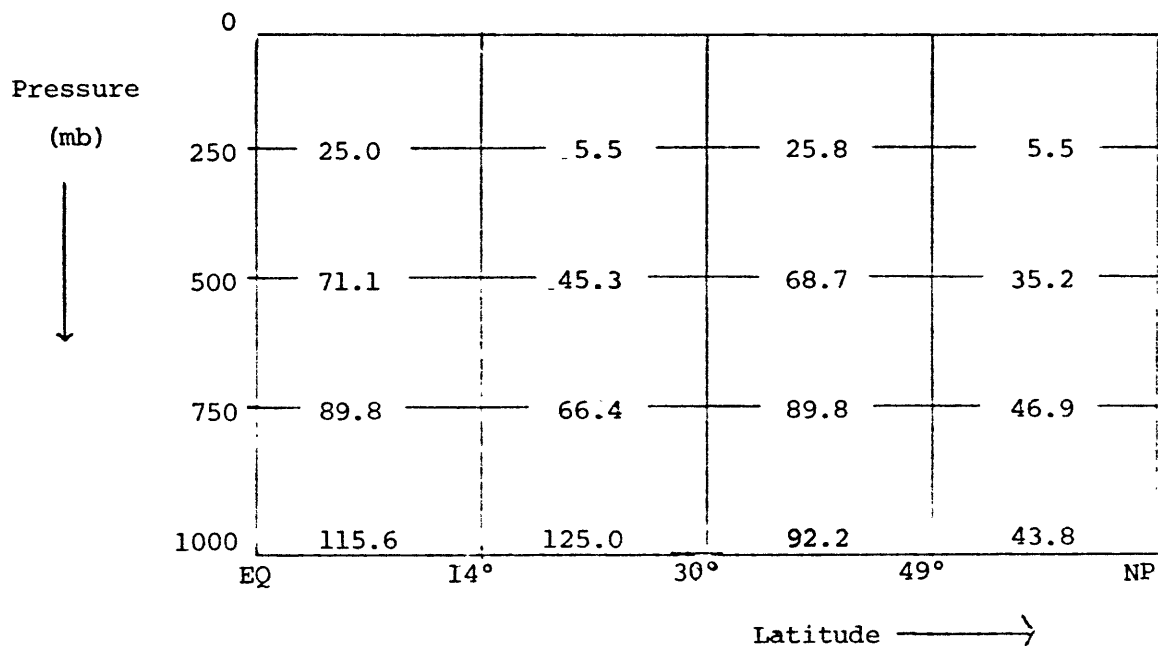


Figure 6.3: Upward vertical eddy flux (in W m^{-2}) in 'annual mean'. Taken from Hantel (1976, Figure 6).

Presumably, we should use the 30-49° column for comparison with Table 6.4. Hantel's three levels in the vertical (750, 500, 250 mb) correspond approximately to $x = 0.2$, 0.45 , and 0.8 , respectively. There is not particularly good agreement with either parameter choice of Table 6.4. If anything, the total flux decreases with height even more slowly than indicated

by the $b = \frac{z}{H}$ assumption. Hantel's values require further comment:

- (i) He assumed the eddy flux (W^E in his notation) went to zero at the top of the atmosphere ($p = 0$), whereas we apply the same condition at the tropopause. Hantel's W^E at 250 mb for the mid-latitude column (30-49°N) does appear unreasonably large, although the box imbalance (reflecting the accuracy of current heat budget estimates) is about 40% of this amount.
- (ii) In the polar column (49-90°N), the eddy flux at 750 mb is larger than at the ground. This is due to a very strong downward flux by the mean meridional circulation in winter, which itself is subject to large errors (Oort and Rasmusson, 1971). Moreover, in the mid-latitude column in winter, the total vertical flux (mean + eddy) is larger at 750 mb than at the ground, which is physically unrealistic. Perhaps Hantel's decision to apportion the column energy imbalance equally in the vertical is not the most appropriate one (the large uncertainty associated with the surface fluxes, for example, should be assigned entirely to the lowest box).
- (iii) Hantel also separates the upward eddy heat flux into two components (grid and subgrid scales) according to the GFDL climate model (Manabe et al., 1974). However, these results (his Fig. 8) show the relative transports by the two components are virtually independent of latitude (although the total magnitude decreases monotonically from equator to pole), and therefore the GCM grid-scale transport clearly cannot be identified with the baroclinic eddies.

(iv) Palmén and Newton (1969, p.53) also present estimates of the vertical eddy heat flux. They give a single value (14 W m^{-2}) for the upward eddy flux in winter at 500 mb, averaged from 32-90°N. This appears to agree with the right-hand columns of Table 6.4, except that Palmén and Newton's value for the corresponding surface flux (31 W m^{-2}) is also much lower than the other calculations.

Thus, there is no clear decision from the data between the two postulated choices for the convective parameter b . We have found that our choice of b has a significant effect on the mean gradients predicted by the model (Table 6.3). However, the changes in the global mean parameters of the model ($\langle T \rangle$, A , β , etc.) are much less sensitive to the particular formulation of b , as we see in Table 6.5 below for a 2 1/2% decrease in the solar constant. For comparison, the changes with solar constant are given for two other models: the first has the effect of lapse rate feedback removed by fixing β at the nominal value of $5.881 \text{ }^\circ\text{K/km}$, and the second assumes a constant cloud temperature $T_{CT} = 260^\circ\text{K}$. The important thing to note from this table is that most of the parameters are less sensitive to the choice of b than to other modeling assumptions we might make (i.e. the first row values agree more closely with the second row than with any of the others). This result is not true for the meridional gradient A where the values in the reference state (S_0) are very different (Table 6.3), and also becomes doubtful in polar latitudes (see Table 6.3, 6.6 for the other reference state values).

ϕ_c is the latitude at which sea ice first starts to appear (i.e. $T_w = T_f = 271.2^\circ\text{K}$). The first parameterization of b in Table 6.5 shows

Table 6.5: Variation of model parameters with the solar constant for different b . The corresponding changes when lapse rate feedback is removed or when the cloud temperature is held constant are shown for comparison.

For a quantity X , we define $\Delta X = X \text{ (at } S_0 - 2\frac{1}{2}\%) - X \text{ (at } S_0)$.

i) Mean parameters

	$\Delta \langle T \rangle$	ΔA	$\Delta \beta$	ΔB	$\Delta \phi_c$	$\Delta (\overline{H_S + H_L})$
$b = \frac{z_c}{H}$	-2.18	.0039	-.237	.323	-4.47	-.0061
b given by (6.4)	-2.10	.0085	-.224	.296	-3.68	-.0058
β constant at 5.881 °K/km	-1.67	-.0042	.0	-.016	-3.07	-.0060
T_{CT} constant at 260°K	-2.33	.0025	-.296	.407	-5.09	-.0055

ii) Ground temperature $\Delta T_g(\phi)$

	5	15	25	35	45	55	65	75	85
$b = \frac{z_c}{H}$	-3.44	-3.41	-3.38	-3.39	-3.43	-3.20	-5.00	-3.71	-3.60
b as in (6.4)	-3.43	-3.37	-3.30	-3.24	-3.20	-3.14	-4.24	-3.23	-3.15
β constant	-2.01	-2.03	-2.08	-2.16	-2.26	-2.07	-3.33	-2.61	-2.57
T_{CT} constant	-3.74	-3.71	-3.69	-3.69	-3.86	-3.70	-5.57	-4.19	-4.09

larger changes in ϕ_c , as we expect for a weaker meridional gradient (since a smaller A implies greater movement of the ice line for a given surface temperature change).

6.2.2 Dependence on cloud-height feedback assumption

For the basic model calculation we have chosen to use the cloud-height feedback assumption described as Model 4 in Chapter 5. This correlates the cloud temperature to the surface temperature and gives a more realistic latitude variation. However, as pointed out earlier, the assumption of constant cloud temperature (Model 2) gives closer agreement with empirical results for the variation of thermal flux at the top of the atmosphere ($\frac{\partial F_T}{\partial T_0}$ in Table 5.5). We will look briefly here at the effect of using model 2. Table 6.6 shows the sensitivity of our results to the cloud-height assumption. Some of the parameter changes were noted previously in Table 6.5.

Table 6.6: Parameter sensitivity to cloud-height assumption.

	<T>	A	β	B	\bar{H}	ϕ_c	$(\bar{H}_S + \bar{H}_L)$	\bar{T}_0	\bar{T}_g
<u>S_0:</u>									
i) basic model	242.1	-.438	5.88	5.18	13.79	54.8	.1602	282.8	285.3
ii) fixed cloud temp:									
$T_{CT} = 260$	242.2	-.437	5.92	5.12	13.78	55.5	.1603	283.1	285.6
$T_{CT} = 250$	244.4	-.462	6.61	4.16	13.39	61.0	.1563	288.8	290.1
<u>$S_0 - 2\frac{1}{2}\%$:</u>									
i) basic model	239.9	-.434	5.64	5.50	13.73	50.4	.1541	278.8	281.7
ii) $T_{CT} = 260$	239.9	-.434	5.62	5.53	13.75	50.4	.1548	278.7	281.7

A constant cloud-top temperature $T_{CT} = 260^\circ\text{K}$ corresponds most closely to the observations of Table 5.2, from which we obtained the T_c , T_0 correlations of Model 4. We find the mean model parameters are almost unchanged from the standard case (the cloud-base temperature was assumed to be 10 degrees warmer unless this implied a cloud-height lower than 1 km. This is an obvious difficulty in assuming cloud temperatures are constant with latitude). The results for a 10 degree reduction in cloud temperature are also shown. We see that this gives a mean surface temperature closer to the observed. The mean cloud temperature (in either Model 2 or 4) could therefore be used as another tuning parameter if desired. The mean flux of sensible and latent heat from the surface $(\overline{H_S + H_L})$ (in $\text{cal cm}^{-2} \text{min}^{-1}$), is seen to decrease in spite of the higher ground temperatures with $T_{CT} = 250^\circ\text{K}$. It is interesting to understand why this occurs. For greater surface temperatures, the latent heat flux increases and there is more water vapor in the atmosphere. The short-wave radiation reaching the ground is then reduced (due to increased absorption) and this effect is more important than the change in the net long-wave radiation H_B . From Equation (4.47), this means the sum $(\overline{H_S + H_L})$ must decrease. Note that this behavior (of H_B) occurs only because there is a substantial change in cloud temperature. In other experiments where the surface temperatures are varied, the net convective flux is increased too, as we might expect intuitively.

Table 6.6 also shows the model results for solar insolation 2 1/2% less than its current value. The mean parameters differ very little between models. The sensitivity is shown more clearly in Table 6.5. The hemispheric mean temperature $\langle T \rangle$ and meridional gradient A are only weakly

dependent on the cloud-height feedback assumption. The different lapse rate responses are much more significant in determining the ground temperature changes (e.g. to a first approximation, $\Delta T_0 (90^\circ) \approx \Delta \langle T \rangle - 50 \Delta A + \frac{1}{2} \bar{H} \Delta \beta$). It is no surprise that the surface temperature is more sensitive to climate variations for the fixed cloud temperature case (see results of Section 5.2). The greater surface response in turn implies a more rapid movement of the ice line (ϕ_c).

6.2.3 Dependence on other internal parameters: d, α_i, h_0 .

Table 6.7 demonstrates the behavior of the model to other prescribed changes. The nominal values are repeated for easy reference.

Table 6.7: Further parameter sensitivity studies with the full model.

	$\langle T \rangle$	A	β	B	\bar{H}	ϕ_c	$\overline{(H_S + H_L)}$	\bar{T}_0	\bar{T}_g
Basic model	242.1	-.438	5.88	5.18	13.79	54.8	.1602	282.8	285.3
Halve transition depth $d = 0.5$	242.2	-.437	5.87	5.19	13.81	55.0	.1602	282.9	285.3
Double ice albedo $\alpha_i = 0.70$	239.9	-.489	5.55	5.64	13.80	48.0	.1546	278.3	280.8
Vary relative humidity $h_0 = 0.7$	242.5	-.442	5.74	5.38	13.89	53.8	.1643	282.4	284.3
Remove latent heat flux "h ₀ = 0.0"	241.9	-.471	5.85	5.22	13.81	53.0	.1619	282.5	284.7

(i) The transition depth d was a parameter we found necessary to introduce when solving for the tropopause height. Reducing the nominal value $d = 1.0$ km by 50% has negligible effect on the results.

(ii) Table 6.7 presents the reference state for an ice albedo double the earlier value, i.e. $\alpha_i = 0.70$ instead of $\alpha_i = 0.35$. The temperature is reduced considerably as we might expect (and corresponds quite closely to the nominal model for $S_0 - 2 \frac{1}{2} \%$).

(iii) The basic model assumes a surface relative humidity of 0.8 in close agreement with observed values. The final two rows of Table 6.7 show the model behavior for two distinct changes involving this parameter. In the first, we reduce the surface relative humidity to $h_0 = 0.7$, which affects the dynamical transport of latent heat, the surface latent heat flux and all radiative calculations. In the second experiment, we remove the large-scale eddy transport of latent heat but keep $h_0 = 0.8$ for all other purposes (i.e. radiative calculations and surface evaporation). We see that the changes are quite moderate in both cases. Only minor variations occur for $h_0 = 0.7$, since the fixed cloud amounts place a strong constraint on the radiative feedback. The surface temperatures are reduced slightly as the total absorber amount decreases, although the radiative feedback stabilizes the lapse rate sufficiently to increase the mean tropospheric temperature a small amount.

Comparing with Table 3.5, we find that adding latent heat transport to the full model again weakens the meridional gradient A and, as in the grey model, the static stability is reduced (although the change is now much smaller due to the presence of small-scale convective fluxes).

6.3 Climate sensitivity studies - variation with O_3 , CO_2 and cloud amount.

Table 6.8 shows the same parameters as Table 6.6, but for an imposed variation of some interesting climate variables. We will consider each of the three effects in the order presented in this table.

Table 6.8: Climate sensitivity studies with the full model.

	$\langle T \rangle$	A	β	B	\bar{H}	ϕ_c	$\overline{(H_S + H_L)}$	\bar{T}_0	\bar{T}_g
Basic model	242.1	-.438	5.88	5.18	13.79	54.8	.1602	282.8	285.3
Decrease cloudiness $n = 0.05$	243.8	-.444	6.12	4.85	13.81	58.7	.1638	286.2	288.2
Double CO_2 $u_2(0) = 240$	243.9	-.439	6.19	4.75	13.76	59.9	.1630	286.7	288.7
Halve O_3 $f_{O_3} = 0.5$									
(i)	241.5	-.438	6.03	5.02	14.13	56.8	.1626	284.2	286.6
(ii)	241.6	-.433	5.90	5.20	14.30	56.7	.1625	283.9	286.4

Variation with cloud amount: The cloud amount n is reduced uniformly at all latitudes by 0.05. This corresponds to a mean decrease of 10%, slightly greater in low latitudes. The result is to increase the mean surface air temperature \bar{T}_0 by 3.38°C, and the ground temperature \bar{T}_g by 2.90°C. This makes our model more sensitive than the zonally-averaged 2-level model of Ohring and Adler (1978). They change the cloudiness by $\pm 25\%$. For a 25% reduction in n , the mean surface temperature of their model in-

creases by 4.28°C . Since Ohring and Adler fix the cloud heights in their calculations, we expect their surface temperatures to be less responsive to cloud changes (Section 5.5.2). The finding that the ground temperatures are quite sensitive to cloud amount is also in agreement with earlier one-dimensional vertical coordinate models (Manabe and Wetherald, 1967; and Schneider, 1972). As noted also by Ohring and Adler, our results contradict the suggestion of Cess (1976) that the earth's surface temperature is not particularly sensitive to changes in cloud amount as a result of compensating albedo and 'greenhouse' effects.

Thus, there is the possibility of a strong positive feedback effect on the climate if recent results (Schneider and Washington, 1973; and Roads, 1977) that the cloudiness n decreases with increasing temperature T_0 are to be believed. Our model predicts a small decrease in static stability for reduced cloudiness, and this may have a weakly compensating effect by encouraging convection (although Roads found that reduced n was caused by enhanced convection, producing deep, narrow clouds rather than shallow, wide ones).

Variation with carbon dioxide amount: Schneider (1975) provides an excellent summary of predicted temperature changes for variation in carbon dioxide concentration. Table 6.9 gives a reduced list, along with some more recent results. A general comment, based on Table 6.9, is that the sensitivity increases with the number of degrees of freedom in the model. The final row gives our results for the ground temperature change (with the surface air temperature deviation in brackets). The greater sensitivity of our model is due to the cloud-height feedback assumption that we

Table 6.9: Change in surface temperature, T_s , on doubling the CO_2 amount

ΔT_s ($^{\circ}C$)	Model
+ 1.32	Sellers (1974): Energy balance model with fixed h_0 and n, z_c
+ 0.80	Ohring and Adler (1978): 2-level model, fixed h_0 and clouds (n, z_{CB}, z_{CT}).
+ 1.7	Temkin and Snell (1976): Zonally-averaged hemispheric model with "diffuse" cloudiness (no real height), fixed h_0 and lapse rate.
+ 2.36	Manabe and Wetherald (1967): 1-D radiative-convective model, fixed h_0, β, n, z_c .
+ 2.93	Wetherald and Manabe (1975): 3-D GCM with interactive β, h_0 , but fixed n, z_{CB}, z_{CT} .
+ 3.38 (+3.90)	Present model: $\Delta \bar{T}_g$ ($\Delta \bar{T}_0$).

used. All the other calculations listed in the table kept the cloud height fixed. (Using the constant cloud temperature assumption of Model 2 would increase the response still further).

In our model, the mean tropopause height decreases very slightly (due to greater lapse rate), and the meridional gradient is virtually unchanged (Table 6.8). Some of the factors affecting the lapse rate are shown in Table 6.10. Increasing the carbon dioxide amount has several effects:

(i) The LW flux to space from the upper atmosphere increases, so we expect high level cooling (the model mean tropopause temperature, \bar{T}_H , does decrease slightly; by $-0.18^{\circ}C$).

Table 6.10: Radiative and surface flux changes on doubling CO₂ amount.

	Latitude	Surface flux ($\overline{H_S + H_L}$) $\frac{\text{cal}}{\text{cm}^2 \text{min}}$	Total radiative heating °C/day	Radiative stabilization °C/day
Basic model $u_2(0) = 120$	5	.2198	-1.364	0.408
	25	.1990	-1.206	0.441
	45	.1311	-1.090	0.719
	65	.0522	-1.039	1.006
	85	.0158	-0.966	1.022
Double CO ₂ $u_2(0) = 240$	5	.2228	-1.380	0.417
	25	.2015	-1.227	0.452
	45	.1319	-1.120	0.726
	65	.0567	-1.067	1.003
	85	.0133	-1.050	0.970

(ii) The internal atmospheric heating is magnified. Since there is greater net cooling in the lower troposphere than in the upper troposphere, radiation acts to stabilize the vertical temperature profile. (The values listed for radiative stabilization are the differences in net heating (LW + SW) between the upper and lower halves of the model troposphere weighted by the $(\frac{p_0}{p})^k$ factor).

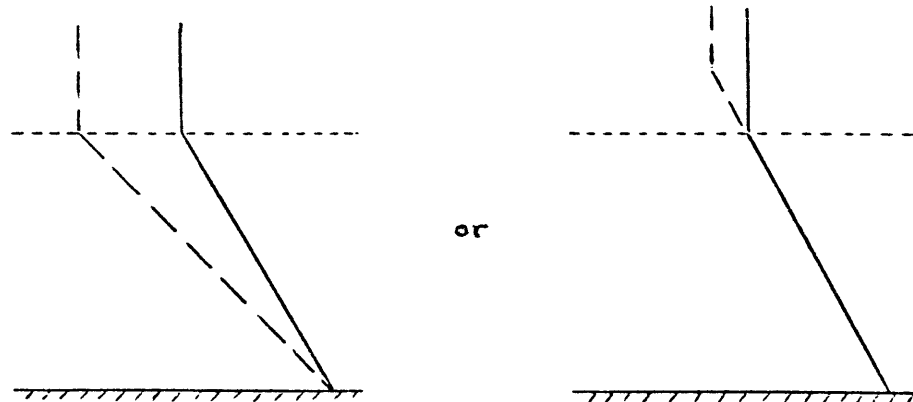
(iii) The downward LW flux to the ground increases, which raises the surface temperatures and the sensible and latent heat fluxes. The increased small-scale heat flux, which is deposited mainly in the lower layer, acts to destabilize the lapse rate.

The net effect is to reduce the model static stability. The increased vertical transport by the baroclinic eddies also acts as a negative feedback to limit the final response. [Note: For the earth-atmosphere system to remain in global balance for a greater CO₂ amount, the temperatures of the lower atmosphere and surface must increase considerably more than the stratospheric temperatures decrease because the atmosphere is now more opaque to infrared radiation.]

Variation with ozone amount: Since the early work by Crutzen (1972) on a possible threat to the earth's ozone layer by supersonic transport flights, many models have studied the effects of ozone depletion. However, most of these were interested primarily in the stratospheric response. The calculations of surface temperature changes have come from one-dimensional radiative-convective equilibrium models (Ramanathan et al., 1976; and Reck, 1976). These models require convective adjustment to a fixed 6.5 °K/km lapse rate and determine the surface response from the net radiation balance condition (our Equation 1.5) applied at the top of the atmosphere. On the other hand, our model treats the stratosphere in a cavalier fashion by assuming isothermal conditions there, and handles the troposphere much more realistically with explicit lapse-rate, cloud-height, and surface flux feedbacks. However, we have also omitted consideration of LW absorption by the 9.6 μm band of ozone (when calculating both $H(\phi)$ and the LW flux at the ground), and this could modify our results. Nevertheless, we do simulate the most important direct features accompanying an ozone reduction; namely, the decrease in stratospheric temperature and a greater short-wave flux at the ground.

Qualitative changes in the temperature structure that may be impor-

tant for tropospheric dynamics are sketched below.



The left-hand figure shows a decrease in stratospheric temperature reducing the stability in the troposphere (for the same tropopause height H), while the right-hand figure has the same lapse-rate but a deeper troposphere. Both these changes might intensify large-scale motions in the lower atmosphere (a deeper troposphere, for example, could increase the integrated horizontal transports). A combination of the two effects is possible, and of course the surface temperature may be altered as well.

The last two rows of Table 6.8 show our model's response when the total ozone column amount is reduced uniformly by 50% at all latitudes. Row (i) uses the basic model with $b(\phi) = z_c/H$ as we have described above. We find that elevating the tropopause height is one major consequence of reducing O_3 amounts (in agreement with Figure 14 of Manabe and Möller, 1961), and this in turn reduces the latitudinal mean \bar{b} from 0.3355 to 0.3273. According to Figure 4.1, such a change in the mean \bar{b} could exactly account for the calculated stability change. We have therefore repeated the computation (Row (ii)) with $b(\phi)$ fixed at the reference model values (Table 6.1). The variation in β is lessened considerably, although the other parameters are much the same. The mean stratospheric tempera-

ture \bar{T}_H decreases by 2.61 and 2.11 °C for cases (i) and (ii), respectively, and the ground temperature increases by 1.29 and 1.12 °C, respectively. In neither case are the stability changes particularly large. However, allowing for a lapse-rate feedback and a more complicated ground temperature response through a surface energy balance condition is sufficient to reverse the findings of Ramanathan et al. (1976) and Reck (1976) that the surface temperature decreases for ozone depletion. Their results are easy to understand. Removing ozone decreases the short-wave absorption and therefore decreases the net incoming SW radiation at the top of the atmosphere. The net thermal emission to space must then decrease to reach a new equilibrium. The lower stratospheric temperature (due to reduced short-wave heating) cannot account for all the required decrease in $F(\infty)\uparrow$, because the stratosphere is optically thin in the infrared. This means that temperatures in the lower atmosphere must decrease, too. For a fixed lapse-rate, this translates into a lowering of the ground temperature.

Complete removal of ozone from the atmosphere causes the temperature reversal that defines the tropopause to vanish (Manabe and Strickler, 1964). The mean temperature profile we have assumed (Figure 4.2) will no longer be valid and we cannot extend our results to this case. (In fact, our calculation of tropopause height will break down). However, Reck (1976) finds the temperature inversion is still present for up to a 90% reduction in stratospheric ozone.

Other radiative effects may also be significant in evaluating surface changes to ozone reduction. For example, Reck (1976) found a surface temperature increase in the presence of a low-lying particulate layer.

6.4 Climate sensitivity studies - variation with solar constant

A number of experiments were made with varying solar constant. Table 6.11 summarizes the surface temperature changes found in some previous studies and compares them with ours. We show the surface (i.e. ground) temperature deviation, and the bracketed values are the changes interpolated quadratically from the actual model results.

Table 6.11: Change in equilibrium surface temperature for different models. ΔT_S ($^{\circ}\text{C}$) changes for indicated ΔS_0 (%). [Bracketed values are interpolated.]

+2½	+2	+1	-1	-2	-2½	
			-4.48			North (1975)
			-2.07			Coakley (1979)
		1.4	-1.0			Temkin & Snell (1976)
		1.35	-1.5			Ohring & Adler (1978)
	2.57	(1.28)	(-1.28)	-2.55		Manabe/Wetherald (1967)
	3.04	(1.69)	(-2.02)	-4.37		Wetherald/Manabe (1975)
3.83	(3.04)	(1.50)	(-1.45)	(-2.85)	-3.53	Present model

The first two results listed in Table 6.11 are for one-dimensional energy balance studies. Early models such as that of North (1975) were extremely sensitive to small changes in the solar constant. They predicted an ice-covered earth for decreases in S_0 as small as 1.6 - 4%. Coakley (1979) found a greatly reduced sensitivity using a climatologically consistent albedo parameterization. His value is now in close agreement with the GCM calculation of Wetherald and Manabe (1975), although this is quite fortuitous because of the different cloud-height feedbacks and the extra physics included in the GCM. (A brief description of the other models

cited is given in Table 6.9).

Our results show a slight asymmetry with respect to solar constant changes. ΔT_S for a 2% increase in S_0 agrees closely with the GCM result, although there is a considerable discrepancy when S_0 is reduced by 2%. A larger ice albedo would increase our surface temperature response to a colder climate. (However, modifying α_i to 0.55, for example, would require tuning the model to present conditions for a sensitivity study to be meaningful. We have decided not to confuse matters with tuning experiments in what is really a process model rather than a genuine climate model).

Many climate studies (e.g. Wetherald and Manabe, 1975; Ohring and Adler, 1978) find a greater sensitivity to S_0 changes in high latitudes (due to ice albedo-temperature feedback). This behavior is not simulated well in our model, primarily because the Legendre polynomial expansion (in P_0, P_2) for the surface temperature is unable to resolve the strong curvature of $T_0(\phi)$ in high latitudes. The smaller ice albedo that we use is, no doubt, partly responsible too. Nevertheless, Table 6.5 (ii) does show a weak preference for larger temperature changes near the pole.

Meridional gradient A: Table 6.12 presents the equilibrium solutions over a large range of solar insolation. Figure 6.2 shows the variation of one particular parameter, the ice line ϕ_c . It is clear that as the solar constant is reduced, the model predicts weaker meridional gradients and greater static stabilities. It is known that the simple 1-D energy balance models show a stronger meridional gradient for colder climates. There are several reasons for the different behavior of our model.

Table 6.12: Equilibrium solutions of the model for varying solar constant S_0 . Results are also shown with a different specification for the convective parameter b (after Equation 6.4) and with the effect of lapse-rate feedback removed.

	$\langle T \rangle$	A	β	B	\bar{H}	ϕ_c	$\overline{(H_S + H_L)}$	\bar{T}_0	\bar{T}_g
<u>Basic model</u>									
$S_0 + 10\%$	251.7	-.451	6.89	3.82	14.14	90.0	.1932	300.5	300.7
+ 5%	246.9	-.442	6.40	4.48	13.95	66.8	.1754	291.6	293.7
+ 2½%	244.4	-.439	6.14	4.83	13.87	60.5	.1672	287.1	289.1
S_0	242.1	-.438	5.88	5.18	13.79	54.8	.1602	282.8	285.3
- 2½%	239.9	-.434	5.64	5.50	13.73	50.4	.1541	278.8	281.7
- 5%	238.1	-.422	5.47	5.73	13.65	47.3	.1486	275.6	279.0
-10%	233.9	-.389	5.06	6.29	13.45	38.1	.1351	268.0	272.3
-15%	229.8	-.365	4.61	6.92	13.31	27.8	.1236	260.5	265.5
-16%	229.2	-.361	4.55	7.00	13.29	26.5	.1222	259.5	264.5
-17%	228.7	-.357	4.49	7.07	13.27	25.2	.1209	258.6	263.6
-17% (i)	228.2	-.350	4.43	7.16	13.23	22.2	.1194	257.6	262.6
<u>b as in Eqn. (6.4)</u>									
S_0	241.0	-.493	6.45	4.36	12.99	52.7	.1621	283.0	285.0
$S_0 - 2½%$	238.9	-.484	6.22	4.66	12.91	49.1	.1563	279.2	281.6
<u>No lapse rate feedback</u>									
$S_0 - 2½%$	240.4	-.443	(5.88)	5.16	13.54	51.8	.1542	280.4	283.1

(i) for $S_0 - 17\%$ refers to the unstable solution (see Figure 6.2).

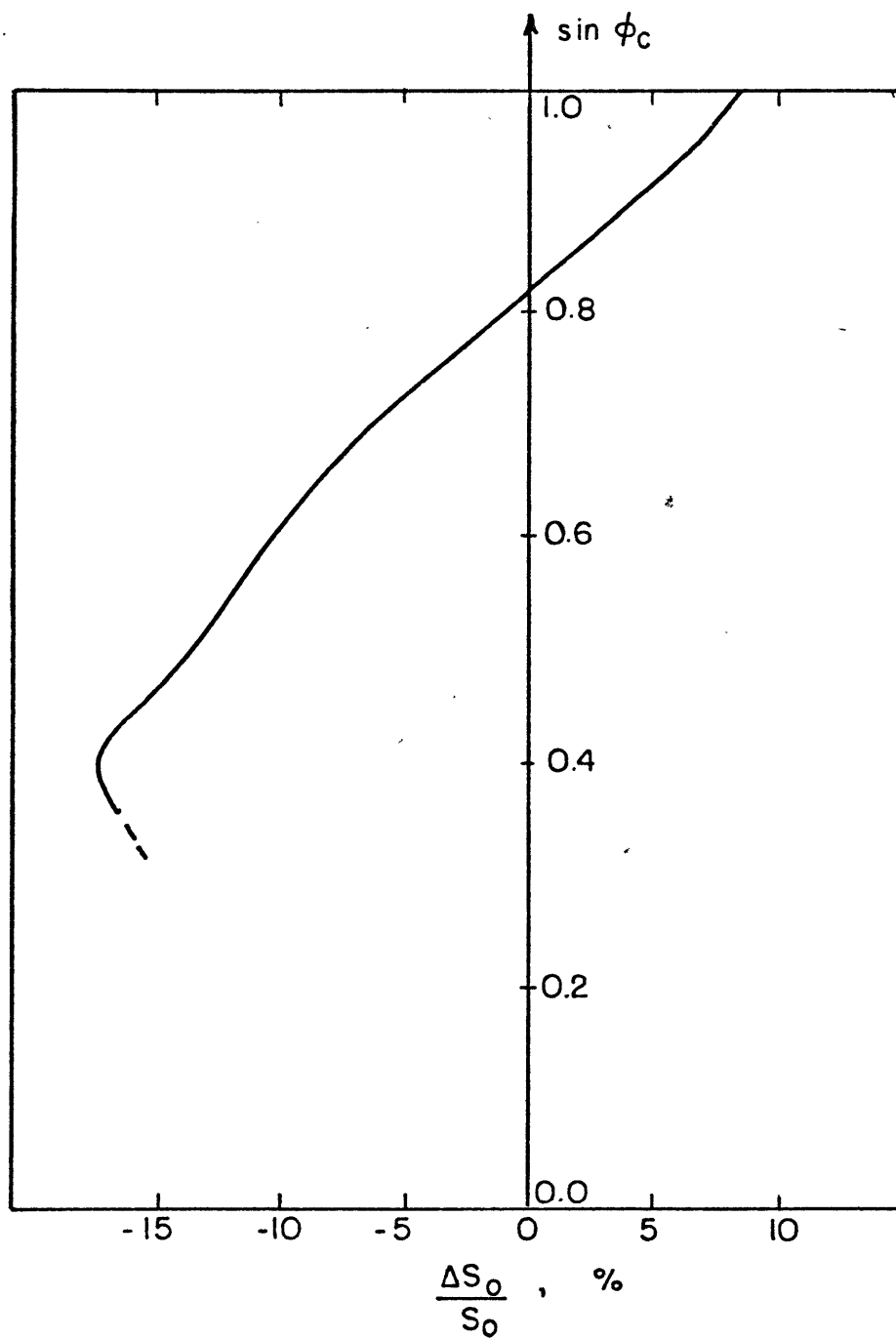


Figure 6.2: Variation of critical latitude (ϕ_c) for ice formation with changing solar constant S_0 .

Firstly, it should be remembered that 'A' in our calculations is a hemispherically averaged value, not just the surface gradient. Table 6.5 (ii) demonstrated that the ground temperatures did indeed vary more at the pole than the equator (although the difference is small). Our value of A is also influenced by a more realistic treatment of clouds. Figure 3 of Wetherald and Manabe (1975) shows the deviation temperature field calculated by a general circulation model for a 2% increase in S_0 . Although the surface temperature change is amplified at high latitudes, this is no longer true at upper levels. In fact, were it not for the strong effect over the polar cap (which our low order expansion for $T(\phi)$ does not simulate well), the sign of the meridional gradient change (as defined by Equation (2.19)) would be uncertain.

The last line in Table 6.12 shows the interesting results when lapse-rate feedback is prevented (the situation with 1-dimensional studies, both energy balance and radiative-convective equilibrium models). This computation was done by fixing the lapse rate β at the nominal value of 5.88 °K/km, and iterating only on the $\langle T \rangle$ and A equations (2.33 and 2.38, respectively). In this case, we see that the meridional gradient increases with reduced insolation. The surface temperature sensitivity is also weakened substantially (for $\Delta S_0 = -2 \frac{1}{2} \%$, ΔT_g is -2.22 °C rather than -3.53 °C, with an interactive lapse-rate).

It should also be remembered that as S_0 decreases the net meridional radiative forcing (as represented by A_r in Equation 3.7, for example) decreases monotonically. Eventually, the atmospheric meridional gradient A must also decrease, although this change can be masked by surface temperature effects for small S_0 deviations.

Lapse rate: Our model predicts the lapse rate will increase with the solar insolation S_0 . This agrees with Wetherald and Manabe's (1975, Figure 3) results in high latitudes only. Their calculations show low and middle latitudes are stabilized because of the predominance of moist convection which adjusts temperatures towards the moist adiabatic lapse rate (which decreases with increasing temperature). This effect is absent in our model and produces serious errors for higher solar constants. However, we expect a better response for reduced S_0 where convection rapidly becomes less important (in magnitude and latitudinal extent). As the solar constant decreases, our model lapse rate (which we have assumed independent of latitude) is progressively decreased. This is because the destabilizing 'surface' heating ($H_S + H_L$) decreases more rapidly than the stabilizing radiative heating field (analogous to Table 6.10). The reduction in lapse rate, together with the decrease in surface temperature, means that there is a smaller change at high altitudes, which is consistent with the GCM results of Wetherald and Manabe (their Figure 5).

Hydrologic cycle: Precipitation is not determined explicitly in our model so there is no true hydrologic cycle. The surface relative humidity is simply held constant at 0.8. In view of this approximation, it is very interesting that the change in intensity of the hydrologic 'cycle' with solar constant (as measured by surface evaporation \bar{H}_L) is remarkably close to that found by Wetherald and Manabe (1975). Table 6.13 compares these changes, where our results are linearly interpolated to match the solar constant changes of Wetherald and Manabe.

Table 6.13: Change in intensity of hydrologic cycle with solar constant. The values of \bar{H}_L (in $\text{cal cm}^{-2}\text{min}^{-1}$) are shown, along with their normalized values in brackets.

	+2%	0%	-2%	-4%
Wetherald & Manabe (1975)	.118 (1.09)	.108 (1.00)	.101 (0.94)	.090 (0.83)
Present model	.1366 (1.10)	.1246 (1.00)	.1138 (0.91)	.1038 (0.83)

The normalized values agree very closely, although our model has consistently higher evaporation (15% greater) because of the larger ocean surface area (100% versus 50%). Our values would be higher still were it not for the lower surface temperatures.

Chapter 7: Summary and Conclusions

We have presented a process model designed to study some of the important features affecting mid-latitude climate. The advantage of such an approach is that we can examine the result of 'turning on' various physical mechanisms one at a time. Comparison with more complete models, or with the atmosphere itself, even allows us to draw some conclusions on processes we have omitted entirely. The main feature of atmospheric motions that we have neglected is the mean meridional circulation. This is of major importance in determining the structure of temperature, pressure and moisture fields at low latitudes. The omission means that the structural parameters we determine (A and β) should be applied only to middle latitudes where baroclinic eddies dominate (e.g. the mean meridional circulation carries less than 20% of the atmospheric flux at 45°N in the annual mean. See Figures 1.1a,b for seasonal extremes). However, since suitable boundary conditions must be chosen to solve the equations describing the atmospheric circulation, we find it convenient in practice to identify the temperature gradients as hemispheric mean values.

Perhaps the major shortcoming in the model is the treatment of the vertical fluxes, both large-scale and small-scale. We have already discussed the small-scale convective fluxes in some detail in section 6.2.1. However, there is also a potential difficulty with the vertical transports by the large-scale baroclinic eddies. It is

pointed out by Held (1978a) that the scaling used by Stone (1972a) may not be appropriate for the shorter waves when the variation of Coriolis parameter with latitude is included. He argues from the quasi-geostrophic pseudo-potential vorticity equation, and assumes the eddy potential vorticity flux has little vertical structure (which is true for the most strongly unstable waves on the idealized flow of Charney & Stern, 1962, and for the more realistic flows of Gall, 1976). After making a few more assumptions about the y, z dependence of the parameters, Held finds that " h_0 " is a measure of the vertical extent of the eddy fluxes where

$$\frac{1}{h_0} = \frac{1}{h} + \frac{1}{H} \quad (7.1)$$

(i.e. half the harmonic mean of h and H), and

$$h = \frac{f^2 \frac{\partial \bar{u}}{\partial z}}{\beta N^2} \quad (7.2)$$

[Note on symbols: Held's h_0 and h are height scales (in km), and should not be confused with our symbols for relative humidity. Likewise, " β " in (7.2) is $\frac{\partial f}{\partial y}$, the meridional derivative of the Coriolis parameter f , and should not be confused with the same symbol we use for the lapse rate]. H is the atmospheric scale height (identified as H_S in section 1.3), and N is the Brunt-Vaisala frequency.

$$N^2 = \frac{g}{\langle \theta \rangle} \frac{\partial \bar{\theta}}{\partial z} \quad (7.3)$$

Stone (1972b) scaled the vertical coordinate by H , but equation

(7.1) indicates this is suitable only when the stability effect of β is negligible (i.e. $h \gg H$). In fact, h and H are typically of the same order. In terms of our model, $h = -\frac{200}{\pi} \frac{A}{B}$ at 45° , and inserting the observed parameter values of Tables 1.5, 1.7, 1.8 we find $H = 7.58$ km, $h = 7.24$ km, and thus, $h_0 = 3.70$ km. (For the nominal model, $H = 7.08$, $h = 5.39$ and $h_0 = 3.06$).

This analysis raises some questions as to the accuracy of Stone's parameterization of the baroclinic fluxes of sensible heat. This question is more important for the vertical flux than for the horizontal one. If we examine the spectral energetics determined by Saltzman (1970) and Tenenbaum (1976), we see that most of the horizontal eddy transport is handled by the longer, and therefore deeper, waves. i.e. $C(P_M, P_E)$, the conversion from zonal to eddy available potential energy, peaks at wave-number 3 in both references. (Note that $C(P_M, P_E)$ is actually a hemispheric average of $[\overline{v'T'}]$, $\frac{\partial [\overline{T}]}{\partial \phi}$, and so is not an exact measure of the horizontal transports). Similarly, we can obtain an approximate estimate of the most important vertical scales from $C(P_E, K_E)$, the conversion from eddy potential to eddy kinetic energy (which is proportional to the integral of $[\overline{\omega'\alpha'}]$ in the terminology of Oort & Peixoto, 1974). Saltzman calculates a peak in $C(P_E, K_E)$ for winter at wave-number 6, the baroclinically most unstable mode, and a scale at which the β effect is of order one. Tenenbaum, however, finds most of the conversion occurring for the longer scales ($k = 1 - 3$), so the importance of the β effect even for the vertical flux is not clear-cut.

These uncertainties in the vertical flux parameterization mean that, while our model is not demonstrably incorrect (e.g., it does give reasonable values for Held's parameter h), we should be cautious in drawing conclusions about the lapse-rate variations predicted by our calculations.

In addition to the sensible heat fluxes by the baroclinic eddies, our model includes latent heat transports, modeled after a suggestion by Leovy (1973). The surface of the earth is idealized as a swamp, so that oceanic meridional transport is eliminated. Strong constraints on the total poleward flux (Stone, 1978) mean that atmospheric eddy transports tend to compensate for the lack of an ocean circulation and mean meridional circulation in the atmosphere. Thus, the calculated meridional gradient is quite reasonable.

Cloud amounts are fixed at climatological values. This removes a climatic feedback of potential importance, although present estimates of its effect vary widely. The full model has a fairly complete treatment of long and short wave radiation. The influence of carbon dioxide and ozone is included so that sensitivity studies with different amounts of these absorbers can be made. Water vapor is the most important constituent in radiative calculations of the lower atmosphere. The relative humidity is fixed (at 0.80), but the absolute humidity responds strongly to temperature changes. Manabe & Wetherald (1967) point out that this is more realistic than specifying the absolute humidity, and it results in an increased

sensitivity to external changes (such as solar constant variation or CO₂ increase).

Applying the philosophy of mechanistic modeling, we present a greatly simplified version of our model, the grey radiation model, in Chapter 3. Small-scale convective heating is explicitly omitted and the net radiative effects approximated by a Newtonian cooling law. There are several conclusions we can draw from this case.

i) The large-scale motions stabilize the vertical temperature profile so that dry convection is eliminated as an important vertical heat transport mechanism. (Duplicates result of Stone, 1972a). The atmosphere is still conditionally unstable to moist convection.

ii) The observed decrease of tropopause height with latitude has a significant effect on the convergence of the large-scale eddies, and influences the distribution of dynamical heating. The main consequence is to provide additional stabilization of the vertical temperature structure.

iii) The addition of latent heat flux by the baroclinic eddies increases the total poleward heat transport, and thus reduces the equator to pole temperature gradient. The sensible heat component is now smaller than its previous value. We may have expected these results intuitively. What we could not foresee, however, was the reduction in stability B that accompanied the increased horizontal flux. This change was confirmed in the full model calculations, and is due to the relative importance of latent heating in the horizontal and vertical fluxes. Allowing for moisture transport by the baroclinic

eddies increases the total meridional flux by nearly 25% (in the grey model), at the same time reducing the sensible heat component. For the vertical transport the latent heat component is less important (22% of the total instead of 45% as with the horizontal transport), and along with the reduced sensible large-scale heating results in reduced stability. Thus, the low stabilities we obtain in the grey radiation model are not caused by the neglect of large-scale vertical latent heat transport (as postulated by Stone, 1973). Instead, we must look to moist convection and radiative effects in the presence of clouds.

iv) In high latitudes, the vertical eddy heating is weak and the strong heating at low levels by the meridional convergence results in net destabilization by the dynamics. This is balanced by radiative stabilization. Held & Suarez (1978) found the same result in their highly truncated two-level primitive equation model.

The full model has detailed calculations of the long and short wave radiation by the atmospheric constituents and by clouds. In view of the consequence of varying tropopause slope found in Chapter 3, we allow an interactive tropopause height in later computations. The slope is found to increase for reduced solar constant, and decrease for reduced ozone amount. Both these changes are consistent with the resulting stability variation (as predicted by Table 3.3). However, it is the existence of a mean slope that is important dynamically, and the small changes in slope for these

experiments are a relatively insignificant factor in the stability balance (i.e. radiative effects dominate).

The tropopause structure that we calculate shows too weak a latitudinal variation. This is due in part to our truncated representation of surface temperature $T_0(\phi)$, which cannot simulate the observed steep temperature gradient near the pole. The assumption of radiative equilibrium also implies the meridional variation of H is smooth. A more realistic profile in extratropical and middle latitudes requires that large-scale motions be considered (as concluded also by Manabe & Wetherald, 1967).

In the grey radiation model we omitted all reference to the surface fluxes and the associated small-scale heating. Section 4.4 describes a reasonable next step that a mechanistic model might take towards a more realistic treatment of these physical processes. The sensible and latent heat provided at the lower boundary are now calculated explicitly. The sum of these two terms is known quite accurately because of our detailed radiation treatment. The partitioning between latent and sensible heat is influenced by the surface wind speed U_g needed in the bulk aerodynamic formulation. We discussed a method for determining this parameter that is consistent with the dynamical parameterization and in accord with observation. In the nominal model we obtain a hemispheric mean Bowen ratio (\bar{H}_S divided by \bar{H}_L) of 1/3.50. The evaporation is somewhat larger than observed because the entire lower boundary provides a moisture supply.

Although the overall intensity of the convective fluxes can respond to the model's climate, we have specified the vertical structure of this small-scale heating. In a simulation climate model, the vertical heating distribution should be free to interact with the large-scale dynamics. The neglect of this feedback has important consequences on the lapse-rate we predict, particularly for hotter climates. Thus, our results correspond more closely to the 'dry' model experiments of Held & Suarez (1978) and Held (1978b). We consider two very different forms of the convective parameter $b(\phi)$, which determines the height of the peak small-scale heating: in the first case b is almost constant with latitude (equation 4.44), while the second experiment has a rapid decrease of $b(\phi)$ between the equator and 45° (equation 6.4). The particular formulation we use significantly affects the mean stability of the basic state, although the changes in the hemispheric mean variables with other model parameters (e.g. S_0) are much less sensitive to our choice of b .

Clouds have an important influence on the radiative heating distribution within the troposphere. Their net effect (LW and SW heating above and below the clouds) is to cool the atmosphere (and heat the surface), and also to stabilize the vertical temperature profile. We have reduced the observed multilayer arrangement to a single effective cloud layer, which is all the sophistication one can justify in what is essentially a two layer model. This single cloud

layer is assumed to be a black body in the infrared, and to have negligible effect on the net heating at the tropopause (see our Figure 5.3 for the long-wave component, and Figure 15 in Lacis & Hansen, 1974 for the short-wave). Various cloud-height feedback assumptions are considered. A parameterization intermediate between fixed height and fixed temperature is used in most of the calculations. As expected, this reduces the model sensitivity compared to a constant cloud temperature assumption which prevents the clouds from compensating for surface temperature and lapse rate changes. The stabilization is not as great as for the commonly used fixed cloud height case, which does not represent observed latitudinal variations at all realistically (Fig. 5.1a).

In the full model we find the addition of small-scale heating and an improved radiative treatment results in a stability B and meridional gradient A more in accord with atmospheric data. Owing to the bias introduced by a single cloud layer (section 5.3.2) and the arbitrary choice of the small-scale heating parameter b , the exact value of the stability is uncertain. (Quantitative results are not to be expected in a mechanistic model in any case). The upward flux by baroclinic eddies is substantially reduced in the presence of a further vertical transport mechanism. This is analogous to the reduction in poleward SH flux when latent heat transport was added.

Several experiments were carried out where we varied the external parameters (solar constant, CO_2 and O_3 amounts, etc.).

Increasing the carbon dioxide amount produces increased thermal emission to space and more downward long-wave radiation at the ground. This results in higher surface temperatures and smaller vertical stability. The ground temperature response is more sensitive than most recent calculations (Table 6.9) where cloud heights were specified.

Reducing the ozone column amount reduces temperatures at upper levels, and increases the short-wave radiation reaching the ground. A greater tropospheric depth and increased lapse rate allow the mean surface temperature to increase (between 1.1 and 1.3 °C for a 50% depletion of O₃), in contrast to the results of the few 1-D radiative-convective equilibrium studies that are available. However, we have neglected LW absorption by the 9.6 μm ozone band. Including this effect will reduce the downward LW flux at the ground (for 50% O₃ depletion) and tend to compensate for the increased SW flux. Using Sasamori's (1968) formula for ozone long-wave absorption,

$$\bar{A}_3(u_3) = 0.00921 \ln u_3 + 0.07480 \quad (7.4)$$

we can calculate (Table 7.1) the total absorption by ozone.

Table 7.1: Fractional ozone absorption of LW and SW radiation (hemispherically averaged).

	LW	SW
Present O ₃ amounts	0.06347	0.03187
50% O ₃ depletion	<u>0.05709</u>	<u>0.02276</u>
Change in absorption	0.00638	0.00911

This table would imply that removal of ozone has a relatively larger effect on the absorption of SW radiation than on the thermal absorption. Definite conclusions cannot be drawn from these numbers however, since long and short wave absorption by water vapor decreases the effect of O_3 changes on the radiation field at the ground. Nevertheless, we might expect the surface temperature variation (with the 9.6 μm band included) to be in the same direction as we have calculated (Table 6.8).

We have also neglected ozone LW absorption when calculating the tropopause height $H(\phi)$. (This was necessary because of the isothermal stratosphere approximation). It is not clear what effect this will have on the resultant surface temperature.

Reducing the solar constant (Table 6.11) by 2% produces a ground temperature change of approximately -2.8 $^{\circ}\text{C}$. This difference is smaller than found in GCM calculations (-4.4 $^{\circ}\text{C}$) by Wetherald and Manabe (1975), owing in part to our choice of a lower ice albedo. Closer agreement with other values in Table 6.11 (Manabe and Wetherald, 1967; and Ohring and Adler, 1978) is fortuitous. Ohring and Adler fixed the cloud heights which reduces their model's sensitivity unrealistically. Manabe and Wetherald used a one-dimensional model where the fixed lapse rate also reduces sensitivity.

The lapse rate changes predicted by our model are more appropriate to cold (or dry) climates where moist convection becomes relatively less important. Under these circumstances, we predict the mean lapse rate to decrease uniformly as the solar constant is reduced, in line with present high latitude changes found by Wetherald and Manabe (1975) and Held (1978b).

However, in view of the uncertainties associated with the vertical fluxes that we discussed earlier in this summary, our results should be interpreted as indicating only potentially important effects accompanying lapse-rate feedback.

The intensity of the hydrologic cycle (as measured by surface evaporative flux) is found to be extremely sensitive to the change in solar constant. The percentage increase is about 4.4 times as much as that of S_0 . This is almost exactly the result of GCM calculations (Wetherald and Manabe, 1975), and highlights the usefulness of mechanistic models. Wetherald and Manabe list a number of factors they believe responsible for this sensitivity. Our model indicates that the decisive factor in the hydrologic response is the strong dependence of saturation vapor pressure on temperature (i.e. the Clausius-Clapeyron relation). Thus, the same sensitivity is found for \overline{H}_L , although our response of \overline{H}_B (net upward LW radiation at the surface) is considerably weaker than theirs (by about 50%), due to opposite lapse-rate variation and a different cloud temperature feedback. (The smaller sensible heat flux \overline{H}_S also exhibits a different variation, of course).

In conclusion, we find this process model is useful in suggesting the relative importance of various processes in more complicated simulation models. However, in view of the many simplifying assumptions we have made, this study should not be interpreted as giving quantitative answers to climate sensitivity problems.

Appendices

A1 Leovy parameterization (referenced by Section 1.4)

From the Clausius-Clapeyron relation (1.10), we have

$$\frac{\partial q_s}{\partial T}(\bar{T}) = \frac{L_v}{R_v \bar{T}^2} q_s$$

$$\frac{\partial^2 q_s}{\partial T^2}(\bar{T}) = \frac{L_v}{R_v \bar{T}^3} q_s \left(\frac{L_v}{R_v \bar{T}} - 2 \right)$$

$$\frac{\partial^3 q_s}{\partial T^3}(\bar{T}) = \frac{L_v}{R_v \bar{T}^4} q_s \left[\left(\frac{L_v}{R_v \bar{T}} \right)^2 - 6 \frac{L_v}{R_v \bar{T}} + 6 \right]$$

assuming $\frac{L_v}{R_v}$ is independent of temperature.

$$\text{Ratio of terms: } \frac{\frac{\partial^2 q_s}{\partial T^2}(\bar{T})}{\frac{\partial q_s}{\partial T}(\bar{T})} = \frac{1}{\bar{T}} \left[\frac{L_v}{R_v \bar{T}} - 2 \right] = 0.0654 \quad \text{for } \bar{T} = 273 \text{ K}$$

and $\frac{L_v}{R_v} = 5419 \text{ K}$

$$\frac{\frac{\partial^3 q_s}{\partial T^3}(\bar{T})}{\frac{\partial q_s}{\partial T}(\bar{T})} = \frac{1}{\bar{T}^2} \left[\left(\frac{L_v}{R_v \bar{T}} \right)^2 - 6 \frac{L_v}{R_v \bar{T}} + 6 \right] = 0.00377$$

The eddy correlations are obtained from Stone's model (1972b).

If

$$v' = \text{Re } V_0(z) e^{ik(x+ct)}$$

$$T' = \text{Re } T_0(z) e^{ik(x+ct)}$$

where the amplitudes V_0 , T_0 and phase speed c are complex, then

averaging the correlations over wavelength gives us the result

$$\overline{v'T'} = \overline{\text{Re } v \text{ Re } T} = \frac{1}{2} \text{Re } V_0 T_0^* \quad , \text{ or}$$

$$\frac{1}{2} \text{Re } V_0^* T_0$$

where the factor of $\frac{1}{2}$ comes from averaging $\sin^2\theta$ or $\cos^2\theta$ over a period.

Second order correlation $\overline{v'T'^2} \equiv 0$ upon averaging.

Third order correlation $\overline{v'T'^3} = \frac{3}{8} T_0 T_0^* \text{Re } V_0 T_0^*$, or
 $\frac{3}{8} T_0 T_0^* \text{Re } V_0^* T_0$

AppendixA2 Varying vertical scale H in Stone's model (referenced by Section 2.1)

Refer to Stone (1973). We use the equations and constants of that paper although some of the notation is changed to be consistent with this thesis.

$$\text{Temperature equation: } \frac{\partial}{\partial y} \overline{v'\theta'} + \frac{\partial}{\partial z} \overline{w'\theta'} = \frac{T_r - T}{\tau} \quad (\text{A2.1})$$

$$\text{where } \overline{v'\theta'} = -0.864 \frac{g H_S^2}{f \langle T \rangle} A B \frac{\sqrt{1+Ri}}{Ri} \frac{Y}{L} \left(1 - \frac{Y}{L}\right)$$

$$\overline{w'\theta'} = 0.360 f H_S^2 \frac{B}{Ri \sqrt{1+Ri}} \frac{z}{H} \left(1 - \frac{z}{H}\right)$$

$$Ri = \frac{f^2 \langle T \rangle}{g} \frac{B}{A^2}, \quad H_S = \frac{R \langle T \rangle}{g}$$

$$\tau = \frac{c_p P_0}{\sigma g \langle T \rangle^3}$$

and $A = \left\langle \frac{\partial \theta}{\partial y} \right\rangle$ is expressed units of $^{\circ}\text{K}/(100 \text{ km})$, $B = \left\langle \frac{\partial \theta}{\partial z} \right\rangle$ in $^{\circ}\text{K}/\text{km}$.

$$\langle () \rangle = \frac{1}{HL} \int_0^L \int_0^H () dz dy$$

The only change so far from Stone's paper is that we have distinguished the scale height H_S from the scale H of the vertical dependence.

Case 1: $H = H_S$

This is now exactly like Stone's case, except that we will correct his estimate of $\langle T \rangle$. The mean radiative equilibrium temperature $\langle T_r \rangle$ is given by grey radiation theory to be

$$\langle T_R \rangle = \frac{\langle T_e \rangle}{2^{1/4} H} \int_0^H \left(1 + \frac{3\tau^*}{2} e^{-z/h}\right)^{1/4} dz$$

$$\text{or } \langle T_R \rangle = \frac{\langle T_e \rangle}{2^{1/4}} \int_0^1 (1 + 6e^{-kx})^{1/4} dx \quad (\text{A2.2})$$

where $x = \frac{z}{H}$, $k = \frac{H}{h}$ and the absorber optical depth at the ground τ^* is 4. Assuming that the water vapor scale height $h \approx 2$ km and anticipating $H = H_S \approx 8$ km, we set $k = \frac{H}{h} = 4$. Then, it is very simple to integrate (A2.2) numerically, resulting in

$$\langle T_R \rangle = 1.0229 \langle T_e \rangle$$

On the other hand, Stone evaluated (A2.2) by analytic approximation, and on substitution of the relevant constants his equation (3.18) gives

$$\langle T_R \rangle = 0.9394 \langle T_e \rangle$$

This is the reason for his unrealistically low tropospheric mean temperature $\langle T \rangle$ of 235K. Otherwise, all our calculations follow Stone exactly. The derived radiative parameters and predicted gradients A and B are shown in Table A1.

Case 2: $H = \text{tropopause height} = 12$ km

Now (A2.2) is evaluated assuming $k = \frac{H}{h} = 6$, and in the manipulations of (A2.1) the vertical average is taken over this new H. The results, shown in Table A1, do not differ greatly from Case 1 or from Stone's original values which are reproduced for comparison.

Table A1:

	<u>Input Parameters</u>						<u>Output Values</u>		
	$\langle T_e \rangle$ °K	$\langle T \rangle$ °K	H_s km	τ $\times 10^7$ sec	A_r °K/(100km)	B_r °K/km	A °K/(100km)	B °K/km	R_i
Stone's original values	250	235	6.86	1.41	-0.892	-10.0	-0.378	1.45	25.7
Stone's model with 'corrected' $\langle T \rangle$ calculation	250	256	7.57	1.08	-0.972	-8.4	-0.422	1.62	25.2
Result with $H = 12$ km	250	241	7.14	1.28	-0.917	-2.1	-0.388	1.57	27.2

Appendix

A3 Comparison of horizontal temperature gradients $\frac{\partial T}{\partial \phi}$ and $\frac{\partial \theta}{\partial \phi}$.
(referenced by Section 2.2.2.)

The mean meridional potential temperature gradient A is defined by

(2.30) of Section 2.2.2.

$$A = \frac{\pi}{2L\bar{H}} \int_0^{\pi/2} \int_0^H(\phi) \frac{\partial \theta}{\partial \phi} dz \cos \phi d\phi \quad (\text{A3.1})$$

Substituting from (2.31),

$$\begin{aligned} A &= \frac{\pi c_2}{L\bar{H}} \int_0^{\pi/2} \int_0^H [\kappa\gamma (1 - \frac{\beta z}{T_0})^{1-\kappa\gamma} - (\kappa\gamma - 1) (1 - \frac{\beta z}{T_0})^{-\kappa\gamma}] dz \sin \phi \cos^2 \phi d\phi \\ &= \frac{\pi c_2}{\beta L\bar{H}} \int_0^{\pi/2} T_0 \sin \phi \cos^2 \phi [\frac{2}{2-\kappa\gamma} - \frac{\kappa\gamma}{2-\kappa\gamma} (1 - \frac{\beta H}{T_0})^{2-\kappa\gamma} - (1 - \frac{\beta H}{T_0})^{1-\kappa\gamma}] d\phi \end{aligned}$$

We expand the last two terms in $\epsilon(\phi) = \frac{\beta H(\phi)}{T_0(\phi)} \approx 0.3$

The lowest order parts cancel with the constant $\frac{2}{2-\kappa\gamma}$ and

$$\begin{aligned} A &= \frac{\pi c_2}{L\bar{H}} \int_0^{\pi/2} H \sin \phi \cos^2 \phi \{ 1 + \frac{\kappa\gamma(1-\kappa\gamma)}{6} \epsilon^2 [1 + \frac{(1+\kappa\gamma)}{2} \epsilon + \\ &\quad \frac{3}{20} (1+\kappa\gamma)(2+\kappa\gamma)\epsilon^2 + O(\epsilon^3)] \} d\phi \end{aligned}$$

Since the expression involving ϵ varies slowly with latitude, an adequate approximation for this integral can be found by setting

$$\epsilon = \bar{\epsilon}^* = \frac{\beta \bar{H}}{\bar{T}_0} = 0.299 \quad \text{for } \beta = 6.5, \bar{H} = 13, \bar{T}_0 = 283$$

$$\text{Thus, } A \approx [1 + \delta(\bar{\epsilon}^*)] \frac{\pi c_2}{3L} n_2 = (1 + \delta) \left\langle \frac{1}{r} \frac{\partial T}{\partial \phi} \right\rangle \quad (\text{A3.2})$$

$$\text{where } \delta(\epsilon) \approx \frac{\frac{1}{6} \kappa\gamma (1-\kappa\gamma) \epsilon^2}{(1 - \frac{1}{2}\epsilon)(1+\kappa\gamma)} = -0.017 \quad \text{for } \epsilon = 0.3, \beta = 6.5$$

Hence, the two gradients differ by only 2.3%.

Appendix

A4 Integrated Leory factor L_y (referenced by Section 3.1.1.)

From Section 3.1.1., the integrated Leory factor L_y is defined as

$$L_y = 1 + \int_0^1 \Lambda(\phi_\alpha, x) \check{L}(\phi_\alpha, x) dx$$

where $\check{L}(\phi, x)$ is given by equation 2.6 and $\Lambda(\phi, x)$ by (2.15).

Thus,

$$L_y = 1 + 0.6780 h_0 e^{\frac{a}{T_3}} T_3^2 K_S \left\{ \frac{(e^{-\frac{a}{T_0}} - e^{-\frac{a}{T_H}})}{a \beta H} - \int_{x_*}^1 \left(\frac{e^{-\lambda x_*} - e^{-\lambda x}}{e^{-\lambda x_*} - e^{-\lambda}} \right)^x e^{-\frac{a}{T}} \frac{dx}{T^2} \right\}$$

where $T(x) = T_0 - \beta Hx$.

To evaluate the last integral, we set

$$y = x - x_* \quad \text{and} \quad \varepsilon = \frac{\beta H}{T_*}, \quad \eta = \frac{\varepsilon a}{T_*} = \frac{a \beta H}{T_*^2}$$

where $T_* = T_0 - \beta Hx_*$. Then $T = T_* (1 - \varepsilon y)$

Typical values are $\lambda = 2.5$, $x_* = 0.2$, $\varepsilon = 0.3$, $\frac{a}{T_*} = 20$, $\eta = 6$

Then

$$\begin{aligned} \int_{x_*}^1 (e^{-\lambda x_*} - e^{-\lambda x}) \frac{e^{-\frac{a}{T}}}{T^2} dx &= e^{-\lambda x_*} \frac{e^{-\frac{a}{T_*}}}{T_*^2} \int_0^{(1-x_*)} \frac{e^{-\frac{a}{T_*} (1-x_*)}}{(1-e^{-\lambda y})} \frac{e^{-\frac{a}{T_*} (\frac{1}{1-\varepsilon y} - 1)}}{(1-\varepsilon y)^2} dy \\ &= \lambda e^{-\lambda x_*} \frac{e^{-\frac{a}{T_*}}}{T_*^2} \left\{ \int_0^{(1-x_*)} y \left[1 - \frac{1}{2} \lambda y + \frac{1}{6} (\lambda y)^2 - \dots \right] \left[1 + 2\varepsilon y + 3\varepsilon^2 y^2 + \dots \right] \right. \\ &\quad \left. e^{-\eta y} [1 - \varepsilon \eta (y^2 + \varepsilon y^3 + \dots)] + \frac{1}{2} \varepsilon^2 \eta^2 (y^2 + \varepsilon y^3 + \dots) - \dots \right\} dy \end{aligned}$$

after approximating the various terms by their series expansions.

The integrand is zero at $y = 0$, rises to a maximum near $y = \frac{1}{\eta}$ and thereafter decreases rapidly due to the $e^{-\eta y}$ factor. Therefore, we are able to replace the upper limit $(1 - x_*)$ by infinity and take advantage of the relation

$$\int_0^{\infty} y^k e^{-\eta y} dy = - \left[e^{-\eta y} \sum_{r=0}^k \frac{k!}{(k-r)!} \frac{y^{k-r}}{\eta^{r+1}} \right]_0^{\infty} \equiv \frac{k!}{\eta^{k+1}}$$

Assuming ϵ is small but η is $O(1)$, we order the terms and integrate.

$$\begin{aligned} \int_{x_*}^1 (e^{-\lambda x_*} - e^{-\lambda x}) \frac{e^{-\frac{a}{T}}}{T^2} dx &\approx \lambda e^{-\lambda x_*} \frac{e^{-\frac{a}{T_*}}}{T_*^2} \left\{ \int_0^{\infty} e^{-\eta y} \left[y - \frac{1}{2} \lambda y^2 + \frac{1}{6} \lambda^2 y^3 - \dots \right] x \right. \\ &\quad \left. \left[1 + \epsilon(2y - \eta y^2) + \epsilon^2(3y^2 - 3\eta y^3 + \frac{1}{2} \eta^2 y^4) + \dots \right] dy \right\} \\ &= \frac{\lambda}{\eta^2} e^{-\lambda x_*} \frac{e^{-\frac{a}{T_*}}}{T_*^2} \left\{ \left[1 - \frac{\lambda}{\eta} + \left(\frac{\lambda}{\eta}\right)^2 - \left(\frac{\lambda}{\eta}\right)^3 + \dots + \left(-\frac{\lambda}{\eta}\right)^{k-1} + \dots \right] \right. \\ &\quad \left. - 2! \frac{\epsilon}{\eta} \left[1 - \frac{3\lambda}{\eta} + 6\left(\frac{\lambda}{\eta}\right)^2 - 10\left(\frac{\lambda}{\eta}\right)^3 + \dots + \left(-\frac{\lambda}{\eta}\right)^{k-1} \frac{k(k+1)}{2} + \dots \right] \right. \\ &\quad \left. + 3! \left(\frac{\epsilon}{\eta}\right)^2 \left[1 - 6\frac{\lambda}{\eta} + 20\left(\frac{\lambda}{\eta}\right)^2 - 50\left(\frac{\lambda}{\eta}\right)^3 + \dots + \left(-\frac{\lambda}{\eta}\right)^{k-1} \frac{k(k+1)^2(k+2)}{12} + \dots \right] \right. \\ &\quad \left. + O\left(\frac{\epsilon}{\eta}\right)^3 \right\} \\ &= \frac{\lambda}{\eta(\lambda+\eta)} e^{-\lambda x_*} \frac{e^{-\frac{a}{T_*}}}{T_*^2} \left\{ 1 - \frac{2! \frac{\epsilon}{\eta}}{\left(1+\frac{\lambda}{\eta}\right)^2} + 3! \frac{\left(\frac{\epsilon}{\eta}\right)^2 \left(1-\left(\frac{\lambda}{\eta}\right)^2\right)}{\left(1+\frac{\lambda}{\eta}\right)^4} + O\left(\frac{\epsilon}{\eta}\right)^3 \right\} \end{aligned}$$

For the numerical values above, successive terms in this series are calculated to be

$$\{ 1.0 - .0498 + .003078 - \dots \}$$

ie. They decrease very rapidly, and in fact we will take only the leading behavior and approximate the series by 1.0. Since the entire term is only about 5% of the total $\int_0^1 \Lambda \mathcal{L} dx$, the error is very small. This gives us the final form of equation (3.8).

AppendixA5 Analytical approximation to water vapor amount integral

(Referenced by Sections 3.2 and 4.2.1.)

We consider the column amount integral (4.14)

$$u_1(z) = u_1(H) + \epsilon \frac{k_1 T_3^{\frac{1}{2}}}{g P_0} \int_{P_H}^P \frac{e^{-\frac{a}{T} p} p^{-\frac{1}{2}}}{(1-k_1 e^{-\frac{a}{T}})} dp \quad (\text{A5.1})$$

where $k_1 = \frac{h_0 e_3}{P_0} \exp\left(\frac{a}{T_3}\right)$. The optical depth integral (3.12) is similar and can be handled the same way. Changing variables to $x = \frac{a}{T}$ we have

$$u_1(z) = u_1(H) + \frac{\epsilon \gamma P_0 k_1 T_3^{\frac{1}{2}} a^{2\gamma - \frac{1}{2}}}{G T_0^{2\gamma}} \int_{\frac{a}{T}}^{\frac{a}{T_H}} \frac{e^{-x}}{(1-k_1 e^{-x}) x^{2\gamma + \frac{1}{2}}} dx$$

This integral cannot be evaluated exactly (even for $k_1=0$ in the denominator). However, we will need to calculate the water vapor amount many times in the radiative calculations, so a numerical integration is out of the question. Instead, we take advantage of the rapid decrease of the exponential factor to approximate the integral analytically. By way of illustration, consider $k_1=0$ in the denominator of the integral, and $G = 2\gamma + \frac{1}{2}$. Then

$$\begin{aligned} \int_{x_0}^{x_1} \frac{e^{-x}}{x^G} dx &= \frac{e^{-x_0}}{x_0^G} \int_0^{(x_1-x_0)} \frac{e^{-y}}{\left(1 + \frac{y}{x_0}\right)^G} dy \\ &= \frac{e^{-x_0}}{x_0^G} \int_0^D e^{-y} \left[1 - \frac{Gy}{x_0} + \frac{G(G+1)}{2} \left(\frac{y}{x_0}\right)^2 - \dots \right] dy \end{aligned}$$

Now integrate by parts. The first few terms give a good approximation to the integral (even though the series eventually diverges). In the model, the maximum value of $\frac{y}{x_0} = \frac{D}{x_0} \approx \frac{1}{2}$. In the general case, $k_1 \neq 0$ (This only becomes important near the ground where the water vapor mixing ratio $m = \frac{\epsilon e}{p-e}$ should not be approximated by $\frac{\epsilon e}{p}$). We find

$$u_1(z) = u_1(H) + \frac{\epsilon h_0 e_3}{g} e^{-a(\frac{1}{T} - \frac{1}{T_3})} \frac{\gamma}{a} \sqrt{T_3 T_0} \left(\frac{T}{T_0}\right)^G \frac{F_1}{(1 + \frac{\mu T}{a})^\eta} \quad (\text{A5.2})$$

where $G = 2\gamma + \frac{1}{2}$

$$F_1 = \frac{1}{K} \ln \left(\frac{1 - K e^{-D}}{1 - K} \right); \quad K = k_1 e^{-\frac{a}{T}}$$

$$D = a \left(\frac{1}{T_H} - \frac{1}{T} \right) > 0$$

and μ and η are functions of K , G and D defined by

$$\mu \eta = \frac{G F_2}{F_1}$$

$$\mu(\eta+1) = 2(G+1) \frac{F_3}{F_2}$$

μ and η are chosen so the Taylor expansion of $(1 - \frac{\mu T}{a})^{-\eta}$ matches exactly the first two terms in an asymptotic expansion of the integral.

$$F_2 = \left(1 + \frac{K}{4} + \frac{K^2}{9} + \frac{K^3}{16} + \dots\right) - e^{-D} \left(1 + \frac{K}{4} e^{-D} + \frac{K^2}{9} e^{-2D} + \dots\right) + \frac{D}{K} \ln(1 - K e^{-D})$$

$$F_3 = \left(1 + \frac{K}{8} + \frac{K^2}{27} + \frac{K^3}{64} + \dots\right) - e^{-D} \left(1 + \frac{K}{8} e^{-D} + \dots\right)$$

$$- e^{-D} \left(1 + \frac{K}{4} e^{-D} + \dots\right) + \frac{D^2}{2K} \ln(1 - K e^{-D})$$

K is small. For $h_0 = 1$ and $T = 300$ K, $K = 0.036$. For temperatures away from the surface we can simply set $K = 0$ and the expressions for F_1, F_2, F_3 reduce to those given in Section 3.2 (using the symbols G_1, G_2, G_3). In fact, all terms of order Ke^{-D} ($\sim 8 \times 10^{-6}$) can be neglected. For D very close to zero (in practice less than .01) we use simplified forms to avoid underflow problems in the computer.

$$F_1 \approx D - \frac{1}{2} D^2$$

$$\mu \approx \frac{D}{6} \left[G \left(1 + \frac{D}{6} \right) + \left(4 - \frac{D}{3} \right) \right]$$

$$\eta \approx \left[\frac{4}{3} \frac{G+1}{G} \left(1 - \frac{5}{4} D + \frac{29}{120} D^2 \right) - 1 \right]^{-1}$$

These analytical approximations prove to be extremely accurate.

For example, taking $G = 11$, $T_H = 200$ and $T = 280$, let us evaluate

the integral $I = \int_{x_0}^{x_1} \frac{e^{-x}}{x^G} dx$ by numerical quadrature and by the analytical approximation $I^1 = \frac{e^{-x_0} - e^{-x_1}}{x_0^G \left(1 + \frac{\mu}{x_0} \right)^\eta}$

Using a straight forward trapezium rule quadrature with 1000 subdivisions we calculate

$$I = 1.77847 \times 10^{-23} \quad \text{while the analytical method gives } I^1 = 1.78328 \times 10^{-23} \quad \text{i.e. a 0.27\% error.}$$

In this case where D is large, we can evaluate the integral with a 0.33% error by neglecting all but the zero order terms in the functions F_1, F_2, F_3 . In general, the more complete expressions for μ and η are necessary. The approximation is found to be

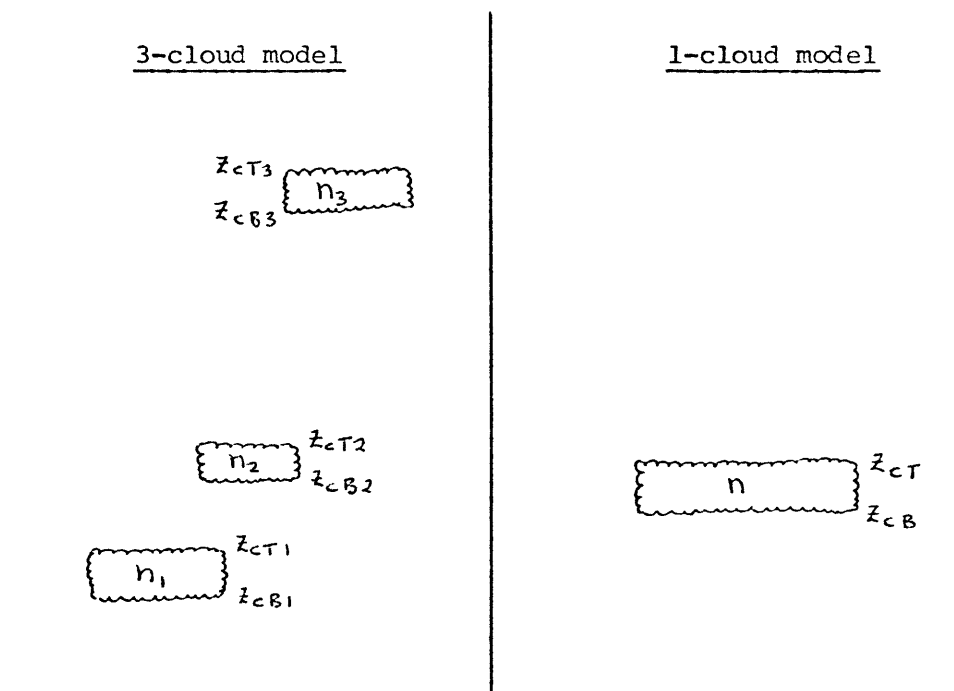
accurate to better than 0.5% over all parameter ranges likely to be encountered in the model, with the largest errors occurring at high temperatures.

Appendix

A6 Appropriate cloud-height weighting for long-wave flux calculations

(Referenced by Section 5.1)

We want to calculate the appropriate top and base for a single effective cloud layer, such that the long-wave fluxes at the upper and lower boundaries of the atmosphere are the same as for a 3 cloud layer model.



Let n_1, n_2, n_3 be the amounts of low, middle and high cloud respectively in the 3-layer model. The cloud-base height and cloud-top height in each layer is z_{cBj} and z_{cTj} , respectively ($j = 1, 2, 3$). If the long-wave flux $F(z)$ has subscript 'R' for clear skies and 'cj' for cloudy skies, then the boundary fluxes can be written as follows.

3-clouds:

For $0 \leq z \leq z_{CB1}$;

$$F(z)\downarrow = [1 - n_1 - n_2(1-n_1) - n_3(1-n_2)(1-n_1)] F_R(z)\downarrow + n_1 F_{C1}(z)\downarrow \\ + n_2(1-n_1) F_{C2}(z)\downarrow + n_3(1-n_2)(1-n_1) F_{C3}(z)\downarrow$$

For $z \geq z_{CT3}$;

$$F(z)\uparrow = [1 - n_3 - n_2(1-n_3) - n_1(1-n_2)(1-n_3)] F_R(z)\uparrow \\ + n_1(1-n_2)(1-n_3) F_{C2}(z)\uparrow + n_2(1-n_3) F_{C2}(z)\uparrow + n_3 F_{C3}(z)\uparrow$$

1-cloud:

For $0 \leq z \leq z_{CB}$;

$$F(z)\downarrow = (1-n) F_R(z)\downarrow + n F_C(z)\downarrow$$

For $z \geq z_{CT}$;

$$F(z)\uparrow = (1-n) F_R(z)\uparrow + n F_C(z)\uparrow$$

The mean cloud amounts n is determined by matching the clear sky fluxes at the boundaries (i.e. $z \leq z_{CB1}$ or $z \geq z_{CT3}$)

$$n = n_1 + n_2(1-n_1) + n_3(1-n_2)(1-n_1) \\ = n_3 + n_2(1-n_3) + n_1(1-n_2)(1-n_3)$$

The effective cloud heights, z_{CB} and z_{CT} , can be found similarly if we assume the long-wave flux F_C varies linearly with cloud height (see Table 5.3) i.e. $F_C(z)\uparrow = a_T + b_T z_{CT}$

$$F_C(z)\downarrow = a_B + b_B z_{CB} \quad (\text{where the}$$

coefficients a_T, b_T, a_B, b_B are functions of z in general).

Then, we have

$$z_{\text{CB}} = \frac{1}{n} [n_1 z_{\text{CB1}} + n_2(1-n_1) z_{\text{CB2}} + n_3(1-n_2)(1-n_1) z_{\text{CB3}}]$$

$$z_{\text{cT}} = \frac{1}{n} [n_1(1-n_2)(1-n_3) z_{\text{cT1}} + n_2(1-n_3) z_{\text{cT2}} + n_3 z_{\text{cT3}}]$$

The two models now predict the same fluxes at the ground and at the top of the atmosphere (within the accuracy of the linearization assumption). However, the fluxes at mid-troposphere, $z = \frac{1}{2} H$, will not coincide. This produces a systematic bias in the long-wave cooling distribution within the atmosphere (Section 5.3.2.).

REFERENCES

- Acton, F. S., 1970: Numerical Methods that Work. New York, Harper & Row, 541 pp.
- Arakawa, A., and W. H. Schubert, 1974: Interaction of a cumulus cloud ensemble with the large-scale environment, Part 1. J. Atmos. Sci., 31, 674-701.
- Budyko, M. I., 1956: Teplevoi Balans Zemnoi Poverkhnosti [English translation: N. A. Stepanova, 1958: The Heat Balance of the Earth's Surface. Washington, D.C., O.T.S., U.S. Dept. of Commerce, 259 pp]. Leningrad, Gidrometeor, 255 pp.
- 1969: The effect of solar radiation variations on the climate of the earth. Tellus, 21, 611-619.
- Burrows, W. R., 1976: A diagnostic study of atmospheric spectral kinetic energies. J. Atmos. Sci., 33, 2308-2321.
- Cess, R. D., 1974: Radiative transfer due to atmospheric water vapor: global considerations of the Earth's energy balance. J. Quant. Spectros. & Radiat. Transfer, 14, 861-871.
- 1975: Global climate change: an investigation of atmospheric feedback mechanisms. Tellus, 27, 193-198.
- 1976: Climate change: an appraisal of atmospheric feedback mechanisms employing zonal climatology. J. Atmos. Sci., 33, 1831-1843.
- Charney, J. G., and M. E. Stern, 1962: On the stability of internal baroclinic jets in a rotating atmosphere. J. Atmos. Sci., 19, 159-172.
- Chiu, W., and R. S. Greenfield, 1959: The relative importance of different heat-exchange processes in the lower stratosphere. J. Meteor., 16, 271-280.
- Coakley, J. A., Jr., 1977: Feedbacks in vertical-column energy balance models. J. Atmos. Sci., 34, 465-470.
- 1979: A study of climate sensitivity using a simple energy balance model. J. Atmos. Sci., 36, 260-269.
- Cox, S. K. 1969: Radiation models of mid-latitude synoptic features. Mon. Wea. Rev., 97, 637-651.
- Crutzen, P. J., 1972: S.S.T.'s: A threat to the earth's ozone shield. Ambio, 1, 41-51.

- Deardorff, J. W., 1972: Numerical investigation of neutral and unstable planetary boundary layers. J. Atmos. Sci., 29, 91-115.
- Dopplnick, T. G., 1970: Global radiative heating of the earth's atmosphere. M.I.T. Planetary Circulations Project Report #24, 128 pp.
- 1971: The energetics of the lower stratosphere including radiative effects. Quart. J. Roy. Meteor. Soc., 97, 209-237.
- Eady, E. T., 1949: Long waves and cyclone waves. Tellus, 1, 33-52.
- Fairbridge, R. W. (Ed.), 1967: The Encyclopedia of Atmospheric Sciences and Astrogeology. Reinhold Publishing Corp., New York, 1200 pp.
- Gal-Chen, T., and S. H. Schneider, 1976: Energy-balance climate modeling: comparison of radiative and dynamic feedback mechanisms. Tellus, 28, 108-121.
- Gall, R., 1976: A comparison of linear baroclinic instability theory with the eddy statistics of a general circulation model. J. Atmos. Sci., 33, 349-373.
- Goody, R. M., 1964: Atmospheric Radiation. Oxford, Clarendon Press, 436 pp.
- Green, A. E. S., 1964: Attenuation by ozone and the earth's albedo in the middle ultraviolet. Appl. Opt., 3, 203-208.
- Green, J. S. A., 1970: Transfer properties of large-scale eddies and the general circulation of the atmosphere. Quart. J. Roy. Meteor. Soc., 96, 157-185.
- Groen, P., 1967: The Waters of the Sea. Van Nostrand, London, 328 pp.
- Hantel, M., 1976: On the vertical eddy transports in the Northern Hemisphere: 1. Vertical eddy heat transport for summer and winter. J. Geophys. Res., 81, 1577-1588.
- Held, I. M. 1978a: The vertical scale of an unstable baroclinic wave and its importance for eddy heat flux parameterizations. J. Atmos. Sci., 35, 572-576.
- 1978b: The tropospheric lapse rate and climatic sensitivity: Experiments with a two-level atmospheric model. J. Atmos. Sci., 35, 2083-2098.

- Held, I. M., and M. J. Suarez, 1978: A two-layer primitive equation atmospheric model designed for climatic sensitivity experiments. J. Atmos. Sci., 35, 206-229.
- Hering, W., and T. R. Borden, Jr., 1964: Ozonesonde observations over North America. Vol 2, Environ. Res. Papers No. 38, AFCRL-64-30 (II).
- Hildebrand, F. B., 1962: Advanced Calculus for Applications. Prentice-Hall Inc., New Jersey, 646 pp.
- Kraus, E. B., 1972: Atmosphere-Ocean Interaction. Clarendon Press, Oxford, 275 pp.
- Lacis, A. A., and J. E. Hansen, 1974: A parameterization for the absorption of solar radiation in the Earth's atmosphere. J. Atmos. Sci., 31, 118-133.
- Leovy, C. B., 1973: Exchange of water vapor between the atmosphere and surface of Mars. Icarus, 18, 120-125.
- London, J. L., 1957: A study of the atmospheric heat balance. New York University Report AF 19(122)-165, 99 pp.
- Manabe, S., 1969: Climate and the ocean circulation: I. The atmospheric circulation and the hydrology of the earth's surface. Mon. Wea. Rev., 97, 739-774.
- , D. G. Hahn and J. L. Holloway, 1974: The seasonal variation of the tropical circulation as simulated by a global model of the atmosphere. J. Atmos. Sci., 31, 43-83.
- and F. Möller, 1961: On the radiative equilibrium and heat balance of the atmosphere. Mon. Wea. Rev., 89, 503-532.
- , J. Smagorinsky and R. F. Strickler, 1965: Simulated climatology of a general circulation model with a hydrologic cycle. Mon. Wea. Rev., 93, 769-798.
- and R. F. Strickler, 1964: Thermal equilibrium of the atmosphere with a convective adjustment. J. Atmos. Sci., 21, 361-385.
- and R. T. Wetherald, 1967: Thermal equilibrium of the atmosphere with a given distribution of relative humidity. J. Atmos. Sci., 24, 241-259.
- Miller, A. J., 1970: The transfer of kinetic energy from the troposphere to the stratosphere. J. Atmos. Sci., 27, 388-393.

- Möller, F., and S. Manabe, 1961: Über das Strahlungsgleichgewicht der Atmosphäre. Zeitschrift für Meteorologie, 15, 3-8.
- Moura, A.D., and P. H. Stone, 1976: The effects of spherical geometry on baroclinic instability. J. Atmos. Sci., 33, 602-616.
- Newell, R. E., J. W. Kidson, D. G. Vincent and G. J. Boer, 1974: The General Circulation of the Tropical Atmosphere and Interactions with Extratropical Latitudes. Vol 2, MIT Press, Cambridge, 371 pp.
- North, G. R., 1975: Theory of energy-balance climate models. J. Atmos. Sci., 32, 2033-2043.
- Ohring, G., and S. Adler, 1978: Some experiments with a zonally averaged climate model. J. Atmos. Sci., 35, 186-205.
- Oort, A. H., and J. P. Peixoto, 1974: The annual cycle of the energetics of the atmosphere on a planetary scale. J. Geophys. Res., 79, 2705-2719.
- and E. M. Rasmusson, 1971: Atmospheric Circulation Statistics. N.O.A.A. Prof. Paper 5, 323pp.
- Palmén, E., and C. W. Newton, 1969: Atmospheric Circulation Systems. Academic Press, New York, 603 pp.
- Pedlosky, J., 1970: Finite-amplitude baroclinic waves. J. Atmos. Sci., 27, 15-30.
- Prabhakara, C., B. J. Conrath, L.J. Allison and J. Steranka, 1971: Seasonal and geographic variation of atmospheric ozone derived from Nimbus 3. NASA TN D-6443, 61 pp.
- Priestley, C. H. B., 1967: Handover in scale of the fluxes of momentum, heat, etc, in the atmospheric boundary layer. Physics of Fluids, Supplement on Boundary layers and turbulence, 38-46.
- Prinn, R. G., 1977: On the radiative damping of atmospheric waves. J. Atmos. Sci., 34, 1386-1401.
- Ramanathan, V., L. B. Callis and R. E. Boughner, 1976: Sensitivity of surface temperature and atmospheric temperature to perturbations in the stratospheric concentration of ozone and nitrogen dioxide. J. Atmos. Sci., 33, 1092-1112.
- Reck, R. A., 1976: Stratospheric ozone effects on temperature. Science, 192, 557-559
- Roads, J. O., 1977: Numerical experiments on the sensitivity of an atmospheric hydrologic cycle to the equilibrium temperature. Ph.D. Thesis, M.I.T., 294 pp.

- Rodgers, C. D., 1967: The radiative heat budget of the troposphere and lower stratosphere. M.I.T. Planetary Circulations Project Report #A2, 99 pp.
- Sagan, C., and J. B. Pollack, 1967: Anisotropic nonconservative scattering and the clouds of Venus. J. Geophys. Res., 72, 469-477.
- Saltzman, B., 1970: Large-scale atmospheric energetics in the wave-number domain. Rev. Geophys. & Sp. Phys., 8, 289-302.
- and A. D. Vernekar, 1971: An equilibrium solution for the axially symmetric component of the earth's macroclimate. J. Geophys. Res., 76, 1498-1524.
- Sarachik, E. S., 1978: Tropical sea surface temperature: an interactive one-dimensional atmosphere-ocean model. Dyn. Atm. & Oceans, 2, 455-464.
- Sasamori, T., 1968: The radiative cooling calculation for application to general circulation experiments. J. Appl. Meteor., 7, 721-729.
- Schneider, E. K. and R. S. Lindzen, 1977: Axially symmetric steady-state models of the basic state for instability and climate studies. Part 1: Linearized calculations. J. Atmos. Sci., 34, 263-279.
- Schneider, S. H., 1972: Cloudiness as a global feedback mechanism: The effects on the radiation balance and surface temperature of variations in cloudiness. J. Atmos. Sci., 29, 1413-1422.
- 1975: On the carbon dioxide-climate confusion. J. Atmos. Sci., 32, 2060-2066.
- and R. E. Dickinson, 1974: Climate Modeling. Rev. Geophys. & Sp. Phys., 12, 447-493.
- and C. Mass, 1975: Volcanic dust, sunspots and temperature trends. Science, 190, 741-746.
- and W. M. Washington, 1973: Cloudiness as a global climatic feedback mechanism (abstract). Bull. Amer. Met. Soc., 54, 742.
- Schutz, C., and W. L. Gates, 1972: Supplemental global climatic data: January. R - 915/1 - ARPA, The Rand Corporation, Santa Monica, Calif., 41 pp.
- Sellers, W. D. 1965: Physical Climatology. Chicago: University of Chicago Press, 272 pp.

- Sellers, W. D. 1969: A global climatic model based on the energy balance of the Earth-atmosphere system. J. Appl. Meteor., 8, 392-400.
- 1976: A two-dimensional global climatic model. Mon. Wea. Rev., 104, 233-248.
- Spiegel, E. A., 1957: The smoothing of temperature fluctuations by radiative transfer. Astrophysical J., 126, 202-207.
- Stephenson, J. A., 1977: The vertical temperature structure of the mid-latitude troposphere: a simple model. M.S. Thesis, M.I.T., 78 pp.
- Stone, P. H. 1972a: A simplified radiative-dynamical model for the static stability of rotating atmospheres. J. Atmos. Sci., 29, 405-418.
- Stone, P. H., 1972b: On non-geostrophic baroclinic stability: Part III. The momentum and heat transports. J. Atmos. Sci., 29, 419-426.
- Stone, P. H. 1973: The effect of large-scale eddies on climate change. J. Atmos. Sci., 30, 521-529.
- Stone, P. H. 1978: Constraints on dynamical transports of energy on a spherical planet. Dyn. Atm. & Oceans, 2, 123-139.
- Telegadas, K., and J. London, 1954: A physical model of Northern Hemisphere troposphere for winter and summer. Scientific Rep. No. 1, Contract AF19(122)-165, College of Engineering, New York University, 55 pp.
- Tenenbaum, J., 1976: Spectral and spatial energetics of the GISS model atmosphere. Mon. Wea. Rev., 104, 15-30.
- Vonder Haar, T. H., and V. E. Suomi, 1971: Measurements of the Earth's radiation budget from satellites during a five-year period. Part I. Extended time and space means. J. Atmos. Sci., 28, 305-314.
- Wetherald, R. T., and S. Manabe, 1975: The effects of changing the solar constant on the climate of a general circulation model. J. Atmos. Sci., 32, 2044-2059.
- Yamamoto, G., 1962: Direct absorption of solar radiation by atmospheric water vapor, carbon dioxide and molecular oxygen. J. Atmos. Sci., 19, 182-188.
- Yanai, M., S. Esbensen and J. Chu, 1973: Determination of bulk properties of tropical cloud clusters from large-scale heat and moisture budgets. J. Atmos. Sci., 30, 611-627.

BIOGRAPHICAL NOTE

I was born on 8 October 1949 in Auckland, New Zealand, where I passed my childhood and attended local schools. The period 1963 to 1967 was spent at Auckland Grammar School, during which time I was credited with first place in the nationwide School Certificate examinations in 1965, and with winning a University Junior Scholarship in 1966.

In 1972 I started work for the New Zealand Meteorological Service in Wellington, spending the rest of that year in their training section, and gaining my first practical and theoretical knowledge of meteorology. After an interim period on shift duty, analyzing weather maps and typing forecasts, I learnt I had won a N.Z. National Research Advisory Council fellowship. This enabled me to study for a doctorate at an overseas university, and in September 1973 I entered the Department of Meteorology at M.I.T.